Multi-scale method for modeling thin sheet buckling under residual stress : In the context of cold strip rolling

Rebecca Nakhoul

ParisTech
INSTITUT DES SCIENCES ET TECHNOLOGIES
PARIS INSTITUTE OF TECHNOLOGY

MINES ParisTech

École doctorale n° 364 : Sciences Fondamentales et Appliquées

Doctorat ParisTech
T H È S E

pour obtenir le grade de docteur délivré par

l'École nationale supérieure des mines de Paris

Spécialité " Mécanique Numérique "

présentée et soutenue publiquement par

Rebecca NAKHOUL

le 19 Février 2014

Multi-scale method for modeling thin sheet buckling under residual stress – In the context of cold strip rolling

~ ~ ~ ~ ~ ~ ~ ~ ~ ~ ~ ~ ~ ~ ~ ~

Méthode multi-échelle pour la modélisation du flambage des tôles minces sous contraintes résiduelles – Application au laminage à froid

Directeur de thèse : **Pierre MONTMITONNET**

Jury

Pr. Ali LIMAM, LGCIE, Insa de Lyon, France	Rapporteur
Pr. Jean-Philippe PONTHOT, LTAS-MN^{2}L, Université de Liège, Belgique	Rapporteur
Pr. Hachmi BEN DHIA, MSSMat, Ecole Centrale de Paris , France	Examinateur
Pr. Jean-Michel BERGHEAU, LTDS, ENI Saint-Etienne, France	Examinateur
Pr. Michel POTIER-FERRY, LEM3, Université de Lorraine, Metz, France	Examinateur
Dr. Laurent BOISSONNET, Constellium CRV, Voreppe, France	Examinateur
Dr. Nicolas LEGRAND, ArcelorMittal Global R&D, Maizières Les Metz, France	Examinateur

MINES ParisTech
CEMEF – UMR CNRS 7635
1, rue Claude Daunesse, CS 207 – 06904 Sophia Antipolis Cedex, France

T H È S E

"FINAL".doc

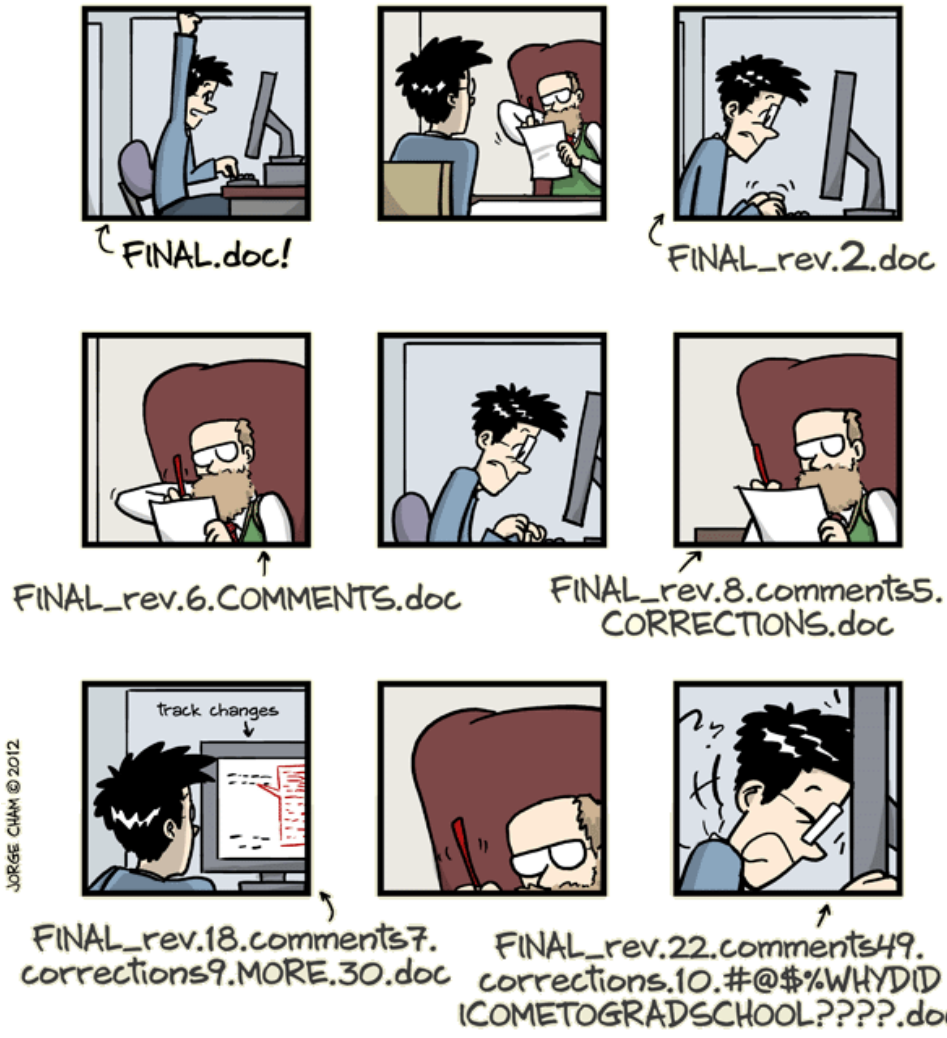

WWW.PHDCOMICS.COM

AVERAGE TIME SPENT COMPOSING ONE E-MAIL

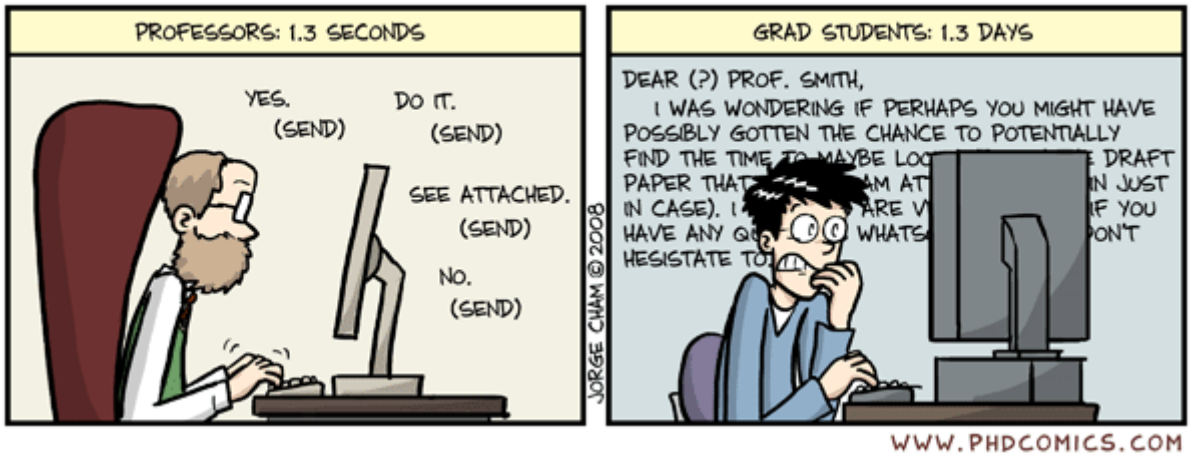

WWW.PHDCOMICS.COM

ACKNOWLEDGMENT

First of all, I thank my supervisor, Professor Pierre Montmitonnet for all of his support, investment, time and guidance. I thank him specially for his confidence in me when proposing such a heavy yet motivating subject.
I like to heavily thank Dr. Sami Abdelkhalek for all the help and guidance he offered during my three years of research.
This work wouldn't have gotten so far without the intellectual rigor contribution and collaboration of both Professsor Michel Potier-Ferry and Professor Hamid Zahrouni. So I would like to express my gratitude for them.

I like to thank Professor Jean-Michel Bergheau in ENI Saint Etienne for giving me the honor of chairing the jury. I thank equally Professors Ali Limam and Jean-Philippe Ponthot for agreeing to be the reviewers of this thesis. For their participation as members of the jury, I thank as well Professor Hachmi Ben Dhi, Professor Michel Potier-Ferry, Doctor Laurent Boissonnet and Doctor Nicolas Legrand.

For all the good times in CEMEF, I say 'HI' to my friends, Ana-Laura, Carole, Ghazza, Ghina, Hong Chau, Koffi, Lionel, Massiel, Meriem, Nadine and Ugo. It was a pleasure meeting you and sharing lovely times and memories with you all.
In addition, I like to thank Hayété Fadi for being there when needed surrounding me with all the support and Love he could offer.
Last but not least, I thank my family: Mom and dad, brothers and friends for supporting me through all the ups and downs. In particular I send a big shout out to Joseph, Simon and Rachelle.

PS: God, i didn't forget about you. I know I wouldn't have gotten this far without you by my-side. THANK YOU!

TO MY FAMILY

NOMENCLATURE

List of Acronyms

ANM	Asymptotic Numerical Method
BUR	Back-Up Roll
BURB	Back-Up Roll Bending
EAS	Enhanced Assumed Strain
FEM	Finite Element Method
FDM	Finite Difference Method
GHTS	Generalized Heterogeneous Time Stepping
IR	Intermediate Roll
IFM	Influence Function Method
RD	Rolling direction
WR	Work Roll
WRB	Work Roll Bending
Lam3/Tec3	The standard version of the rolling-stack deformation model
Lam3/Tec3-Abdelkhalek	Lam3/Tec3 coupled with the buckling model presented by Abdelkhalek
Lam3/Tec3-**MAN**	Lam3/Tec3 coupled with the shell buckling model **MAN**
Lam3/Tec3-**MSBM**	Lam3/Tec3 coupled with the multi-scale buckling model **MAN**
MAN	The shell buckling model based on ANM
MSBM	The Multi-Scale Buckling Model

List of Symbols

$\mathbf{a}$	dimensionless scalar used in **MAN**
a	dimensionless amplitude of a sinusoidal defect used in the multi-scale method
b	size of an Hermite finite element
$\mathbf{C}$	elasticity tensor
D	depth of the defect
$\mathbb{D}$	flexural rigidity of the plate
E	Young's modulus
F	rolling force
F_c	contact force
$\mathbf{F}$	deformation tensor
G	integration Gauss point
h	strip thickness
H	defect height
i, j	numbering subscript
it	Newton-Raphson iteration
l	strip width
L	strip/beam/column length
L_{bite}	bite length
L_{ref}	length of a reference fiber in a strip
$L_t(.)$	tangent operator used in **MAN**
$L_t^0(.)$	initial tangent operator used in **MAN**
$\tilde{l}$	wavelength of a sinusoidal defect
m, n	the number of half waves in the x,y-directions.
$\mathbf{m}$	number of levels of the Fourier series used in the multi-scale method
N	$\sigma.h$
N^{res}	$\sigma^{res}.h$
$\bar{N}_0$	$T_0.h$
N_0, N_2	Fourier coefficient of N used in the multi-scale method
q	half-wave number in the $x-$direction used in the multi-scale method
q_1, q_2	half-wave number in the $x/y-$direction
Q_x, Q_y	Shear forces
R	rolls radius
S	Piola-Kirchhoff stress tensor

S^{res}	residual stress tensor used in **MAN**
T_0	strip tension stress
U	mix variable containing the elementary variables of **MAN** or the multi-scale method
$U_{\mathbf{m}}$	Fourier coefficient of U
$\mathbf{U}$	strain energy
$\mathbf{U}_b$	bending strain energy
$\mathbf{U}_m$	membrane strain energy
V	total energy
u, v, w	displacement components respectively in the x, y, z directions
W	Buckling mode computed by **MSBM**
w_0, w_1	Fourier coefficient of w used in the multi-scale method: the average field and the first envelope
x, y, z	Space coordinates
α	wrap angle between the strip and the flatness roll
α_B	parameter used by Bush et al. to define a stress distribution
α_R	angle introduced by Roddeman et al.
β	$\beta = \widehat{(N_x; \vec{x})}$
β'	$\beta' = \widehat{(N_x + \frac{\partial N_x}{\partial x} dx; \vec{x})}$
β_R	ratio between the fictional and real membrane introduced by Roddeman et al.
γ	Green-Lagrange strain tensor
γ^c	compatible part of γ
γ^l	linear part of γ
γ^{nl}	non-linear part of γ
γ^{wr}	the wrinkling contribution in γ
$\tilde{\gamma}$	enhanced part of γ
Δh	strip thickness reduction
$\Delta\varepsilon$	strain increment computed by either **MSBM** or the buckling model by Abdelkhalek
$\Delta\mu$	bifurcation indicator used in **MAN**
$\Delta\mu f$	fictive perturbation force used in **MAN**
ε	strain tensor
ε^{ms}	mid-surface strain tensor

θ	angle between the principal and the reference axes in Lam3/Tec3-Abdelkhalek
λ	loading parameter
λ_{cr}	critical loading parameter
λ^{res}	loading parameter for the residual stress used in **MAN**
λ^{ten}	loading parameter for the strip tension used in **MAN**
λ_I, λ_{II}	buckling strain computed in the principal frame (I,II) by Lam3/Tec3-Abdelkhalek
μ	Coulomb friction coefficient
ν	Poisson coefficient
σ	stress tensor
σ^{res}	residual stress tensor
σ_{cr}	local critical stress value
σ_{MAN}	stress redistribution after buckling computed by **MAN**
Ω	Potential energy

Contents

INTRODUCTION

Metal sheets are widely used in many different industries and have many applications (see Figure 1): construction (covering roofs, decoration), automotive, aeronautical and more generally transport industry, domestic electrical appliances, packaging and many other applications including tables, storage units...

Figure 1: Different uses of metal sheets.
From left to right: In construction, for medical storage, in automotive bodies, in aircraft parts, in packaging and other applications such as tables.

1 Motivation of this study

The manufacturing of all these goods includes cold rolling as a major step, producing the semi-finished products which are then stamped or deep-drawn, bent, fine cut etc. (sheet metal forming). Stringent quality requirements are imposed on these semi-finished products. The geometry is one of the most critical. The format of the sheets (width / thickness) must be obtained precisely and with as little oversize as possible: extra-width is given for free (material cost) or has to be trimmed (processing cost and material loss). The thickness must be very precise and this is expressed in μm. Moreover, for ease of manipulation at the customers, the thickness variations across the width ("strip profile", or "strip crown") and along the length must be kept to a minimum.

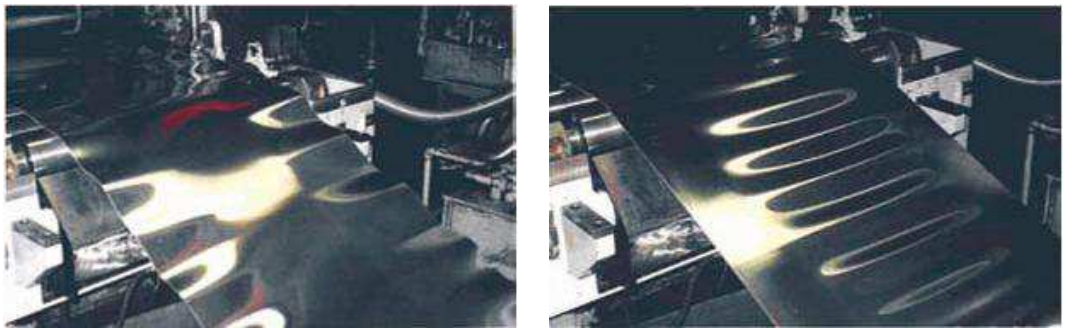

Figure 2: Different types of flatness defects encountered during cold rolling.
From left to right: Wavy edges and center buckles [IHI website].

The shape or flatness is most critical, as any departure from flatness may result in poor further processability and unacceptable defects of the final product. This is the subject of this memoir. The main categories of flatness defects are shown in Figure 2. They cause many problems for both producers and customers. They generate e.g. manipulation or assembling difficulties, put further processing at risk (stamping e.g.); moreover their wavy aspect may remain even after painting, which is not acceptable by the buyer of an expensive car or even a beverage can.
The common nature of these different shapes is elastic buckling, a mechanical instability which induces spurious out-of-plane displacements when a critical in-plane compressive load is applied on a thin product. Their origin is the roll elastic deformation which results in a heterogeneous thickness reduction of the sheet, hence differential elongation. This in turn causes self-balanced residual stress fields in the pre- and post-bite areas, with part of the sheet being in compression. Compression of a very thin sheet almost necessarily means buckling.

Once generated, these defects are difficult to eliminate. This requires careful inspection, further processing such as leveling, with the corresponding investment and labor cost. Flatness defects should therefore be prevented, or at least kept to such a low level that their correction will be a benign operation. This is done by implementing powerful and complex on-line measurement systems (stress-meter rolls), complex stands with numerous actuators (roll bending, shiftable rolls etc.) and automatic control techniques and algorithms, an overview of which is given in the next chapter.

All this equipment is best used if the mechanics of the flatness defects and the response to actuation are accurately known. One way to gain expertise in this multifactorial, highly coupled problem is to develop a rolling model capable of predicting the state of the cold rolled strip. Based on information extracted from such a model, one could adjust the rolling conditions and prevent flatness problems.

To be complete, surface aspect and mechanical properties are other important requirements. The latter is of interest to us as new, harder alloys are being put in service to help build lighter cars e.g. for environmental reasons. Harder alloys, leading to higher rolling loads and more roll deformation, result in enhanced flatness control difficulties.

A final remark: all these technical constraints must be combined with maximum productivity in order to produce even cheaper.

2 Aim of this study

ArcelorMittal and Constellium, two major metal sheets producers, own a Finite Element Method (FEM) based rolling model named Lam3/Tec3. In the case of sheet rolling, the Tec3 module couples roll thermo-elastic deformation with strip plastic deformation. This allows computing the stresses and strains in the roll bite, roll loads and torques, roll deformation and strip transverse thickness profile, thermal fields... It also determines the complex post-bite stress field resulting from heterogeneous strain.
This capacity is easily exploited for the simulation of rolling cases where sheets remain flat on the mill (under interstand or coiling *strip tension forces*). But the standard version of Lam3/Tec3 [Hacquin, 1996] is not equipped to predict defects if sheets do buckle on line. In such cases, one finds major differences between computed and measured post-bite stress profiles, because at buckling a thorough stress redistribution occurs, which is not captured in the absence of a buckling computing algorithm. It has been shown [Abdelkhalek, 2010]

that fortunately, this error made on the out-of-bite fields has no significant impact on the in-bite stress and strain fields, efforts and roll deformation, or final strip profile. If the ambition is limited to such results, the software works perfectly.
If the post-bite stress field is an expected result, or if a fortiori flatness defects are at stake, the standard version is no more sufficient. This limitation is usually fought by transporting the (incorrect) stress field into a structural mechanics tool which detects the buckling bifurcation, telling if a defect will be found or not; if it has a post-buckling capacity, it will also yield the shape of the defects (mode, wavelength, amplitude) and the (corrected) stress field. Note that both the shapes and stresses under strip tension forces (on the mill) and after tension cancellation (at the customers) are of interest.

Abdelkhalek extended the capacity of Lam3/Tec3 towards flatness problems by implementing two models:

1) Lam3/Tec3-Abdelkhalek performs a strong coupling of a fairly simple buckling model with the stress field determination, inside Lam3/Tec3. The strong coupling, at constitutive model level, allows any possible elastic-plastic deformation / buckling interactions to be taken into account. On the other hand, this model is limited to buckling on line, under tension forces. It can detect buckling, but does not give the shape of the defects. It does not require much more time than Lam3/Tec3 itself.

2) Lam3/Tec3-MAN couples in a staggered scheme the rolling software with a powerful shell FEM software concentrating on buckling and post-buckling studies thanks to an advanced non-linear solver based on a method called ANM (Asymptotic Numerical Method). The coupling procedure is unfortunately complex and tedious, and it requires long computing times. But it is able of quantify defects in all respects, describing the post-buckling state of the strip under tension as well as after tension cancellation, in a single computation.

The aim of this study is to develop a buckling model combining the advantages of both models. It should be able to detect the defective zone, describe the flatness defect (mode) and quantify it (amplitude and wavelength), predict the post-buckled state of the strip (including relaxed stresses). Yet it should be simple enough to be completely immersed in the rolling model Lam3/Tec3 in a strong coupling with stress determination. Indeed, the objective is to provide the industrial partners with two tools based on the same buckling theory:

- ◇ a decoupled version which can be used as a post-processor for the stress field determined by Lam3/Tec3;

◇ a coupled version, a rolling-buckling model, similar to Lam3/Tec3-Abdelkhalek but with an additional capacity to quantify the geometry of flatness defects.

3 Structure of this memoir

◇ Chapter 1 presents an overview of the rolling process for unfamiliar readers, with a focus on flatness defects: the rolling mills in so far as their features are connected with flatness defects, the mechanical origin of flatness defects, their measurement, control systems.

◇ Chapter 2 surveys literature on the different methods dealing with buckling, especially those which have been applied to flatness defects in rolling processes.

◇ Chapter 3 completes the description, exploiting one of those, the buckling model implemented in Lam3/Tec3 by Abdelkhalek, in a quick study of the effects of different rolling mill actuators on flatness defects.

◇ Chapter 4 describes the multi-scale buckling model (**MSBM**), the central development of this PhD work. The theoretical presentation is completed with simple applications to academic examples, with a comparison to results in the literature.

◇ Chapter 5 the multi-scale buckling model is used in a decoupled manner to predict on-line flatness defects for a real rolling operation, testing in addition its response to changing friction and work roll bending force.

◇ Chapter 6 explores the coupling of Lam3/Tec3 and **MSBM**, again confronting the results with previous work.

◇ Finally, general conclusions and recommendations are drawn.

CHAPTER 1

AN OVERVIEW ON THE ROLLING PROCESS

Life is not about waiting for the storm to pass....It is about learning to dance in the rain.

by Paulo Coelho

Contents

In this chapter, a quick overview of the rolling process is presented to simplify the subject to unfamiliar readers. The objective of this brief description is a better understanding of the procedure and the origin of the flatness problems and their different types. For more detailed descriptions, the readers are invited to refer to more complete sources such as [Roberts, 1978], [Roberts, 1988], [Ginzburg, 2009] and [Pittner & Simaan, 2011].

From start to finish, the metal forming process is a sequence of continuous sub-processes transforming raw material to semi-finished then, finished products ready to use. The most important ones are:
- Extracting the metal from its ore.
For Steel: Blast furnace / Electric furnace, Oxygen furnace (Figure 1.1).
For Aluminum: Electrolysis method. An Aluminum ore is first converted into pure aluminum oxide Al_2O_3 by the Bayer Process and then electrolyzed into molten aluminum.
- Continuous casting
- Reheating
- Descaling
- Hot rolling and cooling
- Pickling/Rinsing operations
- Cold rolling
- Quality Improvement and finishing
Next, we mainly focus on the steel making process as an example.

1.1 From Blast furnace to cold rolling: A survey of Steel making

In the blast furnace, iron ore, coal and limestone (the raw materials of steel) are continuously supplied through the top of the furnace. From below, a continuous blast of superheated air soften the raw materials and the chemical reactions transform them into molten iron. The molten metal and slag are tapped from the bottom and waste gases exit from the top. Adding steel scrap to molten iron into an oxygen furnace, it is now transformed into molten steel (see Figure 1.1). The molten metal feeds a continuous casting process containing different molds. The shapes of the molds will determine the forms of the semi-finished products. After cooling, straightening and cutting, blooms[1], slabs[2] and billets[3] are ready to be further processed to produce materials in standard form

such as plates, sheets, rails, tubes and structural sections.

The forces shift to forming and finishing which determine even more of the steel characteristics. The semi-finished shapes are refined to final specifications utilizing two main rolling processes[4] : initial rolling steps are done by Hot Rolling then followed by Cold Rolling if needed (see Figure 1.2). This present study is dedicated to flat rolling processes; in particular, to cold rolling of thin strips and to the industrial difficulties encountered during this process, such as flatness defects. From now on, only flat rolling is considered. Since a metal is highly resistant to shaping when cold, it must be hot rolled first. Thus, slabs are reheated in furnaces where the evolution of the piece temperature is monitored. Once the right temperature is reached, the piece is descaled to remove any built up scale then fed into hot rolling mills. During this step, pieces are deformed above their recrystallization temperature. The main reason for hot rolling is that at elevated temperatures, metals weaken and become more ductile. Thus, the thickness reduction will be much easier.

Hot rolling offers the possibility of producing a very large shape change and/or reduction in a single working step, without causing large amounts of internal stress or cracks. Hot rolling can remove some defects that occur in cast metals. It can close gas pockets (bubbles) or voids in a cast billet; and it may also break up non-metallic slag which sometimes get caught in the melt (inclusions).

The surface finish of hot worked metal tends to be coarse and rough because: i) The rolls wear and ii) there is the constant problem of scale formation on the surface of the hot metal due to oxidation.

During hot rolling steps, scale is formed on the metal. The scale must be removed before cold rolling, otherwise surface defects occur. Several processes are used. In the aluminum industry e.g., the skin of the just cast plate is scraped (machined away), no further descaling operation is needed. In steel hot rolling, water jet descaling is by far the most frequent: a high pressure water jet (150 bars) impacts the slab / strip surface; the resulting brutal cooling and the temperature gradient build up very high stresses which fracture the oxide, peel it off and the fragments are finally washed away by the water. This is done first at the exit of the reheating furnaces, and then a second time after the roughing mill (i.e. before the entry into the finishing mill). As oxide re-grows in the finishing mill and on the run-out table, descaling is needed again just before cold rolling. This is usually done by pickling in an hydrochloric acid bath, then, the strip is rinsed to remove any excess acid.

[1]Blooms: bars 150 to 400 mm^2

[2]Slabs: parallelepipeds 500 to 1800 mm wide and 50 to 300 mm thick

[3]Billets: bars 40 to 150 mm^2

[4]Rolling process is the process of plastically deforming metal drawn by means of friction into the gap

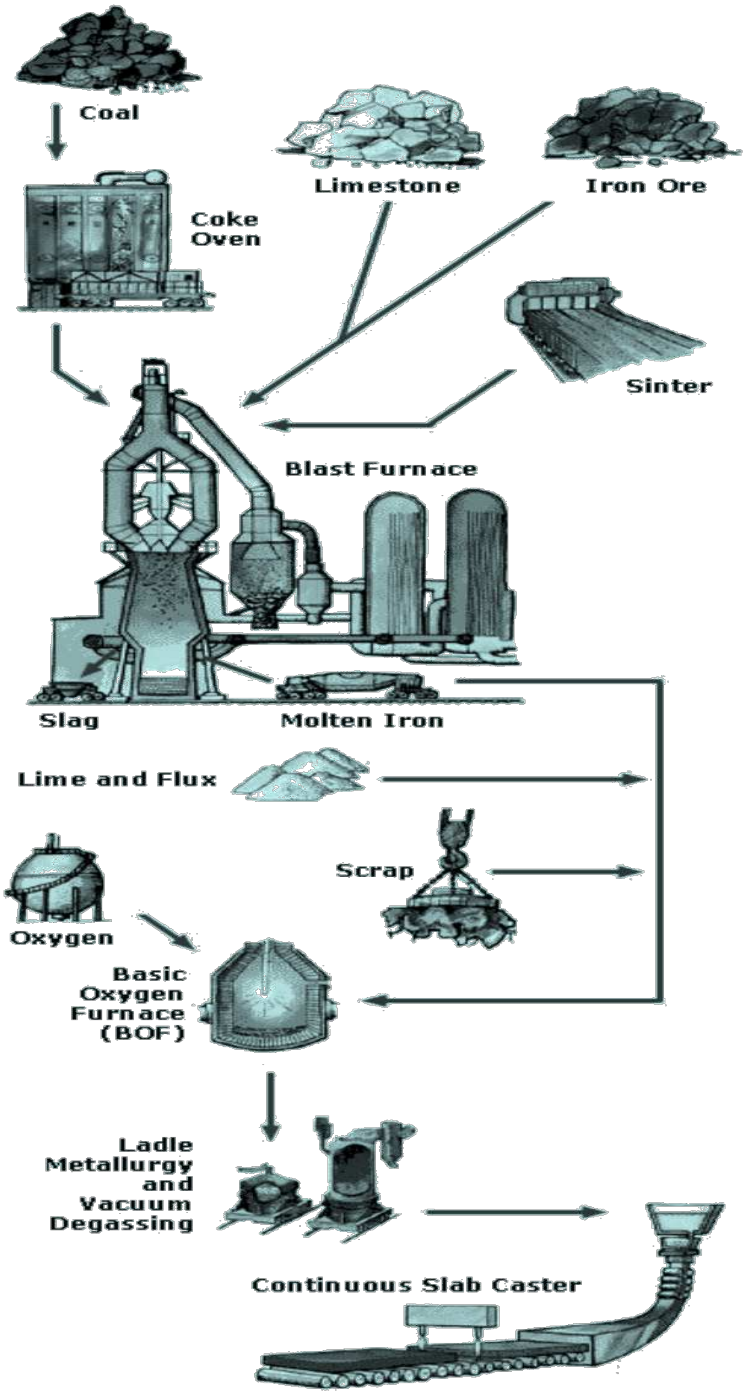

Figure 1.1: The Steel making process [ltvsteel website]

formed by two revolving rolls. The compressive forces applied by the rolls reduce the thickness or shape the cross section area of the rolled material, where the final geometry of the product depends on the contour of the roll gap. For a better understanding and examples, see Figure 1.2

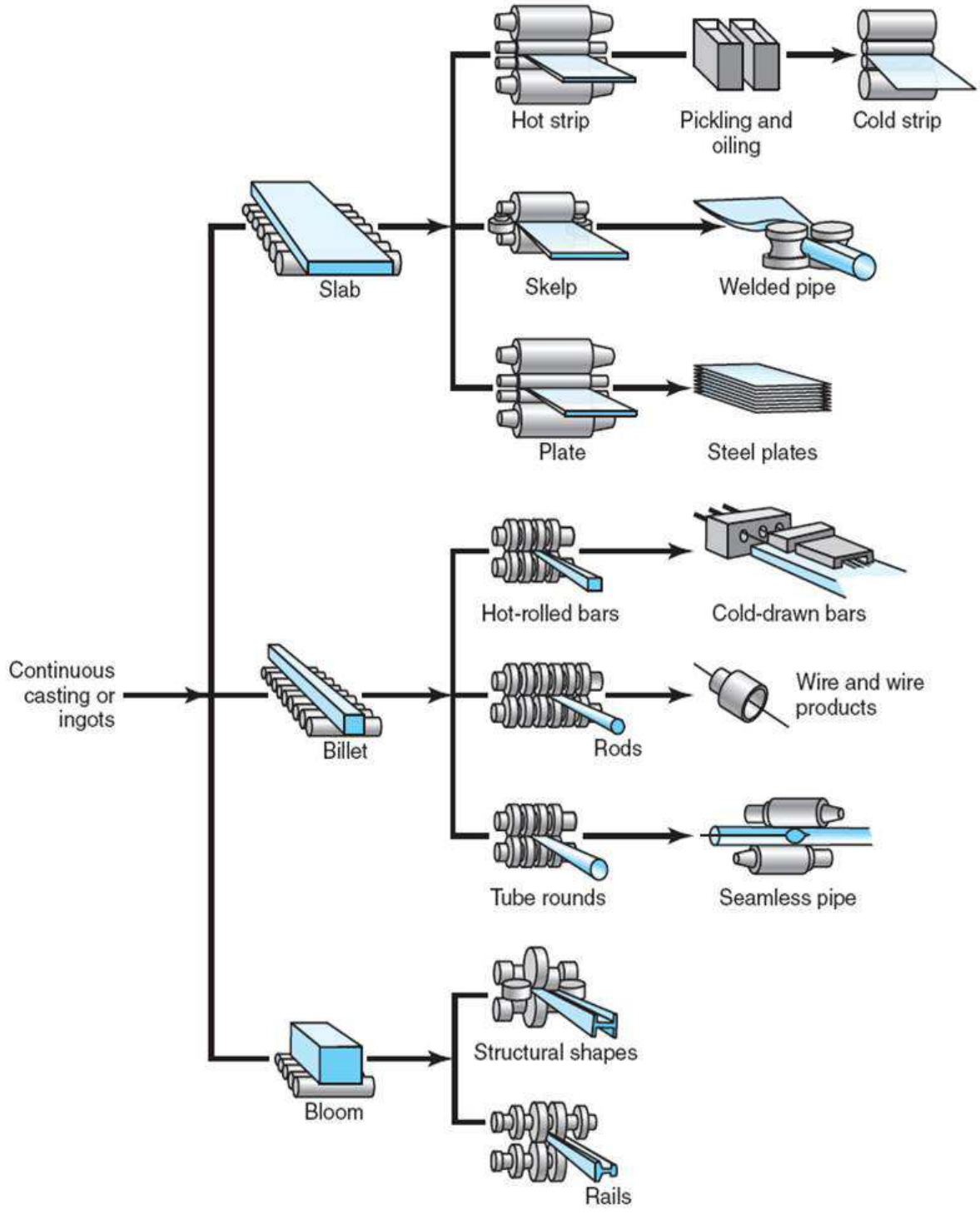

Figure 1.2: Schematic outline of the most important flat-and-shape-rolling operations [Steel website]

1.2 Cold rolling

Metals are plastically deformed at room temperature. Cold rolling is applied after hot rolling to obtain and enable accurate dimensions of the final product as well as a better surface finish and good mechanical properties.
Cold rolling presents several advantages:
i) Thinner walls are possible (thickness < 0.5 mm) ,
ii) Dimensional accuracy can be excellent because the product does not have to shrink on cooling.
iii) Usually there is no significant oxidation.
iv) The final properties of the sheets can be closely controlled and, if desired, the high strength obtained during cold rolling can be retained; alternatively high ductility can be restored by annealing if needed.

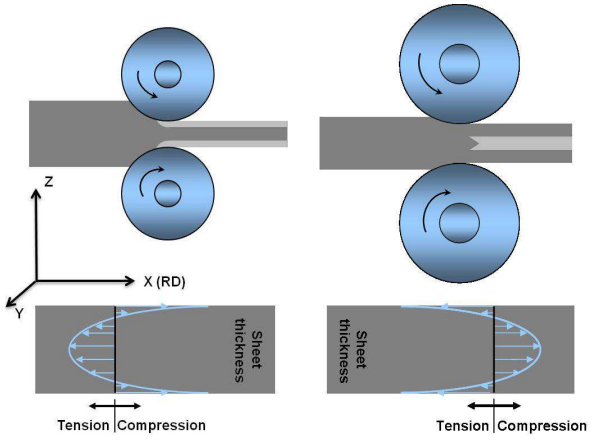

Figure 1.3: Residual stress generated during rolling processes (after [Kalpakian & Schmid, 2003]).

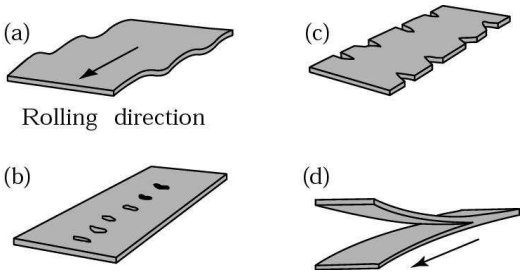

Figure 1.4: Rolling defects: (a) wavy edges; (b) zipper cracks in the center of the strip; (c) edge cracks; and (d) alligatoring (after [Hosfor & Caddell, 1993]).

Defects may be present on the surfaces or in the products. They are undesirable as they compromise surface appearance and adversely affect strength, formability and other manufacturing characteristics. Figure 1.4 shows different types of defect found during cold rolling. For example, cracks are due to poor material ductility at the rolling temperature. However, the main focus of this study is a class of geometrical defects called flatness defects, detailed in section 1.4. Indeed in cold rolling, sheets ($0.1\ mm \sim 1\ mm$ thickness) show a great sensitivity to residual stress[5] which can generate some flatness defect. Figure 1.3 illustrates the appearance of a non-uniform residual stress, in the thickness for instance.

After cold rolling, coils may be shipped directly. A growing proportion of steel strips is however coated to improve / diversify surface properties. In most cases, strips undergo

[5]Residual stress: stress trapped in the rolled product due to nonuniform plastic deformations

further plastic deformation processes (sheet metal forming), which requires ductility. Annealing[6] is introduced in such cases. For carbon steel, it must be followed by temper rolling (or skin pass rolling), a small reduction pass (0.3 -3%) which improves flatness and imparts a specific surface topography on the strip surface[7].

1.3 Cold rolling mills

1.3.1 Description of the main stand geometries

There are many types of rolling mills -to a certain extent, one cannot find two of a kind. In modern cold rolling practice, two-high, four-high, six-high and cluster-type mills, including the Sendzimir mills, constitute the principal examples of single-stand mills. They differ by the number and size of their rolls.
Rolls are classified as work rolls (WR), intermediate rolls (IR) or backup rolls (BUR) depending on their role.
The work rolls are the ones that enter directly in contact with the rolled material and apply the forces that will reduce the section. They are made of material harder than the strip: cast iron, cast and forged quenched and tempered hot working tool steels, High Speed Steels for hot rolling, high-Cr steels for Al cold rolling... The barrel may have a slightly larger diameter in the center, in which case it is said to have a "crown". This feature and its impact on flatness will be discussed in section 1.4.3.
The back-up rolls are intended to provide rigid support to the work rolls to prevent bending upon rolling load. They have usually a larger diameter than the work rolls, up to two or three times greater.

The Two-High mill (illustrated in Figure 1.5) is the oldest type used for cold reduction of steel. Nowadays it is used mainly for temper rolling[7] . The Four-High Mill (illustrated in Figure 1.6) is by far the most frequent mill stand for cold rolling of strip. It is essentially formed by two work rolls backed up with two bigger rolls. Their action is complemented by profile and flatness actuators, the most common are the bending of the mill rolls (Work Roll Bending - WRB - or Back-up Roll Bending - BURB).
The six high-mill arranged in six layers (illustrated in Figure 1.7) finds application mainly in final passes during cold rolling. Once the strip goes through the gap, the shiftable tapered intermediate rolls move laterally in a way to align or dis-align their edge with the strip edge. As shown in Figure 1.8 b), the tapered shape of the intermediate roll can

[6] Annealing is a heat treatment in which the metal is heated, then cooled under controlled conditions to relieve internal stresses and/or soften the metal and restore its ductility
[7] For more details check section 1.4.4 a)

offer more space for the work roll to deflect and thus, less reduction near the edge and less waviness. Combined with the roll bending -used to correct center defects-, this mill allows optimally flat sheets.

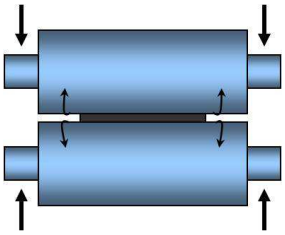

Figure 1.5: Two-High Mill (after [Roberts, 1978])

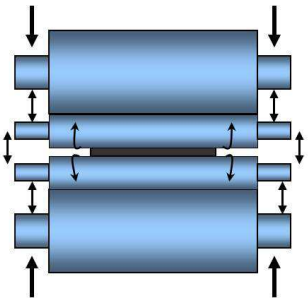

Figure 1.6: Four-High Mill (after [Roberts, 1978])

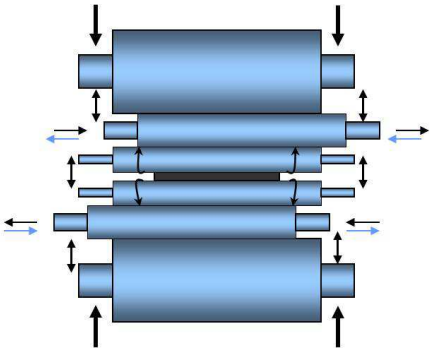

Figure 1.7: Six-High Mill with shiftable intermediate rolls (after [Roberts, 1978])

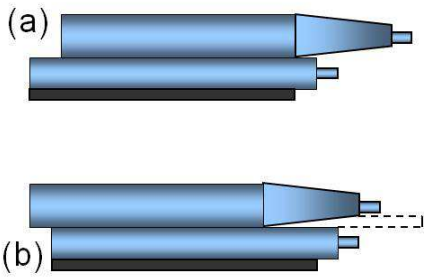

Figure 1.8: Tapered shiftable rolls

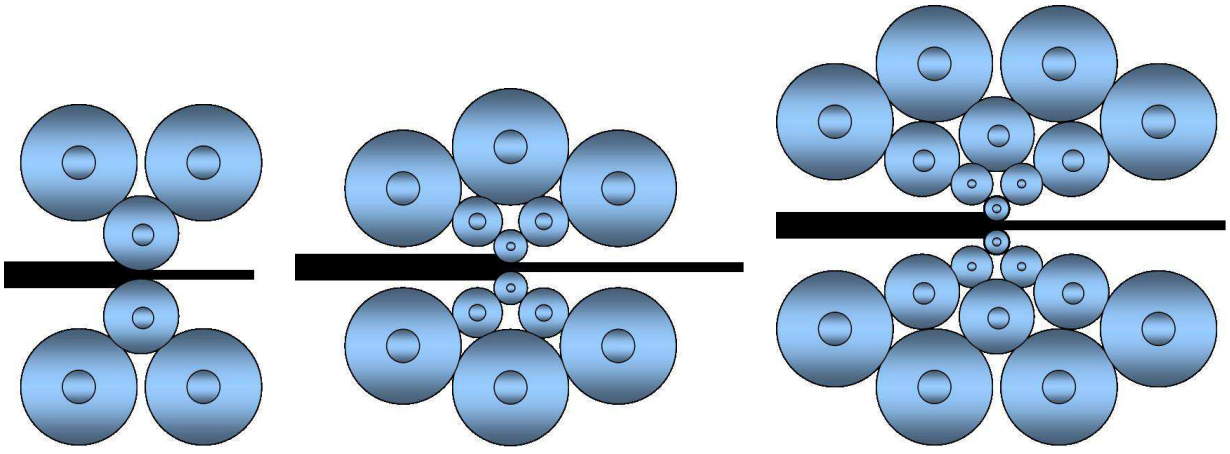

Figure 1.9: From left to right: Six- roll Mill, Twelve-roll Mill, Twenty-roll cluster Mill (known as Sendzimir mill) (after [Roberts, 1978]) .

To utilize still smaller diameter work rolls while maintaining rigidity, the BUR must support the WR not only against vertical bending, but also in the horizontal plane. Six-roll cluster mills organized in four layers (illustrated in Figure 1.9.a)) were put into use for this purpose. However, there is a limit to the BUR / WR ratio attainable due to steric hindrance (the BUR must not touch each other, while making contact with the WR). To overcome this difficulty, stands with BUR organized in several layers have been designed, such as the twelve-high mill illustrated in Figure 1.9.b). One step further, the Sendizmir mills were developed in the 1950s (Figure 1.9.c)) and gained worldwide acceptance for two fundamental reasons. First, these mills can be built more economically than non-reversible four-high mills of comparable reduction capacity. Second, the small work rolls (diameters usually 40 - 100 mm) of this cluster mill promised lower working forces and a much closer accuracy than other mills [Roberts, 1978].

1.3.2 A brief, simple analysis of the roll stack design

With the aim of explaining the different kinds of stands and their evolution, it is important to clarify how roll sizes affect the roll force, and how roll force affects elastic roll deformation. The latter is written as follows in terms of R the roll radius, h and l the strip thickness and width, L_{bite} the roll-strip contact length, Δh the strip thickness reduction , μ the friction coefficient and σ_0 the average yield stress of the strip:

$$F = \sigma_0.l.L_{bite}.(1 + \kappa.\mu.\frac{L_{bite}}{h}) \text{ and } L_{bite} = \sqrt{\Delta h.R} \tag{1.1}$$

This equation is not sufficient to accurately predict the roll force, although this or similar forms can be used for on line models, thanks to the fitting factor κ. It gives a global idea on its evolution with the different interesting parameters such as the roll radius. It shows that the roll force is at least proportional to the square root of the roll radius through L_{bite}. For given friction coefficient, width and thickness, a smaller radius gives a lower roll force to achieve the same reduction Δh.
Lower roll load means either that the mill can be built less strong and therefore cheaper, or that harder or wider strip can be rolled on the same mill.

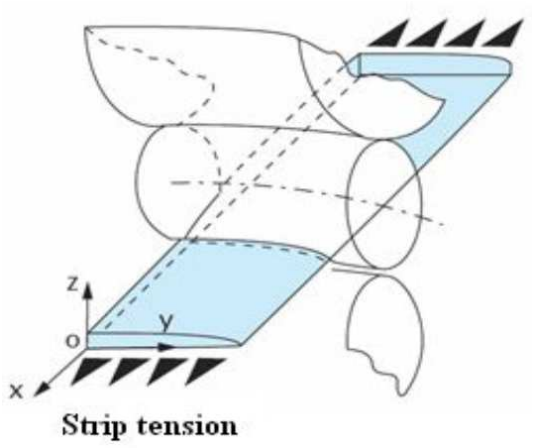

Figure 1.10: Sketch of the roll deformation under the rolling load, showing roll bending and flattening at contact [Gratacos et al., 1992.b)].

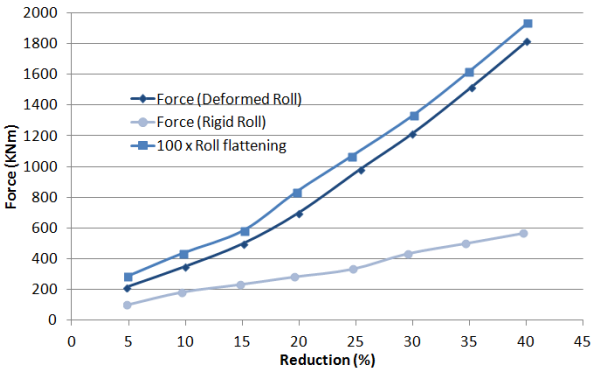

Figure 1.11: The roll flattening component of roll deformation is roughly proportional to the rolling load [Montmitonnet, 2003].

The second point of importance is roll deformation, schematically described in Figure 1.10. Under the contact stress field, rolls undergo a complex 3D elastic deformation, which is often summarized by two major components :

1) roll bending: considering a roll as a (quasi) cylindrical beam loaded by the rolling force F distribution on part of its length (Figure 1.12), an estimate of the deflection at any point x along the beam can be given [Gere & Goodno, 2012]:

$$\begin{aligned} \delta_x &= \frac{F}{24EIL}[2L'x(2L-L')(x^2-L^2) - xL(x^3-L'^3) \\ &- x(L-L')^4 + L(x-L')^4] \\ I &= \frac{\pi \mathbb{D}_{beam}^4}{64} \end{aligned} \tag{1.2}$$

in which L and $\mathbb{D}_{beam}$ are respectively the cylindric beam length and diameter, F the rolling load applied on a part L' of its length, E Young's modulus and I the area moment of inertia.

This shows that bigger rolls are much more resistant to bending. Hence, if small WR are preferred, big BUR are necessary. The formula also shows that the problem is most critical for wide mills (large L) and of course for hard materials (large contact stress).

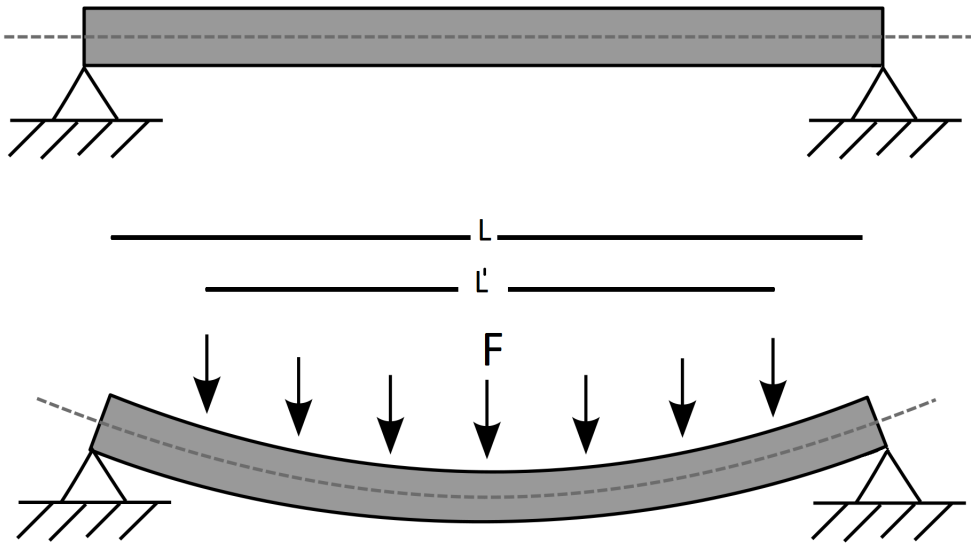

Figure 1.12: Deflection of a simply supported beam under uniform load

2) roll flattening is the local shortening of a roll radius under the compression undergone in the bite. It is limited to the immediate vicinity of the contact surface, and is to a first approximation proportional to the local load distribution or stress (see Figure 1.11) : an important feature is that the larger the roll radius, the larger flattening is (in μm), and the more difficult it is therefore to obtain precise dimensions and a precise shape. Near the edges, the transition between the contact area and the roll outside the contact gives birth to the edge drop defect, an excess of reduction which is also strongly connected with flatness defects in the case of thin strips. Roll flattening and its effect on e.g. the contact length is often estimated (very approximately) by Hitchcock's formula (based on approximations which make the roll / strip contact amenable to Hertz elastic contact) [Hitchcock, 1935] :

$$R = R_0 \left(1 + \frac{16(1-\nu^2)}{\pi E} \frac{F}{\Delta h}\right) \tag{1.3}$$

E and ν are the roll elastic parameters, R_0 the initial and R the deformed roll radius, F the roll load per unit width. As F in turn depends on R as shown above, an iterative scheme is necessary to fully exploit this simple formula (a graphical, simple coupling has been in use for a long time). The formula shows that low reductions as well as high loads are critical factors for roll flattening. For instance, low reduction on a very thin strip under rather high friction (such as occurs in temper rolling) gives high F and small Δh, resulting in a very severe roll deformation problem,

contrary to intuition [Krimpelstätter, 2005].

1.3.3 Multi-stand mills

The total reduction needed cannot be achieved in one single pass. Taking the example of hot steel strip rolling, starting from a cast slab 250 mm thick, it takes about 12 passes to reach thickness between 6 and 1.5 mm (average reduction per pass: 27% to 35%). Cold rolling down to 0.3 - 0.8 mm typically takes 5 more passes, and two stands may be necessary to roll it further down to 0.13 - 0.15 mm as needed for 'can making'. Part of this hot rolling stage can be made on a reversing mill, i.e. a single stand in which the slab passes several times, reversing the rolling direction. This makes the investment lower, but the productivity moderate. To produce millions of tons, a series of non-reversing stands is preferable.

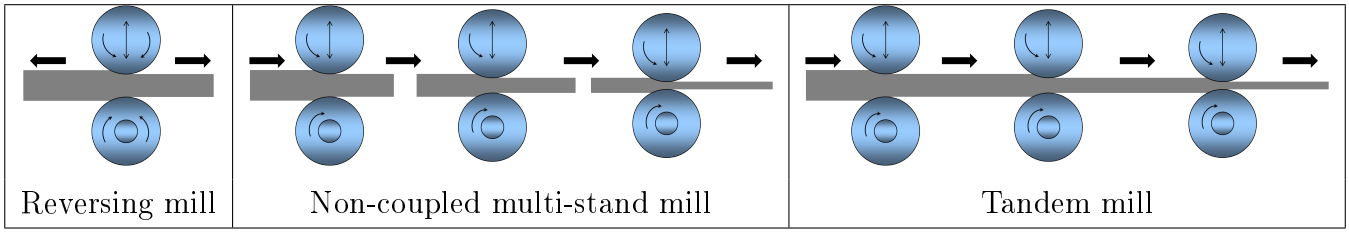

Figure 1.13: Schematic solutions for multi-pass rolling.

Thus, three types of hot strip rolling lines can be found:

i) the whole hot rolling schedule is performed on a reversing mill.

ii) a non-coupled multi-stand mill followed by a 7-stand tandem mill is the standard for large production steel plants.

iii) a reversing mill for the "roughing" stage (first passes on thick slabs) followed by a tandem "finishing" mill; this the case most of the time for light alloys (5 stands finishing mill) and sometimes for steel (6 or 7 stands finishing mill)

For aluminum as well as for steel, the standard cold rolling mill is a tandem mill (3 stands e.g. for Al, 5 stands for carbon steel). But stainless steel, or hard carbon steels (more generally, hard, thin strips), are cold rolled on reversing cluster mills such as Sendzimir mills.

The tandem / non tandem character is important as it conditions the application of strip tensions. These are forces applied in the rolling direction between the stands i) to

guide the strip, keep it in the center of the mill and reasonably flat, ii) to decrease rolling loads - in plasticity, if a tensile stress is applied in RD, the compressive contact stress in ND decreases by the same amount, iii) to take part in flatness control. On reversing cold mills, tensions are applied by coilers, whereas inter-stand tensions are applied by the roll differential velocity from stand to stand in tandem mills. Of course, on a non-coupled multi-stand mill without coilers such as on the hot roughing mill, no tension can be applied (it is not necessary at this stage anyway).

1.3.4 Problem definition

In this study, four-high mills are used for all the simulations (Figure 1.14), where the applied front and back tensions are essential : i) to ensure the flatness of the rolled strip, ii) to prevent the strip from strolling in the transverse direction and iii) to reduce the rolling force.
Common actuators in this mill are bending work and back-up rolls, spot cooling system and tension changing (check section 1.4.3 for a more complete description).

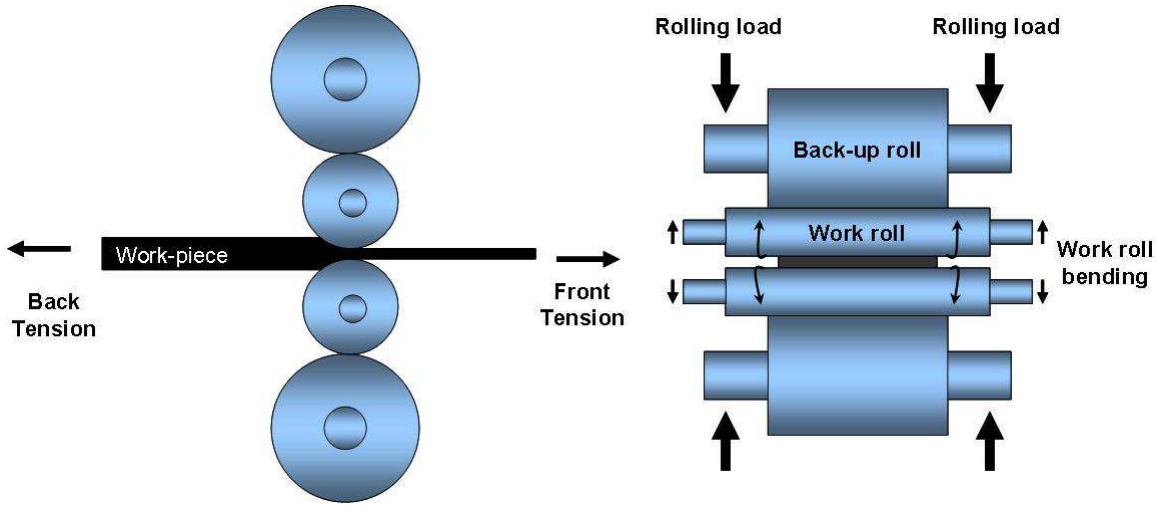

Figure 1.14: 4-hi mill

As mentioned earlier, the next and final step after Cold rolling is the "Quality, flatness Improvement and Surface finishing". Before proceeding, one must understand exactly why it is indispensable: what are flatness defects, their origins and how to prevent their appearance.

1.4 Flatness problems in cold rolling

In this section the problem of flatness defects encountered during cold rolling is presented as well as the best known flatness measurement methods and different actuators available to control and prevent their appearance. Unless specified otherwise, the sources of information used in this section are [Roberts, 1978], [Roberts, 1988] and [Ginzburg, 2009].

1.4.1 Phenomenology of Flatness defects

The term flatness in cold rolling means "the ability of the strip to lie flat when no tension is applied".
During cold rolling, there is no significant width increase of the strip normally but the thickness reduction taking place in the bite leads to proportional increase in the length. To obtain the best strip flatness possible, both the strip thickness profile and the roll-bite profile under load should match perfectly. Otherwise, the thickness reduction and its corresponding length increases non-uniformly across the width of the strip and therefore flatness defects appear.
Another important notion is the "manifest" or "latent" defect. This identification introduced by Wistreich in [Wistreich, 1968] states that "flatness problems may be there, invisible, even if the strip appears to be flat". Residual stress may be trapped inside the metal and can generate flatness defect once the strip is trimmed for instance.

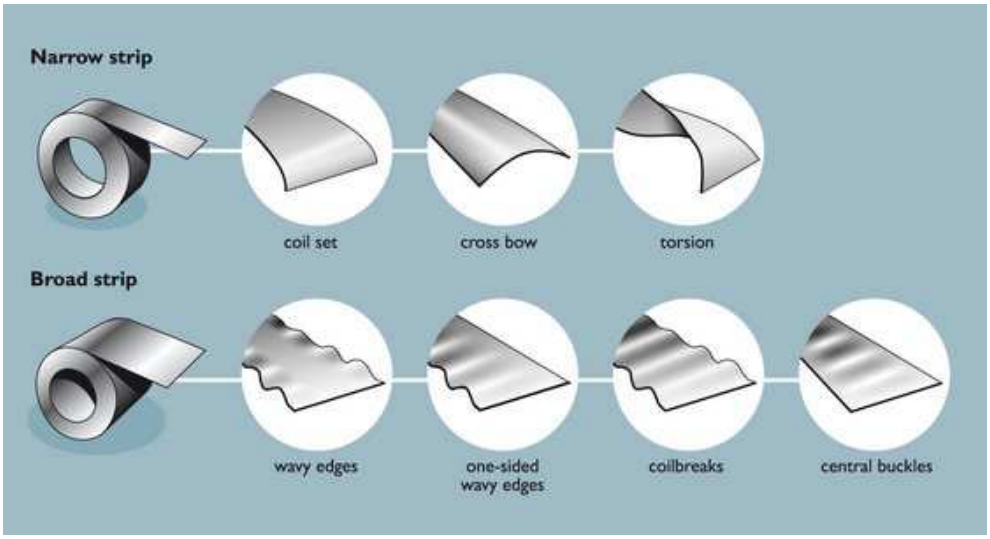

Figure 1.15: Flatness defects in cold rolling: bow shaped defects and waviness defects.[ARKU website]

Two major flatness problems arise during cold rolling (illustrated in Figure 1.15) and

could be corrected using different approaches:

-Bow shaped defects like coil set, cross bow and torsion. The main reason for these types of defects is a corresponding asymmetry between the work rolls. Coil set refers to a dis-symmetric $\sigma_{xx}(z)$ residual stress profile, possibly due to a difference between the rolls speeds or diameters. Cross bow betrays a dis-symmetric $\sigma_{xx}(z)$ stress profile, whereas torsion shows complex gradients of stress. These developable defects (in the mathematical sense of surface geometry) are reversible and can be corrected by passing the strip through a simple plastic bending process.

-Waviness defects (non-developable) like wavy edges, one-sided wavy edges, coil-breaks and central buckles are the most complex types. The elongation gradient combined with a nonuniform residual stress distribution generates waves across the strip length: The difference in length is balanced by residual stress and waves appear once the amount of locally compressive residual stress exceeds the buckling limit of the strip. Wavy edges and center buckles are the most common ones during cold rolling.

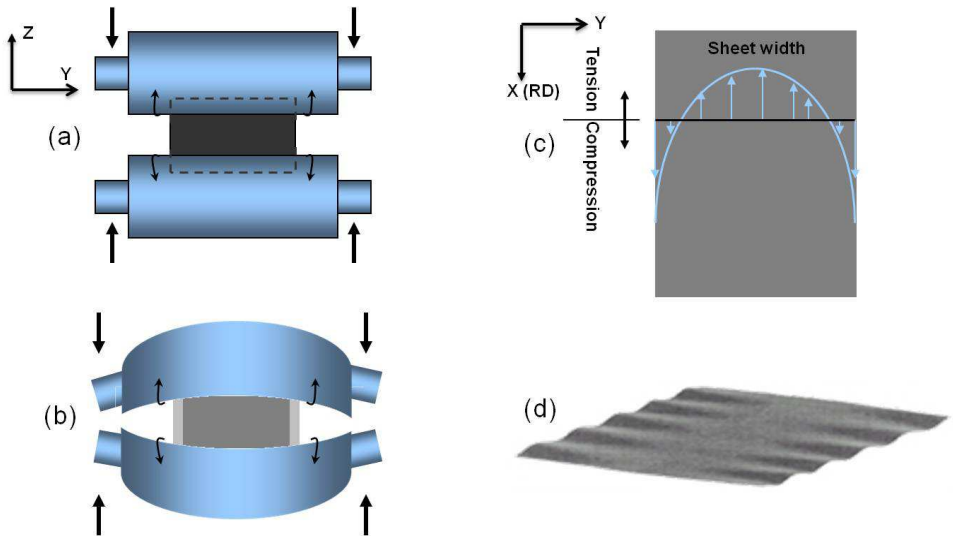

Figure 1.16: From a neutral crowned roll to wavy edges: An increase in rolling force causes more work roll deflection, the space between the rolls is smaller near the edges (b) and gives rise to bigger reduction on the edge, leading to a compressive residual stress on the sides (c) and finally waves along the strip edges (d). (after [Kalpakian & Schmid, 2003])

Buckling edges are the result of a mismatch of strip crown[8] and work rolls crown[8] due to roll flattening near the edge (narrow waves) or to excessive roll bending (wide waves) under higher load. The reduction is thus not uniform, the strip is thinner on the edges. This means that residual stresses are compressive on the edges and if higher than the buckling limit, they cause wavy edges (Figure 1.16).

[8]Check Appendix A

Buckling center is the converse of wavy edges, when non-uniform reduction generates compressive stresses in the center. Note that waviness can also occur in the width or diagonally in the strip. This study is however devoted only to waviness occurring in the rolling direction (across the length of the strip as illustrated in Figure 1.17). All these waviness types cannot be eliminated simply and require post-rolling leveling processes (see section 1.4.4) .
The high demand for an increasing productivity, thinner sheets and optimal quality at the same time requests necessarily a better understanding and control on appearance of flatness defects in the first place. To this aim, different methods and control actuators are presented next in section 1.4.3.

1.4.2 Flatness Measurements

As mentioned earlier, the conventional expression of flatness is the maximum of deviation from a horizontal flat surface (Figure 1.17), described through wave height H and wavelength $\tilde{l}$. The width (or depth) of the defect denoted D was introduced in [Yuen et al., 2003] and used to give even richer characterization for wavy edge problems. The width of the buckles is an interesting parameter particularly in rolling where producers aim to minimize as possible the width of these types of defects. In addition to this conventional expression, two flatness parameters were introduced for characterizing flatness of sheets presenting longitudinal buckles: the steepness and the flatness index.

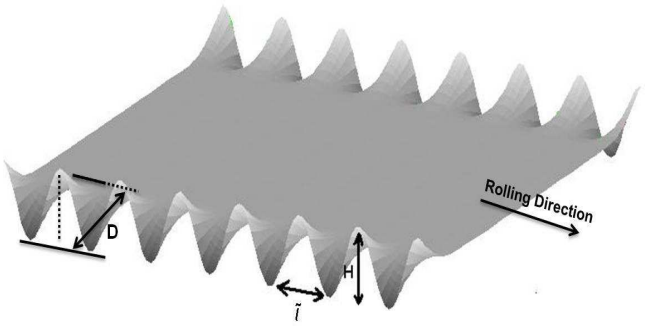

Figure 1.17: Representation of a sheet strip showing wavy edges.

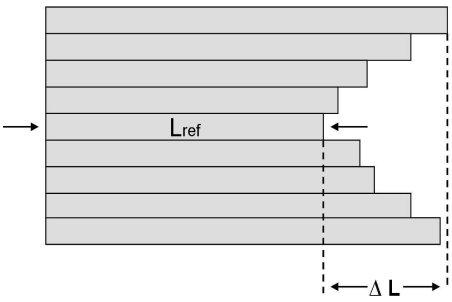

Figure 1.18: Schematic representation of the 'slit' method where the strip is considered as a series of longitudinal cuts of differing length

The steepness index S is defined according to Eq. (1.4) for a sheet presenting waves of height H and a wavelength $\tilde{l}$.

$$S = \frac{H}{\tilde{l}} \tag{1.4}$$

The second parameter is the flatness index noted I. In order to measure the exact flatness,

a series of longitudinal cuts can be made, the elastic stress is relaxed as in (Figure 1.18). Using the length of one of these strips as a reference L_{ref} (usually the shortest one), the I-unit value is defined as follows:

$$I = \frac{\Delta L}{L_{ref}}.10^5 \tag{1.5}$$

where ΔL is the difference between the concerned cut and the reference cut. The scaling with 10^5 was introduced for this flatness unit (I-unit[10]) definition. Since it is impossible to slice every strip to assess its quality, it is important to be able to continuously measure this flatness defect online. In the case of latent defect, with the application of tension, the wave may not appear and the latter method is unable to measure flatness without some adjustments:
Hooke's law expresses ΔL in term of F_e (N) the force (which can be measured) required to elongate the cuts length ΔL from the reference Length L_{ref}:

$$E\frac{\Delta L}{L_{ref}} = \frac{F_e}{A} \tag{1.6}$$

where A is the cross section area and E the Young's Modulus.
Combining Eqs. (1.5) and (1.6), the flatness index I for two adjacent cuts i and j is calculated as:

$$I_{ij} = \frac{\Delta L_{ij}}{L_{ref}} = \frac{F_{eij}}{AE} \tag{1.7}$$

1.4.2.1 Online measurement system for latent defects

a) **Flatness Rolls** During rolling, some defects may not show because of the applied tension giving the strip a flat appearance. The best way to assess the flatness of the strip post-rolling (after releasing the tension), is to be able to measure the residual stress distribution. A flatness rolls system is mainly formed by a roll used as a deflector roll in the mill equipped with a series of sensors (up to 60 sensors with a resolution of 52 mm) giving measurements on each zone. The roll should be placed with a slight deflection with the strip, the radial force is measured under the applied tension, then the stress value given by each sensor i is determined as:

$$\sigma_{xx}^i = \frac{F_c^i}{2.h^i.y^i.sin(\frac{\alpha}{2})} \tag{1.8}$$

where α is the wrap angle between the strip and the roll, h^i, y^i, F_c^i and σ_{xx}^i are respectively the thickness, the width, the force of contact and the stress value determined on the zone i.

[10] $1I - unit = 10\frac{\mu m}{m}$

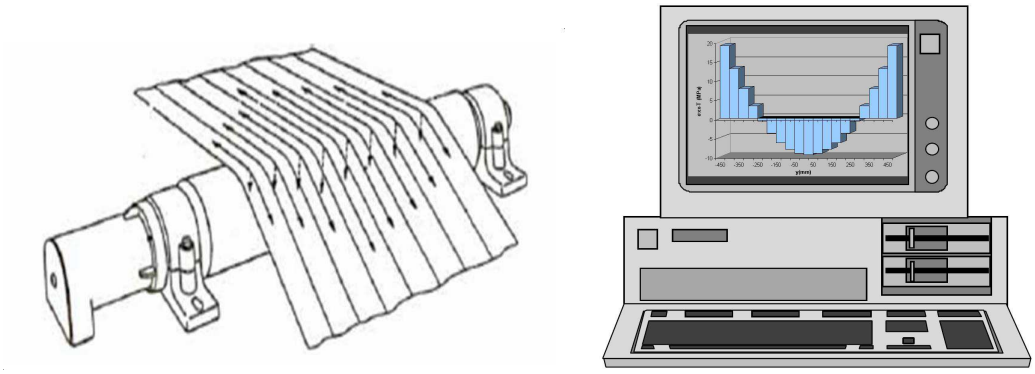

Figure 1.19: On the left: Schematic representation of the 'flatness rolls' measurement system. On the right: An example of measurement

Once the stress distribution is determined, one can predict the post-rolling flatness by deducting the tension T_0. If the profile of $\sigma_{xx} - T_0$ (illustrated in Figure 1.19) shows a compression in the center for instance, the expected defect is center buckles.
Stress measuring systems present some uncertainties due to several deficiencies. For instance, in the case of thermal originated stress, a stress distribution is measured and analyzed to predict the type of the flatness defect. Once the strip cools down, the same distribution is no longer valid and the expected defect is not necessarily the same as predicted earlier. Another limitation is due to insufficient number of sensors on the edges where most of the problems occurs during cold rolling.

b) **Speed Sensor Meter** The first flatness system based on speed sensors was developed by Person in [Person, 1964]. It is based on the idea of non-uniform deformation in cold rolling which contributes in a difference in speed and length from a zone to another. Using the tangential speed, flatness was determined in terms of $\frac{\Delta V}{V_{ref}}$ where V_{ref} is the reference speed value. And since $\frac{\Delta V}{V_{ref}}$ is directly proportional to $\frac{\Delta L}{L_{ref}}$, once again the flatness can be measured using Eq. (1.7).
Note that this measurements system can easily be disturbed due to sliding between the rolls and the rolled piece. In addition, it is not effective in the case of manifest defects; the measurements are disturbed by the defects translated as noise affecting the corresponding data.

1.4.2.2 Online measurement system for manifest defects

a) **Shapeline** The shapeline system, illustrated in Figure 1.20, is based on a laser line triangulation. The line is spread in one dimension to make a fan of light. The shape of the line determines the flatness of the strip. A straight line means the strip is flat.

Otherwise, the flatness measure is determined by using the deflection of the line.

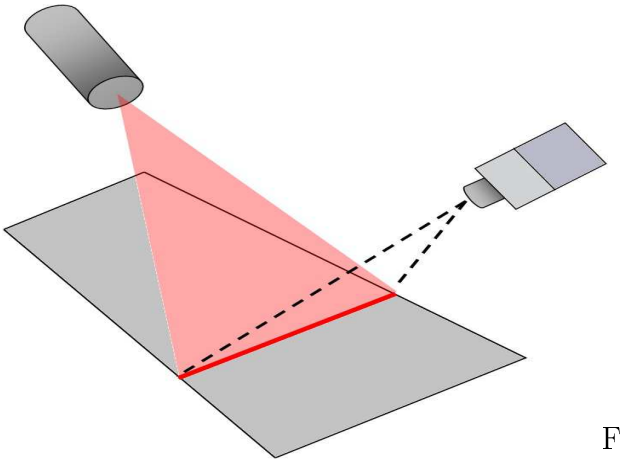

Figure 1.20: Schematic representation of the 'shapeline' flatness measurement system

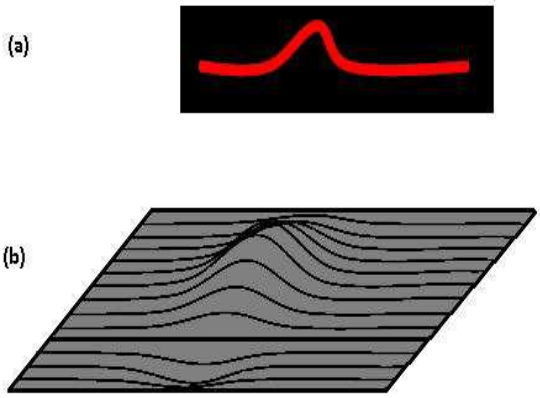

Figure 1.21: (a) an example of the camera photo of the defect line, (b) the topography describing the shape of the sheet.

This procedure can be repeated periodically and series of the 2D-shapelines observed with a 2D matrix camera can be transformed into a 3D topographical data (see Figure 1.21b)).

b) **Moiré Method** was first developed by Meadows et al. in [Meadows et al. , 1970] and Takasaki [Takasaki, 1970], then applied to flatness measurements during strip rolling in [Kantola et al., 1996] and [Paakkari, 1998]. This system presented in Figure 1.22 consists in projecting a grating on the rolled strip. It is called reference plane grating. Then the deformed grating is captured. The aim is superposing the reference image and the image of the actual strip. The result is a Moiré image (Figure 1.23) saved, treated and converted into 3D topographic image representing the strip contour and flatness.

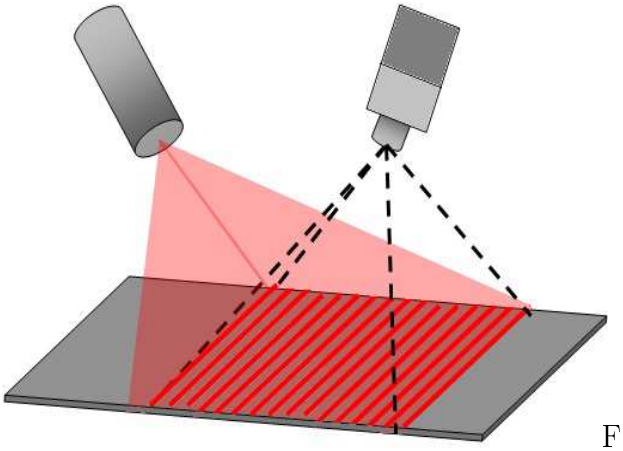

Figure 1.22: Schematic representation of the 'Moiré projection' flatness measurement system

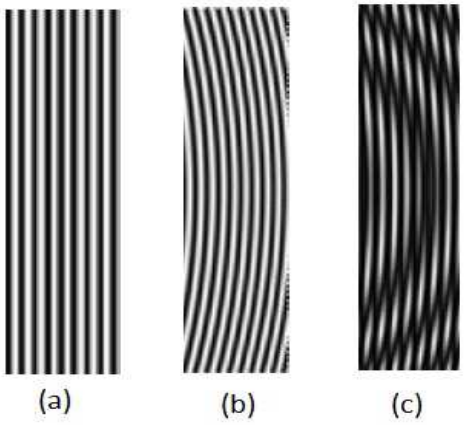

Figure 1.23: (a) projected reference grid, (b) captured deformed grid (c) Moiré photo superposing the latter two grids and illustrating the state of the defective sheet.

Shapeline, Moiré as well as any other laser based measurement method show serious difficulties for high speed rolling processes. That's why these types of measurement systems are normally installed on inspection lines or in the case of low speed rolling process.

c) **Meplaca**

Figure 1.24: The 'Meplaca' measurement system [Indwitech website]

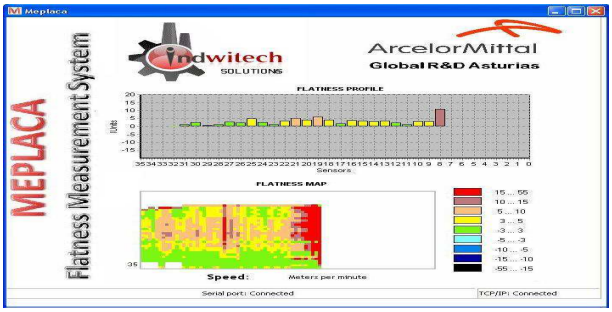

Figure 1.25: An example of manifest flatness defect map measured by Meplaca [Arcelormittal website]

Developed by Arcelormittal, Meplaca is a new contactless measurement device for strip flatness online (see Figure 1.24) . It is basically a series of condensers aligned to match the width of the rolled sheet, distant of a few centimeters (5 cm $\sim$ 10 cm) from each other (strip/condenser). This distance should be chosen carefully in the case of a sheet presenting strong geometrical defects so that the device does not run up against the strip. When the rolled strip is passing by, Meplaca records the variation of the electric tension. It corresponds to the distance separating the condensers from the sheet sur-

face. These variations are transformed using a specialized software into a geometrical description which allows viewing the state of the strip immediately during rolling (Figure 1.25) . Despite its capacities, this device is considered expensive compared to the latter ones, and shows calibration difficulties. As stated earlier, the distance between the strip and the condensers should be chosen carefully for each strip depending on the type and the magnitude of the manifest defect.

1.4.3 Online Flatness control and actuators

As explained in section 1.4.1, uneven roll gap leads to non-uniform reduction i.e. different length increase from strip fiber to another. Thus flatness defects will take place. To adjust the roll gap, several methods consisting in adjusting the work roll shape are available and thus improving the shape and flatness of the strip. We cite :

a) **Roll bending** Roll bending is the most powerful method to change the shape of the work roll. A positive bending results in a negative roll crown; it offers less reduction in the center and therefore is useful to prevent the appearance of center buckles. A negative bending force gives a positive crown (less reduction on the edges) and therefore is used to correct wavy edges.

Note that, the work roll crown can be adjusted also by the use of bending backup rolls or intermediate (shiftable or not) rolls. Even better, these two actuators (WR bending and BR bending) can be combined (linearly) as illustrated in Figure 1.26 and the resulting bending can prevent the appearance of more complex type of waviness such as quarter buckles.

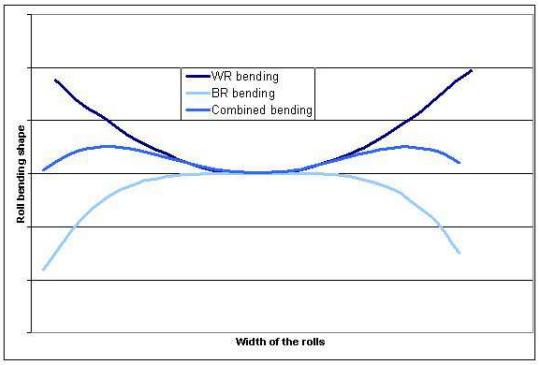

Figure 1.26: Combined work roll bending and backup roll bending- issued from a Lam3/Tec3 simulation.

b) **Changing Tension** Changing the applied strip tension is considered also an important and very effective actuator for on-line flatness of thin strips (0.5 mm). Roberts states in [Roberts, 1978] that "The choice of the tension depends on the chosen friction coefficient and the shape of the contact zone". If the tension increases, roll separating force decreases and results in more crowned roll. Thus, if the strip presents center buckles (the center is too long), the solution is to decrease the work roll crown i.e. the application of a smaller tension stress. Note that for a given coefficient of friction, the interval of tension variation is narrow. A drastic increase/decrease can cause

breaking/tracking strip problems.

c) **Shiftable intermediate rolls** Mills organized using intermediate rolls can be equipped with a shiftable rolls system (For instance in the six-high mill illustrated previously in Figure 1.7). These rolls can move back and forth in the axial direction, adjusting their edges on the edges of the strip or work roll, and can clear efficiently the appearance of edge defects.

d) **Changing lubricant** The rolling lubricant is another important actuator. Lubrication reduces friction between the rolled strip and the work rolls. As a consequence, it reduces the roll separating force, and therefore rolls present less flattening effects and roll wear which improves the surface of the rolled strip. If lubricity is improved in the roll bite for instance, roll flattening[11] is reduced and the roll diameter increases and causes a local over-rolling. This can be clearly used to over/under-roll certain thinner/thicker areas to ensure a uniform reduction and prevent the appearance of waves.

e) **Differential Watering/Cooling rolls** Cold rolling mills use large amounts of energy and it is transformed later on into heat trapped in the work rolls. As a result, work rolls present a thermal crown[12] which causes control and flatness problems. Localized cooling by spraying water on the problematic zone (different patterns, pressure flow and temperatures) is the best solution for this irregularity. It reduces the roll crown and minimizes control problems.

1.4.4 Post-rolling Flatness Improvement

As for flatness improvement, many procedures are available like Temper or skin pass rolling and leveling processes.

a) **Temper rolling process** is the process of light cold rolling sheet steel (reduction $0.3\% \sim 3\%$) . It is used to improve flatness, to minimize stretching and straining, to fix the gauge consistency and to add hardness to the steel sheet and finally to obtain a specific surface texture. Two-high mills are perfect match for this process.

[11] Roll flattening means the roll diameter is smaller than its initial value, in this case it will cause a local under-rolling.

[12] Due to friction, plastic deformation and energy used by the mills, a high amount of heat can be generated resulting in expansion of the rolls and giving them a crowned shape called 'thermal crown'.

b) **Roller leveling process** is used to improve flatness of the strip after hot rolling. The strip is passed through a number of work rolls organized into two layers and aligned on a common center point (illustrated in Figure 1.27). The rolls bend the strip slightly to deform it plastically in a way to have uniform thickness all over the strip. Rolls are closer together at the entry than the exiting side. This arrangement insures less bending toward the exit and prevents therefore introducing additional residual stress to the strip. The result strip is straightened and free of defects.

c) **Tension leveling process** treats sheets to improve flatness after cold rolling. The combination tension-bending pulls the sheet beyond its yield point. Shape imperfections are corrected in this process where the strip is passed around a series of rolls to initiate bending and stretching, finally the strip is flattened out to correct the bend (Figure 1.28). The result strip is ideally flat and is free of residual stresses.

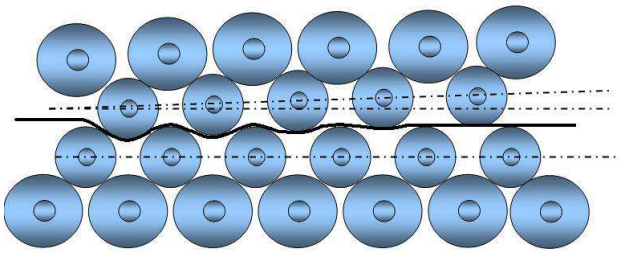

Figure 1.27: Roller leveling process (after [Roberts, 1978]).

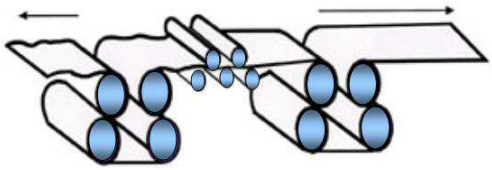

Figure 1.28: Tension leveling process (after [Roberts, 1978]).

1.5 Résumé en Français

Dans ce chapitre une introduction générale du procédé de laminage est présentée pour simplifier le sujet aux lecteurs peu familiers. Le but de cette brève description est une meilleure compréhension des différents types de défauts de planéité et leurs origines durant une opération de laminage à froid.
La notion de "flambage sous contraintes résiduelles" a été introduite en catégorisant les défauts en deux types: défaut manifeste et défaut latent. Les dispositifs de mesure de planéité les plus connus (rouleau de planéité, moiré, shapeline ....) ont été présentés. En plus, les actionneurs de planéité disponibles en ligne pour corriger et éviter l'apparition de ces défauts ont été exhibés. Enfin, quelques procédés de post-traitement utilisés pour améliorer la planéité des tôles minces ont été brièvement exposés.

CHAPTER 2

LITERATURE SURVEY: SHEETS AND PLATES BUCKLING THEORIES

Our greatest weakness lies in giving up. The most certain way to succeed is always to try just one more time.

by Thomas A. Edison

Contents

As described previously, the form of the gap between the rolls affects the shape of the rolled strip. The main reasons are the work rolls elastic deformations such as the rolls crown, flattening and bending. These deformations create a non-uniform reduction in the width of the strip and generate a heterogeneous residual stress distribution. If the compressive residual stress goes past the critical value tolerated by the strip, it buckles and becomes wavy. Since the defect is manifest, the gap between the critical value and the compressive stress is balanced by the appearance of geometrical displacements. The residual stress is once more modified to respect the equilibrium state after buckling and can affect what happens in the bite.The defective sheet can be improved by post-rolling operations, which is time and energy consuming. Rather than correcting defects, it is better to avoid them, i.e. to control flatness during rolling (Chapter 1). Many parameters are available for that, corresponding to the diversity of the physical phenomena and the flatness actuators installed on the rolling mills. Their complexity requires models of prediction, which can be only Computational.
After this summary, one can deduce that the rolling process is complex and every aspect affecting the residual stress should be included. The ideal rolling model should couple many aspects:

a) The elastic deformation of the work rolls (flattening, bending..);

b) The elastic-plastic deformation of the rolled strip in-bite;

c) The buckling out of the bite and its effect on the bite;

d) The thermal deformation and thermal stress development.

Note that since this study is dedicated to the appearance of flatness defects during cold rolling, all thermal effects were neglected (check Chapter 3 section 3.5). As for coupling the rolling load with the stack deformation, the existing work roll-deformation model "Tec3" will be used in coupling with "Lam3". The objective is to find a suitable buckling model capable of describing the state of the defective strip and adequate to be coupled with the rolling model "Lam3".
The literature proposes several approaches. So far, most of these models are based on an uncoupled approach dealing with the problem in two parts:

- A computation of the rolling process without buckling, giving the residual stresses.

- A calculation of the rolled sheet buckling under the effect of these residual stresses.

Taking into account that buckling is a direct consequence of what occurs under the bite, a strongly coupled analysis bite-buckling is preferable for a better representation

of the complexity of this process. The only exceptions treating a model of buckling integrated in rolling are the models of Counhaye [Counhaye, 2000] and Abdelkhalek [Abdelkhalek, 2010]. In this chapter, a survey of the available modeling methods is presented with the aim of finding powerful approaches to carry out buckling and post-buckling computation -with capacity to be coupled with the existing rolling model "Lam3"-.
First a quick description of the treated problem is presented, next different modeling methods for general buckling and post-buckling problems are explored. Finally, the last part is devoted to describing the approaches applied to rolled strip flatness.

2.1 Description of the problem

The modeling of buckling and post-buckling is a very delicate problem. The aim is to find methods able to describe the stability of the problem. Stability can be defined as "the capacity of the system to return to balance when slightly disturbed". For instance, in the case of strips under compressive stress, the solution stops being stable once the residual stress exceeds the critical value noted σ_c. To describe the problem, it is necessary to study the behavior of the system at and beyond its critical point.
Buckling theories for structures began with the study of Euler for beam buckling [Euler, 1744]. Next, von Kármán formulated equations describing buckling of thin elastic plates under compressive stress and these equations bear his name [von Kármán, 1910]. Many studies were based on a variant form of these equations and presented different methods and solutions for many different applications. We mention in particular, the semi-analytical approaches presented by Fisher [Fisher et al., 2001] and Bush [Bush et al., 2001] with application to strip rolling.
Later on, a new theory for buckling of elastic structures taking into account the initial imperfections, was presented by Koiter in [Koiter, 1970].
Koiter used in his study, the bifurcation and stability theories. They first appeared in the mathematical studies of Poincaré [Poincare, 1885] and Schmidt [Schmidt, 1908] where asymptotic expansions were used in almost every buckling and post-buckling theories. Many recent studies, like the ones presented by Potier-Ferry in [Potier-Ferry, 1987] and Budiansky in [Budiansky, 1974], were developed using modern mathematical approaches of the bifurcation theory and presented several applications in the domain of buckling and post buckling problems.

2.2 Modeling methods for buckling and post-buckling problems

The literature survey presented next, introduces available methods capable of describing the buckling problem (i.e. determining the critical load of stability and the mode of the defect), as well as the post-buckling problem (i.e. the magnitude of the defect).

2.2.1 General methods for determining the critical load

The critical load of a system can be determined using two methods: by **direct resolution of the equilibrium equations** or by **approximate methods based on an energetic description of the problem**.

2.2.1.1 Column buckling: Equilibrium Method

According to the equilibrium method, the critical values of applied forces may be found from the solution of the governing differential equation where the solution takes often a sinusoidal form. This assumption is a form of a semi-inversed method used frequently in the theory of elastic stability, in which a specific solution is chosen and helps find which problem it solves.
For a column of length l with both ends pinned, subjected to a force P as illustrated in Figure 2.1, the equation describing the deflection is

$$E.I.\frac{d^2y}{dx^2} - P.y = 0 \tag{2.1}$$

Where E is Young's modulus and I is the inertia moment.
Note that the solution y should verify the boundary conditions presented below:

$$y = 0 \text{ for } x = 0 \tag{2.2}$$

$$y = 0 \text{ for } x = L \tag{2.3}$$

A proposed solution by Timoshenko [Timoshenko & Gere, 1961] takes the form

$$y = Asin(kx) + Bcos(kx) \tag{2.4}$$

where $k = \sqrt{\frac{P}{EI}}$, and A and B are two constants determined using the boundary conditions.

Equations (2.2) and (2.3) give respectively ($B = 0$) and ($A = 0$ or $sin(kl) = 0$) i.e. $kl = n\pi$ where n is an integer to be determined.
Replacing all the above information in the governing equation (2.1) , the critical load is determined as follows:

$$P_{cr,n} = \frac{n^2\pi^2 EI}{L^2} \tag{2.5}$$

n is the number of half-waves -developed in the axial direction of the column- and for every n corresponds a different buckling mode.
The lowest buckling load corresponds to the first buckling mode i.e. $n = 1$. So ,

$$P_{cr} = \frac{\pi^2 EI}{L^2} \tag{2.6}$$

is the smallest critical load and corresponds to the classical solution of Euler [Euler, 1744]. Figure 2.2 illustrates the first three buckling modes for $y = Asin(\frac{n\pi x}{L})$. $n = 1, 2$ and 3 means that the column buckles respectively into one, two and three half-waves. Note that A, the buckling amplitude, remains undetermined.

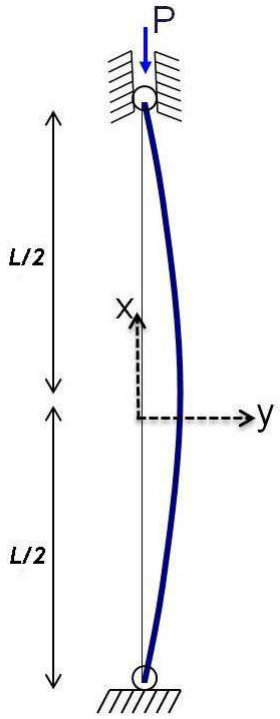

Figure 2.1: Column under compressive force

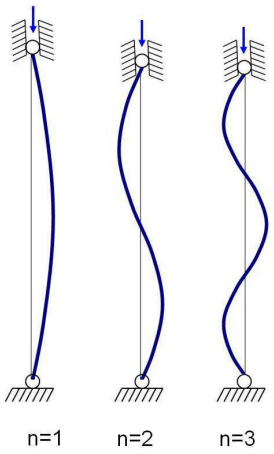

Figure 2.2: The first three column buckling modes

In reality, it is nearly impossible to find exact solutions for practical applications. The equilibrium method shows serious mathematical difficulties when determining the buckling loads for complex geometry, mixed boundary conditions and complex loads. Under these circumstances a possibility for obtaining a rigorous solution of the differential

equation becomes very complicated. Therefore, the use of the energy method can be very advantageous.

2.2.1.2 Column buckling: Energy Method

Energy methods are based on the principle of the existence of a minimum of energy when the system is at its equilibrium state. If $V = U + \Omega$ is the total energy of the system where U and Ω are respectively the strain and potential energy, the stable equilibrium state is defined by the set of the following equations:

$$\delta V = 0 \text{ and } \delta^2 V > 0 \tag{2.7}$$

To compute the critical buckling load, equation (2.8) is often used i.e. the load at which the equilibrium passes from stable to unstable ($\delta^2 V$ changes from positive to negative).

$$\delta^2 V = 0 \tag{2.8}$$

in which δ indicates the variation of V. Many methods where proposed to find the critical load such as Rayleigh's coefficient method, Rayleigh-Ritz method and Galerkin's method. The same example presented earlier is used to illustrate the energetic approach method by Rayleigh-Ritz method for instance. This method proposes to write the solution y as a linear combination of a family of functions $(\Phi_i)_i$: $y = \sum_m y_m.\Phi_m$.
In this $1D$ buckling problem, the solution y is written as

$$y(x) = y_1.\Phi_1(x) + y_2.\Phi_2(x) \tag{2.9}$$

where Φ_1 and Φ_2 are two shape functions that verify the boundary conditions $y = 0$ for $x = -\frac{L}{2}$ and $x = \frac{L}{2}$

$$\Phi_1(x) = x^2 - \frac{L^2}{4} \text{ and } \Phi_2(x) = x^4 - \frac{L^4}{16} \tag{2.10}$$

The total potential energy of this mechanical system is

$$V = U + \Omega = 2.\frac{1}{2}\left[\int_0^{L/2} EI(\frac{d^2y}{dx^2})^2 dx - P\int_0^{L/2}(\frac{dy}{dx})^2 dx\right] \tag{2.11}$$

Combining Equations (2.9), (2.10) and (2.11), the following form is obtained.

$$V = y_1^2(2EIL - \frac{PL^3}{6}) + y_2^2(\frac{9EIL^5}{10} - \frac{PL^7}{56}) + y_1y_2(2EIL^3 - \frac{PL^5}{10}) \tag{2.12}$$

Thus the second variation of the total potential energy is computed using the partial derivatives with respect to y_1 and y_2.

$$\mathbf{M}(\delta^{\mathbf{2}}\mathbf{V}) = \begin{pmatrix} \dfrac{\partial^2 V}{\partial y_1^2} & \dfrac{\partial^2 V}{\partial y_1 \partial y_2} \\ \dfrac{\partial^2 V}{\partial y_1 \partial y_2} & \dfrac{\partial^2 V}{\partial y_2^2} \end{pmatrix} = \begin{pmatrix} 4EIL - \dfrac{PL^3}{3} & 2EIL^3 - \dfrac{PL^5}{10} \\ 2EIL^3 - \dfrac{PL^5}{10} & \dfrac{9EIL^5}{5} - \dfrac{PL^7}{28} \end{pmatrix} \tag{2.13}$$

The critical load is the smallest value for which the matrix $\mathbf{M}$ is singular i.e. the determinant is equal to zero.

$$P_{cr} = 9.875\frac{EI}{L^2} \tag{2.14}$$

Note that the critical loads obtained in both equations (2.6) and (2.14) are quite similar; knowing that the chosen shape functions eq. (2.10) can affect the precision of the computed solution.

2.2.1.3 Plate buckling: Equilibrium Method

Let us consider a simply supported plate subjected to uniform compressive stress as shown in Figure 2.3(a). The buckling problem is described by the following set of equations:

$$\begin{gathered} \frac{\partial^4 w}{\partial x^4} + 2\frac{\partial^4 w}{\partial x^2 \partial y^2} + \frac{\partial^4 w}{\partial y^4} = \frac{1}{\mathbb{D}} N_x \frac{\partial^2 w}{\partial y^2} \\ w = 0 \text{ and } \frac{\partial^2 w}{\partial x^2} = 0, \text{ for } x = 0 \text{ and } x = L \\ w = 0 \text{ and } \frac{\partial^2 w}{\partial y^2} = 0, \text{ for } y = 0 \text{ and } y = l \end{gathered} \tag{2.15}$$

where $\mathbb{D}$ is the plate flexural rigidity.
A proposed solution of equation (2.15) takes the following form

$$w = Asin(\frac{m\pi x}{L})sin(\frac{n\pi y}{l}) \tag{2.16}$$

in which A denotes the magnitude of the buckling, m and n are respectively the number of half-waves in the directions x and y.
Replacing (2.16) in the governing equation, the characteristic equation of the load can be formulated as:

$$N = \frac{\pi^2 L^2 \mathbb{D}}{m^2}\left[\frac{m^2}{L^2} + \frac{n^2}{l^2}\right] \tag{2.17}$$

The smallest load N satisfying (2.17) corresponds to the buckling load. Thus, in order to find the critical load, the minimum of the problem should be studied.

$$N_{cr} = \underset{(m,n)}{Min} N(L, l, n, m) \tag{2.18}$$

Once again, the buckling amplitude is undetermined, the buckling plate is only described by the buckling load and its mode i.e. the number of half-waves in the directions x and y. Figure 2.3(b) illustrates the defected plate presenting two half-waves in the $x-$direction ($m = 2$) and one half-wave in the $y-$direction ($n = 1$).

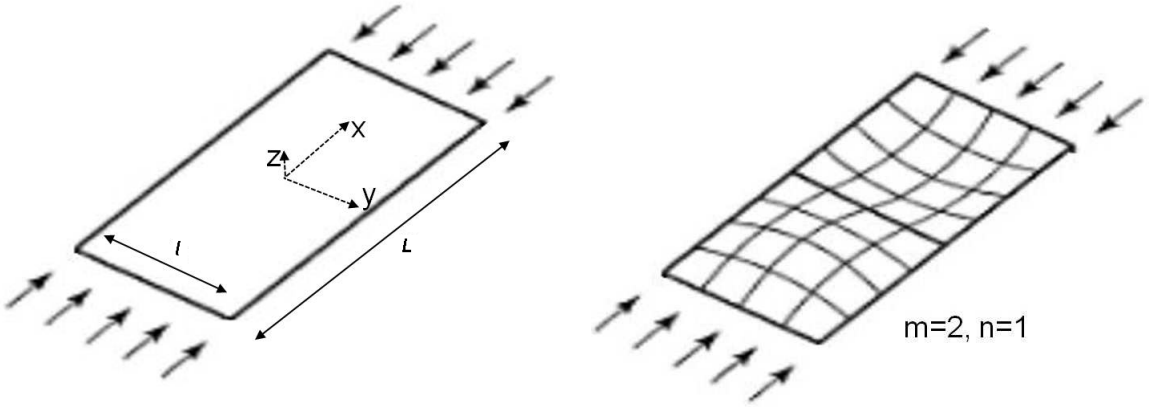

(a) (b)

Figure 2.3: Plate buckling under compressive stress

2.2.1.4 Plate buckling: Energy Method

The total potential energy of this mechanical system is

$$\begin{aligned} V &= U + \Omega \\ &= \frac{1}{2}\int_0^L\int_0^l \mathbb{D}(\frac{\partial^2 w}{\partial x^2}+\frac{\partial^2 w}{\partial y^2})^2 - 2(1-\nu)\left[\frac{\partial^2 w}{\partial x^2}.\frac{\partial^2 w}{\partial y^2} - \left(\frac{\partial^2 w}{\partial x \partial y}\right)^2\right] dxdy \\ &\quad -\frac{1}{2}\int_0^L\int_0^l N\left(\frac{\partial w}{\partial x}\right)^2 dxdy \end{aligned} \tag{2.19}$$

The out of plane displacement w can be written as a double Fourier series. $(\Phi_i)_i$: $y = \sum_m y_m.\Phi_m$ as

$$w = \sum_m\sum_n w_{mn} sin(\frac{m\pi x}{L}) sin(\frac{n\pi y}{l}) \tag{2.20}$$

Combining (2.20) with the equilibrium equation $\delta^2 V = 0$, the characteristic load equation is written as:

$$N = \pi^2 L^2 \mathbb{D} \frac{\sum_m\sum_n \left[\frac{m^2}{L^2}+\frac{n^2}{l^2}\right]^2 w_{mn}}{\sum_m\sum_n m^2 w_{mn}} \tag{2.21}$$

If each coefficient w_{mn} is positive then $\delta^2 V$ is positive definite. Thus, buckling is visible

when all coefficients except one are equal to zero, which gives the following buckling load:

$$N = \frac{\pi^2 L^2 \mathbb{D}}{m^2}\left[\frac{m^2}{L^2} + \frac{n^2}{l^2}\right] \tag{2.22}$$

The smallest value of N in (2.22) corresponds to the buckling load. Thus, in order to find the critical load, the minimum of the problem should be studied.

$$N_{cr} = \underset{(m,n)}{Min} N(L, l, n, m) \tag{2.23}$$

Once again, we find the same buckling load. To consult more buckling problems with complicated loads and mixed boundary conditions and more details on how to pick the general solutions, the readers are invited to refer to Timoshenko's book [Timoshenko & Gere, 1961]. The deflection under the buckling load is undetermined in magnitude yet determined in shape.

Remark 1

Numerical methods such as Finite Elements Method (FEM) and Finite Difference Method (FDM) are used often to solve stability problems (to determine the critical load and the buckling mode). The main reason for these methods is overcoming the difficulties encountered to find analytical values for problems with complex geometries and boundary conditions.

All the above approaches give neither an idea about the precision of the solution, nor an actual error estimation. In addition, when based on minimizing the total potential energy, a minimum is detected without being sure if it is a global or just local minimum of the system. Thus, some have proposed to solve the problem by iterative methods replacing the non-linear problem by a series of linear problems converging to a **unique** solution. We mention well known algorithms such as the Newmark-Vianello algorithm [Newmark, 1943] dedicated to stability problems. This algorithm will not be described in details since a similar iterative method, proposed by Tozawa in [Yukawa, 1986] with direct application on buckling in rolled strips under residual stress, will be presented in the next section.

Remark 2

Generally, stability problems, solved either by equilibrium method or energy methods, are transformed into eigenvalue problems. The stress or load is multiplied by a load parameter λ. For instance, the problem (2.15) is transformed to the generalized

eigenvalue problem:

$$\frac{\partial^4 w}{\partial x^4} + 2\frac{\partial^4 w}{\partial x^2 \partial y^2} + \frac{\partial^4 w}{\partial y^4} = \frac{1}{\mathbb{D}} \lambda N_x \frac{\partial^2 w}{\partial y^2} \tag{2.24}$$

Combined with a numerical method such as the Finite Element Method the problem is transformed into

$$AX = \lambda BX \tag{2.25}$$

in which $\lambda = (\lambda_1, \lambda_2, ..., \lambda_n)$, n is the dimension of the matrices A and B, and $(\lambda_i)_{i=1,..,n}$ are the eigenvalues of this problem. The smallest eigenvalue not equal to zero is the solution and it is noted λ_{cr}, the critical load parameter. The corresponding eigenvector describes the buckling mode. Finally, the critical load is found using the critical load parameter as $N_{cr} = \lambda_{cr} N$.

2.2.2 Post-buckling methods

All the methods described above were able to determine the buckling load and mode but remain insufficient to quantify the waves amplitude. In this section, a review of a few available approaches to determine the defect magnitude and to follow its evolution during the post-buckling stage will be presented briefly.
Note that the following approaches were already or have the potential to be coupled with the rolling model Lam3/Tec3.

2.2.2.1 Asymptotic Numerical Method (ANM) based on the Perturbation theory

These methods are generally introduced for physical system presenting strong geometrical non-linearities such as the post-buckling of elastic and plastic structures. They belong to perturbation theories, which allow finding an approximate solution for the problem E_λ dependent of a dimensionless parameter λ (generally supposed small) under the condition that the solution of E_0 is known [Howison, 2005, Cochelin, 1994] and [Cochelin et al., 1994].
The plate buckling problem is equivalent to the stationarity of the Hu-Washizu functional:

$$\delta\phi_{HW} = \int_V [\delta S : [\gamma - \mathbb{D}^{-1} : S] + S^t : \delta\gamma] dV - \lambda P_e(\delta u) = 0 \tag{2.26}$$

where $\mathbb{D}$ is the flexural rigidity of the plate, S is the second Piola-Kirchhoff stress tensor

and γ the Green-Lagrange strain tensor. The operator $.^t$ is the transpose operator. P_e presents the virtual work of the external loads λN_x, u the displacement field and λ a loading parameter.
The principle of the ANM consists in looking for a solution in a fixed neighborhood in the form of a finite converging sum, written as power expansions of a parameter a:

$$\begin{aligned} U(a) &= U_0 + \sum_{i=1}^{n} a^i U_i \\ \lambda(a) &= \lambda_0 + \sum_{i=1}^{n} a^i \lambda_i \\ N_x(a) &= N_{x_0} + \sum_{i=1}^{n} a^i N_{x_i} \\ a &=< u - u_0, u_1 > +(\lambda - \lambda_0)\lambda_1 \end{aligned} \tag{2.27}$$

where $U = (u, \tilde{\gamma}, S)^t$. In other words, it is equivalent to improve the solution by adding the extra-terms corresponding to $n > 0$.
For the sake of clarity, equation (2.26) is written in its residue form:

$$L(U) + Q(U, U) - \lambda F = 0 \tag{2.28}$$

F results from the external forces, L and Q are respectively a linear and quadratic operator.
Using the expansion (2.27) and provided that (U_0, λ_0) is well known, the non-linear equation (2.28), is transformed into n linear ones by identification of coefficient of each power of the parameter a:

$$\begin{aligned} \text{order 1:} \quad & L_t^0(U_1) = \lambda_1 F \\ & < u_1, u_1 > +\lambda_1^2 = 1 \\ \text{order } p\text{:} \quad & L_t^0(U_p) = \lambda_p F - \sum_{r=1}^{p-1} Q(U_r, U_{p-r}) \\ (1 < p \leq n) \quad & < u_p, u_1 > +\lambda_p \lambda_1 = 0 \end{aligned} \tag{2.29}$$

where L_t^0 is the tangent operator depending on the initial solution only.
To determine the bifurcation indicator, a fictive perturbation force $\Delta\mu f$ is introduced into the system:

$$L(U + \Delta U) + Q(U + \Delta U, U + \Delta U) = \lambda F + \Delta\mu f \tag{2.30}$$

The bifurcation indicator takes the following form:

$$\Delta\mu = \frac{< \Delta U_0, f >}{< L_t^{-1}(f), f >} \tag{2.31}$$

The critical value is defined as the smallest point canceling $\Delta\mu$ i.e. $\Delta\mu = 0$. Then, one by one, the linear problems for each order, going from 0 to n, are solved until all the expansion coefficients are identified. U is computed, in particular the out of plane displacement w which quantifies the waves.
This method has a high potential. Unlike other approaches, it can describe both buckling and post-buckling problems. Figure 2.4 illustrates a simply supported buckling strip under a uniform compressive stress $\sigma_x = -85$ MPa. The amplitude of the wave, computed using ANM, is equal to 0.12 mm.

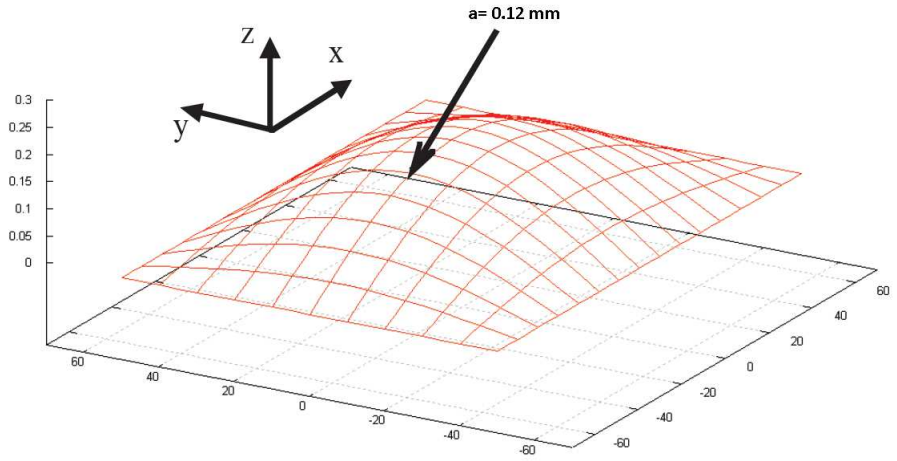

Figure 2.4: A simply supported plate buckling under a uniform compressive stress $\sigma_x = -85$ MPa.

Using this approach and a Shell Finite Element formulation, a model called **MAN** was developed in [Zahrouni et al., 1999] [Zahrouni, 1998] and applied later on to flat rolling and buckling strips by Abdelkhalek in [Abdelkhalek, 2010, Abdelkhalek et al., 2009]. The model **MAN** will be presented in details in section 2.3.1.3.2.

2.2.2.2 Multi-scale Method based on Fourier series expansion

This approach proposed in [Damil & Potier-Ferry, 1986, Damil & Potier-Ferry, 2006, Damil et al., 2013] for beam and plate buckling, aims to define "macroscopic models" coupling the linear elasticity with equations governing the evolution of buckles.

Such local instabilities can be described by bifurcation analysis according to the Landau-Ginzburg theory [Wesfreid & Zaleski, 1984] using an asymptotic double scale analysis. At the local level, one accounts for the periodic nature of the buckles, while the slow variations of the envelope are described at the macroscopic scale. Therefore the 'Multi-scale' notation. [Damil & Potier-Ferry, 1986, Damil & Potier-Ferry, 2006, Damil et al., 2013] propose a modification to this latter approach in which the nearly periodic fields are explicitly expressed by Fourier series with slowly varying coefficients. This leads to macroscopic models defined by Fourier coefficients of the microscopic model.
The essence of this approach relies on a specific description of the nearly periodic fluctuations by at least two slowly varying functions as illustrated in Figure 2.5

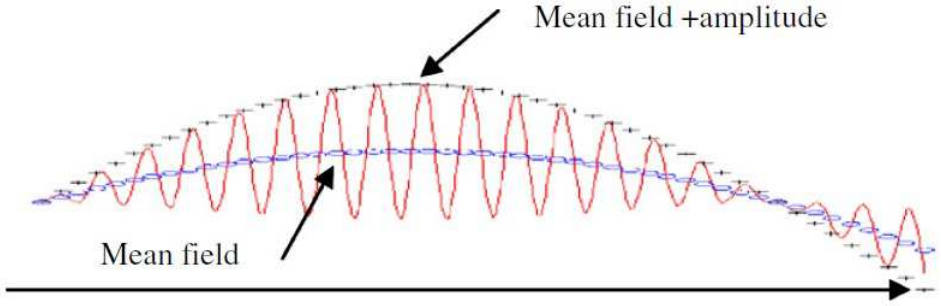

Figure 2.5: A nearly periodic buckling response described by two macroscopic fields: the mean field and the amplitude of the undulation otherwise called the first envelope.

The unknowns $U = (u, v, w)$ of the problem are written in the form of Fourier series, with slowly variable coefficients:

$$U(x) = \sum_{-\infty}^{+\infty} U_m(x) e^{imqx} \tag{2.32}$$

in which x is the direction of the buckling and q is the number of the half-waves developed in this direction.
To give a quick description, the following example is presented: a strip is double loaded as described in Figure 2.6: $N_x = \sigma_x.h$, $N_y = \sigma_y.h$ under the condition $\sigma_y << \sigma_x$. L and l are respectively the length and width of the plate.

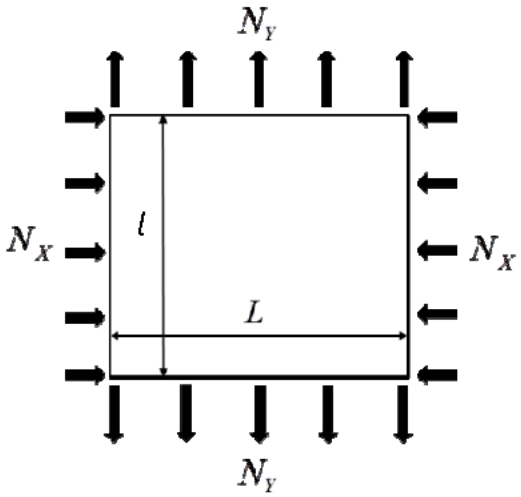

Figure 2.6: Rectangular membrane under biaxial load.

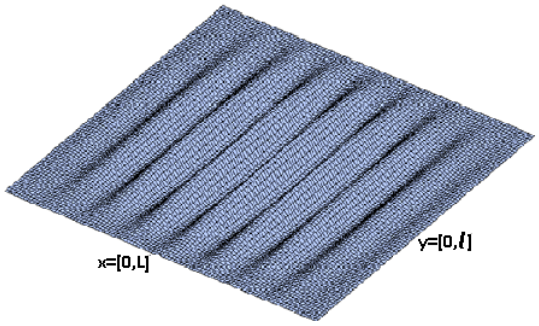

Figure 2.7: Sketch of the wrinkled membrane under biaxial load.

The chosen Fourier expansion for the displacement w is limited to the first order in which the mean field w_0 can be canceled -since sinusoidal waves have a mean field equal to zero- and the envelope w_1 is supposed real.
The macroscopic model can be deduced from the stationarity of the total energy. And the envelope w_1 will verify the following differential equations of the macroscopic model:

$$\begin{aligned} &divN = 0 && \text{(a)}\\ &N = \mathbf{C} : [\varepsilon(u) + \gamma^{wr}] && \text{(b)}\\ &-6\mathbb{D}q^2\frac{\partial^2 w_1}{\partial x^2} - (2\mathbb{D}q^2 + N_y)\frac{\partial^2 w_1}{\partial y^2} + \mathbb{D}q^4 w_1 = -N_x\left[-\frac{\partial^2 w_1}{\partial x^2} + q^2 w_1\right] && \text{(c)} \end{aligned} \tag{2.33}$$

The nonlinear model (2.33) couples the bifurcation equation verified by the envelope w_1 (2.33.c) with the nonlinear membrane equation (2.33.b).
To recover the buckling mode and load, the authors propose an analytical form by choosing a particular solution verifying (2.33.c): $w_1 = sin(\frac{\pi x}{L})sin(\frac{\pi y}{l})$. Taking into account that $1 << qL$ and $2\mathbb{D}q^2 \approx |N_x| << N_y$, the following relation between the stress and the wavenumber is deduced:

$$|N_x(q)| = \frac{N_y \pi^2}{q^2 l^2} + \mathbb{D}q^2 \tag{2.34}$$

The wave-number q is determined by minimizing (2.34) as a function of the wavenumber. Finally the analytical form of the buckling stress is determined as:

$$|\sigma_x^{wr}| = \frac{\pi\sqrt{E\sigma_y}h}{l\sqrt{3(1-\nu^2)}} \tag{2.35}$$

Once the load threshold (2.35) and the mode (the number of waves q) are known, the bifurcation equation verified by the envelope w_1 can be solved. The stress post-buckling

state is established by adding γ^{wr}, the wrinkling contribution, computed in terms of q and w_1, to the usual behavior law (2.33.b).
For quantifying the amplitude (i.e. the envelope), the authors propose to seek the envelope w_1 and the compression load as Taylor series with respect to a scalar a (denoting the amplitude):

$$\begin{aligned} w_1(a) &= w_0 + w_1^{(1)}.a + w_1^{(2)}.a^2 \\ \lambda(a) &= \lambda^{(0)} + \lambda^{(2)}.a^2 \\ N_x(a) &= N_x^{(0)} + N_x^{(2)}.a^2 \end{aligned} \tag{2.36}$$

where λ is a loading parameter introduced to insure the bifurcation of the equation (2.33.c), i.e. N is replaced by λN.
Replacing the expansion (2.36) in (2.33.c), the problem is transformed into three linear problems (corresponds to $n = 0,\ 1$ and 2). Several steps lead to identifying λ_0 and λ_2.
Once λ_0, λ_2 are known, the amplitude can be defined from (2.36) as :

$$a = \sqrt{\frac{\lambda - \lambda^{(0)}}{\lambda^{(2)}}} \tag{2.37}$$

Finally, the authors establish this relation connecting the wrinkling amplitude as a function of the compressive stress:

$$\frac{a}{h} = C\left(\frac{l}{L}\right)\sqrt{\frac{l|\sigma_x|\sqrt{3(1-\nu^2)}}{h\sqrt{E\sigma_y\pi}} - 1} \tag{2.38}$$

where $C\left(\frac{l}{L}\right)$ is an amount depending of the ratio $\frac{l}{L}$ and integrals resulting from a Galerkin approximation imposed by the authors. To understand the different steps into computing λ_0, λ_2 and $C\left(\frac{l}{L}\right)$, please refer to [Damil et al., 2013].

As a numerical result, the authors gave the following example: A clamped rectangular membrane is subjected to bi-axial tension-compression load. The side lengths L and l are respectively 400 mm and 200 mm and the thickness h is 0.05 mm. The applied tension is $N_y = 10\ N/mm$ and the compression force N_x increases. In the macroscopic model, a wavenumber q has to be chosen. The authors choose the one predicted by minimizing the analytic formula 2.34.
By comparison with the shell model Abaqus, Figure 2.8 confirms that the wrinkling pattern, predicted by the macroscopic model, just after bifurcation is correctly described. In addition the envelope is nearly sinusoidal in the $x-$direction and appears to have the same behavior as the one illustrated by the shell model Abaqus.
Quantitatively, Figure 2.9 shows that the new macroscopic model is able to describe

quite perfectly the initial post-bifurcation response, knowing that it requires much less degrees of freedom than the full shell model. This point is significantly important since it reduces the computational time. The curves show that both models predict the same bifurcation point corresponding approximately to $N_x = -0.09\ N/mm$. The evolution of the amplitude predicted by both models is quite similar.

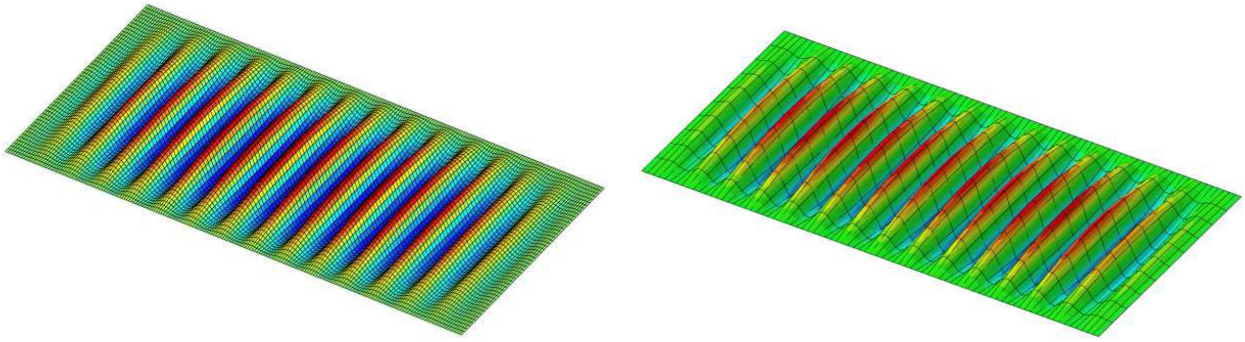

(a) (b)

Figure 2.8: Rectangular membrane submitted to tension and compression. Post-bifurcation patterns near the bifurcation, with the multi-scale model (a) and the full shell model Abaqus (b).
$N_y = 10\ N/mm$, $N_x = -0.09\ N/mm$.

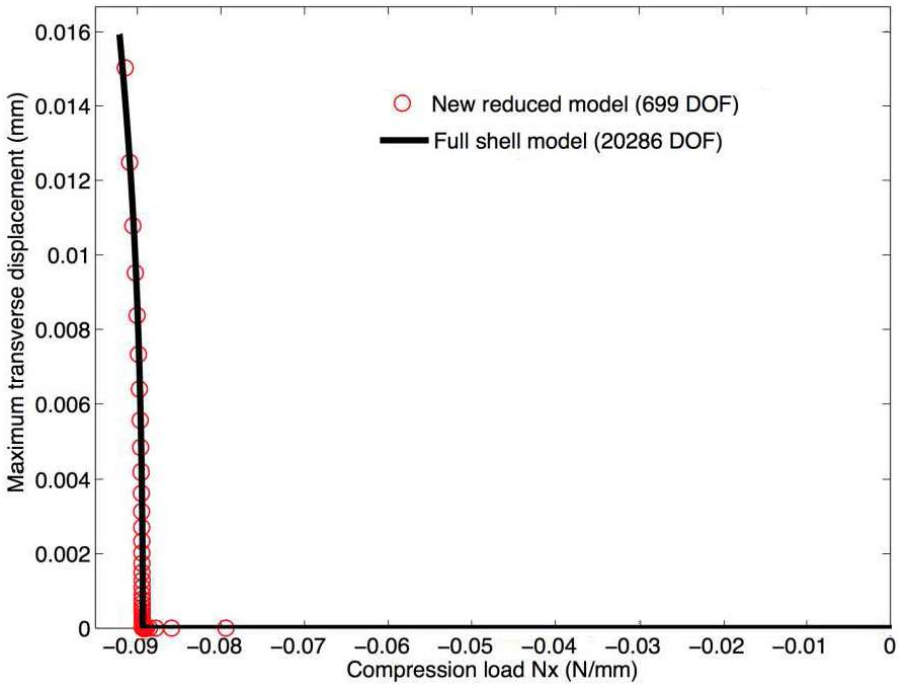

Figure 2.9: Rectangular membrane submitted to tension and compression. Response curves near the bifurcation for the bi-axial load problem of Figure 2.6, with two different models, the new macroscopic model and the shell model Abaqus.

This approach presents novelty in modeling buckling and post-buckling problems. Its multi-scale formulation is capable of identifying the waves using envelopes which give a good geometric description and quantification.
The example presented above with all the simplifications does not do this approach justice. For more complete description and examples, the readers are invited to consult [Damil & Potier-Ferry, 1986, Damil & Potier-Ferry, 2006, Damil et al., 2013] and [Potier-Ferry & Damil, 2010].
This generalized method, by its capacity yet simplicity, is a good candidate for application such as buckling during flat rolling. It will be adapted to the needs of this application and presented in chapter 4.

2.2.2.3 Analytical Method based on the Membrane Theory

The membrane theory, easily applied for very thin plates, forbids the appearance of a negative stress: every time a negative stress is about to appear, the structure buckles; this means that the critical load or stress is equal to zero; $\sigma_c = 0$. Based on this theory, [Roddeman et al. , 1987.a)] and [Roddeman et al. , 1987.b)] define a strain tensor able to describe the situation of the stress after buckling.
In this study, several assumptions are posed:

a- The membrane or eventually the strip is under plane stress.

b- By definition of a membrane, bending does not introduce additional stresses.

The Cauchy stress tensor σ can be written as:

$$\sigma = \frac{1}{J}\mathbf{F}.H(\mathbf{E}).\mathbf{F}^t \tag{2.39}$$

in which $\mathbf{F}$ is the deformation tensor n, $J = det(\mathbf{F})$, $\mathbf{E}$ is Green-Lagrange strain tensor and H the first Piola-Kirchhoff stress tensor.
From the mathematical point of view, the assumption "negative stress does not exist" can be expressed by the following set of equations:

$$\begin{aligned} &\vec{n_1}.\sigma.\vec{n_1} \geq 0 \quad \text{(a)} \\ &\vec{n_2}.\sigma.\vec{n_2} \geq 0 \quad \text{(b)} \\ &\vec{n_1}.\sigma.\vec{n_2} = 0 \quad \text{(c)} \end{aligned} \tag{2.40}$$

in which $\vec{n_1}$ et $\vec{n_2}$ are the orthonormal vectors denoting the principal direction of the real Cauchy stress tensor.
The third equation expresses simply that the shear stresses are equal to zero in the principal frame.

Remark 3:
Since $\vec{n_1}$ and $\vec{n_2}$ indicate a priori the unknown directions of Cauchy principal stress in the buckled membrane, the conditions (2.40) give three possible situations:

- If both principal stresses in directions $\vec{n_1}$ and $\vec{n_2}$ are positive, the membrane stays taut.
- If both principal stresses in directions $\vec{n_1}$ and $\vec{n_2}$ are zero, the membrane is slack.
- If one of the principal stresses is zero (in the direction $\vec{n_1}$ for instance) and the other one is positive (in the direction $\vec{n_2}$), the membrane buckles in the zero direction $\vec{n_1}$.

When studying buckling structures, only the third situation is of interest to us. So conditions (2.40) transform into:

$$\begin{aligned} &\vec{n_1}.\sigma.\vec{n_1} = 0 \quad \text{(a)} \\ &\vec{n_2}.\sigma.\vec{n_2} > 0 \quad \text{(b)} \\ &\vec{n_1}.\sigma.\vec{n_2} = 0 \quad \text{(c)} \end{aligned} \tag{2.41}$$

The buckling phenomena is known to affect the stress distribution in the structure, it relaxes the stresses exceeding the critical values. So it can been said that calculation done without taking into account the buckling would give stresses violating these conditions. The principle of the method is to seek the off-plane deformations which,via the behavior law, will lead the stresses to respect the equations (2.41).
In this situation, the membrane is illustrated in Figure 2.10 (a) and $\vec{n_1}$ is the buckling direction .
The assumption a- allows to straighten the membrane, as described in Figure 2.10 (b), without affecting the situation of the stress. Therefore, the strain tensor of the buckling membrane can be expressed as a function of the fictional tensor as follows:

$$\mathbf{F'} = (\mathbb{I} + \beta_R \vec{n_1}.\vec{n_1}).\mathbf{F} \tag{2.42}$$

in which $\mathbb{I}$ is the unit tensor and $(\mathbb{I}+\beta_R \vec{n_1}.\vec{n_1})$ is the tensor elongating the fictional straight membrane to fit the real buckling membrane length; where β_R can be expressed implicitly as the ratio between the fictional and real membrane length.
Therefore,

$$\sigma = \frac{1}{J}\mathbf{F'}.H(\mathbf{E}').\mathbf{F'}^t \quad \text{with} \quad \mathbf{E}' = \frac{1}{2}(\mathbf{F'}.\mathbf{F'}^t - \mathbb{I}) \text{ and } J = det(\mathbf{F'}) \tag{2.43}$$

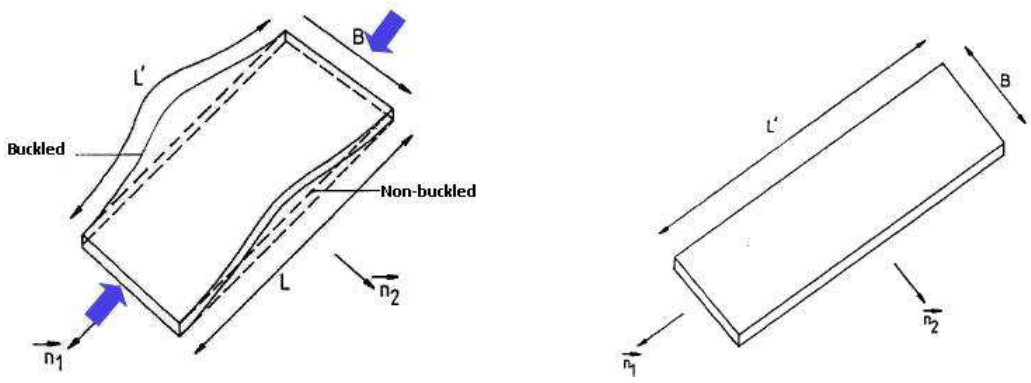

Figure 2.10: (a) A buckling membrane with a deformed length L', and the dotted non-buckling membrane with length $L < L'$, (b) the straightened buckling membrane in the plane determined in $(\vec{n_1}, \vec{n_2})$ [Roddeman et al. , 1987.a)]

Once $\sigma(\mathbf{F'})$ is defined, the new set of conditions to verify are presented below:

$$\begin{aligned} \vec{n_1}.\sigma(\mathbf{F'}).\vec{n_1} &= 0 \\ \vec{n_1}.\sigma(\mathbf{F'}).\vec{n_2} &= 0 \\ \vec{e_3}.\sigma(\mathbf{F'}).\vec{e_3} &= 0 \end{aligned} \tag{2.44}$$

It should be noted that in anisotropic materials, frames $(\vec{n_1}, \vec{n_2})$ and $(\vec{e_1}, \vec{e_2})$ are different, where $(\vec{e_1}, \vec{e_2})$ is the real frame of the membrane. That is why an angle $\alpha_R = (\vec{n_1}; \vec{e_1})$ can appear when solving the set of equations (2.44).
This leads to solve a set of non-linear coupled equations :

$$\begin{aligned} h_1(\alpha_R, \beta_R, \delta h) &= 0 \\ h_2(\alpha_R, \beta_R, \delta h) &= 0 \\ h_3(\alpha_R, \beta_R, \delta h) &= 0 \end{aligned} \tag{2.45}$$

where δh is the variation in the thickness of the membrane upon buckling.
This method, despite the assumptions, provides post-buckling informations such as the direction of the buckling, the additional elongation of the membrane, the new stress distribution due to buckling and the variation in the thickness of the membrane. This is a clearly rich approach and its capacity will be explored in the following sections when applied to rolling thin strip and coupled with a rolling model as in [Counhaye, 2000] and [Abdelkhalek, 2010].

2.3 Review of methods applied to rolled strip defect

Now that a brief survey of approaches used to treat buckling and post-buckling problems have been presented, this section is dedicated to the methods applied for modeling defect problems during rolling processes.
It is divided into two parts. The first describes the uncoupled approaches where the buckling is treated as a consequence of the rolling process. The second is the coupled approaches where not only the rolling can activate the appearance of buckling but also the effect of buckling on the rolling process is taken into account, so they are treated as two coupled problems.

2.3.1 Uncoupled approaches for Rolling-buckling problems

2.3.1.1 Semi-analytical study by Bush

Again, the deflection of the plate is described by the equation (2.15) introduced by Timoshenko et al. in [Timoshenko & Gere, 1961]. Bush et al. [Bush et al., 2001] took the same example of a simply supported plate but proposed that the plate is subjected to a residual stress distribution not necessarily uniform along the width. Thus,

$$N_x(y) = -\sigma_x(y).h \tag{2.46}$$

Next the authors introduced a non-dimensional compressive stress distribution $k(y) = \frac{N_x(y)b^2}{\pi^2 \mathbb{D}}$, where $\mathbb{D}$ is the flexural rigidity of the plate and l is the width of the plate.
Taking into consideration the form of k and the fact that every stability problem can be converted into an eigenvalue problem, a loading parameter λ is introduced. The governing equation is transformed into:

$$\frac{\partial^4 w}{\partial x^4} + 2\frac{\partial^4 w}{\partial x^2 \partial y^2} + \frac{\partial^4 w}{\partial y^4} = -\frac{\lambda k(y)\pi^2}{l^2}\frac{\partial^2 w}{\partial y^2} \tag{2.47}$$

According to Bush, a realistic example of a stress distribution during flat rolling can take the form:

$$k(y) = -1 + \alpha_B \left(\frac{2y}{l}\right)^r \quad -\frac{1}{2} < \frac{y}{l} < \frac{1}{2} \tag{2.48}$$

This stress distribution has a tensile central region and a compressive one at the edges with maximum compression $\alpha_B - 1$. Note that when the even integer r, the order of this polynomial distribution increases, the center region grows and the defect will be more localized on the edges.
As proposed in [Timoshenko & Gere, 1961], the general solution of equation (2.47) takes

the following form:

$$w(x,y) = f(y)sin\left(\frac{n\pi x}{L}\right) \tag{2.49}$$

in which n is the number of half waves developed under the buckling load, L is the length of the plate and $f(y)$ is the cross-width deflection function. Replacing (2.49) in (2.47), the new equation to solve is the ordinary differential equation (2.50) along with the appropriate boundary conditions.

$$\frac{d^4f}{dy^4} - 2\left(\frac{n\pi}{L}\right)^2\frac{d^2f}{dy^2} + \left[\left(\frac{n\pi}{L}\right)^4 - \lambda k\frac{\pi^2}{l^2}\left(\frac{n\pi}{L}\right)^2\right]f = 0 \tag{2.50}$$

Since equation (2.50) is simple to solve if k is constant, the authors propose to replace the continuous function $k(y)$ by a discretized set of constant values over the discretized width of the plate: $k(y) = k_i$; $i = 1, 2, ..., 2m$ where the width is discretized into $2m$ elements. Since the domain is divided into $2m$ sub-domains, equation (2.50) is transformed into $2m$ sub-equations i.e. $2m$ solutions.
The solution f_i on each sub-domain takes the following form:

$$f_i(y) = \sum_{j=1,...,4} C_{ij}.e^{\alpha_j} \quad \text{where} \quad \alpha_i = \pm\frac{\pi y_i\sqrt{nl(nl \pm L\sqrt{\lambda k_i})}}{lL} \tag{2.51}$$

The constant C_{ij} are identified using the four boundary conditions and the continuity condition of f i.e. $f \in C^4(\Omega)$.
The matrix form of these $8m$ equations used to determine $C_{J,J=1,...,8m}$ is

$$\begin{aligned}\sum_{J=1}^{8m} M_{IJ}C_J = 0 \quad I = 1,..,8m \\ \iff AC - \lambda BC = 0\end{aligned} \tag{2.52}$$

The problem is turned now into a generalized eigenvalue problem, where the only non-trivial solution can be obtained when the determinant of the matrix M is equal to zero. The minimum of the eigenvalues is called the critical value λ_{cr} and the corresponding eigenvector is the mode of the plate buckling.

Remark 4:
In Bush's buckling study applied to flat rolling, there is no mention of the tension applied normally during this process. One may interpret it in two different ways:

1) The tension was taken into consideration in the form of N_x i.e. k; if this is the case, the loading parameter λ should not multiply k but a part of it.
or,

2) The tension was never taken into account in this model and for that this model does not describe the on-line flatness of a rolled strip. It studies the strip buckling under residual stress after the strip tension cancellation (i.e. off-line flatness).

2.3.1.2 Semi-analytical study by Fischer

[Fisher et al., 2001] and [Fisher et al., 2003] took the same buckling plate example but the plate is loaded this time not only by a self equilibrating residual stress distribution $N_x(y) = N\hat{g}(y)$ but also by a constant global tension N_0. Thus, the cross-width force load distribution is given by:

$$N_x(y) = N\hat{g}(y) + N_0 \tag{2.53}$$

New dimensionless quantities were introduced:

$$\begin{array}{l} \eta = \dfrac{y}{l} \quad \text{where} \quad -\dfrac{l}{2} < y < \dfrac{l}{2} \\ \tilde{N} = \dfrac{Nl^2}{\mathbb{D}\pi^2} \quad \text{and} \quad \tilde{N}_0 = \dfrac{N_0 l^2}{\mathbb{D}\pi^2} \\ \hat{g}(y) \to g(\eta) \quad \text{and} \quad N_x \to N_x(\eta) = Ng(\eta) + N_0 \end{array} \tag{2.54}$$

$$w(x,y) = a|2\frac{y}{l}|^n (sign(\frac{y}{l}))^{\varphi} cos(\frac{\pi x}{\tilde{l}}) \tag{2.55}$$

in which $\tilde{l}$ is the half-wave length, φ (integer) determines the symmetry/antisymmetry of the buckling mode, n (real) describes the profile of the cross-width deflection function and a is the amplitude of the buckling waves which should minimize the total potential energy V. The total potential energy takes the same form as presented in (2.19) by replacing N by $N\hat{g}(y) + N_0$.
Combining the solution with the concept of minimization of the total energy $\dfrac{\delta V}{\delta a} = 0$ the buckling load characteristic equation $\tilde{N}(\tilde{l}, n)$ can be obtained. Minimizing $\tilde{N}(\tilde{l}, n)$ according to $\tilde{l}$ and n the load critical value and the corresponding half-wave length i.e. the buckling mode is determined.
In [Fisher et al., 2001], the authors propose two different residual stress distributions.

$$\begin{array}{lll} \text{A cosine distribution:} & N_x(\eta) = C_m cos^m(\pi\eta) & \text{with } m = 1, 2... \\ \text{A polynomial distribution:} & N_x(\eta) = \dfrac{1}{m}\left[(m+1)(2|\eta|)^m - 1\right] & \text{with } m = 1, 2... \end{array} \tag{2.56}$$

Combining the polynomial stress distribution in the energy minimizing problem $\frac{\delta V}{\delta a} = 0$, the analytical characteristic equation of the dimensionless buckling load was established:

$$\begin{aligned} &\tilde{N}_c(n) = f_1(n) + f_2(n)\tilde{N}_0 \\ &f_1(n) = \frac{4n+2m+2}{\pi^2}\left[(2n-2)\left[\sqrt{\frac{2n+1}{2n-3}} - \frac{2n+1}{2n-1}\right] + 2(1+\nu)(2n+1)\right] \\ &f_2(n) = 1 + \frac{m+1}{2n} \end{aligned} \tag{2.57}$$

Again, the buckling load form can be retrieved by removing the non-dimensionalization

$$N_c(n) = \frac{\tilde{N}_c(n)\mathbb{D}\pi^2}{l^2} \tag{2.58}$$

Finally, the critical load is obtained by minimization of (2.58) according to n and the half-wave length $\tilde{l}$ corresponds to the smallest buckling load.

$$N_{cr} = \underset{n}{Min} N_c(n) \tag{2.59}$$

Remark 5

The novelty of this study is that the chosen solution can represent the symmetry of the mode thanks to the parameter φ. But still, the solution proposed in [Bush et al., 2001] remains more general where the cross-width deflection function is not bound to have a polynomial form.

Note that these two semi-analytical studies are limited to the linear analysis i.e. determining the mode and the buckling load. The amplitude of the defects remains undetermined.

2.3.1.3 Buckling analysis problem with shell finite element method

Two buckling studies, applied on defect appearance during flat rolling processes, using Shell Finite Elements Methods stand out from the rest: the first is an iterative method presented in [Yukawa, 1986] and the second uses an asymptotic analysis and it is detailed by Abdelkhalek in his work [Abdelkhalek, 2010, Abdelkhalek et al., 2009, Abdelkhalek et al., 2011].

2.3.1.3.1 Iterative method for plate buckling under residual stresses

As mentioned earlier in Remark 1, when the stability study is based on minimizing

the total potential energy, a minimum may be detected without being sure if it is a global or just local minimum of the system. Thus, iterative methods replacing the non-linear problem by a series of linear problems converging to a **unique** solution are the answer to this doubt. By unique we mean that the minimum of the system corresponds to the global one. Another upside for such algorithms is that there is no need for imposing an a priori form for the out of plane displacement. Few algorithms have been proposed and fewer still applied to rolling strips.

One exception is the method of [Yukawa, 1986] with direct application to buckling of rolled strips under residual stress.

The principle is to find the bifurcated branch verifying the concept of minimization of the total potential energy V.

To solve the non-linear problem by iterative methods, for every increment the following form (2.60) is adopted:

$$\Delta V = \delta V + \frac{1}{2}\delta^2 V + ... \tag{2.60}$$

As explained in section 2.2.1.2, in the case of stable equilibrium state, the linear term δV must be equal to zero and the quadratic term $\delta^2 V$ positive definite. The critical buckling load is the smallest value corresponding to $\delta^2 V$ changing sign i.e. $\delta^2 V = 0$.

$$V = \int \{\gamma\}^t : S d\Omega - \{\xi\}\{P\} \tag{2.61}$$

in which $\xi = (u, v, w)^t$ is the displacement vector, S is the second stress tensor of Piola-Kirchhoff, γ is the Green-Lagrange strain tensor and P the tension applied on the plate during rolling.

Note that, for a plate, the strain tensor γ is the combination of two terms: a linear one γ^l and a non-linear one γ^{nl}:

$$\begin{aligned} \gamma &= \gamma^l + \gamma^{nl} \\ &= \left(\frac{\partial u}{\partial x}, \frac{\partial v}{\partial y}, \frac{\partial u}{\partial y} + \frac{\partial v}{\partial x}, \frac{\partial^2 w}{\partial x^2}, \frac{\partial^2 w}{\partial y^2}, 2\frac{\partial^2 w}{\partial x \partial y}\right)^t + \left(\frac{1}{2}\left(\frac{\partial w}{\partial x}\right)^2, \frac{1}{2}\left(\frac{\partial w}{\partial y}\right)^2, \frac{\partial w}{\partial x}\frac{\partial w}{\partial y}, 0, 0, 0\right)^t \end{aligned} \tag{2.62}$$

When discretized using a finite elements method, the matrix form of the strain tensor is written as follows:

$$\{\gamma\} = [B]\{\tilde{\xi}\} \tag{2.63}$$

where the matrix $[B]$ contains the derivatives of the chosen basis functions and it is divided into two matrix $[B_L]$ and $[B_{NL}]$ corresponding respectively to the terms γ^l and γ^{nl}:

$$[B] = [B_L] + [B_{NL}] \tag{2.64}$$

[Yukawa, 1986] suppose that the behavior law can be written as:

$$\{S\} = [C]\{\gamma^{nl}\} \tag{2.65}$$

where $[C]$ is the matrix containing the elastic coefficients, then the quadratic term $\delta^2 V$ can take the following form:

$$\delta^2 V = \left(\int \left([B]\{S\} + [B]^t[C][B] \right) d\Omega \right) \{\delta\tilde{\xi}\} \tag{2.66}$$

The following notation are adopted:

$$\begin{aligned} [K_L] &= \int [B_L]^t[C][B_L] d\Omega \\ [K_{NL}] &= \int \left([B_{NL}]^t[C][B_L] + [B_L]^t[C][B_{NL}] + [B_{NL}]^t[C][B_{NL}] \right) d\Omega \\ [K_\sigma] &= \int [B]^t\{S\} d\Omega \\ [K_T] &= [K_L] + [K_{NL}] + [K_\sigma] \end{aligned} \tag{2.67}$$

Replacing (2.67) in (2.66), the final form of $\delta^2 V$ is:

$$\delta^2 V = [K_T]\{\delta\tilde{\xi}\} \tag{2.68}$$

Finding the point of bifurcation gives the exact limit for buckling. Before bifurcation, the plate is flat ($w(x, y) = 0$) so that $[K_{NL}] = 0$. Having clarified this point, we can proceed to the different steps of the algorithm.
First, the algorithm (presented in Figure 2.11) computes the matrix $[K_L]$, $[K_\sigma]$ and the initial displacement $\{\tilde{\xi}_0\}$ for an initial loading parameter equal to zero:

$$\text{Linear problem:} \quad \{\tilde{\xi}_0\} = [K_L]^{-1}\{P\} \text{ and } [K_{NL}] = 0 \tag{2.69}$$

So, the critical loading parameter λ_c is determined and should verify:

$$\delta^2 V = [K_L] + \lambda_c[K_\sigma] = 0 \tag{2.70}$$

Then, the displacement vector describing the buckling mode is defined by :

$$\text{Non-linear problem:} \quad \{\delta\tilde{\xi}^*\} = [K_T]^{-1}\{P\} \text{ and } [K_{NL}] \neq 0 \tag{2.71}$$

A prediction/correction algorithm using the Newton-Raphson method provides the follow up of the strip post-buckling, once the loading parameter λ surpasses the first bifurcation point λ_c. In the expression of δV, S is replaced by λS where λ is the loading parameter

i.e. the load (here the residual stress S) is applied gradually on each step:

$$\delta V = \left(\int \{\gamma\}^t : \lambda S d\Omega - \{P\} \right) \{\delta\tilde{\xi}\} = 0 \tag{2.72}$$

For every increment, the displacement, the loading parameter λ and the loading increment $\Delta\lambda$ are initialized: $\{\tilde{\xi}\} = 0$, $\lambda = 0$ and $\Delta\lambda = 0$.

Finally, if the equilibrium is verified i.e. $\delta V = 0$ and the loading parameter hits the real load applied on the strip i.e. $\lambda = 1$, the solution has been found. If not, λ is replaced by $\lambda + \Delta\lambda$ and the step is repeated until reaching these conditions. Analyzing this model shows more potential than others presented earlier:

- All the stress tensor components may be taken into account, not only the component σ_x.
- Although it is not mentioned if the authors determined the magnitude of the buckling, the displacement vector was described in the equation (2.71).

Note that, similar to the semi-analytical models presented earlier, this algorithm uses additional boundary conditions to control the type of the buckling mode i.e. a fixed center is imposed if wavy edges are expected and fixed edges are imposed if center buckles are expected.

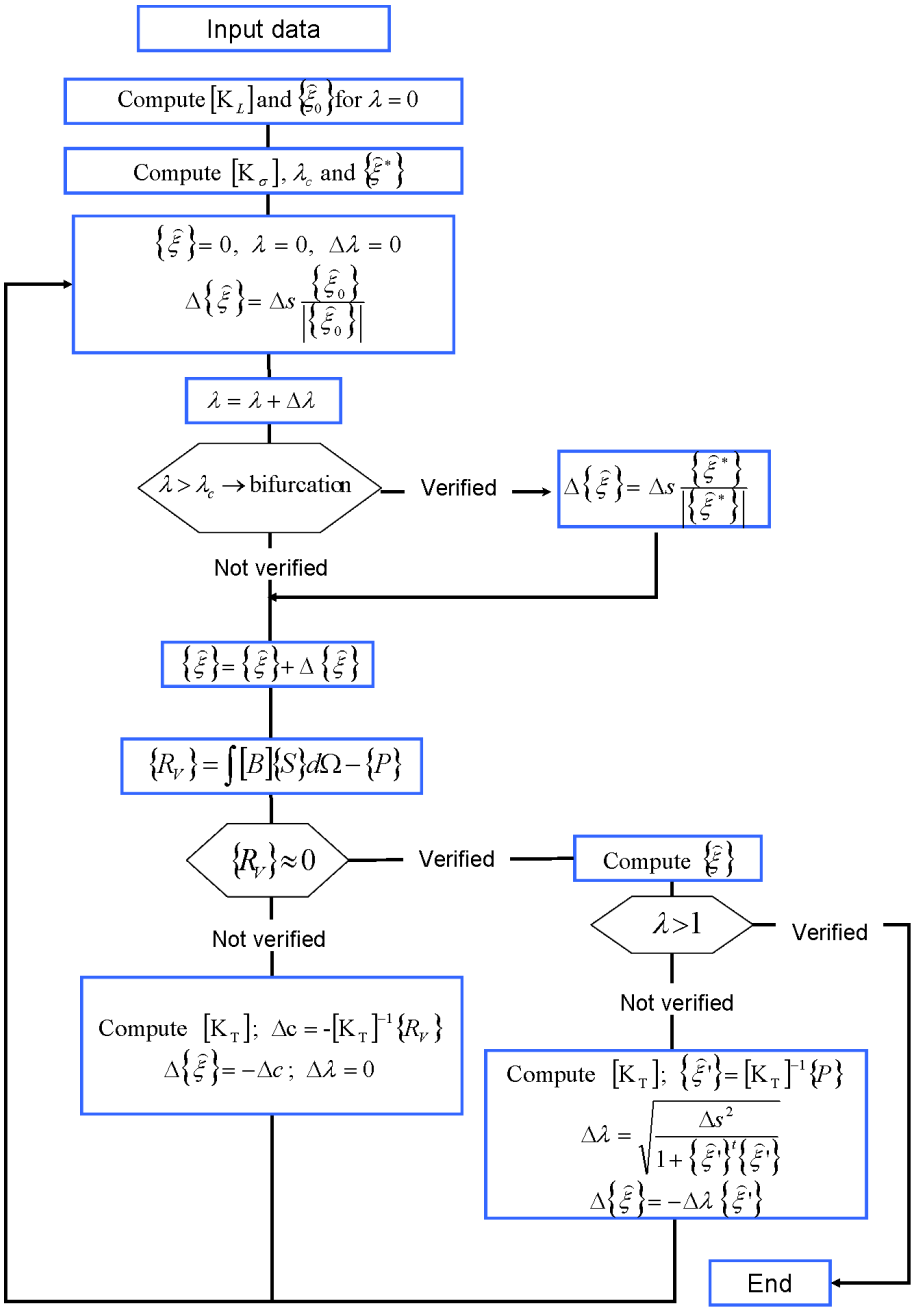

Figure 2.11: General algorithm of Tozawa's buckling model presented in [Yukawa, 1986].

2.3.1.3.2 MAN model based on an asymptotic analysis and shell finite elements formulation

Based on a shell finite elements formulation[1] and an asymptotic method, a buckling model called **MAN** was developed and presented in [Zahrouni et al., 1999, Zahrouni, 1998, Boutyour et al., 2004]. This model was adapted to predicting flatness defects problems during Flat rolling by Abdelkhalek in [Abdelkhalek, 2010, Abdelkhalek et al., 2009].

The three dimensional formulation is based on the stationarity of the Hu-Washizu functional taking into account a double loading (2.73); i) the tension applied on the strip and ii) the residual stress distribution trapped inside the strip mainly due to the plastic deformation :

$$\begin{cases} \int_\Omega S^t : \delta\gamma^c d\Omega = \lambda^{ten} \int_{\partial\Omega_3} P\delta\xi dS & \text{(a)} \\ \int_\Omega S^t : \delta\tilde{\gamma} d\Omega = 0 & \text{(b)} \\ S = \mathbf{C} : (\gamma^c + \tilde{\gamma}) + \lambda^{res} S^{res} & \text{(c)} \\ \gamma^c = \gamma^l(\xi) + \gamma^{nl}(\xi, \xi) & \text{(d)} \\ \delta\gamma^c = \gamma^l(\delta\xi) + 2\gamma^{nl}(\xi, \delta\xi) & \text{(e)} \\ \tilde{\gamma} = \gamma - \gamma^c & \text{(f)} \end{cases} \tag{2.73}$$

in which the unknowns are the displacement field ξ, the Green-Lagrange strain γ and the second Piola-Kirchhoff stress tensors S. $\tilde{\gamma}$ is an extra unknown called the enhanced part of the strain (eq. (2.73f)) incorporated via the Enhanced Assumed Strain (EAS) concept which has been introduced by Simo and Rifai [Simo & Rifai, 1990] to improve the performance of displacement finite element. It does not depend on the displacement and is required to be orthogonal to the stress field as shown in (2.73 b).
The loading parameters λ^{ten} and λ^{res} allow respectively the control of the applied tension P and the residual stress S^{res}.
In the buckling model **MAN**, only one loading parameter is applied at a time. Thus, it is divided into four steps as follows:

Step 1: The tension P is applied gradually to the strip (on $\partial\Omega_3$) which gives it some rigidity and brings it one step closer to the flat rolling conditions. The loading parameter λ^{ten} varies from 0 to 1 , where $\lambda^{ten} = 0$ corresponds to no tension applied and $\lambda^{ten} = 1$ means the whole tension P, chosen by the user, is applied. In this step, the residual stress is not yet considered, so $\lambda^{res} = 0$.

Step 2: In this step, the tension is kept at $\lambda^{ten} = 1$. The aim is to determine the buckling load λ_{cr} and its corresponding buckling mode by applying $\lambda^{res} S^{res}$.
The buckling load parameter λ_{cr} is determined by means of a bifurcation indicator. The problem is disturbed by a fictive force and its singularity gives the critical parameter value.

Step 3: Now that the critical value and the mode are determined, the post-buckling is to be studied in this step. λ^{res} increases from 0 to 1 and the evolution of the strip state is followed for every increment.

[1] The shell element used by **MAN** is described in Appendix B.III

Step 4: The final step is to study the buckling of the strip under residual stress ($\lambda^{res} = 1$) once the tension is canceled i.e. λ^{ten} decreases from 1 to 0. Accomplishing this step allows the prediction of latent flatness defects that only show after tension release.

Combined with the power series expansions (2.74) of $U = (\xi, \tilde{\gamma}, S)^t$ and λ, the non-linear problem (2.73) is transformed into n linear problems by identifying coefficients of each power of the length parameter a, where only one loading parameter is unknown at a time.

$$\begin{aligned} U(a) &= U_0 + \sum_{i=1}^{n} a^i U_i \\ \lambda(a) &= \lambda_0 + \sum_{i=1}^{n} a^i \lambda_i \end{aligned} \tag{2.74}$$

This model is capable of detecting the flatness defects area, determining the buckling mode, the buckling load and following its evolution. **MAN** gives a geometrical description of the flatness defect both before and after tension release (see Figure 2.12). For more details on the equations of each step check [Abdelkhalek, 2010].

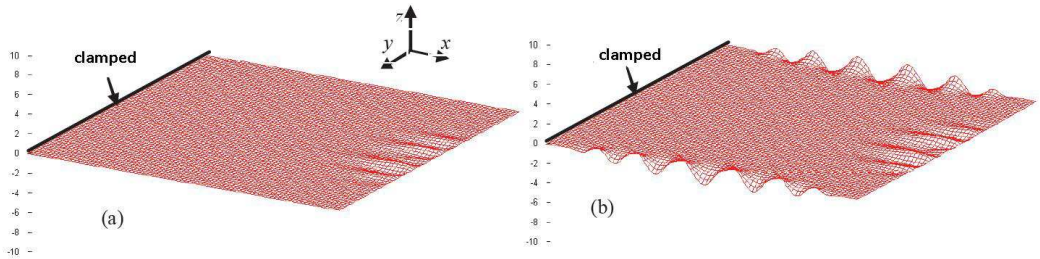

Figure 2.12: The defective plate: (a) under strip tension (b) after strip tension release [Abdelkhalek, 2010].

Remark 6

In the decoupled approach, the buckling model **MAN** is used with Lam3/Tec3 in the following way:

i) First, a rolling simulation is launched using Lam3/Tec3 without taking into account buckling, supplying fields of residual stress for the buckling model.

ii) Then, these fields of residual stress are used as loads in the shell buckling model **MAN** which gives the critical load, the buckling mode as well as the post-buckling state and the new distribution of the stress in the steel strip.

Remark 7

An approach which deserves mentioning is the one proposed by Marchand et al. [Marchand, 2000] where a first attempt to couple buckling under residual stress with a commercial rolling model such as Abaqus was established. Since it is near impossible to inject a residual stress distribution in Abaqus [Abaqus, 2008], it was done via the thermal field: starting from a heterogeneous temperature field, cooling induces a thermo-elastic stress field distribution considered as the residual stress. This method is a good alternative, yet it presents some limitations: a complex nonuniform stress distribution cannot be expressed easily using the thermal field and thus is not able to model a realistic buckling-rolling problem.

2.3.2 Coupled approaches for Rolling-buckling problems

All the models presented earlier were dedicated to studying buckling during flat rolling but decoupling the buckling phenomenon from the rolling process.Taking into account that buckling is a direct consequence of the strip plastic deformation happening in the bite and that buckling can relax the residual stresses generated by these deformations, the best representation of the complete process can be described by coupling these two phenomenons. Such models are hard to find in the literature but two particular works stand out: the works of Counhaye [Counhaye, 2000] and Abdelkhalek [Abdelkhalek, 2010].

2.3.2.1 Rolling-buckling model by Counhaye

Counhaye in his work, was one of the first to include simple yet efficient method to deal with sheet buckling in a rolling model. The rolling model used is based on Finite Difference Method (FDM) where steady state formulation based on streamlines is used. The buckling representation is founded on the hypothesis that when the structure is saturated by residual compressive stress, buckling occurs and relaxes the stress distribution to respect a certain value and remain in its vicinity. This value is the critical stress and was estimated in [Counhaye, 2000] by:

$$\sigma_{cr} = \frac{\pi E h^2}{3\tilde{l}^2} \tag{2.75}$$

in which E is Young's Modulus, h is the rolled strip thickness and $\tilde{l}$ is the wavelength estimation. This form is similar to what is proposed by Timoshenko in [Timoshenko & Gere, 1961]. Similar to the work of Roddeman et al. [Roddeman et al. , 1987.a)], the foundation of

the model consists in determining an extra deformation ε^{bu} which elastically brings the stress in the buckled direction back to σ_{cr}.

$$\varepsilon = \varepsilon^{el} + \varepsilon^{pl} + \varepsilon^{bu} \tag{2.76}$$

where ε^{el}, ε^{pl} and ε^{bu} present respectively the elastic strain tensor, the plastic strain tensor and the additional strain tensor added by buckling.

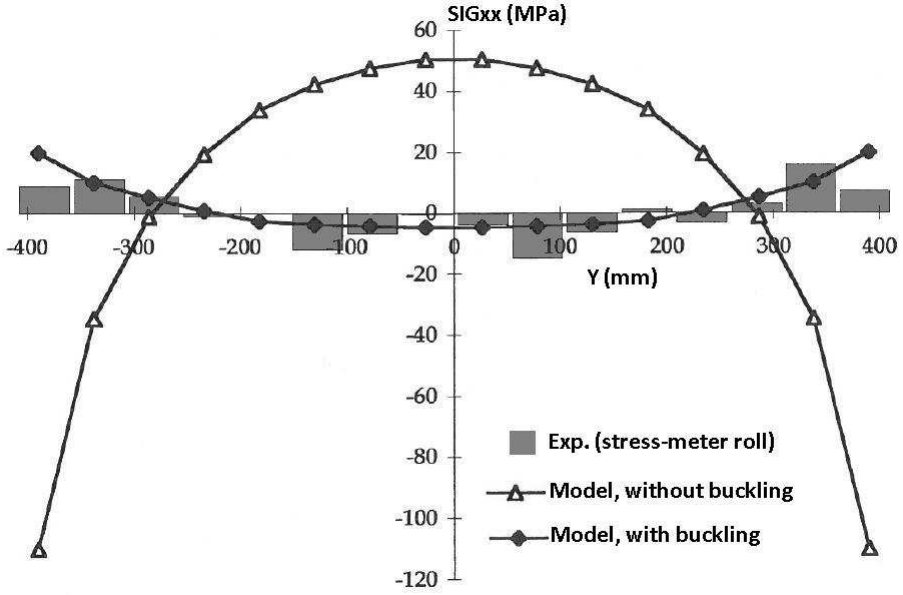

Figure 2.13: Longitudinal Stress distribution after tandem n.5 bite exit. Comparison between experimental measurements and numerical results with two models, one taking the buckling effect into account and the other neglecting it [Counhaye, 2000].

Although this method is based on the simplest hypothesis, this first of a kind coupling (between the buckling phenomenon and the strip-roll deformation model) proves its importance. Its efficiency can be closely inspected via the stress profile σ_x. A comparison between the experiment results (measured on the mill by a flatness roll) and the numerical results proves that taking into account the buckling effects in the rolling simulations upgrades the results to: i) respect the buckling criterion σ_{cr} and ii) be in a good agreement with measurements (see Figure 2.13). Note that this method can detect successfully the buckling directions and zones but still is not able to describe the geometric form of the defect neither determine its amplitude.

2.3.2.2 Rolling-buckling model Lam3/Tec3 by Abdelkhalek

2.3.2.2.1 Lam3/Tec3

As Lam3/Tec3, used by Abdelkhalek, is also the basis of our own work, it is worth taking this opportunity to present it in a few words.
The basis of the present approach is an implicit FEM based rolling model called Lam3/Tec3, developed in the 90's and early 2000's. It couples strip and roll stack deformation models, as described in [Hacquin et al., 1998.a), Hacquin et al., 1998.b), Hacquin, 1996]. Its general flow chart is given in Figure 2.15. For the strip deformation (Lam3), the most salient feature is a steady state formulation based on streamline integration to correct the shape for spread, anticipation of deformation at bite entry etc... This can be considered as a variant of Eulerian-Lagrangian formulation. A great care is devoted to the determination of the contact onset and exit, a difficulty in streamline techniques [Yamada et al., 1992], since, due to the space integration, strip surface streamlines may penetrate the roll surface, or on the contrary lose contact artificially (see Figure 2.14).

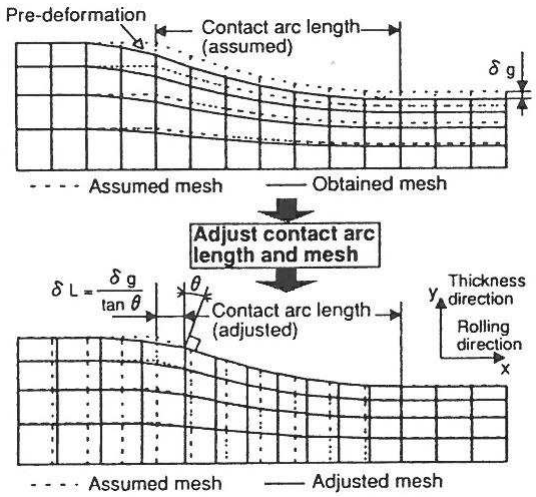

Figure 2.14: An illustration of the streamline technique presented in [Yamada et al., 1992].

Another important point is the thermal-mechanical coupling. Due to the high Peclet number (advection dominates conduction heat flow), a Streamline Upwind method is used [Pardo & Weckman, 1990].
As many aspects of the formulation rely on streamlines, a structured mesh has been preferred. It is based on 8-node, tri-linear hexahedra, with reduced integration of the pressure in the Principle of Virtual Power [Gratacos et al., 1992.a)]. Figure 2.16 illustrates the structured mesh, formed by "extrusion in the rolling direction" of a rectangular grid of the upstream plane. Structuring the mesh allows a very efficient local refinement of the mesh, in particular at bite entry and exit. As residual stresses are essential here,

an elastic-visco-plastic constitutive model is used. It is based on Prandtl - Reuss additive decomposition of strain rate. Jaumann objective derivative is used to write the elastic model in rate form, and associated von Mises behavior is assumed for plasticity. The incremental consistency is based on the standard radial return technique. In the principle of virtual work, the updated stress is obtained by streamline integration, where the time needed for matter to move from an integration point to the next in the streamline is a substitute for time step [Hacquin, 1996]-since time does not exist properly speaking in a steady state formulation. As the pseudo-time step is therefore point dependent due to the adapted mesh, the formulation has been termed "Generalized Heterogeneous Time Stepping" (GHTS).

The roll stack deformation model is another essential feature. Like most of the previous ones [Shohet & Townsend, 1968], the single roll bending and flattening model is based on Timoshenko beam theory, Boussinesq solution for a half-space under general loading, combined after the results in [Berger et al., 1976]. Based on extensive FEM simulations, corrections have been brought for end effect and the barrel / axle transition. Hertzian contact mechanics is assumed for work roll (WR) / back-up roll (BUR) contact. The Influence Function Method (IFM) is used to discretize the system, with particular refinement near the edge of the strip-WR contact. A global non-linear system is formed with all displacements of all contact lines, with external forces (rolling load, WRB or BURB) in the right-hand side. This non-linear system is solved by Newton-Raphson method. Details can be found in [Hacquin et al., 1998.a), Hacquin et al., 1998.b)].

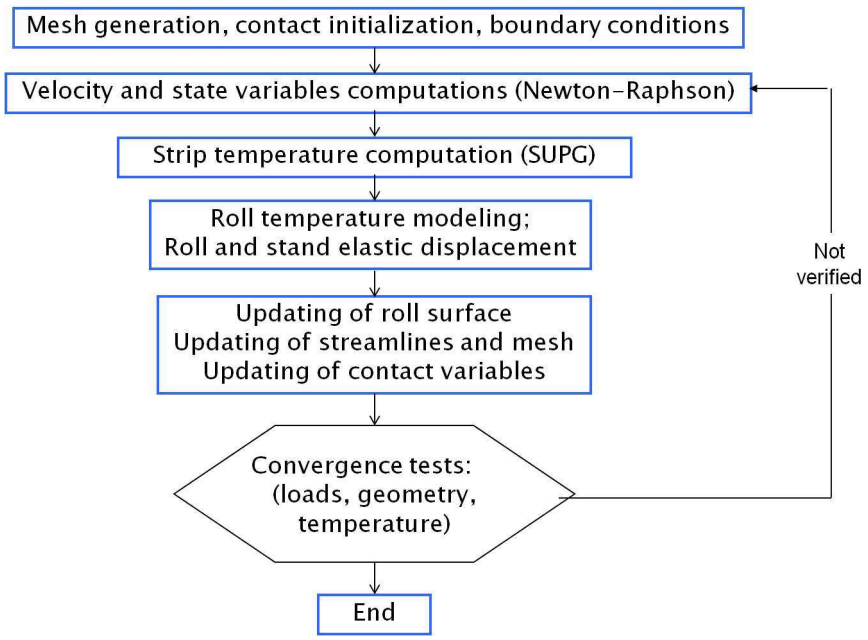

Figure 2.15: General algorithm of the Lam3/Tec3 FEM strip rolling model.

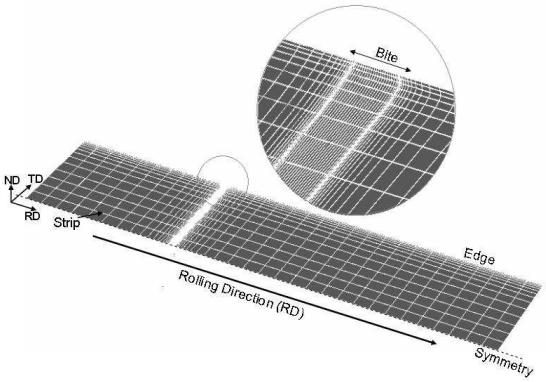

Figure 2.16: The structured mesh used in Lam3. Note axes x = Rolling Direction [RD], y = Transverse Direction [TD], z = Normal Direction [ND].

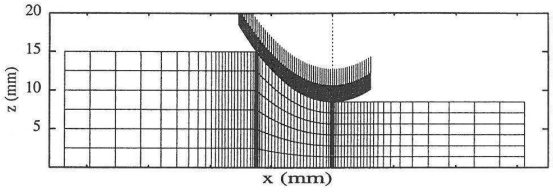

Figure 2.17: A side view of the structured mesh containing several elements in the thickness.

2.3.2.2.2 Rolling-buckling model Lam3/Tec3-Abdelkhalek

The simple approach proposed by Counhaye in [Counhaye, 2000] to deal with sheet buckling in a FDM rolling model, seems quite similar to the one presented in a more general context by Roddeman et al. in [Roddeman et al. , 1987.a), Roddeman et al. , 1987.b)]. The same has been implemented in Lam3/Tec3 by Abdelkhalek in [Abdelkhalek, 2010, Abdelkhalek et al., 2011].

In the context of small incremental deformation, the strain tensor is the sum of two components: if buckling happens in the direction 1 (respectively 2), the conditions (2.44) introduced by Roddeman et al. in [Roddeman et al. , 1987.a), Roddeman et al. , 1987.b)] hold for $\sigma_c \neq 0$

$$\begin{array}{lll} \vec{n_1}.\sigma.\vec{n_1} = \sigma_c & & \vec{n_1}.\sigma.\vec{n_1} > 0 \\ \vec{n_2}.\sigma.\vec{n_2} > 0 & \text{respectively} & \vec{n_2}.\sigma.\vec{n_2} = \sigma_c \\ \vec{n_1}.\sigma.\vec{n_2} = 0 & & \vec{n_1}.\sigma.\vec{n_2} = 0 \end{array} \tag{2.77}$$

If the thin strip is subjected to plane stress, then $\sigma = \begin{pmatrix} \sigma_{11} & \sigma_{12} & 0 \\ \sigma_{12} & \sigma_{22} & 0 \\ 0 & 0 & 0 \end{pmatrix}$ and

$\varepsilon = \begin{pmatrix} \varepsilon_{11} & \varepsilon_{12} & 0 \\ \varepsilon_{12} & \varepsilon_{22} & 0 \\ 0 & 0 & \varepsilon_{33} \end{pmatrix}$ are respectively the stress and strain tensor.

Consider $\Lambda = \begin{pmatrix} \lambda_I \\ \lambda_{II} \end{pmatrix}$ where λ_I et λ_{II} are the extra deformations representing buckling computed in the principal directions I et II.

Solving conditions (2.77),

$$\lambda_i = \frac{|\sigma_c - \sigma_i|}{E},\ i = I.II \tag{2.78}$$

where E is Young's Modulus.
λ_i for $i = I, II$ could be computed using the stress components σ_{ij} pour $i, j = 1, 2$ in the reference frame as:

$$\lambda_I = \frac{1}{E}\left(\left|\sigma_c - \left(\frac{\sigma_{11}+\sigma_{22}}{2}\right) - \sqrt{\left(\frac{\sigma_{11}-\sigma_{22}}{2}\right)^2 + \sigma_{12}^2}\right|\right) \tag{2.79}$$

$$\lambda_{II} = \frac{1}{E}\left(\left|\sigma_c - \left(\frac{\sigma_{11}+\sigma_{22}}{2}\right) + \sqrt{\left(\frac{\sigma_{11}-\sigma_{22}}{2}\right)^2 + \sigma_{12}^2}\right|\right) \tag{2.80}$$

Moving back to the reference frame (Figure 2.18 (b)) with $\theta = \frac{1}{2} tan^{-1}\left(\frac{\sigma_{12}}{|\sigma_{11}-\sigma_{22}|}\right)$, the buckling strain is computed then added to the global strain increment:

$$\Delta\varepsilon_{11}^{bu} = \begin{pmatrix} cos\theta \\ sin\theta \\ 0 \end{pmatrix}^t \begin{pmatrix} \lambda_I & 0 & 0 \\ 0 & \lambda_{II} & 0 \\ 0 & 0 & 0 \end{pmatrix} \begin{pmatrix} cos\theta \\ sin\theta \\ 0 \end{pmatrix} = \lambda_I.cos^2\theta + \lambda_{II}.sin^2\theta \tag{2.81}$$

$$\Delta\varepsilon_{22}^{bu} = \begin{pmatrix} -sin\theta \\ cos\theta \\ 0 \end{pmatrix}^t \begin{pmatrix} \lambda_I & 0 & 0 \\ 0 & \lambda_{II} & 0 \\ 0 & 0 & 0 \end{pmatrix} \begin{pmatrix} -sin\theta \\ cos\theta \\ 0 \end{pmatrix} = \lambda_I.sin^2\theta + \lambda_{II}.cos^2\theta \tag{2.82}$$

$$\Delta\varepsilon_{12}^{bu} = \begin{pmatrix} cos\theta \\ sin\theta \\ 0 \end{pmatrix}^t \begin{pmatrix} \lambda_I & 0 & 0 \\ 0 & \lambda_{II} & 0 \\ 0 & 0 & 0 \end{pmatrix} \begin{pmatrix} -sin\theta \\ cos\theta \\ 0 \end{pmatrix} = |\lambda_{II} - \lambda_I|.sin\theta.cos\theta \tag{2.83}$$

This strain increment is added to the standard one computed by the module solving the constitutive differential equations as illustrated in Figure 2.18(a).

After implementing this simplified buckling model in the rolling model Lam3/Tec3, the new stress distribution taking into account the relaxing effect of the buckling is i) more realistic than the one neglecting the impact of the buckling appearance, ii) respects the buckling criterion and iii) is in a good agreement with the experimental measurements (see Figure 2.19).

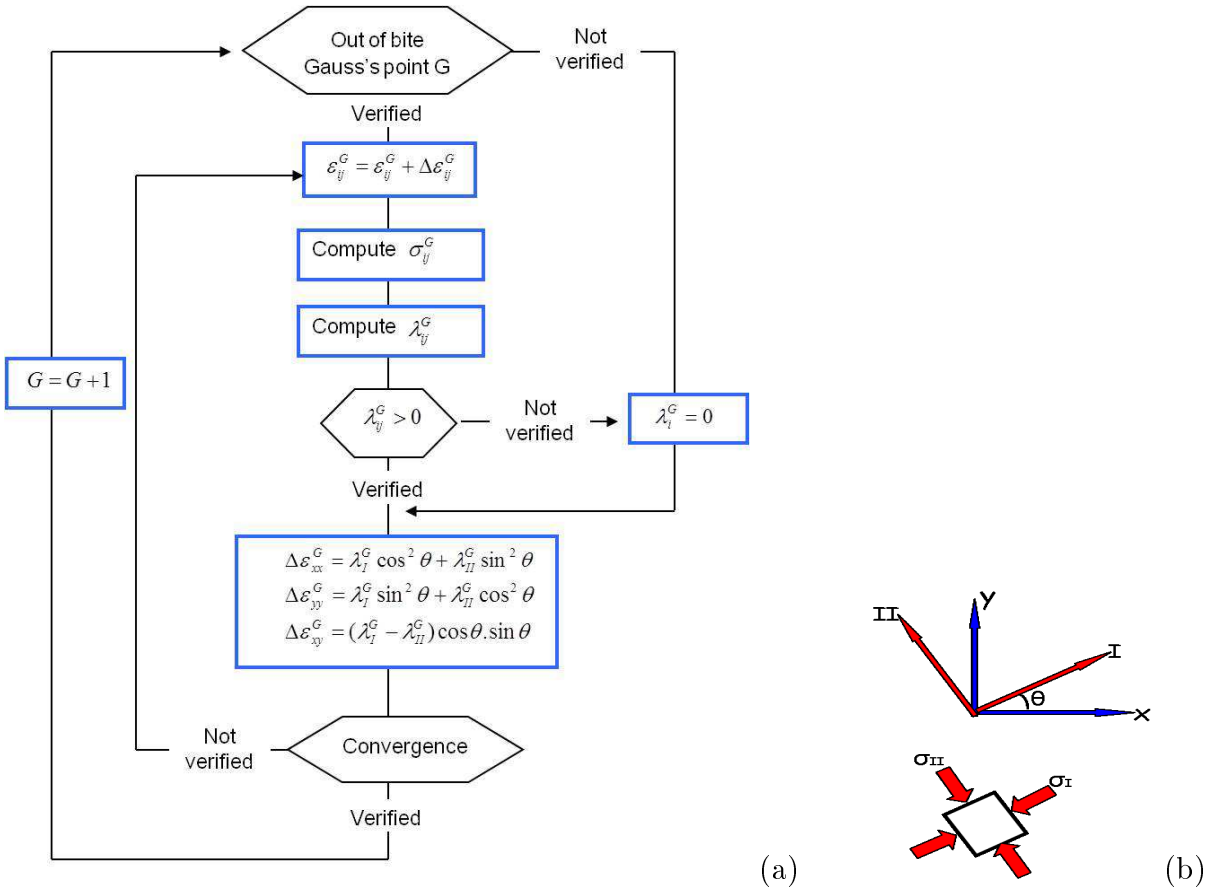

Figure 2.18: On the left: General algorithm of the buckling model implemented directly in Lam3 . On the right: the principal axes rotated by an angle θ from the reference ones.

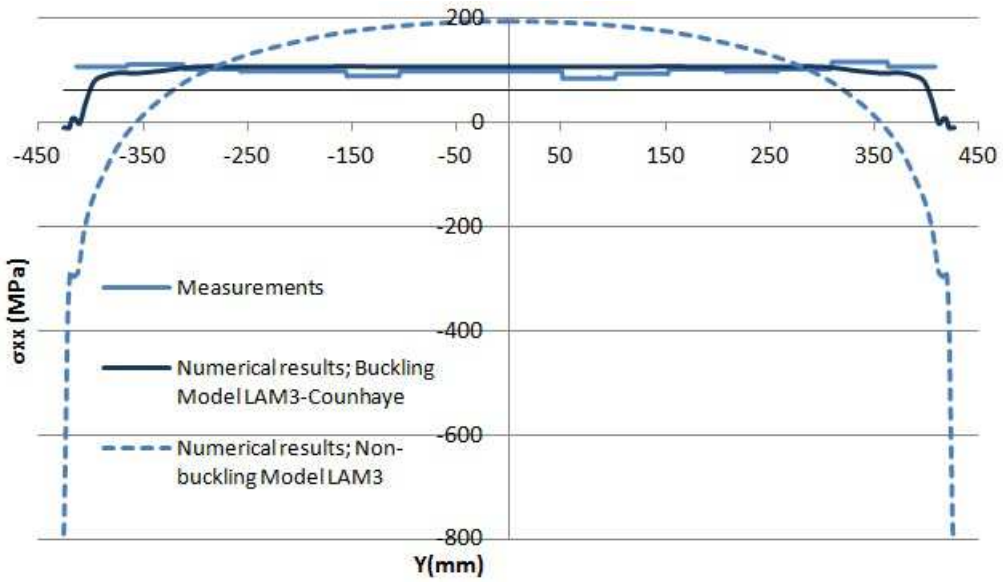

Figure 2.19: Comparison of the longitudinal stress distribution σ_x between the experimental results and the numerical one using i) a non-buckling rolling model (Lam-Tec3) and ii) a buckling-rolling model (Lam3/Tec3/Counhaye) [Abdelkhalek, 2010].

Remark 8

This coupled rolling-buckling model is one of the few treating the buckling problem completely integrated in the rolling process.
It provides a post-buckling description by means of additional deformations and can detect were the defects appear i.e. where $\lambda_i \neq 0$. This model however fails to quantify the amplitude and the form of the defect.

2.3.2.3 Rolling-Buckling model Lam3/Tec3-MAN

The coupling between the strip and roll stack deformation model Lam3/Tec3 and the shell buckling model **MAN** is built in a way that the roll stack deformation is described by Tec3, the strip deformation in the bite by Lam3 (3D FE) and strip buckling outside the bite is described by **MAN** (shell FE) (See Figure 2.21).
A coupling interface (or connecting section) is defined by the red dots in Figure 2.21, in which Lam3/Tec3 receives the additional stress field caused by the strip buckling via the boundary conditions (2.84.a).

$$\begin{aligned} \overrightarrow{T}^{c}_{Lam3} &= -\overrightarrow{T}^{c}_{MAN} \quad \text{(a)} \\ \overrightarrow{T}^{c}_{MAN} &= \sigma_{MAN}.\overrightarrow{n}_r \quad \text{(b)} \end{aligned} \tag{2.84}$$

where $\overrightarrow{n}_r$ is the normal vector to the coupling section and σ_{MAN} is the stress field computed by **MAN**.

The coupling algorithm, described in Figure 2.20, begins with a standard Lam3/Tec3 simulation, which supplies the out-of-bite residual stress distribution σ_{res}. This stress distribution is then transferred to the buckling model **MAN**. A new post-buckling stress distribution $\overrightarrow{T}^{c}_{MAN}$ is computed by **MAN**. It is used as a new boundary condition for Lam3/Tec3: $\overrightarrow{T}^{c}_{Lam3} = -\overrightarrow{T}^{c}_{MAN}$. Next, a new simulation is run using Lam3/Tec3 but only treating a part of the strip rolling: the bite vicinity. The purpose of this step, called the truncated simulation, is to insure the interaction between buckling and what happens in-bite i.e. the buckling will possibly change the roll geometry. If the roll stack geometry is unchanged the program is put to an end. If not, the new roll stack geometry is imported and used to repeat the first step and loop all over again until converging i.e. the roll geometry remains stable.

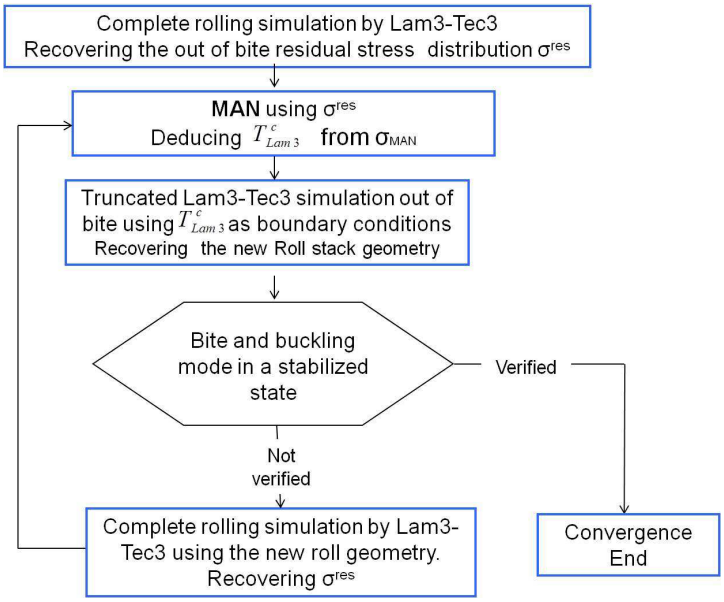

Figure 2.20: Lam3/Tec3/**MAN** coupling algorithm

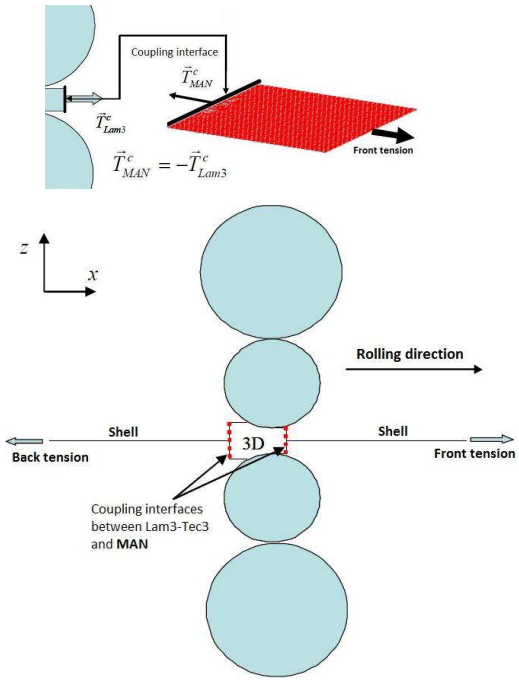

Figure 2.21: Lam3/Tec3-**MAN** coupling scheme [Abdelkhalek, 2010].

Before presenting the defective strip described by Lam3/Tec3-**MAN**, one important point should be clarified: the initial version of **MAN** presented in section 2.2.2.1 and in [Abdelkhalek, 2010], was found reliable for the simulation of academic cases, but presents limitations when coupled with Lam3/Tec3 to simulate industrial problems. Figure 2.23a) confirms the difficulties where no waviness on the edges were detected despite the stress profile presenting very large compressive stresses near the edges.

To correct this defect, an optimized version called MAN v2 [Note MAN v2.0, 2013] was introduced. It is a combination of the method **MAN** with a Newton-Raphson algorithm allowing to control the chosen bifurcation branch: it chooses a nearby solution verifying the equilibrium state. In other words the combination **MAN**-Newton-Raphson helps managing nearby solution branches showing smaller energy. This resolution procedure is called HOPC (High Order Prediction Correction).

The new version **MAN** v2 is an implicit resolution of the problem which guarantees a good residue along the branch solution; while the older version **MAN** v1 is an explicit resolution where the system can stray away progressively from the solution (see Figure 2.22).

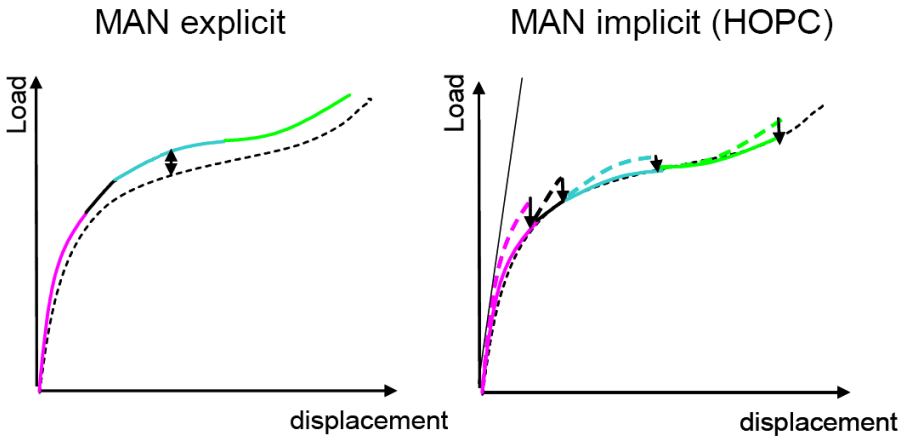

Figure 2.22: On the left: Explicit **MAN** (version 1), on the right implicit **MAN** (version 2).

Using the optimized version, Lam3/Tec3-**MAN** is now able to detect the wavy edges with an amplitude of 3.5 mm, which seems more realistic and compatible with the conclusions presented by Counhaye in [Counhaye, 2000]: small wavy edge defects of the order of $\simeq$ 1 mm with a wavelength equal to 70 mm and a depth of 10 mm.

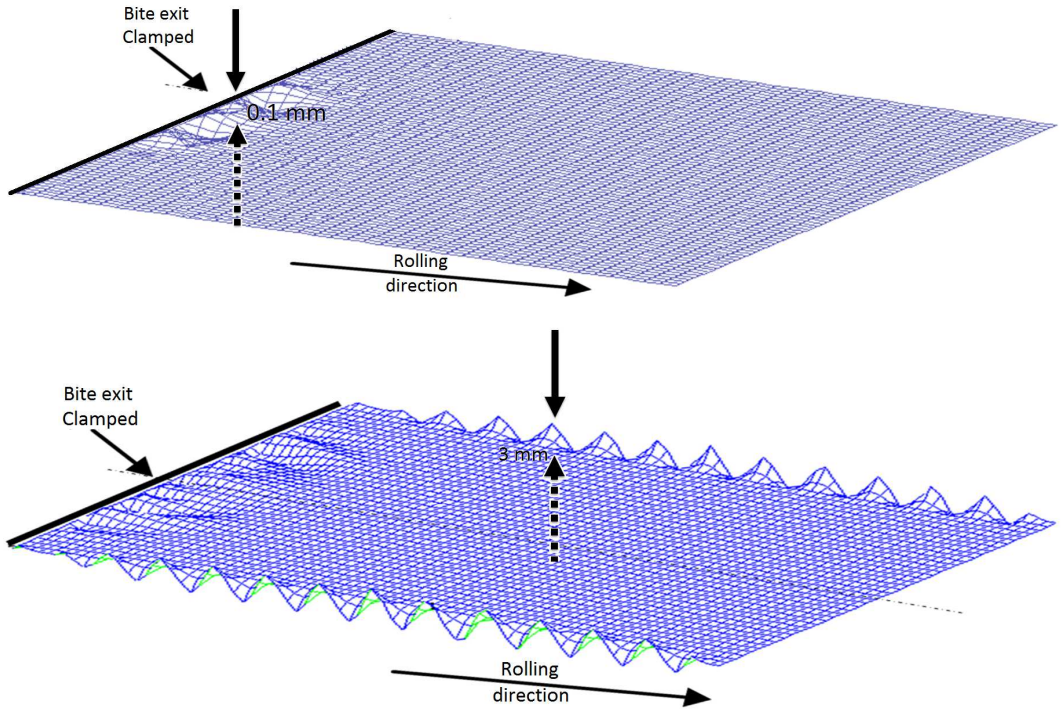

Figure 2.23: The defective plate under strip tension described using the coupled approach Lam3/Tec3-MAN: (a) the initial Lam3/Tec3-MAN version called Lam3/Tec3-MAN2010 and (b) the optimized version called Lam3/Tec3-**MAN**2013.

When compared with the experimental measurements (provided by the flatness roll), the new stress distribution shows a great improvement and good agreement. By that it is concluded that taking the buckling effects into account is a must (see Figure 2.24).

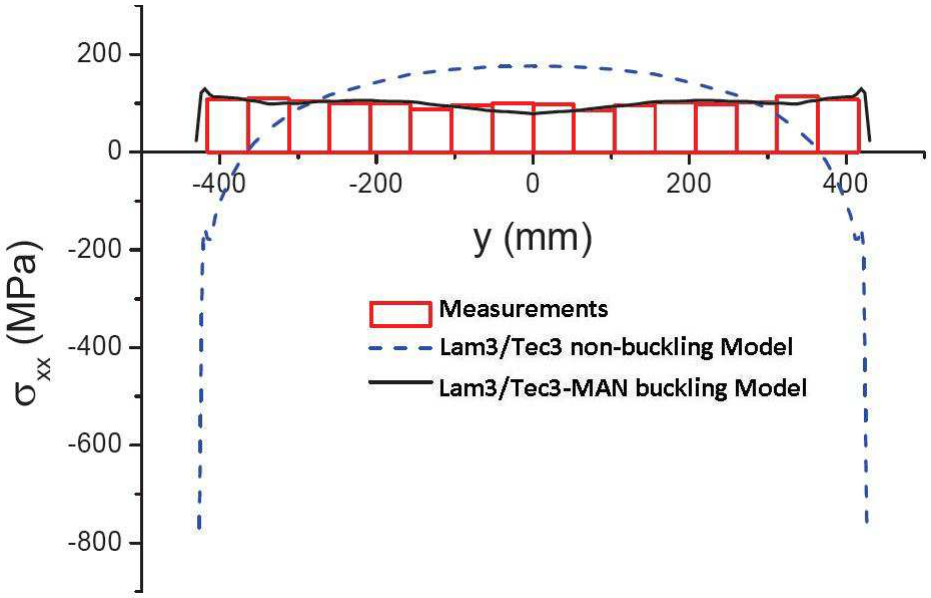

Figure 2.24: Comparison of the longitudinal stress distribution σ_x between the experimental result and the numerical one using i) a non-buckling rolling model (Lam-Tec3) and ii) a buckling-rolling model (Lam3/Tec3-MAN2010) [Abdelkhalek, 2010].

Note that in his thesis [Abdelkhalek, 2010], Abdelkhalek did not detect any buckling-bite interaction for this special rolling operation: The buckling appearance has minimal to no effect on what happens in the bite (redistribution of the stress, rolling speed and strip thickness).
Until now, the model Lam3/Tec3-MAN seems to be the most powerful model predicting a complete rolling operation presenting flatness defects. It can predict the type and form of the flatness defects, quantify the defect amplitude and provide the new stress distribution post-buckling.
In spite of its strong points, it presents some downsides such as its complicated coupling method leading to difficult use and significantly more computing time.

Remark 9

This type of coupling presents several difficulties regarding the coupling interface such as i) where to choose exactly the coupling interface position after the bite exit and ii) how to make it straight. And since the coupling is done via the stress field, there is some simplifications taken to ensure its continuity; which is not evident due to the non uniform geometry especially at bite exit.

A more rigorous way is to couple two different finite elements models such as Lam3/Tec3 (3D FE) and **MAN** (shell FE) by the Arlequin coupling or what is called bridging technique [Ben Dhia & Jamond, 2010, Ben Dhia, 1998, Ben Dhia & Rateau, 2001]. It ensures the continuity and the coexistence of the two different domains (the same energy for the two sub-domains) in the overlapping zone called gluing zone (Figure 2.25). The Arlequin coupling for this particular case is relatively delicate due to two completely different formulations: one is a velocity based formulation (in Lam3) and the other a displacement based formulation (in **MAN**). Such a coupling is being attempted presently within the ANR PLATFORM project (K. Kpogan - Y. Tampango, personal communication, August 2013).

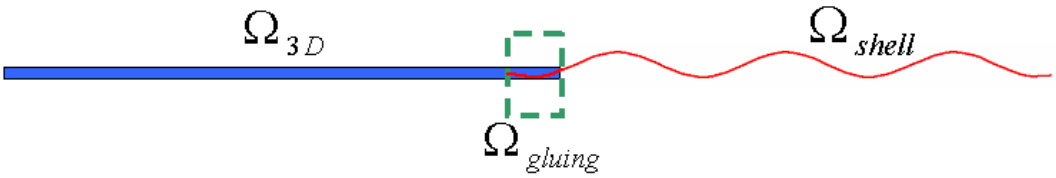

Figure 2.25: Arlequin framework for two different finite elements domains

The mixed Arlequin problem based on an energetic coupling is:

$$\begin{aligned}
&\text{Find} && (u_{3D}, u_{shell}, \lambda^A) \in W_{3D} \otimes W_{shell} \otimes W_{gluing};\\
&\forall v_{3D} \in W_{3D} && , \int_{\Omega_{3D}} \alpha_{3D}\sigma(u_{3D}) : \varepsilon(v_{3D}) + C(\lambda^A, v_{3D}) = \int_{\Omega_{3D}} \beta_{3D} f.v_{3D}\\
&\forall v_{shell} \in W_{shell} && , \int_{\Omega_{shell}} \alpha_{shell}\sigma(u_{shell}) : \varepsilon(v_{shell}) - C(\lambda^A, v_{shell}) = \int_{\Omega_{shell}} \beta_{shell} f.v_{shell}\\
&\forall \mu \in W_{gluing} && , C(\mu, u_{3D} - u_{shell}) = \int_{\Omega_{gluing}} \sigma(\mu) : \varepsilon(u_{3D} - u_{shell}) = 0
\end{aligned} \tag{2.85}$$

in which f is the volume density of the applied forces, σ and ε are respectively the stress and strain tensors. The couples $(\alpha_{3D}, \alpha_{shell})$ and $(\beta_{3D}, \beta_{shell})$ are respectively the unity partition of the internal and external energies. The form of the coupling operator $c(.,.)$, chosen in equation 2.85, is one of many others available depending of the problem complexity.
W_{3D}, W_{shell} and W_{gluing} are Sobolev spaces defined as follows:

$$\begin{aligned}
&W_{3D} = H_1(\Omega_{3D}) = \{v_{3D} \in L^1(\Omega_{3D}), Dv_{3D} \in L^1(\Omega_{3D})\}\\
&W_{shell} = H_1(\Omega_{shell}) = \{v_{shell} \in L^1(\Omega_{shell}), Dv_{shell} \in L^1(\Omega_{shell})\}\\
&W_{gluing} = H_1(\Omega_{gluing}) = \{v_{gluing} \in L^1(\Omega_{gluing}), Dv_{gluing} \in L^1(\Omega_{gluing})\}
\end{aligned} \tag{2.86}$$

Remark 10

The notion of "critical stress" is inadequate language, it can be only used when the stress distribution is homogeneous all over the domain. Otherwise, to an heterogeneous loading corresponds a "critical loading".
Not all researchers respected this naming. For instance, Counhaye in his work [Counhaye, 2000], defined a unique critical value (typical Timoshenko form) to be respected globally on each point of the strip. Rigorously, this is only valid for a homogeneous stress distribution, contradicting what is used in his study. To overcome this contradiction, Counhaye treated every element separately discretizing the heterogeneous stress distribution into constant field per element. It cannot be said that the followed approach is a good presentation of the reality.

In our study, "critical stress" corresponds to a value determined locally: on the edge or center depending on the compressive zone position. For an heterogeneous transverse stress profile $\sigma_x(y)$ the stress value σ_{cr} corresponding to the critical loading λ_{cr} is equal to $\lambda_{cr}.Min(\sigma_x(y))$ where $Min(\sigma_x(y)) < 0$.

2.4 Conclusion

This survey cited sources of available approaches for treating plate buckling problem, whether they were applied to flatness defects during flat rolling or not. Then, the few available approaches treating buckling and rolling as a coupled problem were presented evoking both their capacities and deficiencies.
The aim is to complete the available rolling model Lam3/Tec3 by a buckling model capable of detecting and describing the buckling of the plate. This model should be simple enough to be integrated completely in the rolling model Lam3/Tec3, avoiding coupling interfaces such as the one used to couple Lam3/Tec3 with **MAN**. The resulting model is expected to be able i) to detect flatness defects zones, ii) to determine the mode and the buckling load, iii) to quantify the buckling amplitude, iv) to relax the stress distribution by an additional stress distribution to respect the buckling criterion and v) to take into account the bite-buckling interactions.
None of the previous works was able to fulfill all of these demands:

1) The simplified buckling model presented by Counhaye and then implemented by Abdelkhalek in Lam3 is capable of detecting the zone with flatness problems and relax-

ing the stress distribution to respect both the buckling load and the experimental results but fails to quantify the buckled geometry.

2) The shell buckling model **MAN** is capable of describing the buckling and post-buckling state of the strip and can give a good approximation of the buckling amplitude. By itself, it cannot take the interaction between the bite and the buckling into account.

3) When coupled with the rolling model Lam3/Tec3, the shell buckling model **MAN** was subject to several problems. A smooth transition between the shell and 3D finite elements formulation such as given by the Arlequin coupling could not be insured, because of the displacement versus velocity based formulation of **MAN** and Lam3/Tec3. Instead, the coupling was done going back and forth between the two models transmitting the results of each model as boundary conditions to the other one via the coupling interface.

The purpose is to find a simple yet pertinent approach; pertinent means capable of doing what **MAN** and Counhaye's model combined can do i.e. describing the buckling and post-buckling state, and simple means that it should be integrated completely in the rolling model Lam3/Tec3.
The only approach that seems to respond to these needs is the Multi-Scale Method based on Fourier series expansion presented in section 2.2.2.2. By its simplicity, it is capable of describing the flatness defects and seems to have a similar way as Counhaye's buckling model to be coupled with Lam3/Tec3. The application of this approach on flatness defects during cold rolling processes will be treated, developed and studied in Chapters 4 and 5 then coupled with Lam3/Tec3 in chapter 6.

Before proceeding, an illustration of Lam3/Tec3-Abdelkhalek model capacities will be presented by a full description with application to real rolling problems. The purpose of Chapter 3 is to clarify the notion of flatness defects and its direct relation with the stress distribution in view of a comparison in Chapter 5.

2.5 Résumé en Français

Dans ce chapitre, une enquête citant différentes approches disponibles dans la littérature pour le traitement de flambage des tôles a été présentée. Ensuite, quelques approches traitant le flambage durant le laminage de façons couplées et découplées ont été exposées évoquant à la fois leurs capacités et leurs lacunes .
Le but est de compléter le modèle de laminage disponible Lam3/Tec3 par un modèle de déformation capable de détecter et de décrire la déformation de la plaque . Ce modèle devrait être assez simple pour être complètement intégré dans le modèle de laminage Lam3/Tec3, évitant les interfaces de couplage telles que celles utilisées pour coupler Lam3/Tec3 avec **MAN**. Le modèle résultant devrait être capable de i) détecter les défauts de planéité, ii) déterminer le mode et la charge de flambement, iii) quantifier l'amplitude des vagues, iv) redistribuer les contraintes post-flambement et v) prendre en compte les interactions cage-flambement.
Aucun des travaux antérieurs n'est apte à remplir toutes ces exigences :

1) Le modèle de flambement simplifié présenté par Counhaye puis mis en oeuvre par Abdelkhalek dans Lam3 est capable de détecter la zone présentant des problèmes de planéité et de redistribuer les contraintes post-flambage pour respecter les mesures expérimentales, mais ne peut pas quantifier l'amplitude des défauts.

2) Le modèle de flambage (EF coques) **MAN** est capable de décrire l'état de flambage et post-flambage de la tôle et peut donner une bonne approximation de l'amplitude de la déformation. Découplé, il ne peut pas prendre en compte l'interaction entre la cage et le flambage.

3) Pour être couplé avec le modèle de laminage Lam3/Tec3, **MAN** rencontre plusieurs problèmes. Une transition entre l'élément fini coque et l'élement fini 3D, comme proposée par le couplage Arlequin, n'a pas pu être assurée en raison des deux formulations différentes utilisées (en vitesse dans **MAN** et en déplacement dans Lam3/Tec3). Le couplage a donc été fait via des allers-retours entre les deux modèles transmettant les résultats de l'un comme conditions limites de l'autre.

Le but est de trouver une approche pertinente et simple à la fois. 'Pertinente' signifie être capable d'accomplir ce que **MAN** et le modèle de Counhaye combinés peuvent faire (décrire l'état flambé et post-flambé de la tôle), et 'simple' signifie qu'il doit être complètement intégré dans le modèle de laminage Lam3/Tec3 pour éviter des problèmes de couplage.
La seule approche qui semble répondre à ces besoins est la méthode multi-échelle utilisant

des développements en série de Fourier (section 2.2.2.2). Par sa simplicité, elle est capable de décrire les défauts de planéité et semble avoir la même façon de se coupler avec Lam3/Tec3 que le modèle de Counhaye. L'application de cette approche sur la modélisation de défauts de planéité au cours des opérations de laminage à froid sera traitée et étudiée dans les chapitres 4 et 5, ensuite couplée avec Lam3/Tec3 dans le chapitre 6.

Avant de commencer, une illustration des capacités du modèle Lam3/Tec3-Abdelkhalek sera présentée avec application sur de vrais problèmes de laminage . Le but du chapitre 3 est de clarifier la notion de défaut de planéité et sa relation directe avec la répartition des contraintes en vue d'une comparaison dans le chapitre 5.

CHAPTER 3

FLATNESS ACTUATORS ON LINE: USING LAM3/TEC3-ABDELKHALEK

Never give up on something you really want. It is difficult to wait, but worse to regret.

by Xuan Ta

Contents

Flatness defects in thin strip cold rolling are a consequence of roll thermo-elastic deformation, from which heterogeneous strip plastic deformation results (i.e. residual stress).
To study the effects of several parameters on the flatness of a thin strip, the model presented in section 2.3.2.2 will be used in this chapter. Mainly, the impacts of friction, work roll bending (WRB) and strip tension on the flatness of thin rolled strips are examined. In addition, a friction-WRB relation is established in order to obtain the optimal flatness. Finally, the effects of temperature on cold rolled strip flatness are studied. The latter part is a means to justify why thermal effects on buckling appearance are neglected later on in this study.

The goal of this chapter is not to provide a complete abacus to run a specific rolling mill, but to highlight interactions between several actuators.
Friction on the one hand, strip tensions on the other hand, have been proved to impact strip profile after cold rolling [Jiang et al., 2003, Jiang et al., 2007, Wang et al., 2007]. In [Jiang et al., 2008], the effect of a parabolic variation of friction in the transverse direction has been evaluated. The following study examines the effects of friction, work roll bending force and strip tension on the shape of the strip.

All examples shown next refer to the same rolling pass, the last stand of a tinplate sheet mill, with very low thickness. All the characteristics are detailed in Table 3.1 and Figure 3.1.

Strip width	855 mm
Strip entry thickness	0.355 mm
Strip exit thickness	0.252 mm
Strip crown	4.81 %
Rolling speed	22 m/s
Back and front tension	170 MPa - 100 MPa
Type of mill	4-high
Work Roll diameter	555 mm
Work Roll length	1400 mm
Work Roll crown	0.0322 %
Back Up roll diameter	1300 mm
Back Up roll length	1295 mm
Back Up roll crown	No crown
Work Roll bending Force	$F = 480$ KN
Work Roll bending Force position	$y = 1010$ mm
Coulomb Friction Law	$\tau = 0.025\sigma_n$
Young's Modulus	$E = 210\ GPa$
Poisson's ratio	$\nu = 0.3$
Critical stress	$\sigma_{cr} = -10$ MPa
Stress-Strain curve $\sigma_0 = (470.5 + 175.4\bar{\varepsilon}) \times (1 - 0.45e^{-8.9\bar{\varepsilon}}) - 175)$	

Table 3.1: The characteristics of the investigated rolling pass.

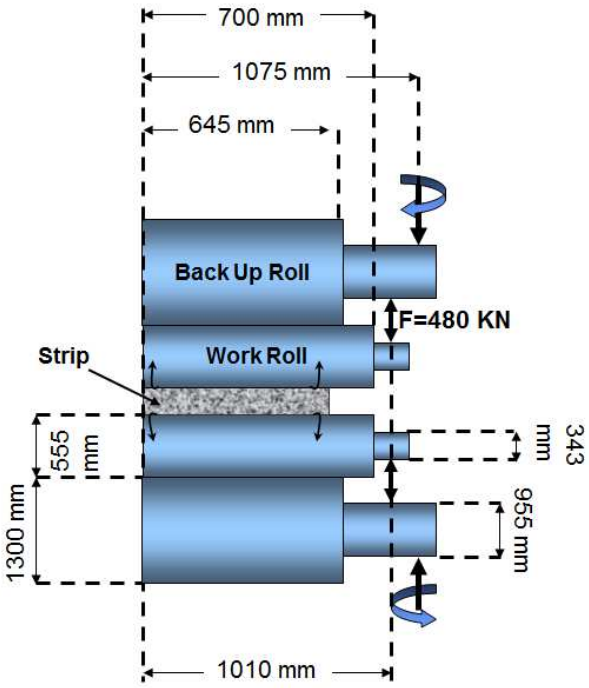

Figure 3.1: The mill structure (4-Hi) and dimensions.

3.1 Friction and Flatness

In this section, a quick study on how friction influences flatness of a thin strip is presented. The strip flatness is mainly judged via the thickness profile and the residual stress profile which can easily generate flatness defects.

The rolling operation detailed in Table 3.1 and Figure 3.1 has been modeled using coefficients of friction between 0.01 and 0.035. Figures 3.2(d) and 3.2(e) present respectively the strip thickness profile and the stress profile in a cross section about 1 m after roll bite

exit.
Figure 3.2(d) shows that as friction increases, the thickness of the strip on the edges decreases. Note that a perfect strip gauge control has been assumed, so that the central thickness is maintained at its nominal value. The reason for the growing profile defect is the higher rolling load resulting in more WR bending, hence a larger edge-drop defect. This occurs in spite of the roll crown, which is normally planned to compensate for bending, but is not adaptable when the roll load varies.

Proceeding with the stress distribution downstream of the roll bite, Figure 3.2(e) shows that changing friction may transform the on-line residual stress distribution in the strip. The profiles must be compared with the average tension 100 MPa: wherever the stress is smaller, there is a suspicion of compression after tension release, therefore of waviness. For the central value $\mu = 0.025$, the profile is slightly concave in the center, where $\sigma_{xx} < 100$ MPa. The strip might remain flat on the mill, but a wavy center is not excluded after tension release - wavy edges may also occur simultaneously as the stress, there, is close to $\sigma_{xx} = 0$. For the highest friction, $\mu = 0.035$, the tension is slightly above 100 MPa in the center, rather constant, and drops only in the last 100 mm. The curve is concave except near the edge where waviness of limited dimension might occur.
Finally, the lowest friction $\mu = 0.01$ leads to a dramatic change in the stress profile: even under strip tension, the center is practically slack, whereas the edges are extremely tensile: the WRB force 480 kN, added to the roll crown, is too large for the lower roll load, the gap is thinner in the center, the elongation of the strip is too large there (this is also where the strip is thickest at entry) and a wavy center will obviously result after tension release. It can be said that the bending force used is poorly adapted to such a low friction.
Note that as shown by the roll load transverse profile (Figure 3.2(a)) and the roll profiles (Figure 3.2(b)), "roll kiss" has occurred for $\mu = 0.035$ (mutual contact of the two WR on either side of the strip). The increasing friction results in a higher rolling load, thus the work rolls present more flattening (Figure 3.2(c)) and smaller gap in between near the edges (Figure 3.2(b)) which justifies the edge drop (i.e. higher reduction near the edges).

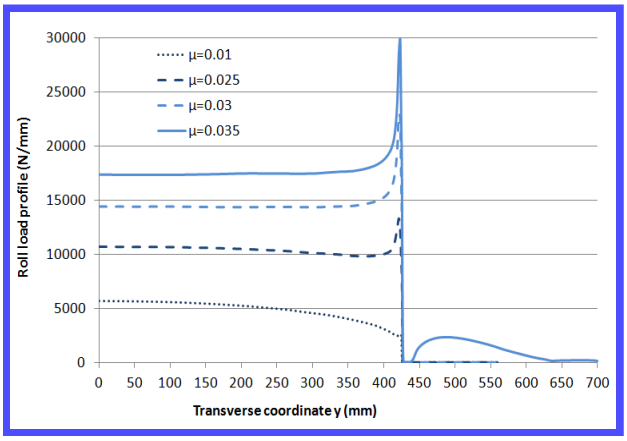

(a)

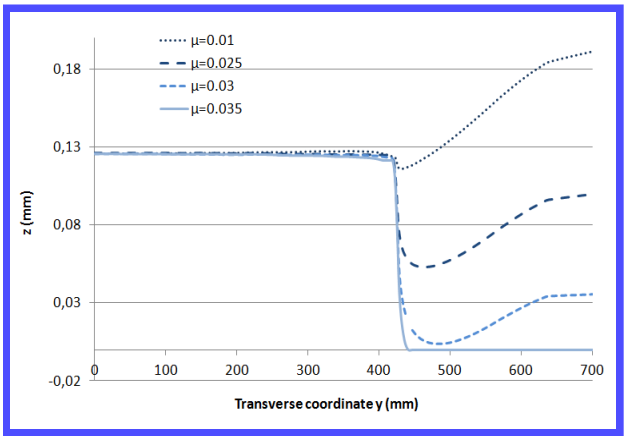

(b)

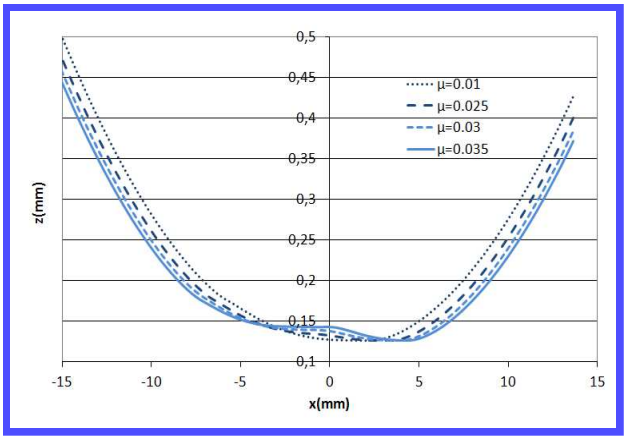

(c)

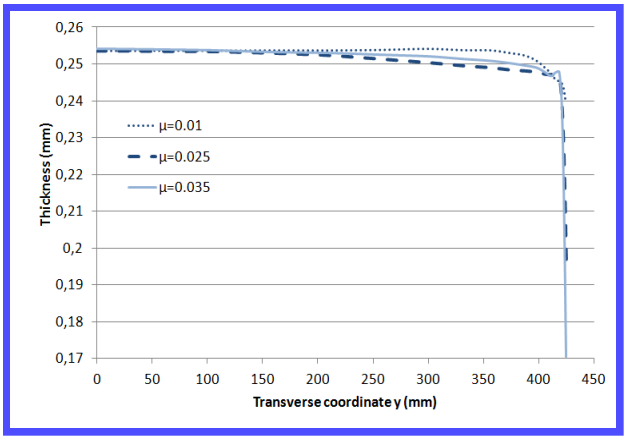

(d)

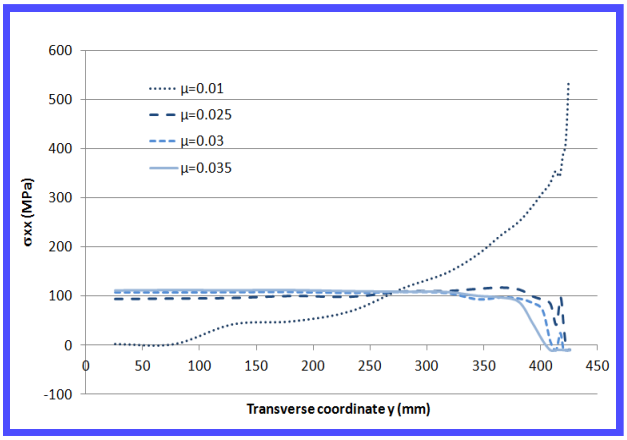

(e)

Figure 3.2: The impact of friction on (a): Roll load transverse distribution. (b): Roll active generator shape $z(y)$, (c): Roll flattening, (d): Strip thickness profile and (e): Post-buckling stress distribution under strip tension

3.2 Roll bending and Flatness

The aim of this section is to understand how changing work roll bending can impact flatness of a thin strip and how it can be adjusted to neutralize the effects of changing friction.
The rolling operation detailed in Table 3.1 and Figure 3.1 has been modeled using WRB values ranging from 350 kN to 900 kN. Again, the strip thickness profile and stress profile are presented on the same cross section used before.
Though the thickness of the strip on the edges in not dramatically affected, Figure 3.3(d) shows that as the WRB increases, the thickness profile i.e. the crown of the strip is clearly affected. One of the aims is to maintain the most flat homogeneous thickness profile along the width of the strip which is clearly not respected in the case of WRB equal to 900 kN. The reason for the thickness profile defect is the higher WR bending resulting in a more convex profile of the roll load (Figure 3.2(a)) and a bigger gap between the rolls near the edges (Figure 3.2(b)); hence a non-homogeneous thickness profile.

As for the stress distribution downstream of the roll bite, Figure 3.2(e) shows that changing the work roll bending can transform drastically the on-line and off-line residual stress distribution in the strip. The profiles must be compared with the average tension 100 MPa: wherever the stress is smaller, there is a suspicion of compression after tension release, therefore of waviness. For the central value WRB= 480 kN, the stress profile is slightly concave in the center, where $\sigma_{xx} < 100$ MPa. The strip might remain flat on the mill, but a wavy center is not excluded after tension release - wavy edges may also occur simultaneously as the stress there is close to zero. For the smallest bending value, WRB= 350 kN, the stress is slightly above 100 MPa in the center, rather constant, and drops only in the last 100 mm. This means the strip will probably remain flat except on the edge where waviness of limited dimension might occur.
Finally, the highest bending WRB= 900 kN leads to a dramatic change in the stress profile: $\sigma_{xx} << 100$ MPa in the center, whereas the edges presents compressive stresses. After tension release, this will result in a strong wavy center covering a great part of the strip width. In this case, one can deduce that this WRB force 900 kN, is badly adapted to the chosen friction coefficient $\mu = 0.025$.

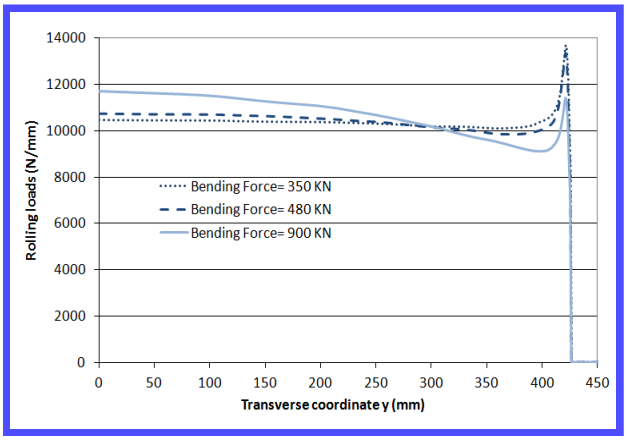

(a)

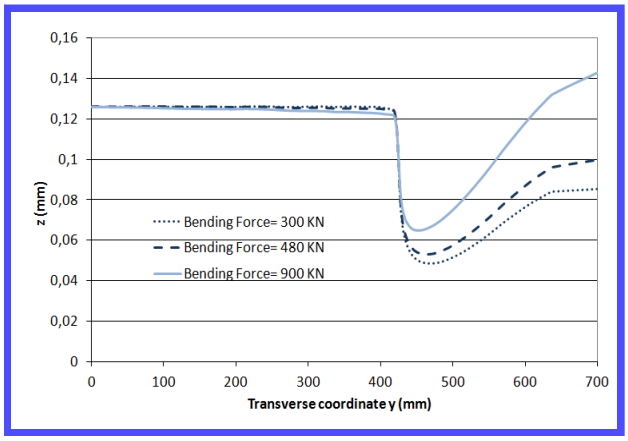

(b)

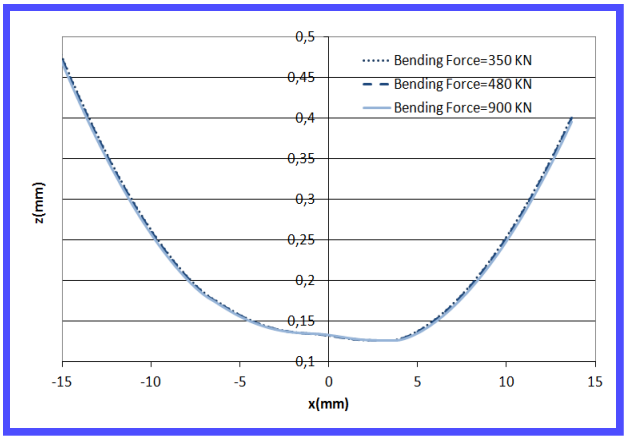

(c)

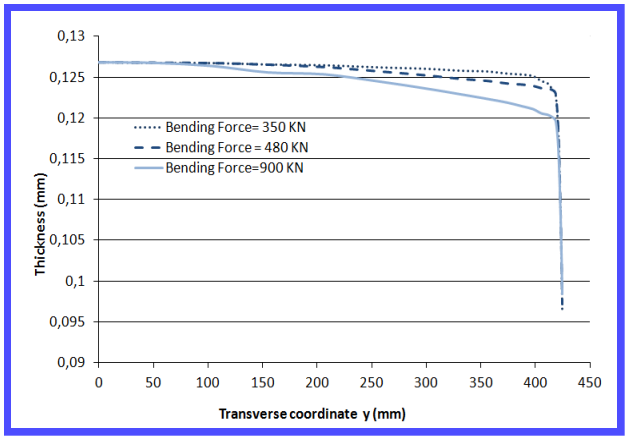

(d)

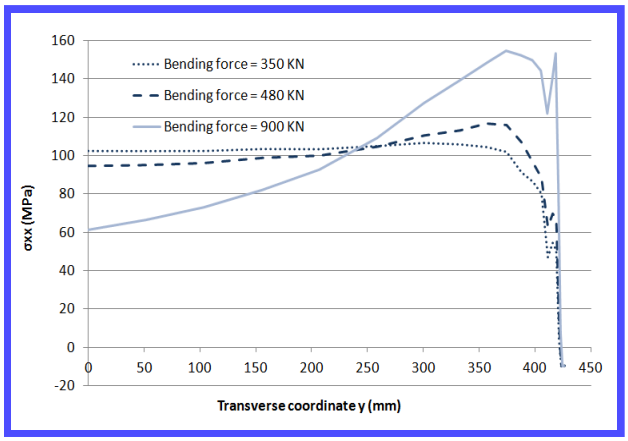

(e)

Figure 3.3: The impact of varying bending force on (a): Roll load transverse distribution. (b): Roll active generator shape $z(y)$, (c): Roll flattening, (d): Strip thickness profile and (e): Post-buckling stress distribution under strip tension

3.3 Best-adapted WR bending force for a given friction level

The previous analysis shows i) that friction affects the strip thickness profile, the stress distribution, and will therefore impact the defect type and amplitude. ii) One of the flatness actuators which can be used to improve flatness is the Work Roll Bending (WRB) force. Its effect, at constant μ, is illustrated in Figure 3.4(a). Increasing it to large values clearly exaggerates counter-bending, with too large reduction in the center resulting in a concave profile, leading to a wavy center.

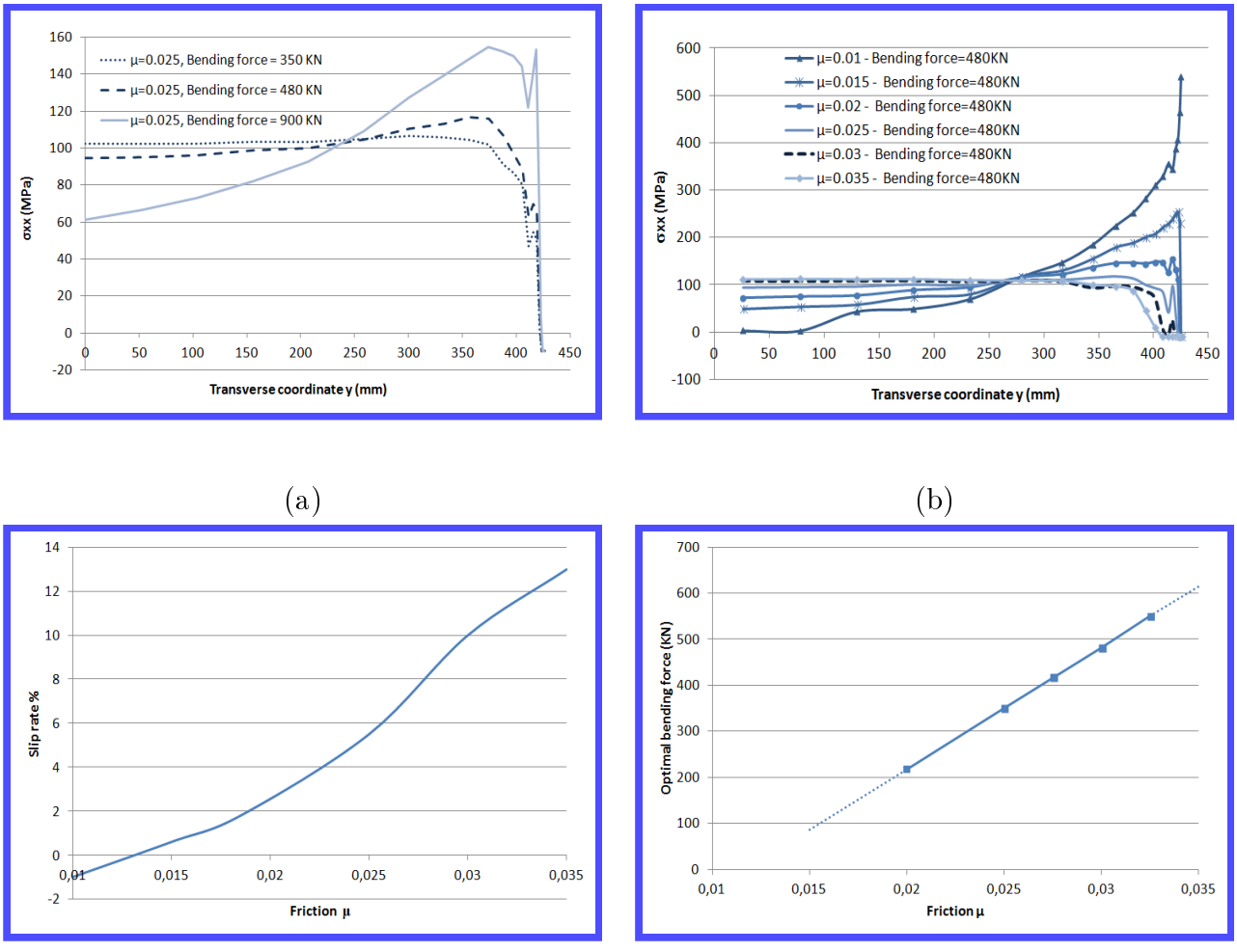

(a) (b)

(c) (d)

Figure 3.4: (a): The $\sigma_{xx}(y)$ stress profile for varying bending force and fixed friction coefficient ($\mu = 0.025$).
(b): The stress profile for varying friction and fixed bending force (480 KN).
(c): Evolution of the forward slip rate as friction changes
(d): The relationship between friction and optimal bending force.

Since the effect of WRB can neutralize the effects of varying friction on flatness, a good idea is to establish a relation between friction and the corresponding WRB giving the best flat strip profile.
Thanks to a set of numerical experiments, the relation between friction, bending force and stress profile $\sigma_{xx}(y)$ has been established for the rolling operation investigated. For each value of the friction coefficient, the "optimal bending force" is defined here as the one giving the most flat stress profile (as judged by eye). For instance, from Figure 3.4(a), it can be concluded that 350 kN is the optimal bending force for $\mu = 0.025$. Inversely, in Figure 3.4(b), $F = 480$ kN gives a flat profile with $\mu = 0.03$, so that the optimal bending force for$\mu = 0.03$ is 480 kN. The results obtained for the whole range of parameters are given in Figure 3.4(d). It shows how the bending force could be preset as a function of friction when the latter varies, e.g. during mill acceleration or deceleration.
The relationship has been established for $\mu = 0.02$ to 0.035. $\mu < 0.02$ is not desirable, due to a risk of skidding shown by the negative forward slip below $\mu = 0.015$ in Figure 3.4(c). "High" friction, $\mu > 0.03$, leads to "Roll Kiss"

3.4 Tension and Flatness

Another possible actuator is the strip tension itself. It is examined in the following if, for a given rolling operation, it can be used to control -and minimize- the stress variations $\sigma_{xx}(y)$. Average tension stresses of 50 and 150 MPa have been tested.
Curves of Figures 3.5(c) and 3.5(d) present respectively the stress profile (average tension T has been subtracted) and the strip thickness profile in a cross section ≈ 1 m after roll bite exit. Decreasing the tension (50 MPa) does not change the stress profile too much, but increasing it above 100 MPa clearly affects the stress distribution (Figure 3.5(c)). As tension increases, the stress on the edge is kept at the buckling threshold (-10 MPa), but in relative terms, it is more compressive after tension subtraction. Increasing the tension to 150 MPa increases $\sigma_{xx}(y)$ everywhere, but the profile is almost three times more concave, suggesting a wavy center upon cancellation of the tension force. Figures 3.5(d,e) show that as the tension decreases, the thickness of the strip on the edges decreases (the edge-drop defect is larger). This is because lower tension results in increased roll load, giving more roll flattening 3.5(b), also shown by the large peak at the edge of the roll load profile (Figure 3.5(a)). The total rolling force increases linearly from 8380 to 9180 and to 10100 kN as tension decreases from 150 to 100 and to 50 MPa.

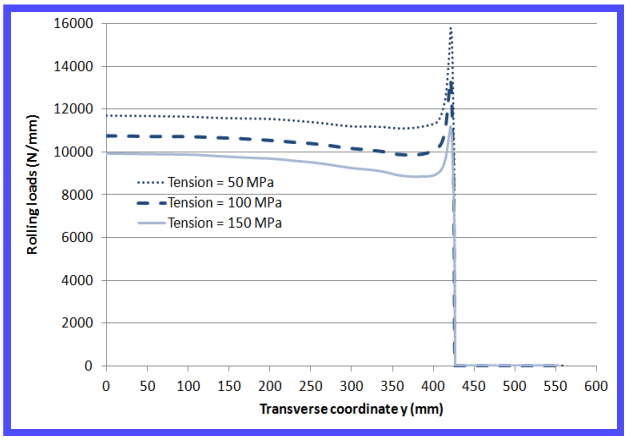

(a)

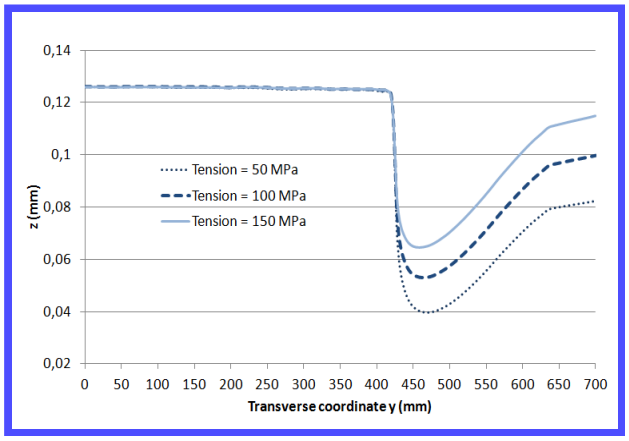

(b)

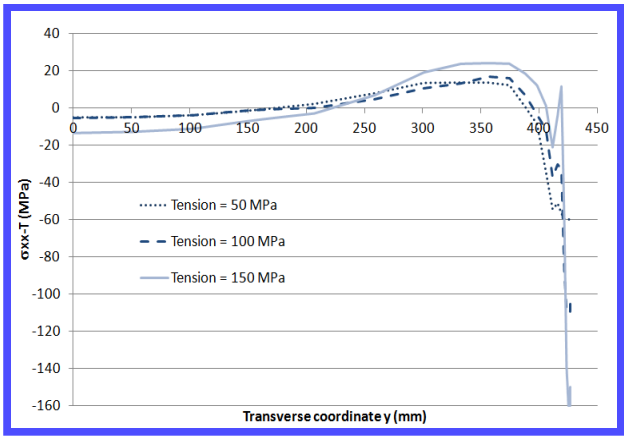

(c)

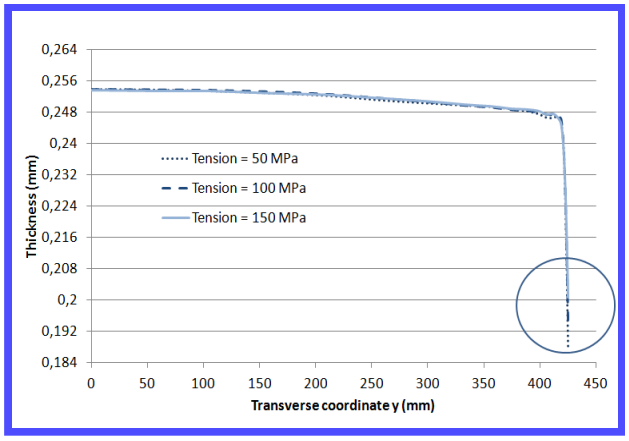

(d)

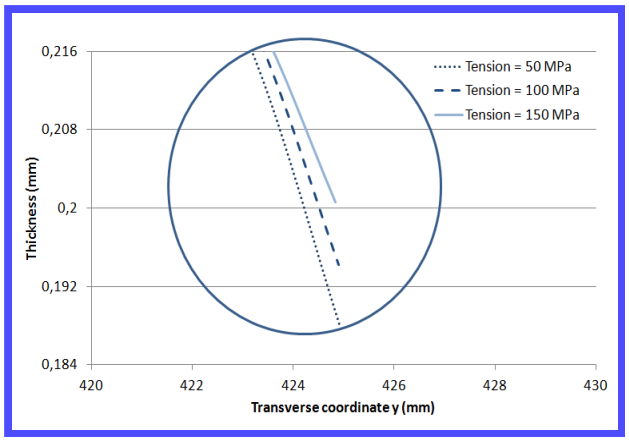

(e)

Figure 3.5: The effect of increasing strip tension on (a): Roll load transverse distribution, (b): Roll active generator shape $z(y)$, (c): stress profile ($\mu = 0.025$, WRB force = 480 kN, strip tension stress T has been subtracted for easier comparison, (d): Strip thickness (e): -Zoom of the strip thickness near the edge-

3.5 Temperature and Flatness

In this section, the friction, the tension and the bending force are fixed and take the values described in Table 3.1. Only the temperature effects on flatness defects are studied. This will help deduce if taking into account the thermal contribution is crucial or not.

At bite exit, temperature is much larger at the edge than in the center (Figures 3.6(a) and 3.6(b)), about 165^{o}C versus 110^{o}C. This is due to larger reduction and plastic heating on the edges (3.2(d)). Due to the corresponding differential dilatation, the stress pattern could be affected. A series of simulations has therefore been run. The first is an isothermal case and it is taken as a reference. In the second case, the strip is allowed to cool after bite exit under the effect of the strip cooling system, with $H_{cool} = 5\ kW.m^{-2}.K^{-1}$ for heat transfer coefficient (HTC); strip - roll contact is kept adiabatic ($H_{roll} = 0$). Temperature increases in the roll bite and slowly decays afterwards.

In the third case, the roll - strip interface is represented by $H_{roll} = 100\ kW.m^{-2}.K^{-1}$. The temperature increase is less in the bite, cooling is similar to the previous case. Finally, in the fourth case, $H_{cool} = 5\ kW.m^{-2}.K^{-1}$, $H_{roll} = 100\ kW.m^{-2}.K^{-1}$, but rolls are moreover cooled efficiently by water sprays, so that strip temperatures are significantly lower.

However, the temperature difference between strip edge and center is very similar in all three cases, 40 to 50^{o}C. Figure 3.6(e) shows that these temperature differences, even in the isothermal case ($T = 25^o$C everywhere), have negligible impact on the stress pattern once relaxed by edge buckling.

In this operation, the edge is significantly thinner than the center (in the case studied, central thickness is kept fixed at 0.252 mm by a supposedly perfect gauge control system, but it may drop to 0.18 mm on the edge). This means less rigidity against buckling of long edges as is the case here. In spite of its vulnerability to buckling, the temperature effect on the stress profile e.g. the flatness defect is very small to non-existent.

It can be concluded that in cold rolling, or rather for this operation in particular, the thermal effects are negligible and can be dropped.

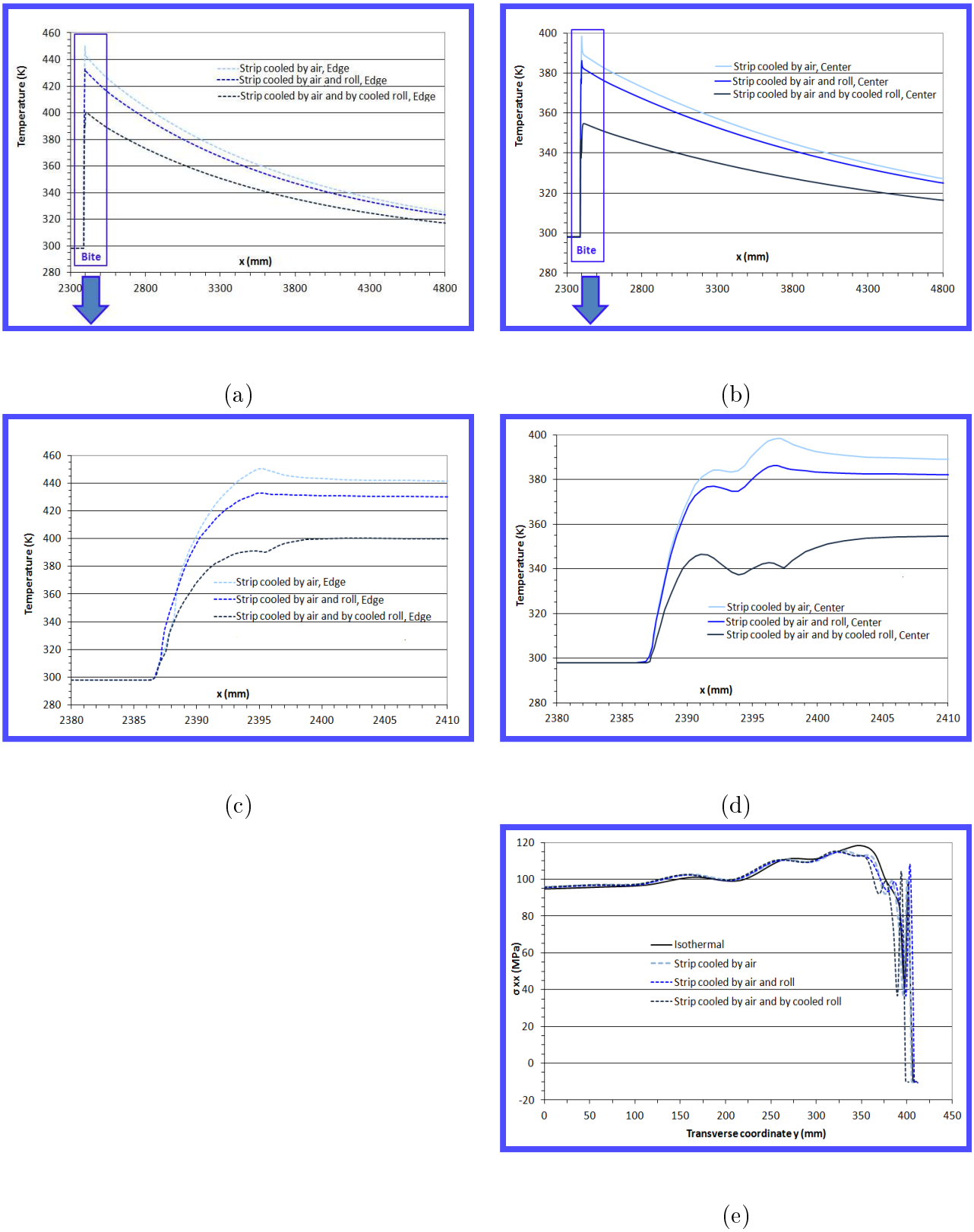

Figure 3.6: Effect of all thermal boundary conditions on (a): edge longitudinal temperature profiles in the rolled strip post-bite, (b): central longitudinal temperature profiles in the rolled strip post-bite, (c): edge longitudinal temperature profiles in the bite, (d): central longitudinal temperature profiles in the bite and (e): the longitudinal stress transverse profile $\sigma_{xx}(y)$

3.6 Conclusion

The problem of flatness defects has been addressed using a completely coupled model combining the FEM for strip elastic-viscoplastic deformation "Lam3", a powerful semi analytical model of roll elastic deformation "Tec3", and a simple model of buckling based on elastic / buckling deformation decomposition described in section 2.3.2.2.

A study of the effect of friction concludes that, in the thin sheet (tinplate) case, friction is an essential parameter for flatness. An adaptive set up of the bending force is shown to be able to compensate for unavoidable friction variations: to each coefficient of friction corresponds a bending force ensuring the best possible flatness. For the time being, the expected optimal flatness is judged only by the homogeneity of the stress profile, but this criterion could be refined in the future.
Front tension has been studied as well. The effect of an increased tension is positive on the roll load and roll deformation, but raises a flatness issue. Probably, this could be again partly compensated by changing simultaneously the WRB force. Playing with two actuators together however raises the question of the local / global character of their effects, a question which will be examined in Chapter 5 section 5.3.
It has been shown also that the temperature increase in cold rolling is not large enough to introduce thermal residual stress. Thus it does not affect the on-line/off-line strip flatness and therefore its effect can be neglected later on.

Now that we have a good vision of Abdelkhalek's model capacities, in the following chapters we turn to the model developed in the present work: the Multi-Scale Buckling Model (**MSBM**).

3.7 Résumé en Français

Dans ce chapitre de transition le problème des défauts de planéité a été abordé avec un modèle complétement couplé combinant le modèle éléments finis de déformation élastique-viscoplastique de tôle "Lam3", un puissant modèle semi analytique de déformation élastique de cage "Tec3" et un modèle simple de flambage (décrit dans la section 2.3.2.2).

D'abord, une étude de l'effet de frottement a conclu que, pour une tôle mince, le frottement est un paramètre essentiel affectant sa planéité. Mais nous montrons que nous pouvons compenser son effet en jouant sur la force d'équilibrage: à chaque coefficient de

frottement correspond une force d'équilibrage optimale assurant la meilleure planéité possible. Les effets du changement de traction ont été étudiés aussi. Une traction croissante diminue la déformation des cylindres de travail, mais augmente les risques d'apparition de défauts de planéité après relâchement. Probablement, ceci pourrait être de nouveau en partie compensé en changeant simultanément la force d'équilibrage. Enfin, les effets de température sur les contraintes résiduelles ont été trouvés faibles. Ainsi, elle n'affecte pas la planéité de la tôle en/hors ligne, c'est pourquoi nous négligeons son incidence dans les chapitres suivants.

Maintenant que nous avons une bonne vision des capacités du modèle d'Abdelkhalek, dans les chapitres suivants nous passons au modèle développé dans le présent travail: le modèle de flambage multi-échelle (**MSBM**).

CHAPTER 4

FROM VON KÁRMÁN EQUATIONS TO MULTI-SCALE BASED BUCKLING MODEL

If you only walk on sunny days you'll never reach your destination.

by Paulo Coelho

Contents

In 1910, T. von Kármán [von Kármán, 1910] introduced a pair of fourth order elliptic partial differential equations. This system describes out of plane large deflections and stresses produced in a thin elastic plate subjected to in-plane compressive forces. Following his work, attempts for more complete studies of these equations -without additional assumptions on the shape, symmetry and boundary conditions of the buckled plate- were proved to be nearly impossible due to the nonlinear nature of these equations. Despite all these difficulties, it is assumed that the von Kármán equations give a valid description of buckling plates problems. Thus, these equations are rewritten for thin elastic strip buckling under residual stress and the different steps will be presented in section 4.1. From the mathematical point of view, the buckling of a thin strip is expressed by the multiplicity of solutions associated to the von Kármán system. Many works have addressed this problem to obtain a qualitative uniqueness solution theory for this problem. Thus, a quick mathematical description of the problem is explored in section 4.3.
Since the von Kármán equations are well known to be derivable from a variational principle i.e the **Constant Internal Energy** principle, the energetic formulation of this problem will be detailed and adapted to the needs of buckling during cold flat rolling processes in section 4.4.
Once the appropriate equations are established, they will be combined in section 4.5 with the multi-scale method presented in [Damil & Potier-Ferry, 1986, Damil & Potier-Ferry, 2006] to offer a simple yet performant buckling and post-buckling model. The resulting model will be called the **Multi-Scale Buckling Model** (**MSBM**) from now on for simplicity reasons. Finally, the numerical results are presented then validated with different available studies in section 4.7.
The readers are invited to consult the works of von Kármán [von Kármán, 1910], Timoshenko [Timoshenko & Gere, 1961], Berger [Berger, 1967, Berger & Fife, 1996], Lewicka [Lewicka et al. , 2011] and Ventsel [Ventsel & Krauthammer, 2001] for interesting descriptions from both 'mathematical' and 'physical' points of view.

4.1 Von Kármán Equations

A thin flat elastic plate subjected to compressive forces along its edges, remains flat when these forces are small. It deflects when they exceed a certain critical value. The buckling of the plate under compressive stress is described by the set of equations (4.1) called the von Kármán equations:

$$\begin{aligned} \frac{1}{E}\Delta^2\Phi(x,y) &= \frac{1}{E}g(x,y) - \frac{1}{2}[w,w] \\ \mathbb{D}.\Delta^2 w(x,y) &= [w,\Phi] \end{aligned} \tag{4.1}$$

in which $w(x,y)$ is the out-of-plane displacement, $\Phi(x,y)$ is the Airy stress function (i.e. the stress components are computed in terms of the second derivatives of Φ), $g(x,y)$ is a stress function that could be present initially in the plate and can cause its deflection if sufficiently large, E denotes Young's modulus and $\mathbb{D} = \dfrac{Eh^3}{12(1-\nu^2)}$ the plate rigidity.
Note that Δ^2 and $[.,.]$ are respectively the biharmonic and the bracket operators defined as follows

$$\begin{aligned} \Delta^2 = & \quad \frac{\partial^4}{\partial^4 x} + 2\frac{\partial^4}{\partial^2 x \partial^2 y} + \frac{\partial^4}{\partial^4 y} \\ [u,w] = & \quad \frac{\partial^2 u}{\partial x^2}\frac{\partial^2 w}{\partial y^2} + \frac{\partial^2 u}{\partial y^2}\frac{\partial^2 w}{\partial x^2} - 2\frac{\partial^2 u}{\partial x \partial y}\frac{\partial^2 w}{\partial x \partial y} \quad \text{for any } u \text{ and } w \end{aligned} \tag{4.2}$$

Since buckling occurs when g is sufficiently large, it can be written as a linear function depending on a loading parameter λ. From now on, g can be replaced by λg. When this parameter is small enough and does not surpass a critical value denoted λ_{cr}, buckling does not manifest. Thus the displacement $w = 0$ and g verify the equation 4.3.

$$\Delta^2 f(x,y) = g(x,y) \tag{4.3}$$

where f is the Airy stress function corresponding to the force g when the plate is not loaded enough to buckle.
If $F = \Phi - \lambda f$ is the stress function produced once the plate begins buckling i.e. λ exceeds λ_{cr}, or what is called usually the buckling additional stress function, then the von Kármán system 4.1 is replaced by the new system 4.4:

$$\begin{aligned} \frac{1}{Eh}\Delta^2 F(x,y) &= -\frac{1}{2}[w,w] \\ \mathbb{D}.\Delta^2 w(x,y) - \lambda[f,w] &= [w,F] \end{aligned} \tag{4.4}$$

4.2 Von Kármán Equations for buckling plate under residual stress

To obtain the governing differential equations for deflection of a thin rectangular plate, the equilibrium of the plate, the compatibility and the constitutive relations will be put into use. Introducing the residual stresses as initial loading, we will retrieve the von Kármán Equations for buckling plates under residual stress. As mentioned earlier, the von Kármán system is a set of two partial differential equations (4.4), so we will proceed in two steps to write each one of them.

The First Equation:

Consider a thin plate of thickness h illustrated in Figure 4.1 subjected to a normal

load $p(x,y)$ and to in-plane forces (in this case residual ones) $N_x^{res}(x,y)$, $N_y^{res}(x,y)$ and $N_{xy}^{res}(x,y)$ i.e. $g = (N_x^{res}, N_y^{res}, N_{xy}^{res})^t$. Let us denote once and for all, $N = \sigma.h$ where σ is a stress tensor.
if $\varepsilon^{ms} = \begin{pmatrix} \varepsilon_x^{ms} & \varepsilon_{xy}^{ms} \\ \varepsilon_{xy}^{ms} & \varepsilon_y^{ms} \end{pmatrix}$ is the strain deformation tensor in the plate mid-surface, its components are computed as follows:

$$\begin{aligned} \varepsilon_x^{ms} &= \frac{\partial u}{\partial x} + \frac{1}{2}\left(\frac{\partial w}{\partial x}\right)^2 \\ \varepsilon_y^{ms} &= \frac{\partial v}{\partial y} + \frac{1}{2}\left(\frac{\partial w}{\partial y}\right)^2 \\ \varepsilon_{xy}^{ms} &= \frac{1}{2}\left(\frac{\partial u}{\partial y} + \frac{\partial v}{\partial x} + \frac{\partial w}{\partial x}\frac{\partial w}{\partial y}\right) \end{aligned} \tag{4.5}$$

where u, v and w represent respectively the mid-surface displacement components in the directions of Cartesian coordinates x, y and z.

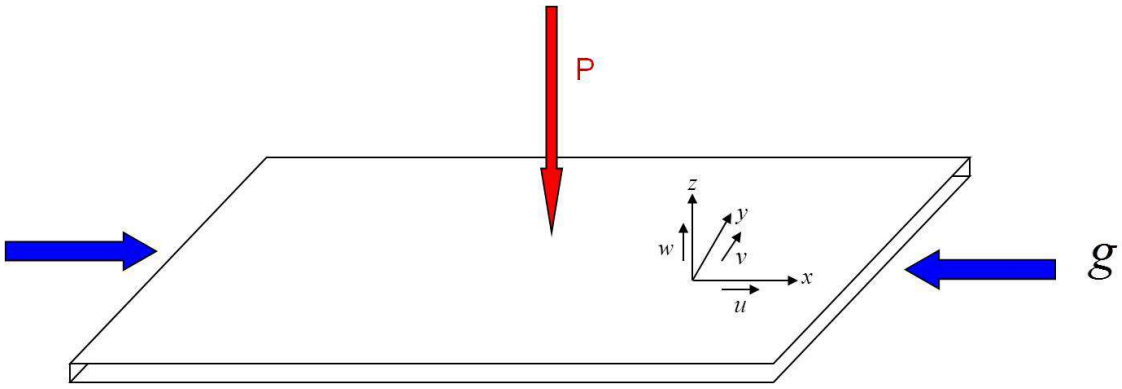

Figure 4.1: A thin plate subjected to a normal load and in-plane forces.

Eliminating the tangential components of the displacement u and v by the relevant differentiation combination, the compatibility equation of the middle surface is retrieved:

$$\frac{\partial^2 \varepsilon_x^{ms}}{\partial y^2} + \frac{\partial^2 \varepsilon_y^{ms}}{\partial x^2} - 2\frac{\partial^2 \varepsilon_{xy}^{ms}}{\partial y \partial y} = \left(\frac{\partial^2 w}{\partial x \partial y}\right)^2 - \frac{\partial^2 w}{\partial x^2}\frac{\partial^2 w}{\partial y^2} \tag{4.6}$$

Hooke's law allows writing the following relation (small perturbation amplitude):

$$N = \bar{\lambda}.tr(\varepsilon^{ms})\mathbb{I} + 2\mu\varepsilon^{ms} \tag{4.7}$$

in which $\mathbb{I}$ is the identity tensor, $\bar{\lambda}$ and ν are Lame coefficients. Now we can take into

account the residual stresses (i.e forces) by introducing N^{res}

$$N - N^{res} = h.(\bar{\lambda}.tr(\varepsilon^{ms})\mathbb{I} + 2\mu\varepsilon^{ms}) \tag{4.8}$$

Inversing equation (4.8), we can write:

$$\varepsilon^{ms} = \frac{1}{Eh}[(1+\nu)(N - N^{res}) - \nu tr(N - N^{res})\mathbb{I}] \tag{4.9}$$

Introducing the loading parameter λ, the component of ε^{ms} and its derivatives can be expressed easily as:

$$\begin{aligned}
\varepsilon_x^{ms} &= \frac{1}{Eh}\left[N_x - \nu N_y - \lambda(N_x^{res} - \nu N_y^{res})\right] \\
\varepsilon_y^{ms} &= \frac{1}{Eh}\left[N_y - \nu N_x - \lambda(N_y^{res} - \nu N_x^{res})\right] \\
\varepsilon_{xy}^{ms} &= \frac{1}{Eh}\left[(1+\nu)N_{xy} - \lambda(1+\nu)N_{xy}^{res}\right] \\
\frac{\partial\varepsilon_x^{ms}}{\partial y} &= \frac{1}{Eh}\left[\frac{\partial N_x}{\partial y} - \nu\frac{\partial N_y}{\partial y} - \lambda(\frac{\partial N_x^{res}}{\partial y} - \nu\frac{\partial N_y^{res}}{\partial y})\right] \\
&\vdots
\end{aligned} \tag{4.10}$$

Note that this supposes that the thickness of the strip is constant (homogeneous). Finally, replacing the partial derivatives of ε^{ms} in the compatibility equation (4.6), we get the following equation:

$$\begin{aligned}
\frac{1}{Eh} &\left[\frac{\partial^2 N_x}{\partial y^2} - \nu\frac{\partial^2 N_y}{\partial y^2} - \lambda\frac{\partial^2 N_x^{res}}{\partial y^2} + \lambda\nu\frac{\partial^2 N_y^{res}}{\partial y^2} + \frac{\partial^2 N_y}{\partial x^2} - \nu\frac{\partial^2 N_x}{\partial x^2}\right. \\
- &\left.\lambda\frac{\partial^2 N_y^{res}}{\partial x^2} + \lambda\nu\frac{\partial^2 N_x^{res}}{\partial x^2} - 2(1+\nu)\frac{\partial^2 N_{xy}}{\partial x\partial y} + 2\lambda(1+\nu)\frac{\partial^2 N_{xy}^{res}}{\partial x\partial y}\right] \\
= &\left(\frac{\partial^2 w}{\partial x\partial y}\right)^2 - \frac{\partial^2 w}{\partial x^2}\frac{\partial^2 w}{\partial y^2}
\end{aligned} \tag{4.11}$$

Since N represents the resultant force in the plate, it can be expressed as a combination of the residual force present initially in the plate λN^{res} and $\bar{N}$ the one created by the plate buckling once λ is greater than the critical value λ_{cr}.
So if ϕ is the Airy stress function associated to N then, $\phi = F + \lambda f$ where f is the stress function associated to N^{res} and F is the one associated to the redistribution of the stress after buckling.
Φ is the Airy function associated to N i.e. $\Phi = \phi.h$ and $N_x = \dfrac{\partial^2\Phi}{\partial y^2}$, $\quad N_y = \dfrac{\partial^2\Phi}{\partial x^2}$, $N_{xy} = -\dfrac{\partial^2\Phi}{\partial x\partial y}$.

Replacing the above information in equation (4.11)

$$\begin{array}{ll} \frac{1}{Eh} & \left[\frac{\partial^4\Phi}{\partial y^4}+\frac{\partial^4\Phi}{\partial x^4}+2\frac{\partial^4\Phi}{\partial x^2\partial y^2}\right]=-\frac{1}{2}[w,w] \\ +\frac{\lambda}{Eh} & \left[\frac{\partial^2 N_x^{res}}{\partial y^2}-\nu\frac{\partial^2 N_y^{res}}{\partial y^2}+\frac{\partial^2 N_y^{res}}{\partial x^2}-\nu\frac{\partial^2 N_x^{res}}{\partial x^2}+-2(1+\nu)\frac{\partial^2 N_{xy}^{res}}{\partial x\partial y}\right] \end{array} \tag{4.12}$$

To find the same form as the system (4.4), let us write the residual force components using the stress function f: $N_x^{res}=\frac{\partial^2 f}{\partial y^2}$ $N_y^{res}=\frac{\partial^2 f}{\partial x^2}$ $N_{xy}^{res}=-\frac{\partial^2 f}{\partial x\partial y}$ and replace it in equation (4.13),

$$\Delta^2\Phi=-\frac{Eh}{2}[w,w]+\lambda\Delta^2 f \tag{4.13}$$

And since $\Phi=F+\lambda f$, we find:

$$\boxed{\Delta^2 F=-\frac{Eh}{2}[w,w]} \tag{4.14}$$

The Second Equation:

To establish the second equation, let us consider an infinitesimal mid-plane element of sides dx and dy (illustrated in Figure 4.2). Let us examine the contribution of the normal loading, the in-plane forces and their moments in the plate equilibrium equation ; more specifically on the chosen reference element.

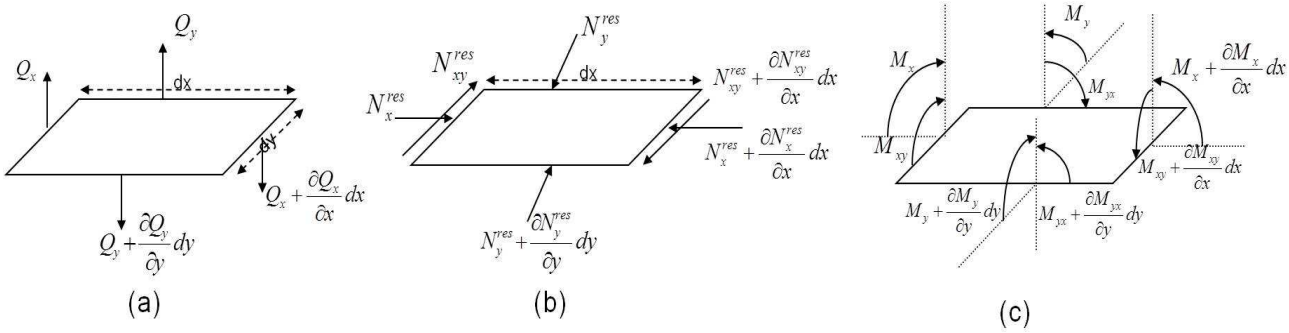

Figure 4.2: The contribution of the in-plane forces, normal loading and their moments on the equilibrium of a reference element.

Before writing the equilibrium equations and since the main interest is to compute the strip deflection, one must understand that the effect of the in-plane stresses on the plate bending should not be neglected. w is large enough that its derivatives and their products are of the same order as the shear forces denoted Q_x et Q_y.
Initially, the forces acting on the reference element are the in-plane forces N_x^{res}, N_y^{res} and N_{xy}^{res} and the normal load $P(x,y)$. Note that P can represent the body forces. Let us

adopt the same notations as earlier: $N = \lambda N^{res} + \bar{N}$ where $\bar{N}$ is the additional stress introduced by the buckling occurrence.
From Figure 4.2(a), the equilibrium of the forces in the x-direction can be written as

$$\sum F_x = 0 \tag{4.15}$$

$$(N_x + \frac{\partial N_x}{\partial x}dx)dxdy.cos\beta' - N_x dy.cos\beta + (N_{xy} + \frac{\partial N_{xy}}{\partial x}dx)dy.cos\beta' - N_{xy}dy.cos\beta = 0 \tag{4.16}$$

where $\beta = \widehat{(N_x; \vec{x})}$ and $\beta' = \widehat{(N_x + \frac{\partial N_x}{\partial x}dx; \vec{x})}$. Since we are in a context of small deflections, $cos\beta,\ cos\beta' \simeq 1$. Hence,

$$\frac{\partial N_x}{\partial x} + \frac{\partial N_{xy}}{\partial y} = 0 \tag{4.17}$$

In the same manner, the equilibrium equation in the y-direction is established:

$$\frac{\partial N_{xy}}{\partial x} + \frac{\partial N_y}{\partial y} = 0 \tag{4.18}$$

Now, to write the equilibrium equation in the $z-$direction, the forces acting should be projected on the $z-$axis. To simplify the projection, let us write the contribution of each force separately.
The projection of N_x on the $z-$axis gives

$$-N_x dy.sin\beta + (N_x + \frac{\partial N_x}{\partial x}dx)dy.sin\beta' \tag{4.19}$$

and since we are in the context of small deflections, $sin\beta \simeq \beta = \frac{\partial w}{\partial x}$ and $sin\beta' \simeq \beta' = \beta + d\beta \simeq \beta + \frac{\partial \beta}{\partial x}dx = \frac{\partial w}{\partial x} + \frac{\partial^2 w}{\partial x^2}dx$.
Replacing this new information in (4.19), the contribution of N_x is equal to $N_x\frac{\partial^2 w}{\partial x^2}dxdy + \frac{\partial N_x}{\partial x}\frac{\partial w}{\partial x}dxdy$.

The same steps are followed to determine, N_{xy} and N_{yx} contributions to the equilibrium equation in the $z-$ direction: $N_{xy}\frac{\partial^2 w}{\partial x \partial y}dxdy + \frac{\partial N_{xy}}{\partial x}\frac{\partial w}{\partial y}dxdy$.
Finally, the equilibrium equation

$$\sum F_z = 0 \tag{4.20}$$

is equivalent to

$$\frac{\partial Q_x}{\partial x}+\frac{\partial Q_y}{\partial y}+P+N_x\frac{\partial^2 w}{\partial x^2}+N_y\frac{\partial^2 w}{\partial y^2}+2N_{xy}\frac{\partial^2 w}{\partial x\partial y}+\left(\frac{\partial N_x}{\partial x}+\frac{\partial N_{yx}}{\partial y}\right)\frac{\partial w}{\partial x}+\left(\frac{\partial N_{xy}}{\partial x}+\frac{\partial N_y}{\partial y}\right)\frac{\partial w}{\partial y}=0 \tag{4.21}$$

Since the in-plane forces do not introduce moments on the element boundaries, the sum of the moments in the x and y directions are respectively:

$$\frac{\partial M_{xy}}{\partial x}+\frac{\partial M_y}{\partial y}-Q_y=0\Leftrightarrow Q_y=\frac{\partial M_{xy}}{\partial x}+\frac{\partial M_y}{\partial y} \tag{4.22}$$

Thus, the shear forces Q_x and Q_y are expressed in terms of the moments as:

$$\frac{\partial M_{xy}}{\partial y}+\frac{\partial M_x}{\partial x}-Q_x=0\Leftrightarrow Q_x=\frac{\partial M_{xy}}{\partial y}+\frac{\partial M_x}{\partial x} \tag{4.23}$$

Note that,

$$\begin{aligned} M_x &= -\mathbb{D}\left(\frac{\partial^2 w}{\partial x^2}+\nu\frac{\partial^2 w}{\partial y^2}\right)\\ M_y &= -\mathbb{D}\left(\nu\frac{\partial^2 w}{\partial x^2}+\frac{\partial^2 w}{\partial y^2}\right)\\ M_{xy} &= -\mathbb{D}(1-\nu)\frac{\partial^2 w}{\partial x\partial y} \end{aligned} \tag{4.24}$$

Replacing equations (4.17), (4.18), (4.22), (4.23) et (4.24) in equation (4.21), the following relation is established:

$$\frac{\partial^4 w}{\partial x^4}+2\frac{\partial^4 w}{\partial x^2\partial y^2}+\frac{\partial^4 w}{\partial y^4}=\frac{1}{\mathbb{D}}\left(P+N_x\frac{\partial^2 w}{\partial x^2}+N_y\frac{\partial^2 w}{\partial y^2}+2N_{xy}\frac{\partial^2 w}{\partial x\partial y}\right) \tag{4.25}$$

To retrieve the same form as the one presented in (4.4), Let us consider Φ the Airy function associated to N:

$$\frac{\partial^4 w}{\partial x^4}+2\frac{\partial^4 w}{\partial x^2\partial y^2}+\frac{\partial^4 w}{\partial y^4}=\frac{1}{\mathbb{D}}\left(P+\frac{\partial^2\Phi}{\partial y^2}\frac{\partial^2 w}{\partial x^2}+\frac{\partial^2\Phi}{\partial x^2}\frac{\partial^2 w}{\partial y^2}-2\frac{\partial^2\Phi}{\partial x\partial y}\frac{\partial^2 w}{\partial x\partial y}\right) \tag{4.26}$$

We decide to neglect the body forces of a thin strip since we are mainly interested in the buckling phenomenon under in-plane compressive forces: $P=0$:

$$\boxed{\Delta^2 w=\frac{1}{\mathbb{D}}[\Phi,w]} \tag{4.27}$$

Combining (4.27) and (4.14), the von Kármán system describing the buckling of a plate

under residual stress is finalized.

$$\begin{array}{rcl} \frac{1}{Eh}\Delta^2 F(x,y) & = & -\frac{1}{2}[w,w] \\ \mathbb{D}.\Delta^2 w(x,y) - \lambda[f,w] & = & [w,F] \end{array} \tag{4.28}$$

4.3 Existence and non-uniqueness solution of the von Kármán equations

As mentioned earlier, the most interesting phenomenon associated to the von Kármán equations is the buckling of the plate described as the appearance of wrinkling when the loading reaches a critical value. From the mathematical point of view, this phenomenon is expressed by the existence of multiple solutions of the boundary value problem (the variational formulation). Many mathematical studies where devoted to proving the existence and the non-uniqueness of solutions associated to this problem. We mention in particular the work of Berger and Fife [Berger, 1967, Berger & Fife, 1996] where they dealt not only with buckling of clamped plate but also with mixed boundary conditions for w and F. Knightly in [Knightly, 1967, Knightly & Sather, 1970] has presented, for a plate under direct and normal forces, an existence theorem and detailed bifurcation solutions results of the von Kármán equations under Dirichlet conditions for both w and F. Another outstanding work presented by [Naumann, 1974] uses a novel approach to prove the existence theorem for the system under Free Boundary Conditions.
Our main interest is finding a solution of the von Kármán system (4.28) for a buckling plate under residual stresses with free edges. It is equivalent to finding a solution for the following variational problem:

$$\begin{array}{l} \text{Find the couple } (w,F) \in H^2(\Omega)\times H^2(\Omega) \text{ such as:} \\ \forall \tilde{w} \in H^2(\Omega),\ \frac{1}{Eh}\int_\Omega \Delta^2 F\tilde{w}d\Omega = -\frac{1}{2}\int_\Omega [w,w]\tilde{w}d\Omega \qquad (a) \\ \forall \tilde{u} \in H^2(\Omega),\ \mathbb{D}.\int_\Omega \Delta^2 w(x,y)\tilde{u}d\Omega = \lambda\int_\Omega [f,w]\tilde{u}d\Omega + \int_\Omega [w,F]\tilde{u}d\Omega \qquad (b) \\ \frac{\partial^2 w}{\partial y^2} + \nu\frac{\partial^2 w}{\partial x^2} = 0 \quad \text{on } \partial\Omega \\ \frac{\partial^3 w}{\partial y^3} + (2-\nu)\frac{\partial^3 w}{\partial x^2 \partial y} = 0 \quad \text{on } \partial\Omega \\ \frac{\partial F}{\partial x} = \frac{\partial F}{\partial y} = \frac{\partial f}{\partial x} = \frac{\partial f}{\partial y} = 0 \quad \text{on } \partial\Omega \end{array} \tag{4.29}$$

where Ω notes the plate domain and $H^2(\Omega)$ is the Sobolev space defined as the set of all functions $u \in L^2(\Omega)$ such that for every multi-index α with $|\alpha| \leq 2$, the weak partial derivative $D^\alpha u$ belongs to $L^2(\Omega)$ as well.

Next, the existence and non-uniqueness (or bifurcation) theorems will only be quoted. For more details and proofs, the readers are invited to consult the articles mentioned above. For the linearized problem (4.29 (b)), ($F = 0$ since the buckling did not happen yet); Berger and Fife in [Berger, 1967, Berger & Fife, 1996] proved that a spectrum of eigenvalues λ_n exists such as:

$$0 < \lambda_1 \leq \lambda_2 \leq ... + \infty$$

where the smallest eigenvalue of this spectrum λ_1 is the first bifurcation point and called the critical value.
As for non-uniqueness theorem for the non-linear problem, they proved that:

1) For all values $\lambda \leq \lambda_1$ the system (4.29) has no nontrivial solutions i.e. the only solution is $w = F = 0$.

2) The only bifurcation points of the non-linear problem are the eigenvalues λ_n of the linearized problem. In addition, for higher eigenvalues the bifurcation happens only on the right of the specific bifurcation point.
This means that if a simple eigenvalue $\lambda_{i,i\neq 1}$ is a bifurcation point, for all $\varepsilon > 0$, and $\lambda \in [\lambda_i, \lambda_i + \varepsilon]$, at least one nontrivial solution w ($w \neq 0$) exists.

4.4 Physical-Energetic formulation of the problem

Before applying the multi-scale approach proposed in [Damil & Potier-Ferry, 2006, Damil et al., 2013, Potier-Ferry & Damil, 2010] and since equation (4.26) is derived from a variational problem, it is appropriate to present the energetic formulation of the von Kármán problem before proceeding. The stationarity energetic principle is equivalent to the weak formulation of the problem and will definitely become handy later on.
The strain energy stored in a thin plate due to deformation is defined as:

$$U = \frac{1}{2}\int\int\int (\sigma_x\varepsilon_x + \sigma_y\varepsilon_y + 2\sigma_{xy}\varepsilon_{xy})dxdydz \tag{4.30}$$

in which $\sigma^t = (\sigma_x, \sigma_y, \sigma_{xy})$ is the stress tensor. Note that the strain tensor ε defined at any point of the plate can be expressed in terms of the mid-surface strain tensor ε^{ms}:

$$\begin{aligned}
\varepsilon_x &= \varepsilon_x^{ms} + z\frac{\partial^2 w}{\partial x^2} \quad & \& \quad \varepsilon_x^{ms} &= \frac{\partial u}{\partial x} + \frac{1}{2}\left(\frac{\partial w}{\partial x}\right)^2 \\
\varepsilon_y &= \varepsilon_y^{ms} + z\frac{\partial^2 w}{\partial y^2} \quad & \& \quad \varepsilon_y^{ms} &= \frac{\partial v}{\partial y} + \frac{1}{2}\left(\frac{\partial w}{\partial y}\right)^2 \\
\varepsilon_{xy} &= \varepsilon_{xy}^{ms} + 2z\frac{\partial^2 w}{\partial x\partial y} \quad & \& \quad \varepsilon_{xy}^{ms} &= \frac{1}{2}\left(\frac{\partial u}{\partial y} + \frac{\partial v}{\partial x} + \frac{\partial w}{\partial x}\frac{\partial w}{\partial y}\right)
\end{aligned} \tag{4.31}$$

where $(u, v, w)^t$ is the mid-surface displacement vector. Replacing (4.31) in (4.30) and neglecting the tangential components of the displacements u and v, the strain energy can be expressed as the sum of the membrane strain energy U_m and the bending strain energy U_b:

$$\begin{aligned} U &= U_m + U_b \\ U_m &= \frac{1}{2}\int\int\int (\sigma_x \varepsilon_x^{ms} + \sigma_y \varepsilon_y^{ms} + 2\sigma_{xy}\varepsilon_{xy}^{ms}) dxdydz \\ U_b &= \frac{1}{2}\int\int\int \left(z.\sigma_x \frac{\partial^2 w}{\partial x^2} + z.\sigma_y \frac{\partial^2 w}{\partial y^2} + 2z.\sigma_{xy}\frac{\partial^2 w}{\partial x \partial y} \right) dxdydz \end{aligned} \tag{4.32}$$

Finally, integrating with respect to z, substituting the integrals $z.\sigma$ by there corresponding form and using Hooke' Law, the new relations are:

$$\begin{aligned} U_m &= \frac{1}{2}\int\int \varepsilon^{ms}\mathbf{C}\varepsilon^{ms} = \frac{Eh}{1-\nu^2}\int\int \left(\varepsilon_x^{ms^2} + \varepsilon_y^{ms^2} + 2(1-\nu)\varepsilon_{xy}^{ms^2} + 2\nu\varepsilon_x^{ms}\varepsilon_y^{ms} \right) dxdy \\ U_b &= \frac{D}{2}\int\int \left(\left(\frac{\partial^2 w}{\partial x^2} + \frac{\partial^2 w}{\partial y^2} \right)^2 - 2(1-\nu).\left(\frac{\partial^2 w}{\partial x^2}\frac{\partial^2 w}{\partial y^2} - \left(\frac{\partial^2 w}{\partial x \partial y} \right)^2 \right) \right) dxdy \end{aligned} \tag{4.33}$$

where $\mathbf{C}$ is the elasticity matrix and $\mathbb{D} = \dfrac{Eh^3}{12(1-\nu^2)}$ is the plate bending rigidity. Since the main objective of this study is to find a buckling model applied to flat rolling problems, we introduce the residual stresses σ^{res} and the strip tension T_0 applied in the rolling direction (x-axis). To maintain the same notations, $N^{res} = \sigma^{res}.h$ and $\bar{N}_0 = T_0.h$ where h denotes the plate thickness.

The potential energy introduced by the applied residual stresses N^{res} and the strip tension $\bar{N}_0$ is:

$$\Omega = \frac{1}{2}\int\int \left((N_x^{res} + \bar{N}_0) \left(\frac{\partial w}{\partial x} \right)^2 + N_y^{res} \left(\frac{\partial w}{\partial y} \right)^2 + 2N_{xy}^{res}\frac{\partial w}{\partial x}\frac{\partial w}{\partial y} \right) dxdy \tag{4.34}$$

For equilibrium, the total potential energy functional $V = U + \Omega$ must be stationary i.e. δV should be equal to zero. From this point forward, it is simple to prove that $\delta V = 0$ is equivalent to (4.26).

We can consider now that the stationary energy principle is equivalent to the weak formulation of the von Kármán problem and we can proceed applying the Multi-scale method directly on it.

4.5 From von Kármán equations to the Multi-scale problem

The multi-scale method presented in [Damil & Potier-Ferry, 2006, Damil et al., 2013,

Potier-Ferry & Damil, 2010] proposes a nonlinear membrane model describing buckling by a new bifurcation equation deduced by combining: i) the method of Fourier series with slowly variable coefficient (4.35) and ii) the von Kármán system for elastic isotropic plates (4.36):

$$U(x,y) = \sum_m U_m(x,y) e^{imqx} \tag{4.35}$$

where $U = (u, v, w, \varepsilon, N)^t$, q is the half-wavenumber and $U_m =< Ue^{-imqx} >$ are the new macroscopic unknown fields varying slowly over a single period.
Note that this form chosen in equation (4.35) means that undulations are expected to appear in the $x-$direction, i.e. the rolling direction.

$$\begin{aligned}
&\mathbb{D}\Delta^2 w - div(N\nabla w) = 0 && (a)\\
&N = \mathbf{C}.\varepsilon + N^{res} && (b)\\
&\varepsilon = \frac{1}{2}\left(\nabla\mathbf{u} + \nabla\mathbf{u}^t + \nabla w \otimes \nabla w\right) && (c)\\
&divN = 0 && (d)\\
&\mathbf{u} = (u, v)^t
\end{aligned} \tag{4.36}$$

where $\mathbf{u}$ is the in-plane displacement, w is the out of plane displacement, $\mathbf{C}$ the elasticity tensor, $\mathbb{D}$ the bending stiffness, N and ε are the stress and strain and N^{res} is the residual stress.

Combining the Fourier development with the microscopic system, it is transformed into m macroscopic systems with the Fourier coefficients U_m as new unknowns.

Remark 1

The proposed multi-scale approach is a generalized method offering a rich description for buckling problems. In this study we limited our search to buckling developed in the rolling direction x, hence the chosen Fourier series development. To generalize even more the description in both directions, the Fourier development should be extended as follows:

$$U(x,y) = \sum_m U_m(x,y) e^{imq_1 x + imq_2 y} \tag{4.37}$$

where q_1 and q_2 are respectively the wave-numbers in the direction x and y.

The aim is to develop a simple yet capable Buckling Model. In order to build this model, many hypotheses have to be imposed:

Hypothesis 1

The Fourier series development is limited to the first order for displacements and to the second order for the stress and strain tensors:

$$(u, v) = (u_0, v_0) + (u_2, v_2)e^{2iqx} + (\bar{u}_2, \bar{v}_2)e^{-2iqx} \tag{4.38}$$

$$w = w_0 + w_1 e^{iqx} + \bar{w}_1 e^{-iqx} \tag{4.39}$$

$$N = N_0 + N_2 e^{2iqx} + \bar{N}_2 e^{-2iqx} \tag{4.40}$$

$$\varepsilon = \varepsilon_0 + \varepsilon_2 e^{2iqx} + \bar{\varepsilon}_2 e^{-2iqx} \tag{4.41}$$

where w_0 and w_1 are respectively the mean field and first envelope of the undulations (Figure 4.3).

This specific development, specially the one used for the stresses, was chosen using the same identification method presented in [Budiansky, 1974] . It is the minimal development capable of describing the appearance of undulations in the $x-$direction (Figure 4.3), where the new macroscopic unknowns w_0 and w_1 are sufficient to quantify the magnitude of the waves. It is beneficial to use this minimal development since having less macroscopic unknowns means less equations and computational time.

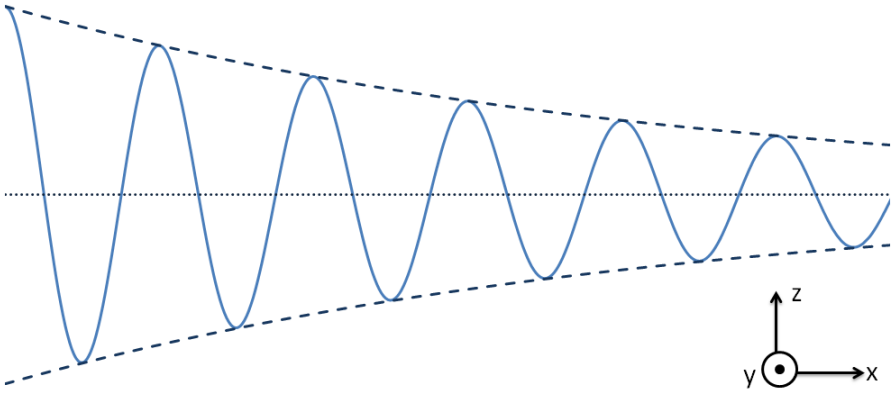

Figure 4.3: A pseudo-periodic undulation developed in the $x-$direction, described by the mean field (in dots) and the first envelope (dashed).

Hypothesis 2

The first envelope w_1 is supposed to be real:

$$\bar{w}_1(x, y) = w_1(x, y) \tag{4.42}$$

On the one hand, such simplification imposed in this early stage can affect the precision of the solution. On the other hand, keeping the envelope complex then taking its real part after solving, will increase considerably the computational time. Taking $w_1 = \bar{w}_1$ means replacing $||w_1||cos(qx + \phi)$ with $w_1 cos(qx)$ by supposing that the phase shift ϕ is equal to zero.

Hypothesis 3

The first envelope w_1 is supposed to vary slowly in the $x-$direction. Thus, its derivatives according to x can be dropped:

$$\frac{\partial w_1(x,y)}{\partial x} = \frac{\partial^2 w_1(x,y)}{\partial x^2} = \frac{\partial^3 w_1(x,y)}{\partial x^3} = \frac{\partial^4 w_1(x,y)}{\partial x^4} = 0 \tag{4.43}$$

This hypothesis allows us transforming the problem to an unidimensional one i.e. all the Fourier coefficients (in particular w_1, N_0 and N_2) are functions depending only of the transverse coordinate y.
In the case of a single stress profile spread all along the plate, this hypothesis is perfectly fit and logic. Even if the stress profiles are slightly-moderately different from one transverse section to another, it is still valid and a good approximation to reality. A difficulty may appear if shockingly different profiles coexist in the same vicinity, this simplification then ceases to be effective.

Hypothesis 4

The first envelope w_1 is approximated by the Galerkin method:

$$w_1(x,y) = a(x).W(y) \tag{4.44}$$

where a is the waves amplitude and $W(y)$ is the buckling mode i.e. the deflection shape in a transverse section.

Hypothesis 4 is a good way to prevent any coupling between different types of finite elements once the final **Buckling Model** is coupled with another software (in particular the rolling model Lam3).

Hypothesis 5

The thickness h is supposed to remain constant:

$$h(y) = h \tag{4.45}$$

In order to clarify the different steps into writing the new macroscopic systems, we begin by expressing the Fourier coefficients ε_0 and ε_2 of the strain tensor ε in terms of the Fourier coefficients of the displacement vector $(u, v, w)^t$.
Combining Hypotheses 1 and 3, the strain tensor Fourier coefficients ε_0 and ε_2 for the levels $m = 0$ and $m = 2$ are:

$$\begin{aligned} \varepsilon_0 &= \frac{1}{2}\left(\nabla\tilde{u}_0 + (\nabla\tilde{u}_0)^t + \nabla w_0 \otimes \nabla w_0 + (\nabla w)_1 \otimes \overline{(\nabla w)_1} + \overline{(\nabla w)_1} \otimes (\nabla w)_1\right) \\ \varepsilon_2 &= \frac{1}{2}\left((\nabla\tilde{u})_2 + (\nabla\tilde{u})_2^t + (\nabla w)_1 \otimes (\nabla w)_1\right) \end{aligned} \tag{4.46}$$

where,

$$\begin{aligned} &\tilde{u} = (u, v)^t \\ &(\nabla w)_1 = \nabla w_1 + iqe_x \otimes w_1 = \begin{pmatrix} iqw_1 \\ \dfrac{\partial w_1}{\partial y} \end{pmatrix} \\ &(\nabla\tilde{u})_2 = \nabla\tilde{u}_2 + 2iqe_x \otimes \tilde{u}_2 \\ &(\nabla w)_1 \otimes (\nabla w)_1 = \begin{pmatrix} iqw_1 \\ \dfrac{\partial w_1}{\partial y} \end{pmatrix} \begin{pmatrix} iqw_1 & \dfrac{\partial w_1}{\partial y} \end{pmatrix} = \begin{pmatrix} -q^2w_1^2 & iqw_1\dfrac{\partial w_1}{\partial y} \\ iqw_1\dfrac{\partial w_1}{\partial y} & \left(\dfrac{\partial w_1}{\partial y}\right)^2 \end{pmatrix} \\ &(\nabla w)_1 \otimes \overline{(\nabla w)_1} + \overline{(\nabla w)_1} \otimes (\nabla w)_1 = \begin{pmatrix} iqw_1 \\ \dfrac{\partial w_1}{\partial y} \end{pmatrix} \begin{pmatrix} -iqw_1 & \dfrac{\partial w_1}{\partial y} \end{pmatrix} + \\ &\begin{pmatrix} -iqw_1 \\ \dfrac{\partial w_1}{\partial y} \end{pmatrix} \begin{pmatrix} iqw_1 & \dfrac{\partial w_1}{\partial y} \end{pmatrix} = 2\begin{pmatrix} q^2w_1^2 & 0 \\ 0 & \left(\dfrac{\partial w_1}{\partial y}\right)^2 \end{pmatrix} \end{aligned} \tag{4.47}$$

Finally, the matrix forms of ε_0 and ε_2 are:

$$\varepsilon_0 = \begin{pmatrix} \varepsilon_{0_x} \\ \varepsilon_{0_y} \\ \varepsilon_{0_{xy}} \end{pmatrix} = \begin{pmatrix} \dfrac{\partial u_0}{\partial x} + \dfrac{1}{2}\left(\dfrac{\partial w_0}{\partial x}\right)^2 + q^2w_1^2 \\ \dfrac{\partial v_0}{\partial y} + \dfrac{1}{2}\left(\dfrac{\partial w_0}{\partial y}\right)^2 + \left(\dfrac{\partial w_1}{\partial y}\right)^2 \\ \dfrac{\partial u_0}{\partial y} + \dfrac{\partial v_0}{\partial x} + \dfrac{\partial w_0}{\partial x}\dfrac{\partial w_0}{\partial y} \end{pmatrix} \tag{4.48}$$

$$\varepsilon_2 = \begin{pmatrix} \varepsilon_{2_x} \\ \varepsilon_{2_y} \\ \varepsilon_{2_{xy}} \end{pmatrix} = \begin{pmatrix} \dfrac{\partial u_2}{\partial x} + 2iqu_2 - \dfrac{1}{2}q^2 w_1^2 \\ \dfrac{\partial v_2}{\partial y} + \dfrac{1}{2}\left(\dfrac{\partial w_1}{\partial y}\right)^2 \\ \dfrac{\partial u_2}{\partial y} + \dfrac{\partial v_2}{\partial x} + iqv_2 + \dfrac{1}{2}iqw_1\dfrac{\partial w_1}{\partial y} \end{pmatrix} \tag{4.49}$$

From the above relations, the wrinkling strain ε^{wr} or what is known as the additional strain introduced due to the appearance of buckling is deduced:

$$\varepsilon^{wr} = \begin{pmatrix} \varepsilon_x^{wr} \\ \varepsilon_y^{wr} \\ \varepsilon_{xy}^{wr} \end{pmatrix} = \begin{pmatrix} q^2 w_1^2 \\ \left(\dfrac{\partial w_1}{\partial y}\right)^2 \\ 0 \end{pmatrix} + \frac{1}{2}\begin{pmatrix} -q^2 w_1^2 \\ \left(\dfrac{\partial w_1}{\partial y}\right)^2 \\ iqw_1\dfrac{\partial w_1}{\partial y} \end{pmatrix} e^{2iqx} \tag{4.50}$$

Compatible with the von Kármán steps presented earlier, the tangential components of u_0 and u_2 are neglected.

Using Hypothesis 1, 2 and 3 and replacing equations (4.48) and (4.49) in $\delta V = 0$, the new macroscopic bifurcation equation corresponding to the level 1 is:

$$\begin{aligned} &\frac{\mathbb{D}}{q^2}\int_{-l/2}^{l/2}\frac{\partial^2 w_1}{\partial y^2}\frac{\partial^2 \delta w_1}{\partial y^2}dy - \mathbb{D}\nu\int_{-l/2}^{l/2} w_1\frac{\partial^2 \delta w_1}{\partial y^2} + \frac{\partial^2 w_1}{\partial y^2}\delta w_1 dy + \\ &2\mathbb{D}(1-\nu)\int_{-l/2}^{l/2}\frac{\partial w_1}{\partial y}\frac{\partial \delta w_1}{\partial y}dy + \int_{-l/2}^{l/2}(\mathbb{D}q^2 + \bar{N}_0)w_1\delta w_1 dy + \\ &\int_{-l/2}^{l/2} N_x^{res} w_1 \delta w_1 dy + \frac{1}{q^2}\int_{-l/2}^{l/2} N_y^{res}\frac{\partial w_1}{\partial y}\frac{\partial \delta w_1}{\partial y}dy + \\ &\int_{-l/2}^{l/2} N_{x_0} w_1 \delta w_1 dy + \frac{1}{q^2}\int_{-l/2}^{l/2} N_{y_0}\frac{\partial w_1}{\partial y}\frac{\partial \delta w_1}{\partial y}dy - \int_{-l/2}^{l/2} N_{x_2} w_1 \delta w_1 dy + \\ &\frac{1}{q^2}\int_{-l/2}^{l/2} N_{y_2}\frac{\partial w_1}{\partial y}\frac{\partial \delta w_1}{\partial y}dy + \frac{i}{q}\int_{-l/2}^{l/2} N_{xy_2}\left(\frac{\partial w_1}{\partial y}\delta w_1 + w_1\frac{\partial \delta w_1}{\partial y}\right)dy = 0 \end{aligned} \tag{4.51}$$

where l is the width of the strip, $\bar{N}_0$ is the strip tension, N^{res} is the residual stress, N_0 and N_2 are respectively the stress Fourier coefficients for the levels $m = 0$ and $m = 2$ and w_1 is the first envelope i.e. the displacement Fourier coefficient for the level $m = 1$.
Note that the problem is transformed into a $1D$ equation since $w_1 = w_1(y)$ i.e. $\dfrac{\partial w_1}{\partial y} = w'$.
As for the macroscopic equations derived from the behavior law, it is complicated to write them directly from the weak formulation. So we proceed into writing it for each level using the strong formulation.

Level 0:

The equilibrium equation gives:

$div(N) = 0 \Leftrightarrow div(N_0) = 0 \Leftrightarrow$ an Airy function $f_0(y)$ exists such that:

$$\begin{aligned} N_{x_0} &= \frac{\partial^2 f_0}{\partial y^2} \\ N_{y_0} &= \frac{\partial^2 f_0}{\partial x^2} = 0 \\ N_{xy_0} &= \frac{\partial^2 f_0}{\partial x \partial y} = 0 \end{aligned} \tag{4.52}$$

According to Hooke's law:

$$\begin{aligned} \varepsilon_{x_0} &= \frac{1}{Eh}\left[N_{x_0} - \nu N_{y_0}\right] = \frac{1}{Eh}\frac{\partial^2 f_0}{\partial y^2} \\ \varepsilon_{y_0} &= \frac{1}{Eh}\left[N_{y_0} - \nu N_{x_0}\right] = -\frac{\nu}{Eh}\frac{\partial^2 f_0}{\partial y^2} \\ \varepsilon_{xy_0} &= \frac{1}{Eh}\left[(1+\nu) N_{xy_0}\right] = 0 \end{aligned} \tag{4.53}$$

Combining (4.48) with ε_0 compatibility equation:

$$\begin{aligned} &\frac{\partial^2 \varepsilon_{x_0}}{\partial y^2} + \frac{\partial^2 \varepsilon_{y_0}}{\partial x^2} - 2\frac{\partial^2 \varepsilon_{xy_0}}{\partial y \partial y} = 0 \\ &\frac{1}{Eh}\frac{\partial^4 f_0}{\partial y^4} = \frac{\partial^2 (q^2 w_1^2)}{\partial y^2} \end{aligned} \tag{4.54}$$

$$\boxed{\frac{1}{Eh}\frac{\partial^4 f_0}{\partial y^4} = 2q^2\left(\left(\frac{\partial w_1}{\partial y^2}\right)^2 + w_1 \frac{\partial^2 w_1}{\partial y^2}\right)} \tag{4.55}$$

Level 2:

In the same manner, the level 2 macroscopic equilibrium equation is built:
$div(N) \Leftrightarrow div(N_2) + 2iqN_2 = 0 \Leftrightarrow$ an Airy function $f_2(y)$ exists such that:

$$\begin{aligned} N_{x_2} &= \left(\frac{\partial^2 f}{\partial y^2}\right)_2 = \frac{\partial^2 f_2}{\partial y^2} \\ N_{y_2} &= \left(\frac{\partial^2 f}{\partial x^2}\right)_2 = -4q^2\frac{\partial^2 f_2}{\partial x^2} \\ N_{xy_2} &= \left(\frac{\partial^2 f}{\partial x \partial y}\right)_2 = -2iq\frac{\partial f_2}{\partial y} \end{aligned} \tag{4.56}$$

According to Hooke's law:

$$\begin{aligned} \varepsilon_{x_2} &= \frac{1}{Eh}\left[N_{x_2} - \nu N_{y_2}\right] = \frac{1}{Eh}\left(\frac{\partial^2 f_2}{\partial y^2} + 4\nu q^2 f_2\right) \\ \varepsilon_{y_2} &= \frac{1}{Eh}\left[N_{y_2} - \nu N_{x_2}\right] = -\frac{1}{Eh}\left(4q^2 f_2 + \nu\frac{\partial^2 f_2}{\partial y^2}\right) \\ \varepsilon_{xy_2} &= \frac{1}{Eh}\left[(1+\nu) N_{xy_2}\right] = -\frac{2}{Eh}(1+\nu)iq\frac{\partial f_2}{\partial y} \end{aligned} \tag{4.57}$$

Combining (4.49) with ε_2 compatibility equation and neglecting the tangential components of the displacements coefficients u_2 and v_2 (following the same steps as for the von Kármán equations):

$$\begin{aligned}
&\frac{\partial^2}{\partial y^2}(\varepsilon_{x_2}) + \left(\frac{\partial}{\partial x} + 2iq\right)^2(\varepsilon_{y_2}) - 2\frac{\partial}{\partial y}\left(\frac{\partial}{\partial x} + 2iq\right)(\varepsilon_{xy_2}) = 0 \\
&\frac{1}{Eh}\left[\frac{\partial^2}{\partial y^2}\left(\frac{\partial^2 f_2}{\partial y^2} + 4\nu q^2 f_2\right) + 4q^2\left(4q^2 f_2 + \nu\frac{\partial^2 f_2}{\partial y^2}\right) - 4iq\left(-2(1+\nu)iq\frac{\partial f_2}{\partial y}\right)\right] = \\
&\frac{1}{2}\left[-\frac{\partial^2}{\partial y^2}(q^2 w_1^2) - 4q^2\frac{\partial}{\partial x}(w_1^2) - 4iq\frac{\partial}{\partial y}(iqw_1\frac{\partial}{\partial y})\right]
\end{aligned} \tag{4.58}$$

$$\boxed{\frac{1}{Eh}\left(\frac{\partial^4 f_2}{\partial y^4} - 8q^2\frac{\partial^2 f_2}{\partial y^2} + 16q^4 f_2\right) = -q^2\left(\left(\frac{\partial w_1}{\partial y}\right)^2 - w_1\frac{\partial^2 w_1}{\partial y^2}\right)} \tag{4.59}$$

Equations (4.55) and (4.59) are quite similar to the von Kármán equation (4.14).
The final step is to use Galerkin approximation proposed in Hypothesis 4:

$$w_1 = a.W \Leftrightarrow \text{ functions } F_0 \text{ and } F_2 \text{ exist such as } f_0 = a^2 F_0 \text{ and } f_2 = a^2 F_2 \tag{4.60}$$

where a is the dimensionless amplitude of the waves and $W(y)$ is the buckling mode computed on a transverse section.
All that is left to do is replacing in the equations (4.51), (4.55) and (4.59) w_1 by aW, N_0 and N_2 by their new expressions in terms of the new Airy functions F_0 and F_2. The new set of equations to solve is:

$$\begin{aligned}
&\frac{1}{Eh}\frac{\partial^4 F_0}{\partial y^4} = 2q^2\left(\left(\frac{\partial W}{\partial y}\right)^2 + W\frac{\partial^2 W}{\partial y^2}\right) && (a)\\
&\frac{1}{Eh}\left(\frac{\partial^4 F_2}{\partial y^4} - 8q^2\frac{\partial^2 F_2}{\partial y^2} + 16q^4 F_2\right) = -q^2\left(\left(\frac{\partial W}{\partial y}\right)^2 - W\frac{\partial^2 W}{\partial y^2}\right) && (b)\\
&a\left[\frac{\mathbb{D}}{q^2}\int_{-l/2}^{l/2}\frac{\partial^2 W}{\partial y^2}\frac{\partial^2 \delta W}{\partial y^2}dy - \mathbb{D}\nu\int_{-l/2}^{l/2}\left(W\frac{\partial^2\delta W}{\partial y^2} + \frac{\partial^2 W}{\partial y^2}\delta W\right)dy + \right.\\
&2\mathbb{D}(1-\nu)\int_{-l/2}^{l/2}\frac{\partial W}{\partial y}\frac{\partial \delta W}{\partial y}dy + \int_{-l/2}^{l/2}(\mathbb{D}q^2 + \bar{N}_0)W\delta W dy + \\
&\left.\int_{-l/2}^{l/2}N_x^{res}W\delta W dy + \frac{1}{q^2}\int_{-l/2}^{l/2}N_y^{res}\frac{\partial W}{\partial y}\frac{\partial \delta W}{\partial y}dy\right] = && (c)\\
&a^3\left[\int_{-l/2}^{l/2}\left(\frac{\partial^2 F_2}{\partial y^2} - \frac{\partial^2 F_0}{\partial y^2}\right)W\delta W dy + 4\int_{-l/2}^{l/2}F_2\frac{\partial W}{\partial y}\frac{\partial \delta W}{\partial y}dy - \right.\\
&\left.-2\int_{-l/2}^{l/2}\frac{\partial F_2}{\partial y}(\frac{\partial W}{\partial y}\delta W + W\frac{\partial \delta W}{\partial y})dy\right]
\end{aligned} \tag{4.61}$$

The weak formulation of equations (4.61(a)) and (4.61(b)) is presented in the next section before presenting the discretized problem.

The problem is divided into two main parts:

- The first is solving the buckling problem where the load critical value, the mode W and the half-waves number q are to be determined. Since the waves did not form yet, it means that no additional stresses (i.e. strain) are introduced: $N_0 = N_2 = 0$ in equation (4.61(c)). Since $W = 0$ is a trivial solution of this equation, a loading parameter λ is introduced to insure the equation bifurcation.
  N_x^{res} and N_y^{res} are replaced by λN_x^{res} and λN_y^{res}. The problem is transformed into an eigenvalue problem, where the loading parameter critical value $\lambda_{cr} = Min(\lambda_i)$, where i is the number of the problem eigenvalues. The critical stress is computed as $N_{cr}^{res} = \lambda_{cr} Min(N^{res})$. The mode W and q are the eigenvector and the half-waves number corresponding to λ_{cr}. The mode W (also referred to as the deflection function) describes the form of the deflection in the transverse direction and q describes the defect sinusoidal form in the longitudinal direction.

- The second is solving the post-buckling problem where the additional stresses N_0 and N_2 (i.e. F_0 and F_2) introduced due to buckling as well as the defect amplitude a are computed. In this part, the mode W, the critical load and the half-waves number q are known from the first step and fixed (not allowed to change). First, equations (4.61(a)) and (4.61(b)) are solved to identify F_0 and F_2. Then, the amplitude a is computed by replacing all the previously determined components in (4.61(c)).

> Remark 2
> Note that the mode (W, q) determined in the buckling problem -corresponding to the critical loading parameter λ_{cr}- is transferred to the post-buckling problem. It means that we are unable to follow the evolution of the buckling mode beyond λ_{cr}. Thus, we are stuck with the same buckling mode for both problems.

4.5.1 Finite elements discretization

First, the basis functions should be defined before proceeding to discretize our equations. We want to find an approximate solution $\tilde{g}$ for an exact solution g on an element containing two nodes (two degrees of freedom) $y_1 = 0$, and $y_2 = b$, i.e. $n = 2$. In addition, we want the first derivative $\tilde{g}'$ (i.e. the slope) to be exactly approximated as well i.e. $m = 1$.

The approximated solution is a polynomial function of a degree equal to $n(m+1)-1=3$, thus the basis is $[1\ y\ y^2\ y^3]$.
To find the four basis functions $\mathbf{N}_1$, $\mathbf{N}_2$, $\mathbf{N}_3$ and $\mathbf{N}_4$, the approximated solution $\tilde{g}$ is written as the following combination:

$$\tilde{g}(y) = \mathbf{N}_1(y)\mathbf{g}(y_1) + \mathbf{N}_2(y)\mathbf{g}'(y_1) + \mathbf{N}_3(y)\mathbf{g}(y_2) + \mathbf{N}_4(y)\mathbf{g}'(y_2) \tag{4.62}$$

The form (4.62) is replaced in the following system:

$$\begin{array}{lcll} \mathbf{g}(y)=1 & \Leftrightarrow & \tilde{g}(y)=1 & \Leftrightarrow \quad \mathbf{N}_1(y)+\mathbf{N}_3(y)=1 \\ \mathbf{g}(y)=y & \Leftrightarrow & \tilde{g}(y)=y & \Leftrightarrow \quad \mathbf{N}_2(y)+\mathbf{N}_3(y)b+\mathbf{N}_4(y)=y \\ \mathbf{g}(y)=y^2 & \Leftrightarrow & \tilde{g}(y)=y^2 & \Leftrightarrow \quad \mathbf{N}_3(y)b^2+2\mathbf{N}_4(y)b=y^2 \\ \mathbf{g}(y)=y^3 & \Leftrightarrow & \tilde{g}(y)=y^3 & \Leftrightarrow \quad \mathbf{N}_3(y)b^3+3\mathbf{N}_4(y)b^2=y^3 \end{array} \tag{4.63}$$

Solving the system (4.68) allows us to identify the four basis functions defined on a $1D$ element of length b:

$$\begin{array}{lll} \mathbf{N}_1(y) = 1-\dfrac{3}{b^2}y^2+\dfrac{2}{b^3}y^3 & ; & \mathbf{N}_2(y) = y-\dfrac{2}{b}y^2+\dfrac{1}{b^2}y^3 \\ \mathbf{N}_3(y) = \dfrac{3}{b^2}y^2-\dfrac{2}{b^3}y^3 & ; & \mathbf{N}_4(y) = -\dfrac{1}{b}y^2+\dfrac{1}{b^2}y^3 \end{array} \tag{4.64}$$

Figure 4.4 illustrates the four basis function for a reference element using the Hermite approximation. It is perfectly clear that N_1 and N_3 are the partition of unity. In addition, N_2 and N_4 are equal to zero on both nodes; As to their derivatives, they are equal to zero or one on the nodes.

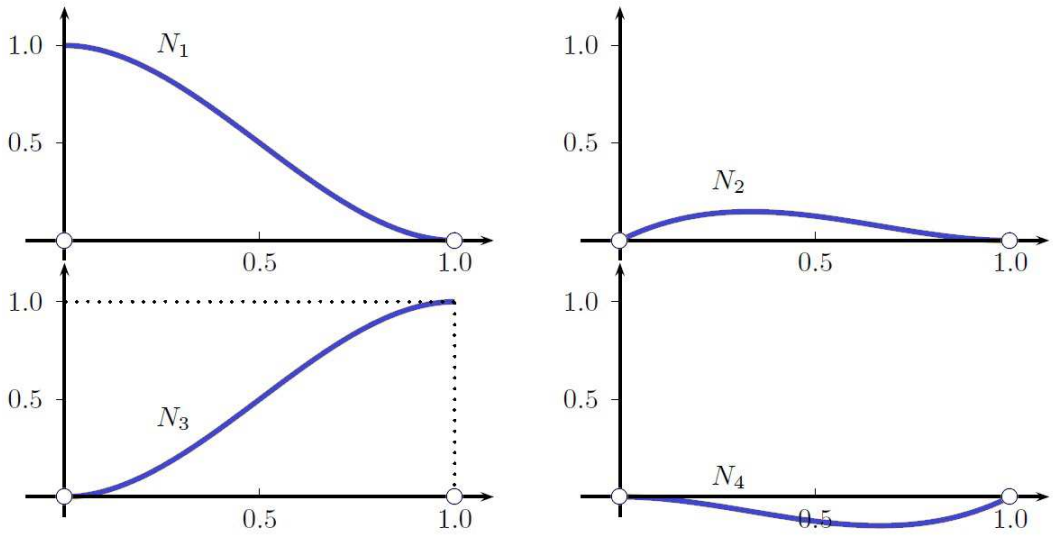

Figure 4.4: The basis functions of the Hermite reference Finite Element of length $b=1$.

Now that the basis functions are defined, we can proceed to discretize the weak formulation and write the matrix form of the problem.

4.5.2 Discretization: Buckling Problem

In the buckling problem, the buckling load and mode should be identified i.e. the critical value, the deflection form W describing the shape in a transverse section and the half-wave number q describing defect form in the $x-$direction. Thus the following equation should be solved:

$$\frac{\mathbb{D}}{q^2}\int_{-l/2}^{l/2}\frac{\partial^2 W}{\partial y^2}\frac{\partial^2 \delta W}{\partial y^2}dy - \mathbb{D}\nu\int_{-l/2}^{l/2} W\frac{\partial^2 \delta W}{\partial y^2} + \frac{\partial^2 W}{\partial y^2}\delta W dy + 2\mathbb{D}(1-\nu)\int_{-l/2}^{l/2}\frac{\partial W}{\partial y}\frac{\partial \delta W}{\partial y}dy + \int_{-l/2}^{l/2}(\mathbb{D}q^2+\bar{N}_0)W\delta W dy = -\int_{-l/2}^{l/2}N_x^{res}W\delta W dy - \frac{1}{q^2}\int_{-l/2}^{l/2}N_y^{res}\frac{\partial W}{\partial y}\frac{\partial \delta W}{\partial y}dy \tag{4.65}$$

Using the Hermite approximation described above, the mode W takes the following form:

$$W(y) = W_1\mathbf{N}_1(y) + W_2\mathbf{N}_2(y) + W_3\mathbf{N}_3(y) + W_4\mathbf{N}_4(y) \tag{4.66}$$

where $\mathbf{N}_i$ and W_i for $i = 1,..,4$ are respectively the four basis functions and the element nodal values of W and $\frac{\partial W}{\partial y}$. Note that both the mode W and its first derivative $\frac{\partial W}{\partial y}$ are continuous over the element and its boundary i.e. $W \in \mathbf{C}^1$ and $\frac{\partial W}{\partial y} \in \mathbf{C}^1$.
Over an element e, we adopt the following notations:

$$U_e = \begin{pmatrix} W_1 \\ W_2 \\ W_3 \\ W_4 \end{pmatrix};\ \delta U_e = \begin{pmatrix} \delta W_1 \\ \delta W_2 \\ \delta W_3 \\ \delta W_4 \end{pmatrix}$$

$$\delta U_e(\frac{1}{q^2}k_1^e + k_2^e + k_3^e + q^2k_4^e + k_5^e - k_6^e - \frac{1}{q^2}k_7^e)U_e = 0 \tag{4.67}$$

where $k_1^e, k_2^e, .., k_7^e$ are the local matrices defined on each element $e = [0, b]$ as:

$$\begin{aligned}
k_1^e &= \mathbb{D}\int_0^b \frac{\partial^2 \mathbf{N}_e^t}{\partial y^2}\frac{\partial^2 \mathbf{N}_e}{\partial y^2}dy \\
k_2^e &= -\mathbb{D}\nu\int_0^b \left(\mathbf{N}_e^t\frac{\partial^2 \mathbf{N}_e}{\partial y^2} + \frac{\partial^2 \mathbf{N}_e^t}{\partial y^2}\mathbf{N}_e\right)dy \\
k_3^e &= \int_0^b \bar{N}_0\mathbf{N}_e^t\mathbf{N}_e dy \\
k_4^e &= \mathbb{D}\int_0^b \mathbf{N}_e^t\mathbf{N}_e dy \\
k_5^e &= 2\mathbb{D}(1-\nu)\int_0^b \frac{\partial \mathbf{N}_e^t}{\partial y}\frac{\partial \mathbf{N}_e}{\partial y}dy \\
k_6^e &= -\int_0^b N_x^{res}\mathbf{N}_e^t\mathbf{N}_e dy \\
k_7^e &= -\int_0^b N_y^{res}\frac{\partial \mathbf{N}_e^t}{\partial y}\frac{\partial \mathbf{N}_e}{\partial y}dy
\end{aligned} \tag{4.68}$$

where $N_e = (\mathbf{N}_1, \mathbf{N}_2, \mathbf{N}_3, \mathbf{N}_4)^t$. These local matrices can be easily computed numerically using Gaussian quadrature rule. Then, the global system is assembled using a binding matrix mapping the relations between the local and global positions of the variable nodes. Note that the different loads ($\bar{N}_0$, N_x^{res} and N_y^{res}) contributions are presented respectively by the matrices k_3, k_6 and k_7. Since $W = 0$ is always a solution (trivial solution), we can already expect that the system is not defined and the global matrix is singular. That is why the loading parameter λ is introduced to ensure bifurcation, thus finding a non-trivial solution. The system is now transformed into a generalized eigenvalue problem:

$$\begin{aligned}
(\frac{1}{q^2}K_1 + K_2 + K_3 + q^2K_4 + K_5)U &= (\lambda K_6 + \frac{\lambda}{q^2}K_7)U \\
AU &= \lambda BU
\end{aligned} \tag{4.69}$$

where $K_1, K_2, .., K_7$ are the global matrices defined on $\left[-\frac{l}{2}, \frac{l}{2}\right]$.
The smallest positive eigenvalue is the critical buckling parameter λ_{cr} and the corresponding eigenvector is its mode W. Along the way, q the half-waves number is also computed using equation (4.65).

4.5.3 Boundary conditions: Buckling Problem

We are interested mainly in using free edges boundary conditions since it is the most realistic boundary condition for treating buckling problems during flat rolling. Nevertheless other boundary conditions are equally interesting and are cited as well.

Remark 3

Do not confuse w with W. w is the out of plane displacement $w(x,y) = w_0 + w_1 e^{iqx} + w_1 e^{-iqx}$ and W is the buckling mode such as $w_1 = a.W$.

Free Edges:

$$\begin{aligned} &\frac{\partial^3 w}{\partial y^3} + (2-\nu)\frac{\partial^3 w}{\partial x^2 \partial y} = 0 \quad \Leftrightarrow \quad W^{(3)} - q^2(2-\nu)W' = 0 \quad ; \quad \text{for } y = -\frac{l}{2}; \frac{l}{2} \\ &\frac{\partial^2 w}{\partial y^2} + \nu\frac{\partial^2 w}{\partial x^2} = 0 \quad \Leftrightarrow \quad W^{(2)} - q^2\nu W = 0 \quad ; \quad \text{for } y = -\frac{l}{2}; \frac{l}{2} \end{aligned} \tag{4.70}$$

Simply supported Edges:

$$\begin{aligned} &w(x,y) = 0 \quad \Leftrightarrow \quad W(y) = 0 \quad ; \quad \text{for } y = -\frac{l}{2}; \frac{l}{2} \\ &\Delta w(x,y) = 0 \quad \Leftrightarrow \quad W''(y) = 0 \quad ; \quad \text{for } y = -\frac{l}{2}; \frac{l}{2} \end{aligned} \tag{4.71}$$

Clamped Edges:

$$\begin{aligned} &w(x,y) = 0 \quad \Leftrightarrow \quad W(y) = 0 \quad ; \quad \text{for } y = -\frac{l}{2}; \frac{l}{2} \\ &\frac{\partial w(x,y)}{\partial y} = 0 \quad \Leftrightarrow \quad W'(y) = 0 \quad ; \quad \text{for } y = -\frac{l}{2}; \frac{l}{2} \end{aligned} \tag{4.72}$$

4.5.4 Discretization: Post-buckling Problem

In the post-buckling problem, two sets of equations should be solved first to compute the Airy functions F_0 and F_2. Once known, the last step is to identify the buckling amplitude a.

$$\begin{aligned} \frac{1}{Eh}\int_{-l/2}^{l/2} F_0''\delta F_0'' dy = 2q^2 \int_{-l/2}^{l/2} (W'^2 + WW")\delta F_0 dy &= 2q^2 \int_{-l/2}^{l/2} S_0 \delta F_0 dy \\ \frac{1}{Eh}\left[\int_{-l/2}^{l/2} F_2''\delta F_2'' dy + 8q^2\int_{-l/2}^{l/2} F_2'\delta F_2' dy + 16q^4\int_{-l/2}^{l/2} F_2\delta F_2 dy\right] &= -2q^2\int_{-l/2}^{l/2}(W'^2 - WW")\delta F_2 dy \\ &= -2q^2\int_{-l/2}^{l/2} S_2\delta F_2 dy \\ a.L_1 = a^3.L_2 \Leftrightarrow a = 0 \text{ or } a = \sqrt{\frac{L_1}{L_2}} & \end{aligned} \tag{4.73}$$

where L_1 and L_2 are the terms between brackets in equation (4.61(c)).
Since the buckling mode W is known in this step, for the sake of clarity, the terms in W

and W' are replaced as follows:

$$(W'^2 + WW") = S_0 \text{ and } (W'^2 - WW") = S_2$$

Once again using the Hermite approximation the unknowns F_0 and F_2 are written as:

$$\begin{aligned} F_0(y) &= F_{0_1}\mathbf{N}_1(y) + F_{0_2}\mathbf{N}_2(y) + F_{0_3}\mathbf{N}_3(y) + F_{0_4}\mathbf{N}_4(y) \\ F_2(y) &= F_{2_1}\mathbf{N}_1(y) + F_{2_2}\mathbf{N}_2(y) + F_{2_3}\mathbf{N}_3(y) + F_{2_4}\mathbf{N}_4(y) \end{aligned} \tag{4.74}$$

where $\mathbf{N}_i$, F_{0_i} and F_{2_i} for $i = 1, .., 4$ are respectively the four basis functions and the element nodal values of F_0 and F_2 and their derivatives.
In the same manner, the local system and matrices are computed from the integrals over an element $e = [0, b]$, then assembled to obtain the global system defined all over the width of the plate l:

$$\begin{aligned} A_0U_0 &= B_0 \\ A_2U_2 &= B_2 \end{aligned} \tag{4.75}$$

in which U_0 and U_2 are the vectors formed by the nodal values of F_0 and F_2.
Now that the Airy functions are known, the buckling amplitude a is computed using the third equation of (4.73).

4.5.5 Boundary conditions: Post-buckling Problem

If needed, the out-of-plane displacement w i.e. the mode W, verify the same boundary conditions used in the buckling problem.
As for the Airy functions, F_0 and F_2 should verify the following boundary conditions:

$$\begin{aligned} F_0(y) = F_0'(y) = 0 \quad ; \quad \text{for } y = -\frac{l}{2}; \frac{l}{2} \\ F_2(y) = F_2'(y) = 0 \quad ; \quad \text{for } y = -\frac{l}{2}; \frac{l}{2} \end{aligned} \tag{4.76}$$

These boundary conditions could be interpreted as vanishing shear forces along the edges of the strip, i.e. the boundaries are free of stresses.

We should mention that a similar buckling model was developed by [Kpogan, 2011] for his Master thesis.

4.6 Numerical results: Qualitative appreciation

A steel sheet ($E = 210$ GPa, $\nu = 0.3$) of length $L = 3000$ mm, width $l = 855$ mm

and thickness $h = 0.25$ mm is used throughout this section. To approach the appearance of on line flatness defects in a rolling simulation, the steel sheet is subjected to a tension $T_0 = 10$ MPa in the $x-$direction or what is called the rolling direction (RD). Note that the edges of the strip are left free from any restrictions. Two different types of defects are investigated, linked with two specific, arbitrarily assumed residual stress profiles: wavy edges and center buckles. In spite of the simplicity of the parabolic residual stress profiles used here compared with a real rolling simulation, they provide a means to assess the capacity of the present **MSBM** in detecting the mode and computing the defect amplitude.

4.6.1 Wavy edges example

The sheet is subjected to σ_x^{res} a self-balanced residual stress distribution uniform along the rolling direction (RD):

$$\sigma_x^{res}(y) = 19.\left(-6\left|\frac{y}{l}\right|^2 + \frac{1}{2}\right) \tag{4.77}$$

In this case, a wavy edge is expected since the stress is compressive at the edges of the sheet (Figure 4.5(a)). This is confirmed once the deflection function describing the deflection form in a particular transversal cut is computed. Indeed Figure 4.5(b) confirms that the-out-of-plane displacement will occur on the edges of the strip.

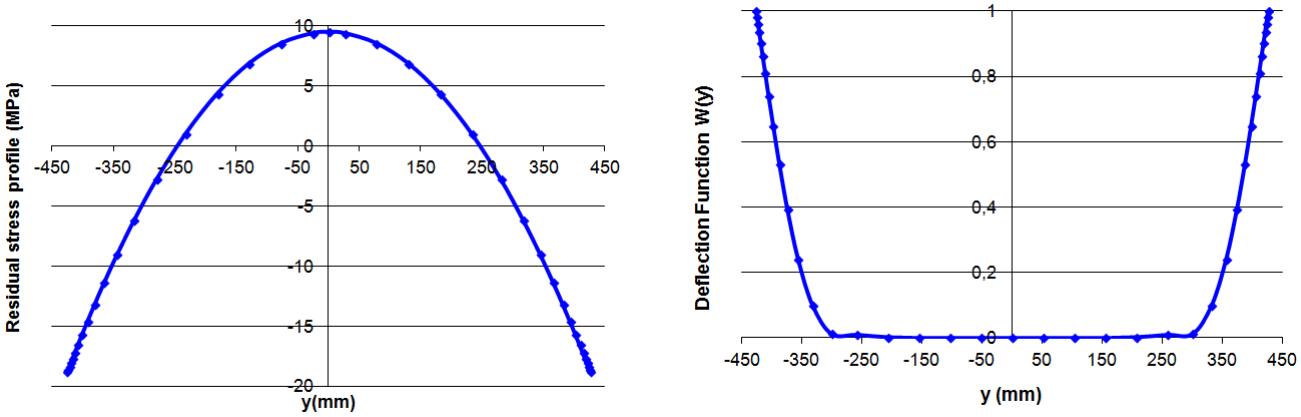

(a) (b)

Figure 4.5: (a): the applied residual stress showing compression along the edges of the sheet. (b): the deflection form on a transversal section showing deflection towards the edges.

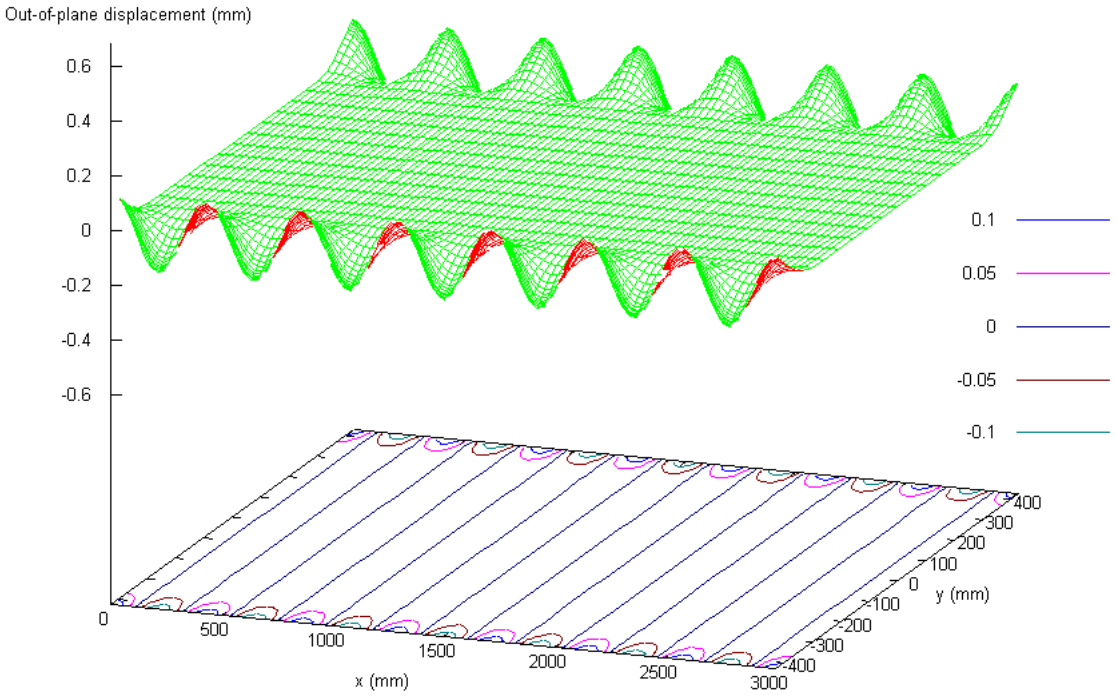

Figure 4.6: Wavy edges under stress profile $\sigma_x^{res}(y) = 19.\left(-6\left|\frac{y}{l}\right|^2 + \frac{1}{2}\right)$ and strip tension $T_0 = 10$ MPa

The stress edge value σ_{cr}, corresponding to $\lambda_{cr} = 0.68$ is equal to -12.962 MPa, the wavelength $(\frac{2\pi}{q})$ is equal to 428.571 mm and the amplitude of the waves is 0.114 mm. The defected sheet under both the tension and the compressive stress is presented in Figure 4.6.

The buckling strain ε^{wr} (the strain introduced due to $w(x)$) computed using equation (4.50) is presented in Figure 4.7(a). The additional stress σ_x^{wr} due to buckling is illustrated along with a comparison of stress distribution before and after in Figure 4.7(b).

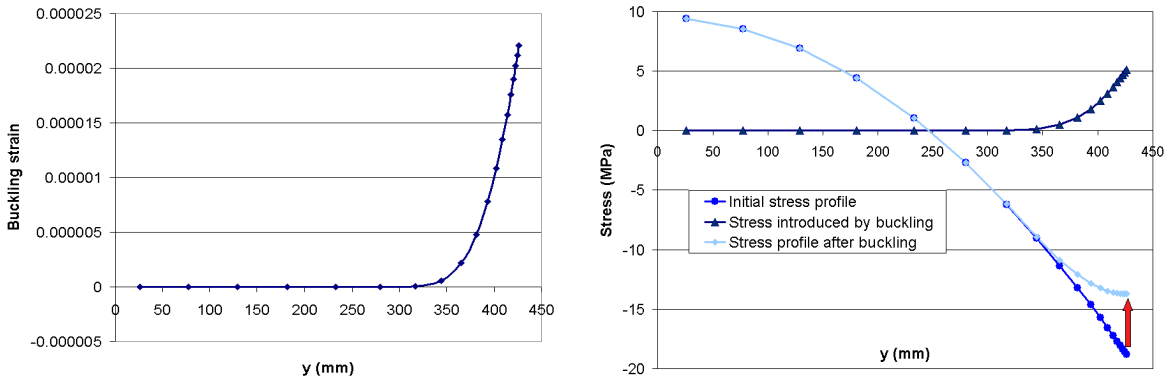

(a) (b)

Figure 4.7: (a): the additional strain introduced due to the strip buckling under residual stress. (b): the additional stress introduced due to buckling along with a comparison between the initial and relaxed stress profiles. The curves are plotted on half of the domain according to the symmetry axis $y = 0$.

4.6.2 Center buckles example

The sheet is subjected to σ_x^{res} a self-balanced residual stress distribution uniform along the rolling direction (RD):

$$\sigma_x^{res}(y) = -57.\left(-6\left|\frac{y}{l}\right|^2 + \frac{1}{2}\right) \tag{4.78}$$

In this case, a buckling center is expected since the stress is compressive along the center of the sheet (Figure 4.8(a)). The deflection function plotted in the transverse direction y illustrated in Figure 4.8(b) confirms that the-out-of-plane displacement will occur in the center of the strip.

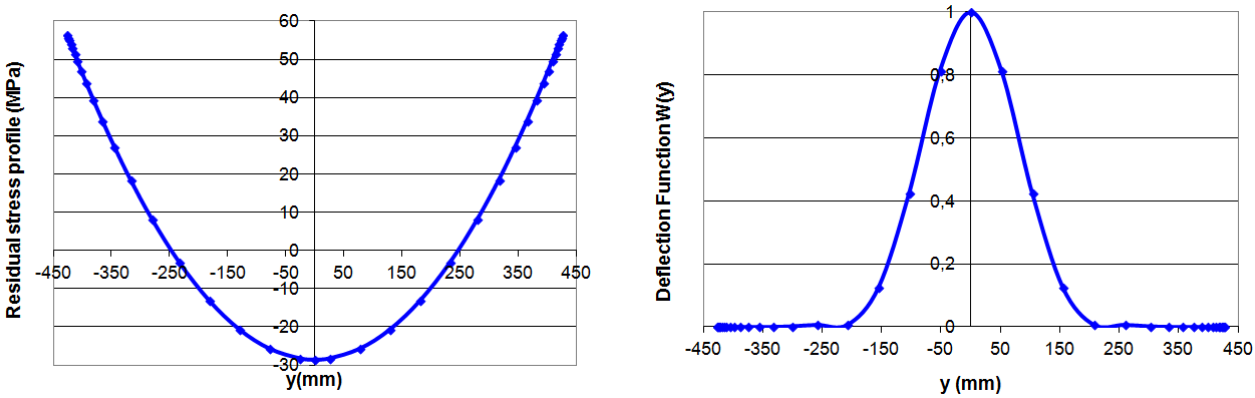

(a) (b)

Figure 4.8: (a): the applied residual stress showing compression along the center of the sheet. (b): the deflection form on a transversal section showing deflection towards the center.

The stress central value σ_{cr}, corresponding to $\lambda_{cr} = 0.36$ is equal to -11 MPa (critical value in the center), the wavelength $(\frac{2\pi}{q})$ is equal to 545.45 mm and the amplitude of the waves is 0.259 mm.

The defected sheet under both the strip tension and the compressive stress along its center is presented in Figure 4.9.

The buckling strain ε^{wr} (the strain introduced due to $w(x)$) computed using equation (4.50) is presented in Figure 4.10(a). The additional stress σ_x^{wr} due to the buckling strip is illustrated along with a comparison of stress distribution before and after 4.10(b) .

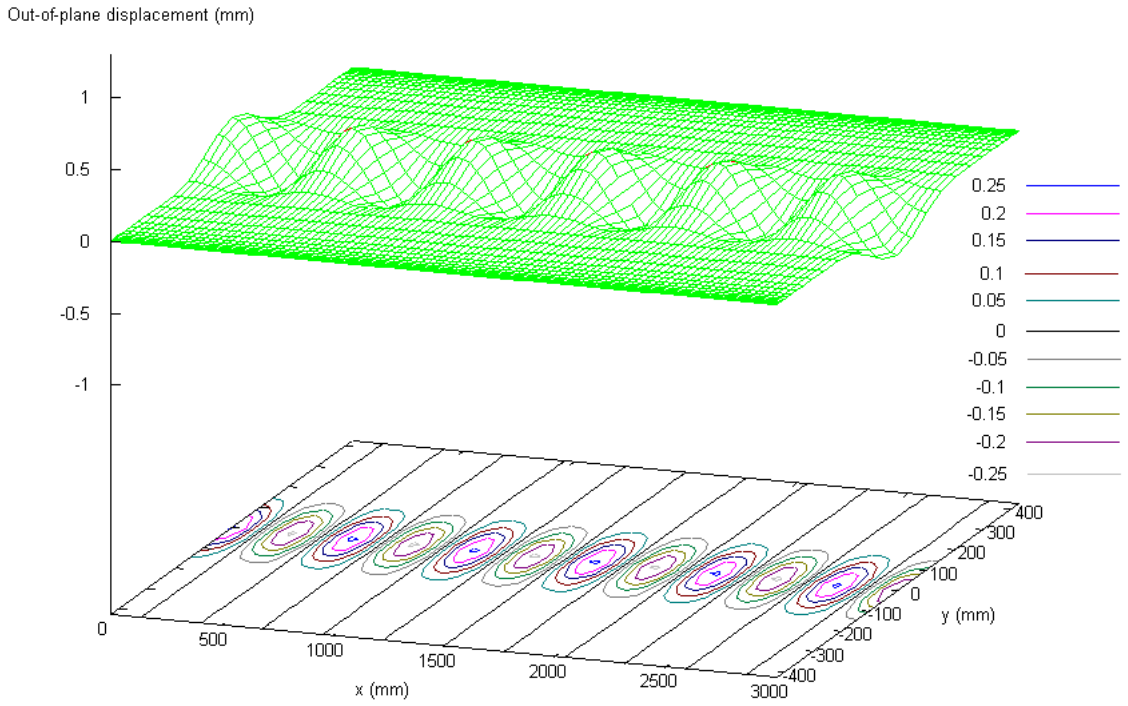

Figure 4.9: Wavy edges under stress profile $\sigma_x^{res}(y) = -57.\left(-6\left|\frac{y}{l}\right|^2 + \frac{1}{2}\right)$ and strip tension $T_0 = 10$ MPa

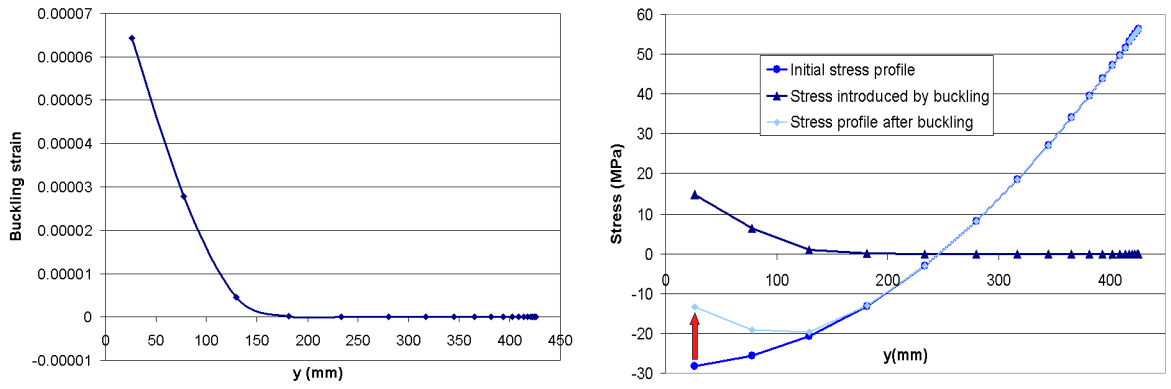

(a) (b)

Figure 4.10: (a): the additional strain introduced due to the strip buckling under residual stress. (b): the additional stress introduced due to buckling along with a comparison between the initial and relaxed stress profiles. The curves are plotted on half of the domain according to the symmetry axis $y = 0$.

4.6.3 Strip tension and the buckling mode/amplitude

The same metal sheet used in the previous examples is used in this study as well. It is subjected to a residual stress distribution exhibiting compression on the edges $\sigma_x^{res}(y) = 19\left(-6\left|\frac{y}{l}\right|^2 + \frac{1}{2}\right)$ and a tensile load in the x-direction or the rolling direction. The tension is used as a parameter in this study. Changing the tension will affect the buckling strip form: mode, buckling load and amplitude. The evolution of each component is followed and assessed.

Table 4.1 summarizes the evolution of the critical stress, the wavelength and the amplitude with an increasing tension.

Tension (MPa)	2	4	6	8	10	12	14	16	18
Critical Stress (MPa)	-3.13	-5.7	-8.17	-10.58	-12.96	-15.31	-17.64	-18.79	-20.1
Wavelength (mm)	750	600	500	461.53	428.57	400	30	0	0
Amplitude (mm)	0.32	0.23	0.17	0.14	0.11	0.08	0.04	0	0

Table 4.1: The evolution of the buckling load, defect mode and amplitude with the strip tension.

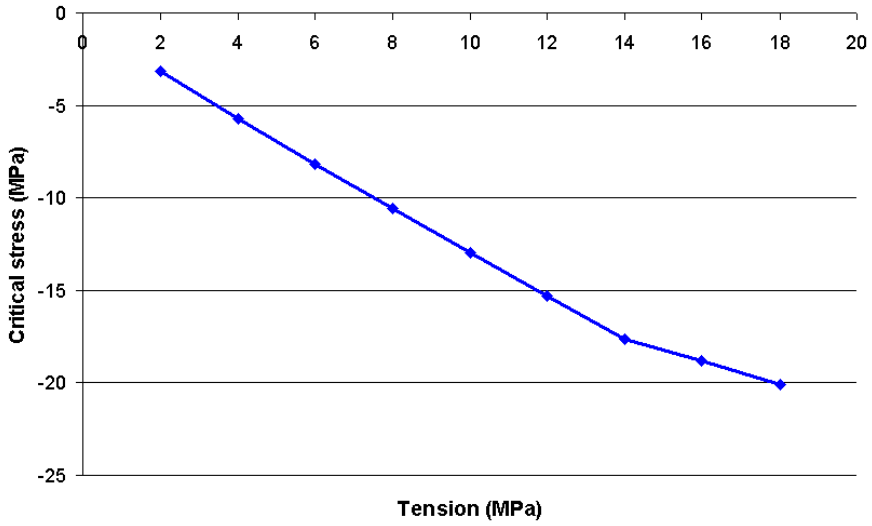

Figure 4.11: The critical stress evolution with an increasing tension.

Table 4.1 and Figure 4.11 show that the critical stress $|\sigma_{cr}|$ increases linearly with an increasing tension, this is expected since the tension gives more stiffness to the strip

to endure more compressive stress in its plane. Figure 4.12 shows that when tension increases, the deflection function is wider in the center and is tighter and localized more towards the edge, until reaching a certain tension value (14 MPa in this case). Once the tension exceeds this value, the deflection function is equal to zero which means the strip stays flat and the amplitude will most definitely be equal to zero. This is represented in Figures 4.13. Both the amplitude and the wavelength decrease until reaching zero with an increasing tension. Once again this is logical since tension gives stiffness to the strip and beyond a certain value the strip is unable to buckle. This value corresponds to the zero-amplitude, the zero-wavelength and the zero-deflection function which is equal to 16 MPa. This means that since $\sigma_x^{res} \in [-19, +9.5]$ when the tension $T_0 = 16$ MPa is added, the stress interval is $[-3, +25]$ and these kinds of compressive stresses are not capable of generating waviness.

Figure 4.14 confirms that increasing tension produces tighter and smaller waves. A side view illustrating the buckling strip under tensions of 2 MPa and 12 MPa shows smaller wavelengths i.e. more but tighter waves in the length of the strip..

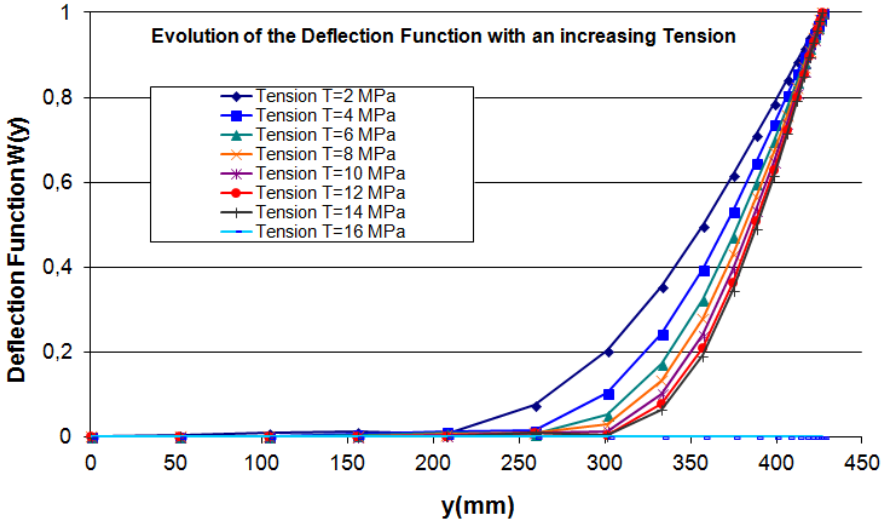

Figure 4.12: The effect of increasing tension on the deflection function. Half of the deflection function is presented in the graph according to the axis of symmetry $y = 0$.

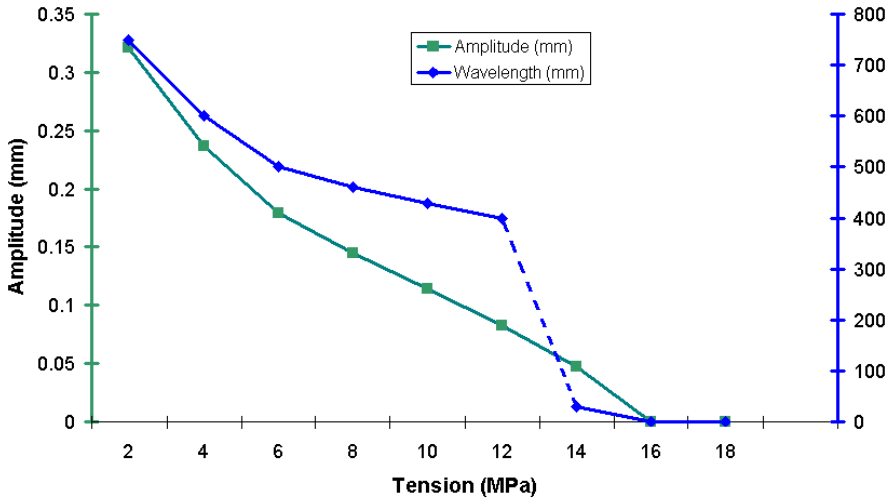

Figure 4.13: The evolution of the waves amplitude and wavelength with changing strip tension.

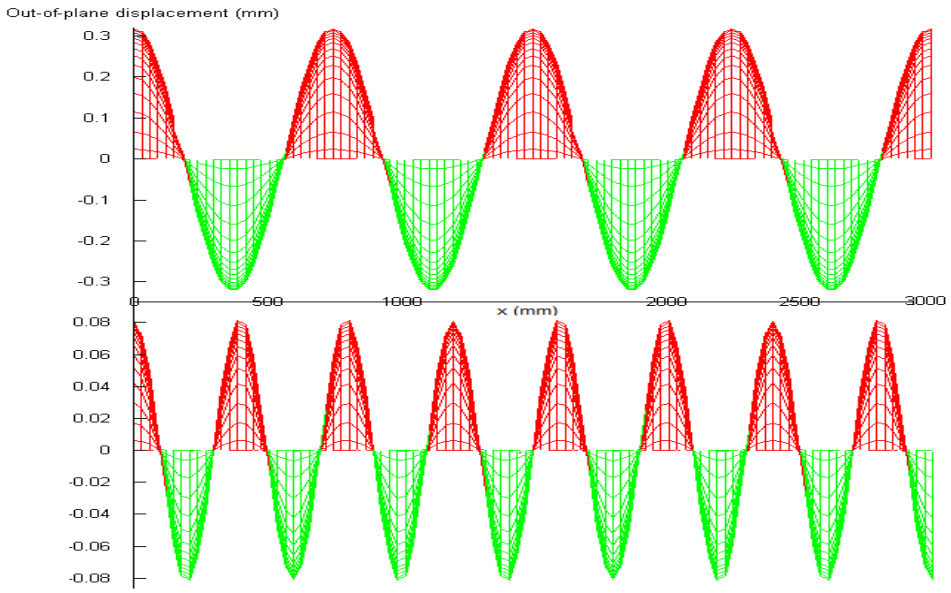

Figure 4.14: A side view for the buckling plate 1) under a tension of 2 MPa, 2) under a tension of 12 MPa

4.6.4 Compression zone and the buckling mode/amplitude

Now that the effects of the strip tension on the on-line flatness have been studied, a new component can be investigated which is the width of the compression zone on the

mode and the amplitude of the defects. To examine its effects, all the other parameters are fixed; the strip is under a tension of 5 MPa and has the same dimensions and characteristics as the one used in section 4.6. Only the compressive zone is adaptable and it is determined by changing the residual stress profile. That is why, the following cosine stress distribution is used:

$$\sigma_x^{res}(y) = -20cos^m(\frac{\pi y}{l} + 5) \tag{4.79}$$

in which the parameter m is the key to controlling the width of the zone under compressive stress. As shown in Figure 4.15, the stress minimum -15 MPa and maximum 5 MPa are the same for the five different profiles (for $m = 1, 2, 3, 4, 5$) and the compressive zone is modified by changing the parameter m. The larger the parameter m is, the smaller the width of the compressive zone. Note that these profiles do not have the same resultant.

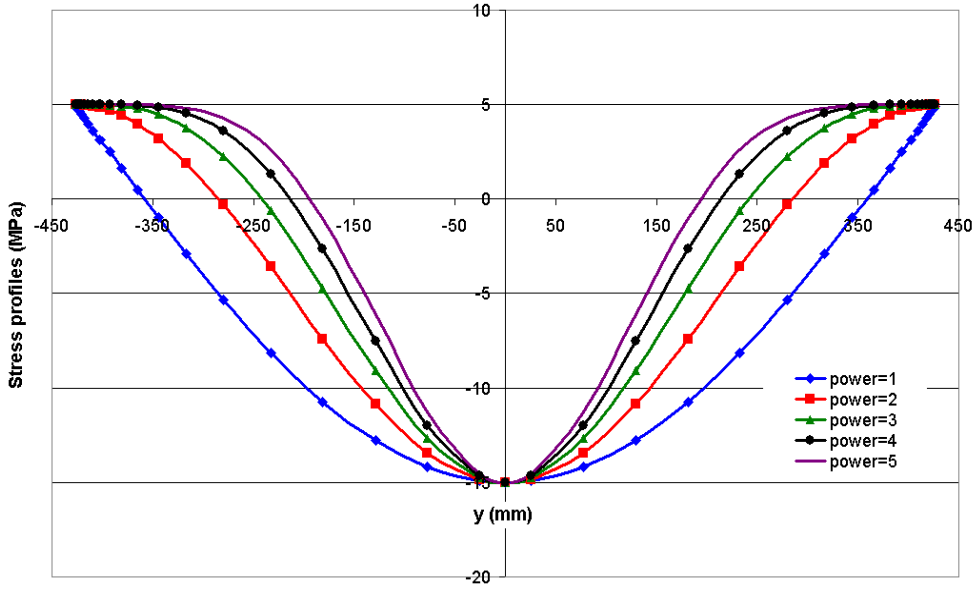

Figure 4.15: The different residual stress distributions obtained for $m = 1, 2, 3, 4, 5$

Since the compression zone is located in the center, a wavy center is expected, if the stresses exceed the critical value. This was already established in the previous section. The aim is to qualify the effect of its width on the defect shape.
Table 4.2 and Figures 4.16 to 4.19 illustrate and summarize the most important effects of changing the width of the compression zone.
Table 4.2 and Figure 4.16 show that the wider the compression zone (m smaller), the greater the defective zone gets. In the same manner, Figure 4.17 shows that when the compression zone is narrower, not only the defective zone gets smaller but the wavelength does as well. This means that the number of waves increases when the defective zone is narrower (confirmed in Figure 4.18). It seems logical that when the wavelength decreases,

the wave amplitude does the same to reach zero when the wavelength is in the vicinity of zero. This is indeed established in Figure 4.18: the parameter m increases, the compression zone width decreases; hence the wavelength decreases and the number of waves increases and simply the waves amplitude decreases gradually to hit zero.
In addition, it is noticeable that the defective zone half-width and the wavelength are proportional where $\frac{\text{wavelength}}{\text{Defect width}} \sim 2.5$. Note that the defect zone width and the compression zone width can be related also via the ratio $\frac{\text{compression width}}{\text{Defect width}} \sim 2$.

m	Compressive zone (mm)	Defective zone (mm)	Wavelength (mm)	wave number	amplitude (mm)
1	360	180	461.538	6.5	0.146
2	280	160	375.00	8	0.108
2	235	140	352.941	8.5	0.0959
4	215	135	333.33	9	0.0856
5	185	120	315.789	9.5	0.0708

Table 4.2: The effect of changing the parameter m i.e. compression zone width on the defect shape and amplitude. Dimensions given for the strip half-width (see Figures 4.15 and 4.16)

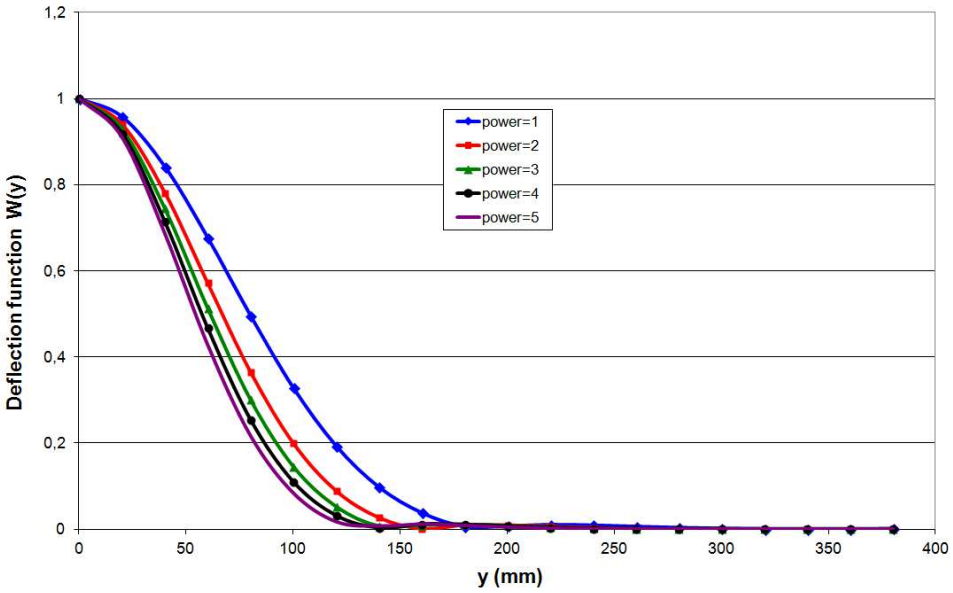

Figure 4.16: The evolution of the deflection function i.e. the defect shape and the defected zone for $m = 1, 2, 3, 4, 5$
The curves are plotted on the strip half-width according to the symmetry axis $y = 0$.

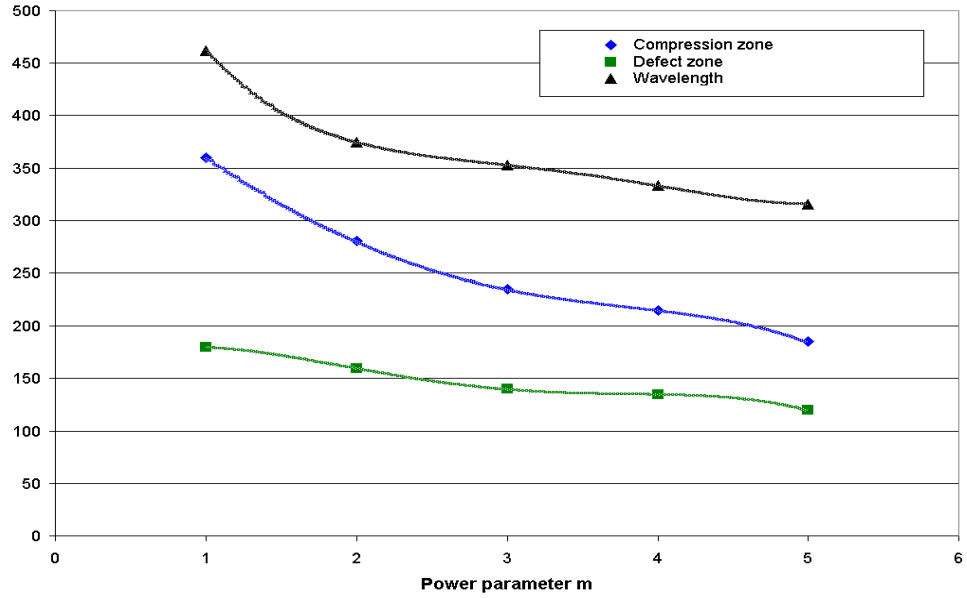

Figure 4.17: Evolution of the compression zone width, the defected zone width and the defect wavelength with the power parameter m.

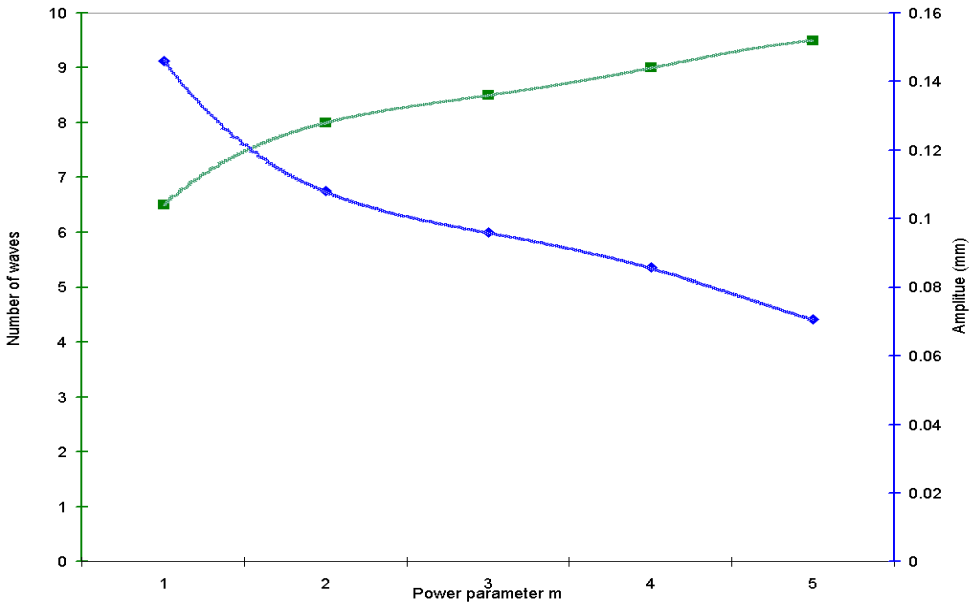

Figure 4.18: Evolution of the defect amplitude and wave number with the power parameter m i.e. the compression zone width.

Finally, the form of the defective plates presenting center buckles are illustrated in Figure 4.19 for $m = 1$ and $m = 5$ respectively. It is clear that the number of waves is higher for $m = 5$, the defected zone is smaller and the amplitude of the undulations is smaller.

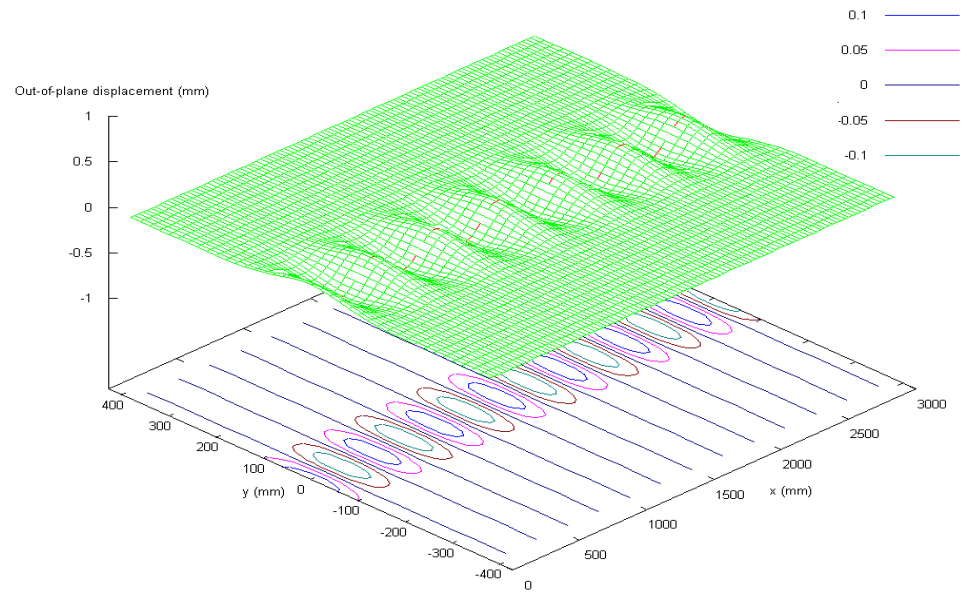

(a)

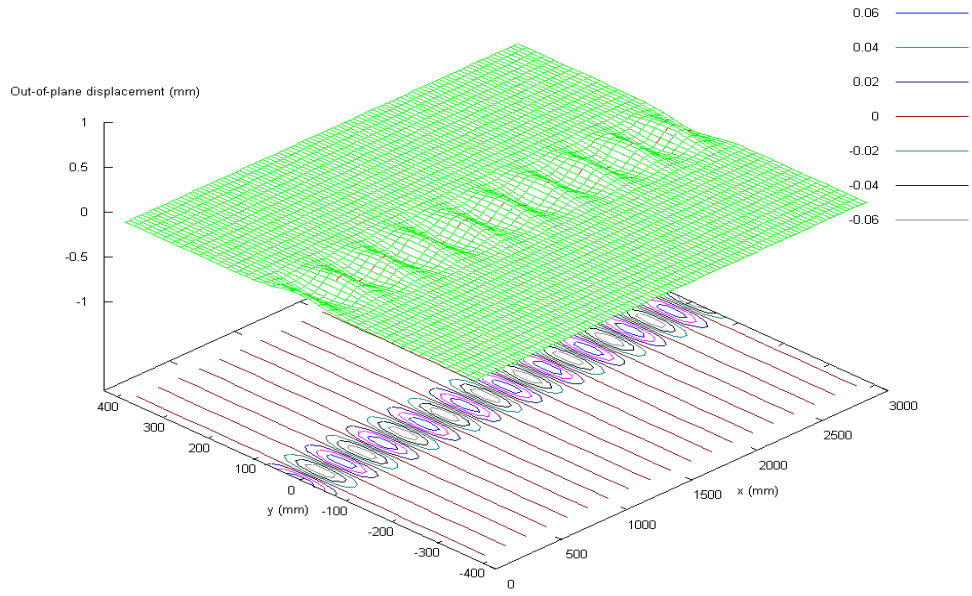

(b)

Figure 4.19: (a) : the defective plate under residual stress distribution for $m = 1$. (b) : the defective plate under residual stress distribution for $m = 5$.

4.7 Numerical results: Quantitative validation

In this section, the results and capacity of the **MSBM** are confronted to other available studies. The first one is the analytical study introduced in [Fisher et al., 2001, Fisher et al., 2003]. It is capable of predicting the buckling mode and load and it is a good means to validate the first part of the **MSBM**.

The second one is an Abaqus simulation capable of providing both the buckling load and

amplitude. The third is a simple buckling problem using the shell model **MAN** which can also provide the buckling amplitude. The last two present the advantage to compare the computed amplitude and thus validate the second part of our **MSBM**.

4.7.1 Buckling Validation via semi-analytical solutions

The same sheet used to illustrate the results in section 4.6 will be used through this study: A steel sheet ($E = 210$ GPa, $\nu = 0.3$) of length $L = 3000$ mm, width $l = 855$ mm and thickness $h = 0.25$ mm. For the sake of this comparison, the same residual stress fields as in [Fisher et al., 2001, Fisher et al., 2003] are adopted for easy quantitative comparison: $\sigma_x^{res}(y) = -6\left|\frac{y}{l}\right|^2 + \frac{1}{2}$ and $\sigma_y^{res}(y) = \sigma_{xy}^{res}(y) = 0$. Please refer to section 2.3.1.2 for a better understanding on how the analytical values where established in [Fisher et al., 2001, Fisher et al., 2003]. Strip tension is the parameter of the study, varying from 20 to 100 MPa; a series of computations (Table 4.3) were carried out i) describing on the one hand the evolution of the critical stress σ_{cr} and the buckled wavelength $\tilde{l}$ with varying tension and ii) comparing on the other hand the numerical values computed using the **MSBM** with the semi-analytical ones found in [Fisher et al., 2001, Fisher et al., 2003].

Table 4.3 and Figure 4.20 describe how the critical stress σ_{cr} and the buckled wavelength $\tilde{l}$ vary with tension. $|\sigma_{cr}|$ increases linearly as expected, since an increased tension makes the sheet stiffer and more resilient to in-plane compression. Moreover, the wavelength $\tilde{l}$ decreases. This means that the compressive stresses on the edge at buckling exceed T_0 by a roughly proportional value: $-\sigma_{cr} \sim (1+k)T_0$; $k \sim 0.22$.

	Semi-analytical Method			Buckling Model **MSBM**		
Tension T_0 (MPa)	Critical stress σ_{cr} (MPa)	$\sigma_{cr}+T_0$	Wavelength $\tilde{l}$ (mm)	Critical stress σ_{cr} (MPa)	$\sigma_{cr}+T_0$	Wavelength $\tilde{l}$ (mm)
20	-26.47	-6.47	383.54	-24.57	-4.57	352.94
40	-50.08	-10.08	298.38	-47.03	-7.03	285.71
60	-73.10	-13.10	244.16	-69.06	-9.06	250
80	-95.77	-15.77	223.82	-90.86	-10.86	222.22
100	-118.24	-18.24	206.6	-112.5	-12.5	206.89

Table 4.3: The evolution of the critical stress and wavelength with the strip tension. Results obtained using a semi-analytical method [Fisher et al., 2001, Fisher et al., 2003] on the left and the Finite Elements **MSBM** on the right.

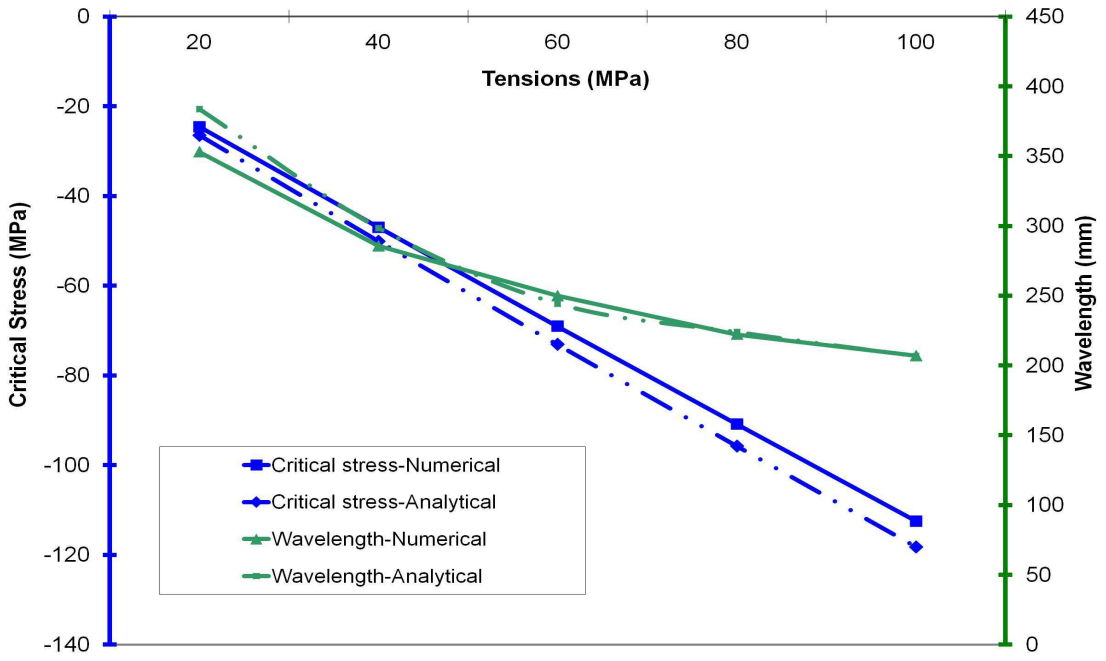

Figure 4.20: Stress σ_{cr} and wavelength $\tilde{l}$ versus growing strip tension stress. Comparison between the semi-analytical values (dashed line) found in [Fisher et al., 2001, Fisher et al., 2003] and the numerical ones (Solid line) computed in the **MSBM**.

Table 4.3 and Figure 4.20 prove a good agreement between the results of the present model and the analytical results of [Fisher et al., 2001, Fisher et al., 2003].

4.7.2 Post-Buckling Validation via the shell elements model MAN

Once again, the same sheet is used to compare the post-buckling results especially the amplitude of the defects. The sheet is doubly loaded by the strip tension $T_0 = 2$ MPa and the residual stress profile $\sigma_x^{res}(y) = 19.\left(-6\left|\frac{y}{l}\right|^2 + \frac{1}{2}\right)$, compressive along the edges. The buckling problem is treated using two different models: the shell buckling model **MAN** and our Finite Element **MSBM**. The results are presented in Figure 4.21. Note that i) the symmetry of the solution is forced in both models **MAN** and **MSBM** i.e. the buckling/post-buckling problems are studied on half the domain $\left[0, \frac{l}{2}\right]$ and extended using the symmetry axis $y = 0$.

ii) The upstream boundary conditions are different: for **MAN** it is clamped, whereas for the **MSBM** it is left free. This causes the symmetry loss in **MAN** as illustrated in Figure 4.21a).

Because in **MAN**, it is necessary to have the upstream boundary clamped or simply supported to insure the existence of the solution, it comes down to comparing these two similar yet not identical problems.

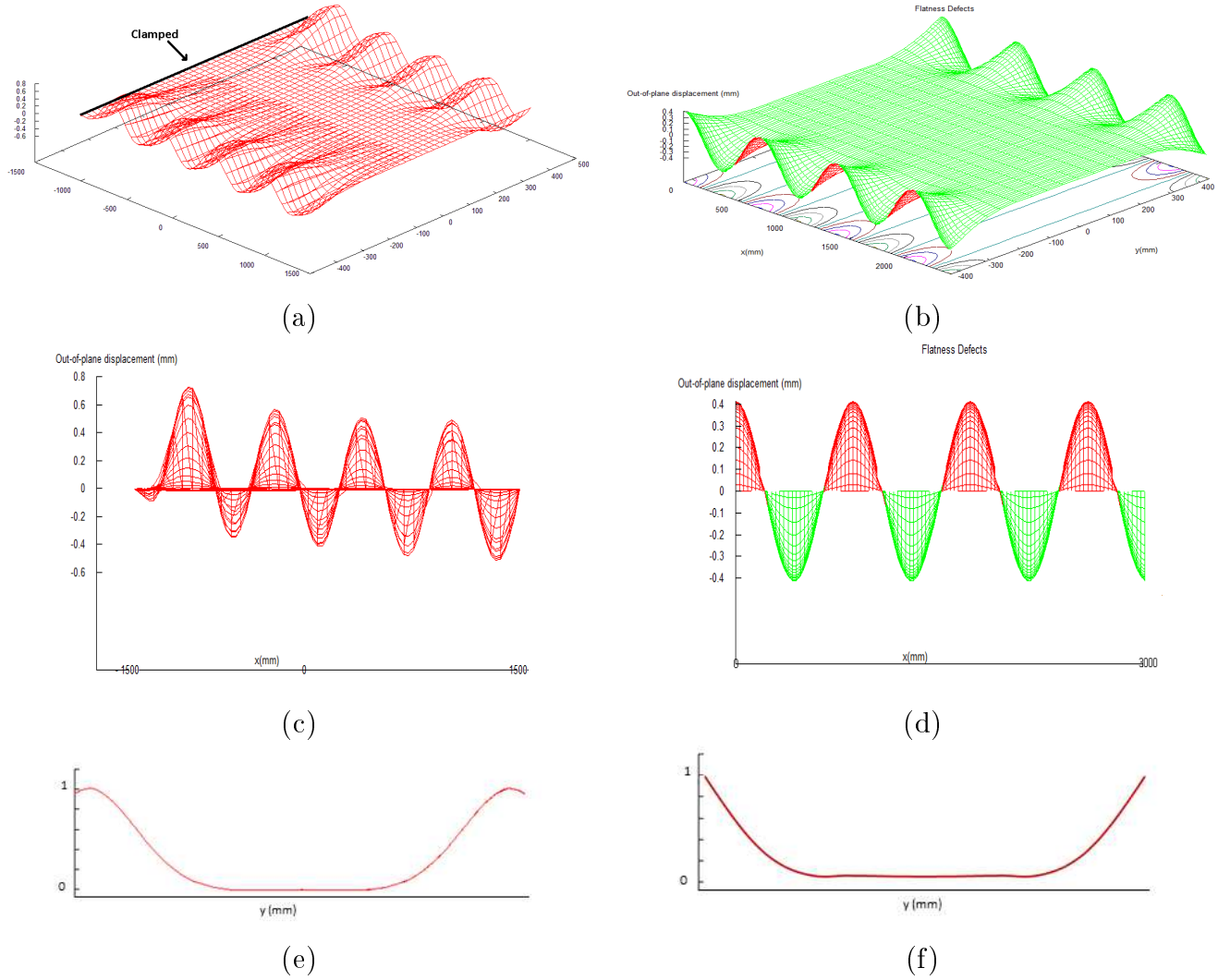

Figure 4.21: (a) & (c) : the defected plate and its side-view obtained by the shell model **MAN**
(b) & (d) : the defected plate and its side-view obtained by **MSBM**
(e) & (f): the deflection form plotted in a transverse section using **MAN** & **MSBM**

As expected, the defected plate presents wavy edges in both models. In addition, the buckling form seems similar (Figure 4.21 (a) & (b)) yet there is a slight change noticed in (Figure 4.21 (e) & (f)); the plate buckles into approximately $4 \sim 5$ waves in 3000 mm. When side-views are compared (Figure 4.21 (c) & (d)), one can confirm that the computed waves amplitudes under strip tension have the same order: for the shell model **MAN** the magnitude is equal to 0.46 mm in the stabilized zone and for the finite element buckling model it is equal to 0.4 mm.

4.7.3 Validation via a simple Abaqus example

Let us take the simplest buckling problem of a square simply supported plate of dimension $[l \times L \times h] = [100mm \times 100mm \times 1mm]$. Young's modulus E is equal to 200 GPa and Poisson's coefficient ν is equal to 0.3.
The plate is subjected to an homogeneous compressive stress σ_x^{res} equal to

$$-\mathbb{D}\left(\frac{\pi}{l}\right)^2\left(\frac{l}{L}+\frac{L}{l}\right)^2 = -\frac{Eh^3}{(1-\nu^2)}\left(\frac{\pi}{l}\right)^2\left(\frac{l}{L}+\frac{L}{l}\right)^2 \text{ and } \sigma_y^{res} = 0$$

in which $\mathbb{D}$ is the plate rigidity, L, l and h are respectively the length, the width and the thickness of the plate. Note that this is the form of the critical stress determined by Timoshenko i.e. λ_{cr} should be equal to 1.
In Abaqus, it is impossible to enter a residual stress field, therefore this stress distribution is used as an initial lateral loading which leads to non-uniform stress distribution in the strip (mainly in the strip center).
To determine the buckling load under this particular stress distribution, σ_x^{res} is multiplied by a loading parameter λ. Using our Finite Elements buckling model, the loading parameter λ_{cr} is equal to 0.98; which gives us the critical stress $\sigma_{cr} = -72.30$ MPa. The corresponding mode is described in Figure 4.22, a cut in the transversal direction shows the form of the out-of-plane displacement which clearly predicts a buckling center.

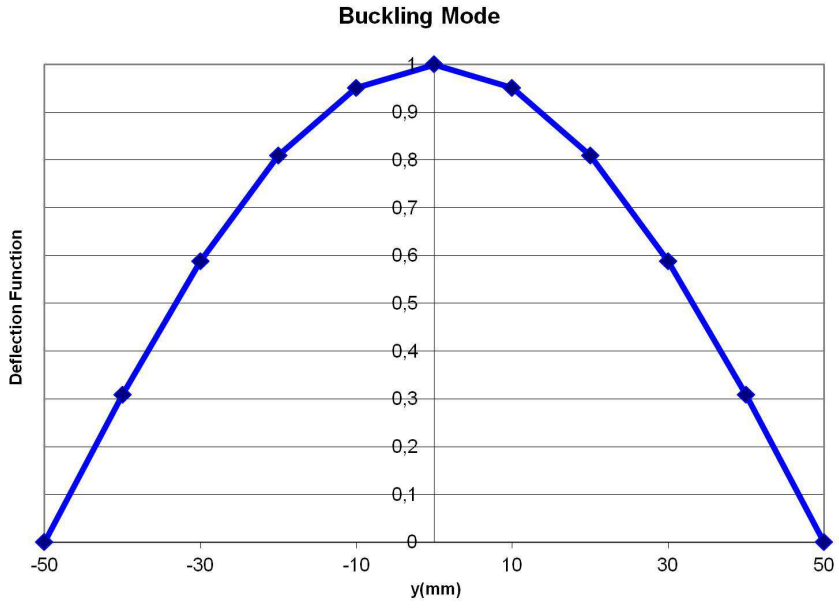

Figure 4.22: The deflection shape viewed according to a transversal cut predicting a buckling center, which means that waviness will definitely appear in the center under this loading and these boundary conditions.

This is totally expected since the edges are simply supported i.e. $w = 0$. Thus, the plate will most definitely deflect in the center under compressive stress as confirmed in Figure 4.22. On the other hand, a simulation using Abaqus, the critical loading was determined equal to $-71.29\ MPa$ ($\lambda_{cr} = 0.96$). This comparison confirms the precision of the used buckling analysis to predict the buckling mode.
Let us proceed to the post-buckling part, and compare the computed amplitudes of the defects using both Abaqus and our buckling model **MSBM**. For this purpose, a series of simulations describing the evolution of the defect amplitude with the applied load λ was carried out. Table 4.4 represents the results obtained for both Abaqus and **MSBM** simulations. This comparison confirms that both models behave similarly, they detect the same defects and the computed amplitudes are comparable. Note that the difference of 20% for particular cases could be explained either by the simplifications in **MSBM** or by the different ways used to apply the stress σ_x^{res} in the respective models:

- In **MSBM**, it is applied as residual stresses uniform all over the strip.
- In Abaqus, it is applied as lateral loading which creates non-uniform stress distribution in the strip.

Abaqus Software			Buckling Model **MSBM**		
λ/λ_{cr}	$\lambda\sigma_{cr}(MPa)$	Amplitude (mm)	λ/λ_{cr}	$\lambda\sigma_{cr}(MPa)$	Amplitude (mm)
1.1	-78.42	0.63	1.1	-79.53	0.81
1.2	-85.55	0.91	1.2	-86.76	1.15
1.3	-92.68	1.13	1.3	-93.99	1.41
1.4	-99.80	1.31	1.4	-101.2	1.63
1.5	-106.94	1.47	1.5	-108.45	1.82
1.6	-114.06	1.62	1.6	-115.686	1.99
1.7	-121.19	1.76	1.7	-115.68	2.15
1.8	-128.32	1.88	1.8	-130.14	2.30
1.9	-135.45	2	1.9	-137.37	2.44
2	-142.58	2.13	2	-144.6	2.57

Table 4.4: The evolution of the defect amplitude with the loading parameter λ. Results obtained using Abaqus Software on the left and the Finite elements Buckling Model on the right.

Finally, Figure 4.23 and 4.24 present respectively in **MSBM** and Abaqus the form of the buckling plate under the applied loading (for $\lambda = 1.1\lambda_{cr}$) as well as a side-view to give a

better idea of the defect amplitude.

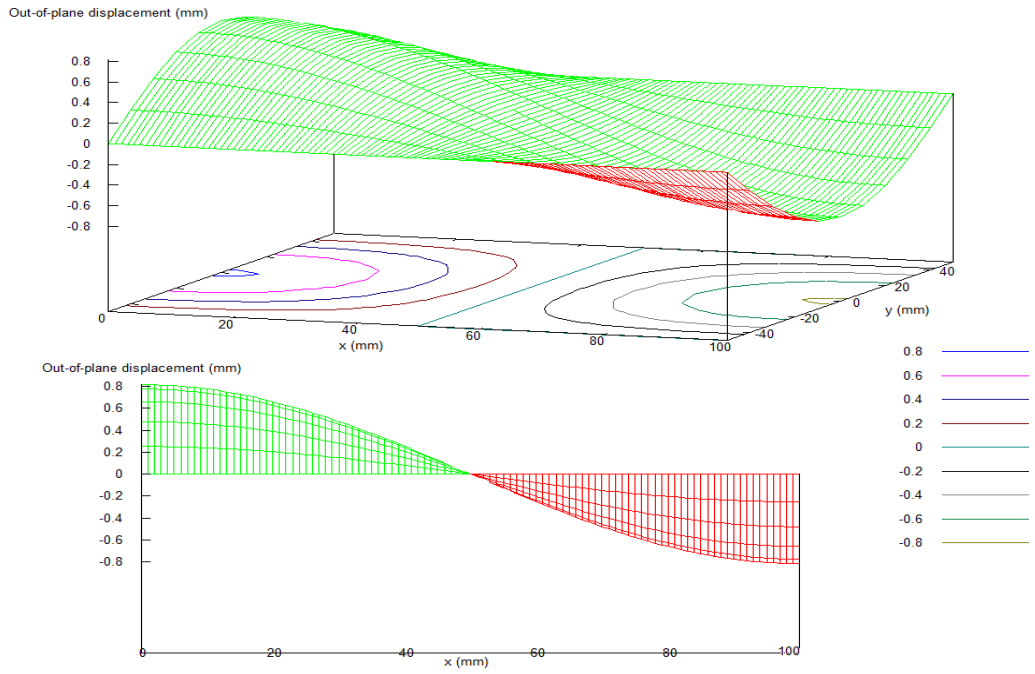

Figure 4.23: The defect form computed by the Buckling Model for $\lambda = 1.1\lambda_{cr}$ with an amplitude of 0.81 mm.

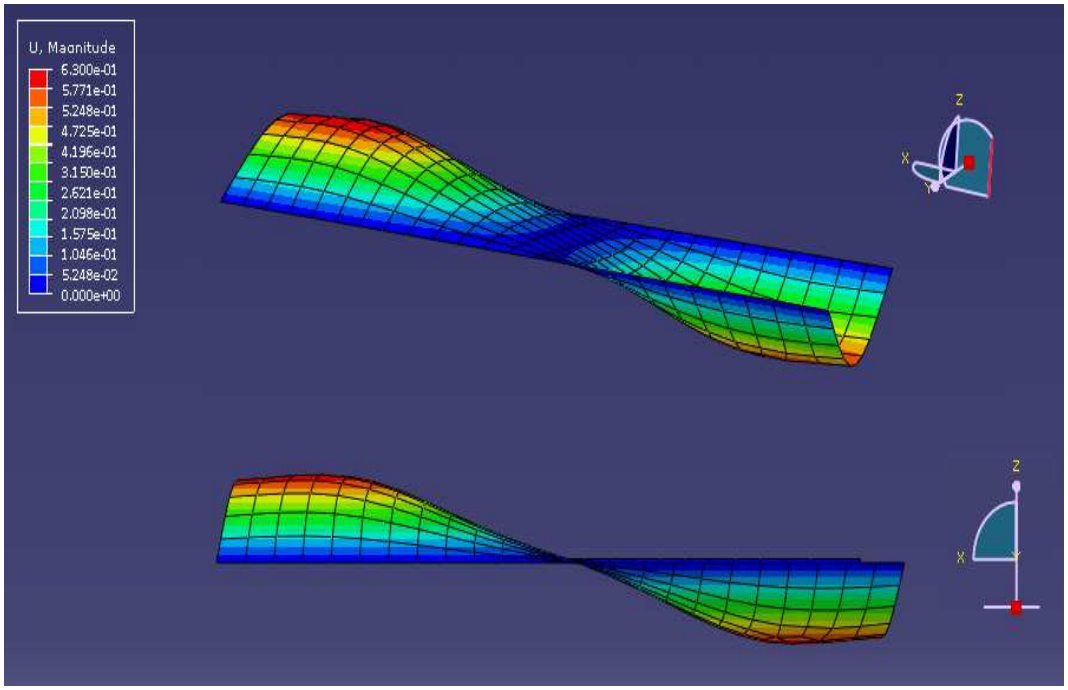

Figure 4.24: The defect form computed by Abaqus for $\lambda = 1.1\lambda_{cr}$ with an amplitude of 0.63 mm.

4.8 Discussions

4.8.1 Buckling criterion

Through the last two chapters, we mentioned several time the 'Buckling criterion' terminology. It means that the stress distribution in the strip should respect a certain critical value/profile if the stress is homogeneous/heterogeneous. Not all researchers agree on how this criterion should be applied. Some propose that one value should be respected globally (generally equal to zero), while others suggest that the value can be respected locally.

For instance, Counhaye in his work [Counhaye, 2000], defined a unique critical value (typical Timoshenko form) for the whole strip and forced it to be respected at every point of the strip. This is only valid for a homogeneous stress distribution contradicting what is used in his study (a heterogeneous distribution). Abdelkhalek in his simple buckling model, tried to do the same but, as shown in his thesis [Abdelkhalek, 2010], it was not respected globally.

Another example is the one presented in [Abdelkhalek, 2010] using the shell buckling model **MAN**. A strip with the following dimensions and characteristics -length of 500 mm, width of 100 mm, thickness of 1 mm, $E = 200$ GPa and $\mu = 0.3$ - is subjected to the residual stress transverse profile illustrated in Figure 4.25.

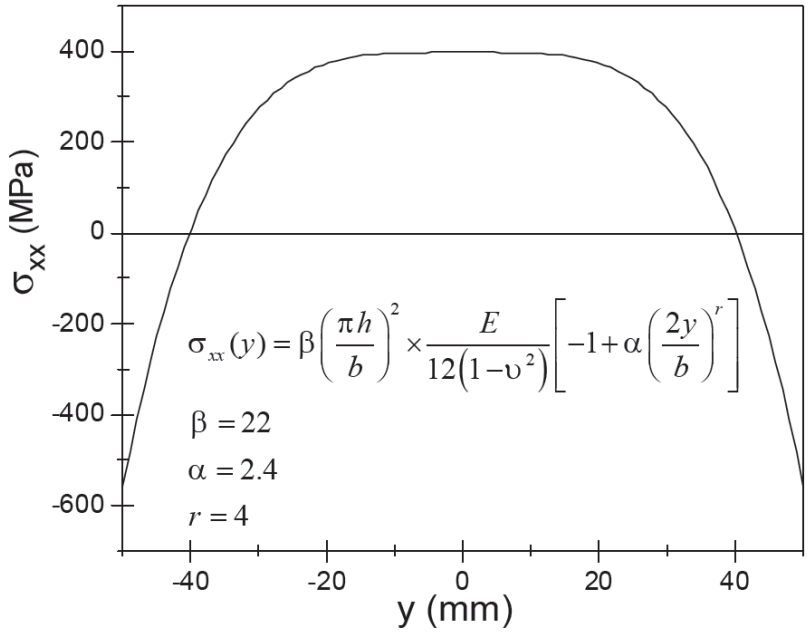

Figure 4.25: Transverse residual stress profile σ_x.

The stress tolerated by the strip under the residual stress distribution and a strip tension

of 150 MPa is approximately equal to −400 MPa on the edges. The defective strip before and after strip tension release are presented in Figure 4.26. Inspecting the stress maps post-buckling (before and after tension release), we notice that buckling did not relax the compressive stresses uniformly all over the strip.

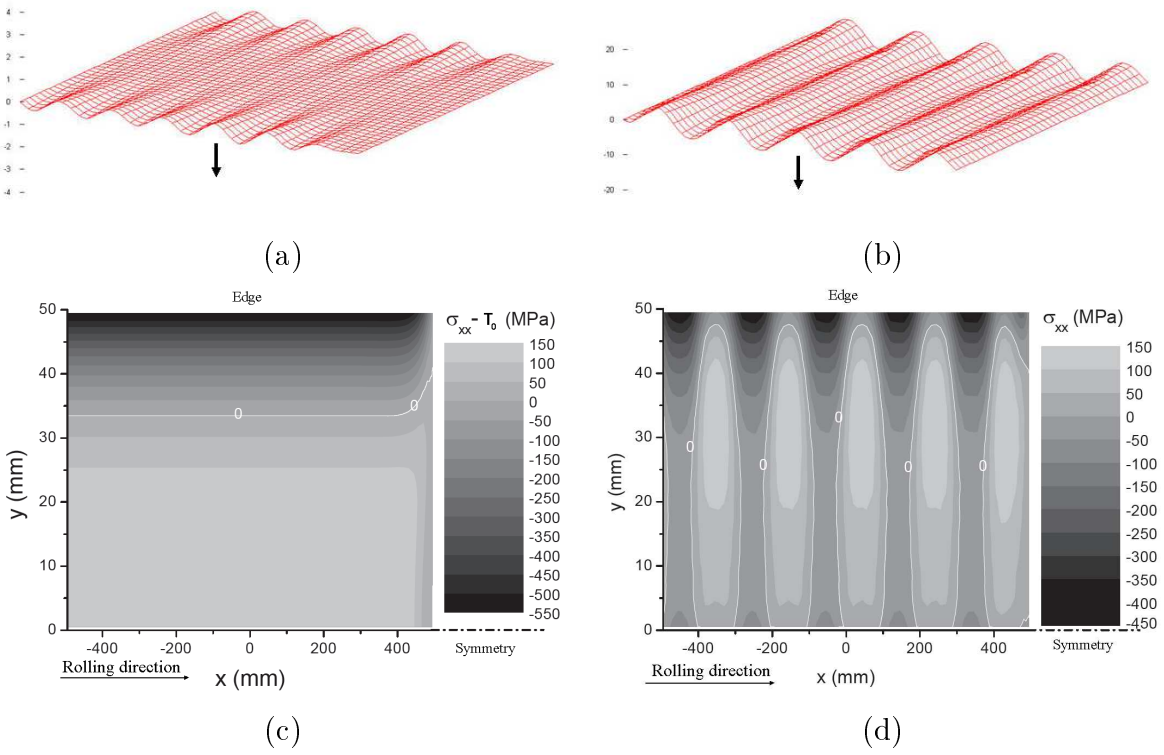

Figure 4.26: Buckling strip: (a) under strip tension $T_0 = 150$ MPa, (b) after strip tension release.
Stress redistribution σ_x due to buckling: (c) under strip tension $T_0 = 150$ MPa, (d) after strip tension release.

In our research, the value tolerated by the strip was determined locally: on the edge or center depending on the compressive zone position (see Remark 2 page 72). If the critical value is reached, waviness appears and the stress in the defective zone is relaxed to respect locally the critical stress. Figures 4.7b) and 4.10b) confirm that though this criterion is respected locally, it does not mean that compressive stresses are forbidden.
We cannot confirm which one is the more appropriate way to apply this concept but one can suggest that it may be excessive to impose "no compressive stress" all over the strip.

4.8.2 Conclusion

Combined with von Kármán equations, a multi-scale approach is the basis of a buckling model capable of describing strip buckling and post-buckling under residual stress. It is capable of determining the buckling load and mode, describing the form of the defect and quantifying it. In addition, new stress distribution due to buckling occurrence is generated.
The buckling model was tested with different academic stress profiles illustrating both wavy edges and center buckles. Note that, the choices and simplifications made in this chapter enable us to predict only undulations developing in the rolling direction. The impact of these simplifications will be discussed in the last chapter.
To assess the abilities of this buckling model, it was subjected to different studies such as:

- The effect of changing tension on the flatness defect.
- The effect of the compression zone width on the form of the defect.

The buckling model gave good results describing flatness defects with very reasonable/logical tendencies depicting their evolution with these different parameters.
In addition, the multi-scale buckling model was confronted to other studies/models available in the literature such as:

- The semi-analytic study by Fisher et al. [Fisher et al., 2001].
- The shell buckling model **MAN** [Abdelkhalek et al., 2008].
- The shell software Abaqus [Abaqus, 2008].

The results were found satisfactory and showed good agreement.
Overall the buckling model behavior was found performant in academic cases, its capacity will be tested in chapter 5 for more complex and stiffer profiles (imported from rolling software) and in chapter 6 when implemented in the rolling software Lam3/Tec3.

4.9 Résumé en Français

Dans ce chapitre, une approche muti-échelle a été combinée avec les équations de von Kármán pour présenter un modèle de flambage/post-flambage des tôles minces sous contraintes résiduelles. Il est nommé **MSBM**. Il est capable de déterminer la charge critique, décrire la forme du défaut (le mode de flambage) et quantifier l'amplitude

des ondulations. En plus, une nouvelle distribution de contraintes est générée en post-flambage.

MSBM a été testé en utilisant différents profils de contraintes académiques (paraboliques) illustrant des bords et centres longs. Notez que les choix et les simplifications imposés dans ce chapitre nous permettent de modéliser seulement des ondulations se développant dans le sens du laminage. Les effets de ces simplications seront discutés dans le dernier chapitre.

Pour évaluer les capacités de **MSBM**, différentes études ont été réalisées, telles que les effets de la traction et de la largeur de la zone en compression sur la forme des défauts de planéité. Le modèle a donné de bons résultats, décrivant les défauts de forme avec des tendances très raisonnables. **MSBM** a été aussi confronté à d'autres études/modèles disponibles dans la littérature comme le modèle semi-analytique de Fisher et al. [Fisher et al., 2001], le modèle de flambage (élément finis coques) **MAN** [Abdelkhalek et al., 2008] et le logiciel Abaqus [Abaqus, 2008]. Les résultats sont en bon accord.

En général le modèle de flambage **MSBM** a été trouvé performant pour les cas académiques traités. Sa capacité sera testée dans le chapitre 5 pour des profils plus complexes importés d'un calcul de laminage et dans le chapitre 6 une fois couplé avec le logiciel de laminage Lam3/Tec3.

CHAPTER 5

UNCOUPLED ROLLING-BUCKLING MODEL

Believe in yourself! Have faith in your abilities! Without a humble but reasonable confidence in your own powers you cannot be successful or happy.
by Norman Vincent Peale

Contents

In the previous chapter, the Multi-Scale Buckling Model (**MSBM**) was presented. Several academic examples illustrating buckling strips under residual stress and strip tension were studied and compared with powerful codes like **MAN** and Abaqus.
In the present one, the same Buckling Model will be explored to predict flatness defects during real rolling operation, i.e. using complex stress profiles supplied by a rolling software Lam3/Tec3. In other words, the buckling and rolling problems will be treated in a decoupled manner:

1) First, a rolling simulation is accomplished using Lam3/Tec3, without taking into account buckling problems, providing residual stress distribution out of the bite zone. Note that these profiles include as well the applied strip tension contribution.

2) These output fields of residual stresses are used as loads in the **MSBM** predicting the critical load, the buckling mode and the state of the strip post-buckling including a new repartition of stress.
Note that the imported stress profiles are extracted far from the bite exit ($\sim$ 1 m) where they are perfectly stabilized.

Why use a decoupled approach ?

As a first attempt to predict flatness defects for real rolling operation, it seems reasonable to study the capacity of the **MSBM** before any coupling. Since decoupled approaches are used in literature (specially for cases presenting minimal to no bite-buckling interactions) this gives us an asset to compare our results to these available approaches (like the comparison presented in chapter 4). In addition, as mentioned by Abdelkhalek in his thesis [Abdelkhalek, 2010], simulations using coupled approaches to treat the rolling and buckling problems (such as the one presented in chapter 5) consume more computational time; thus, the necessity to provide the industrial partners with two assets: one standalone buckling model **MSBM** and one coupled rolling-buckling model Lam3/Tec3-**MSBM**.

Having explained the motivation behind this study, this chapter will be divided into two main parts. The first is dedicated to flatness defects prediction for the rolling operation described in page 79. The second describes the evolution of the defect shape while changing important parameters in rolling operations, such as friction and the work roll bending force (WRB). Since a similar study was accomplished using the software Lam3/Tec3-Abdelkhalek (presented in chapter 3), we take advantage to compare qualitatively the defect prediction offered by each one of those models.

In this chapter, all transverse profiles are plotted only for $y > 0$ by symmetry.

5.1 On-line Flatness prediction using the decoupled approach Lam3/Tec3-MSBM

Once again the same rolling operation presented on page 79 is used. It is simulated using the rolling software Lam3/Tec3 and the transverse residual stress profile illustrated in Figure 5.1a) is recovered.
In the **MSBM**, the exiting strip is defined to have a thickness of 0.252 mm, a width of 855 mm and a length of 3000 mm. It is under a strip tension of 100 MPa and loaded by the recovered residual stress profile. The same elastic characteristics used in the rolling software are chosen as well: Young's modulus E is equal to 210 GPa and Poisson's coefficient ν is equal to 0.3.

For this particular profile, the loading parameter λ_{cr} is computed equal to 0.26; this means that the strip can support -226 MPa of residual stress on the edges under 100 MPa of strip tension . Having exceeded this threshold on the edges, Figure 5.1b) -illustrating the deflection form of the strip per transverse section-, confirms the occurrence of a defect on the strip edges.

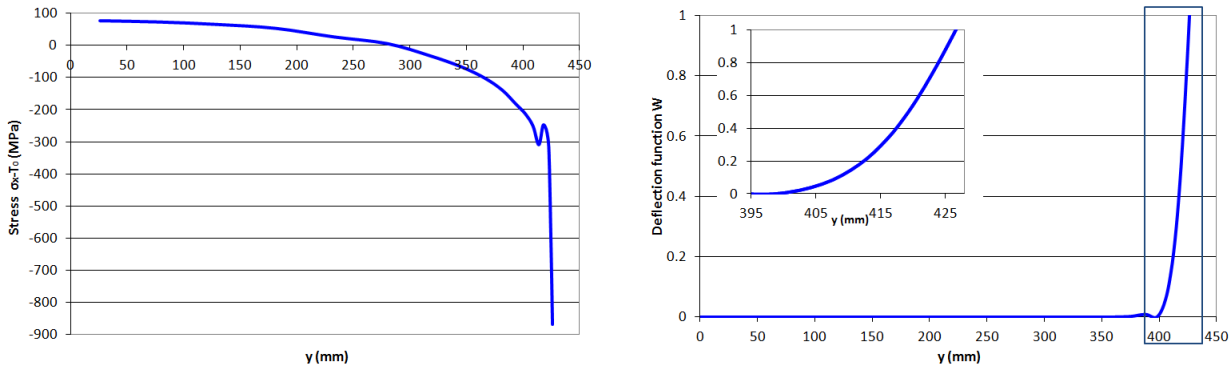

(a) (b)

Figure 5.1: (a) The transverse residual stress profile before buckling plotted on a section at 1 m after bite exit. (b) The transverse deflection function mapping the defect shape.

The shape of the defective strip is presented in Figure 5.2 showing wavy edges where

the undulations are tight and very local. Note that the 3D strip is plotted using the amplitude a, the mode W and the half-wave number q as $Re[a.W(y).e^{iqx}]$. Thus, if the defects amplitude does not seem homogeneous all over the strip, it is because of the coarse meshing used to illustrate the 3D function.

- Judging by the deflection form W (Figure 5.1b)), the depth of the defect is approximately 28 mm. It can be directly connected to the zone width under compression. In this case, when adding the strip tension 100 MPa, the compressive zone width is approximately 61 mm, roughly double the defect zone width.
- The wave-length is 90 mm (35 waves in this 3000 mm long strip).
- The amplitude of the defect is $a = 0.2$ mm.

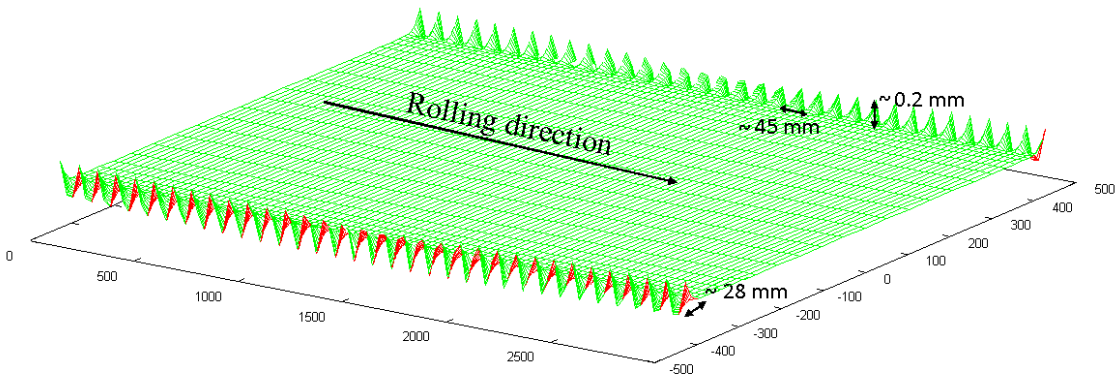

Figure 5.2: The defective strip under a strip tension of 100 MPa and a residual stress profile imported from a rolling operation. ($\mu = 0.025$, $WRB = 480$ KN)

The **MSBM** - even decoupled- is able to predict flatness defects for more complex stress profiles (very large gradient near the edge) like the one imported from a real rolling operation presented above. We now push this study forward predicting flatness defects evolution with different actuators and parameters: friction and work roll bending. This is identical to the study presented in chapter 3 using the rolling-buckling model Lam3/Tec3-Abdelkhalek. The aim is to compare qualitatively the results, qualitatively because Abdelkhalek's model cannot predict shapes and amplitudes.

5.2 Flatness and Friction

To study the effect of changing friction on the flatness defect of thin strips, the rolling operation detailed in page 79 has been modeled using coefficients of friction between

0.01 and 0.03. The stress profiles, corresponding to the different friction coefficients, are imported on a transverse section from the rolling software Lam3/Tec3, (Figure 5.3). We notice that when friction increases, the compressive stress on the edges increases as well. It is expected since more friction means higher load, more roll bending and more edge reduction hence more compressive residual stresses. In addition, it is clear that the width of the compressive zone increases when friction increases. Do not forget adding the contribution of the strip tension 100 MPa to the stress profiles. Thus, from the previous section, it can be expected that the defects depth on the edges will be larger for higher friction. Note that for the smallest chosen coefficient friction $\mu = 0.01$, the compressive stress is migrated from the edge to the center. If sufficient, it can cause center buckles off-line. However, the compression in the center does not surpass -100 MPa so when adding the strip tension 100 MPa, no compression shall be visible i.e an on-line defect is not expected.

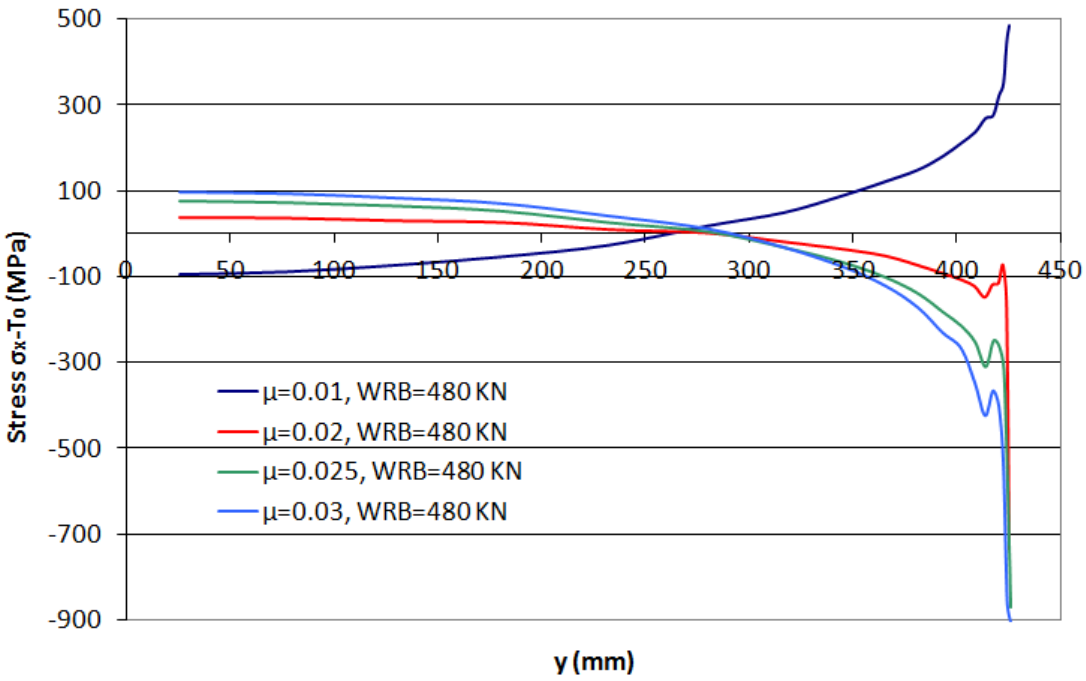

Figure 5.3: The different stress profiles corresponding to WRB= 480 KN and varying friction. Profiles are recovered ~ 1 m downstream of the bite.

Examining Figure 5.4a), the deflection form and the profile of the computed additional strain confirm what has been discussed earlier. For the smallest friction coefficient $\mu = 0.01$, the MSBM does not detect any defect when the strip is under 100 MPa of tension, hence the flat corresponding curve. In addition, when friction increases it is noticed that the defect depth increases and the buckling strain increases as well. It means that it

is expected to find higher amplitudes under higher friction.
Comparing the results with the ones found using Lam3/Tec3-Abdelkhalek, Figure 5.4b) confirms that both models find qualitatively the same defective zone. Moreover, they evolve in the same manner. When friction increases the defective zone is wider and the additional strain is larger as well. It is reassuring that these two models, though based on different assumptions, can give similar results from the defect detection point of view.

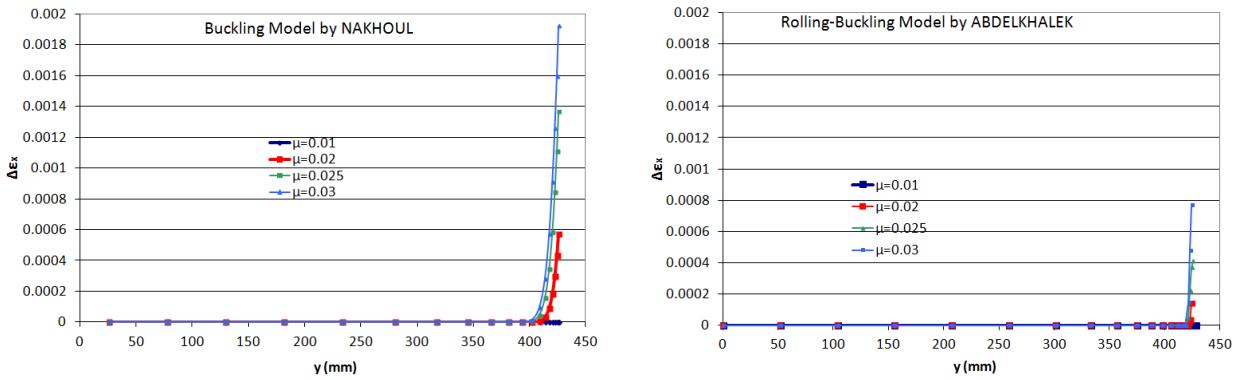

(a): MSBM (b): Lam3/Tec3-Abdelkhalek

Figure 5.4: The additional strain computed due to buckling occurrence for different friction coefficients. The additional strains are computed using the equations presented in pages 65 and 107.

Figures 5.5 to 5.7 complete this discussion. For $\mu = 0.01$ the strip under tension is perfectly flat. Increasing friction leads to waviness on the edges. When friction increases, the amplitude increases quasi-linearly, and simultaneously the wavelength grows quasi-linearly. Since the Lam3/Tec3-Abdelkahelek cannot quantify the amplitude of the defect, it is approximated using the ratio between the additional strains $\Delta\varepsilon_x$ computed by **MSBM** and Lam3/Tec3-Abdelkhalek for each friction. Its evolution is described qualitatively in Figure 5.6 (the red curve).

Since both models predict a flat strip under tension for $\mu = 0.01$, it means that the critical friction value is somewhere between $\mu = 0.01$ and $\mu = 0.02$. To reduce the interval, two new simulations are launched for $\mu = 0.015$ and $\mu = 0.0185$. Again for $\mu = 0.015$ both models give a perfectly flat strip. As for $\mu = 0.0185$ they give a very small but not zero amplitude. These new simulations provide a smaller critical interval, i.e. $0.015 < \mu_{cr} < 0.0185$.

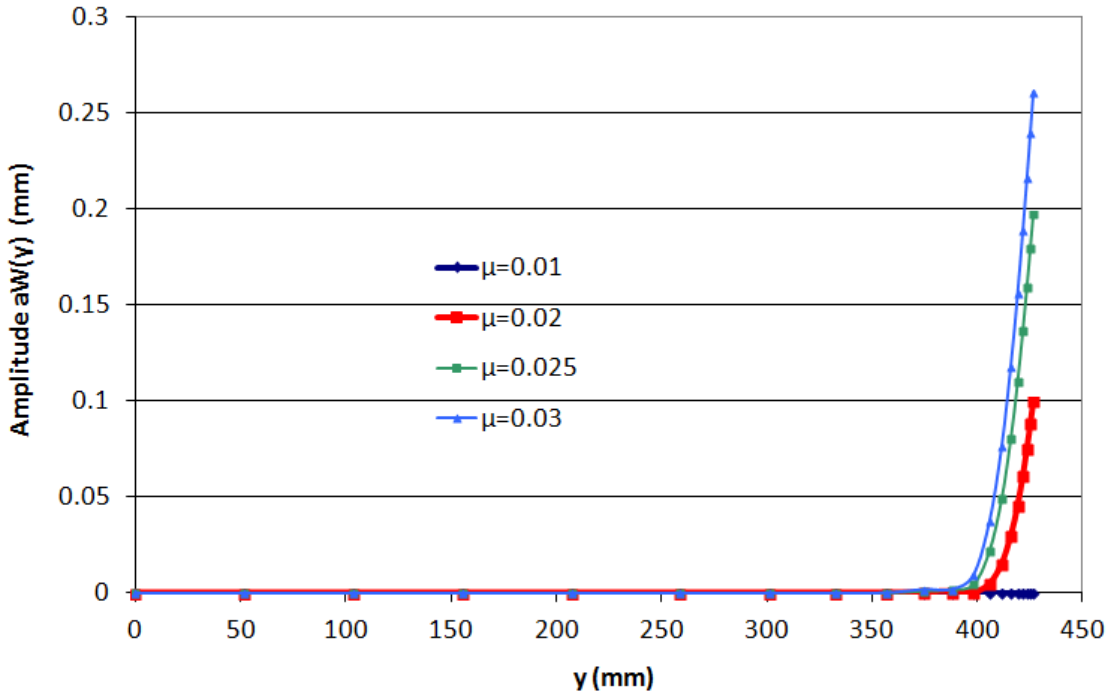

Figure 5.5: Evolution of the defect amplitude transverse profile with and increasing friction.

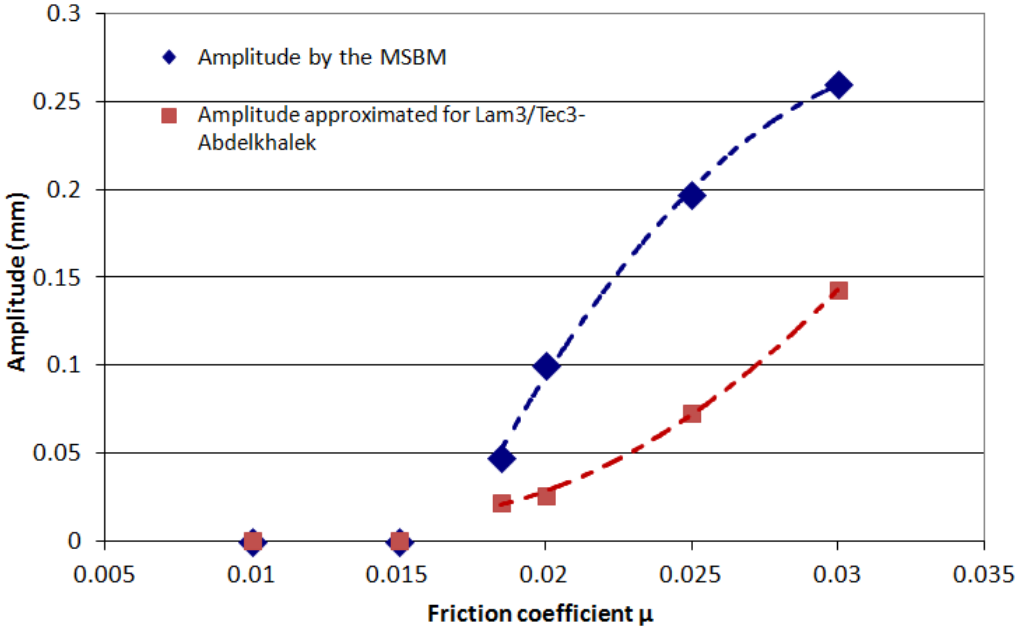

Figure 5.6: Evolution of the defect amplitude with increasing friction.

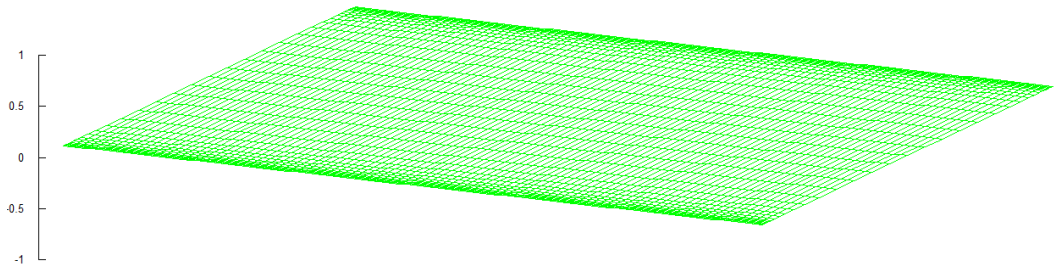

(a): $\mu = 0.01$, WRB= 480 KN, $a = 0$ mm, 0 wave

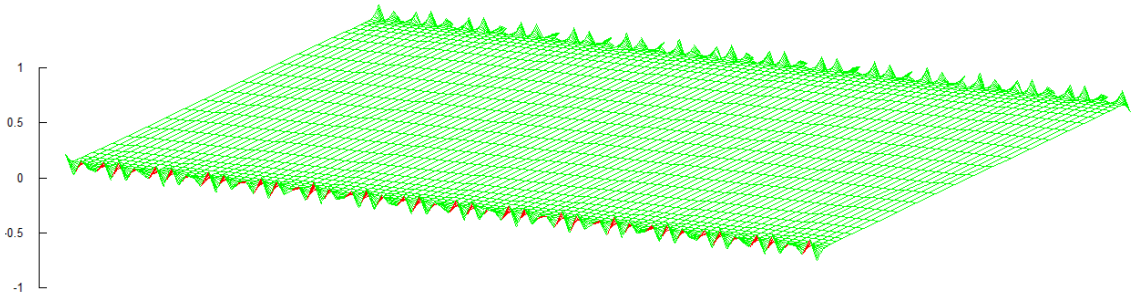

(b): $\mu = 0.02$, WRB= 480 KN, $a = 0.1$ mm, wavelength= 72 mm, 42 waves

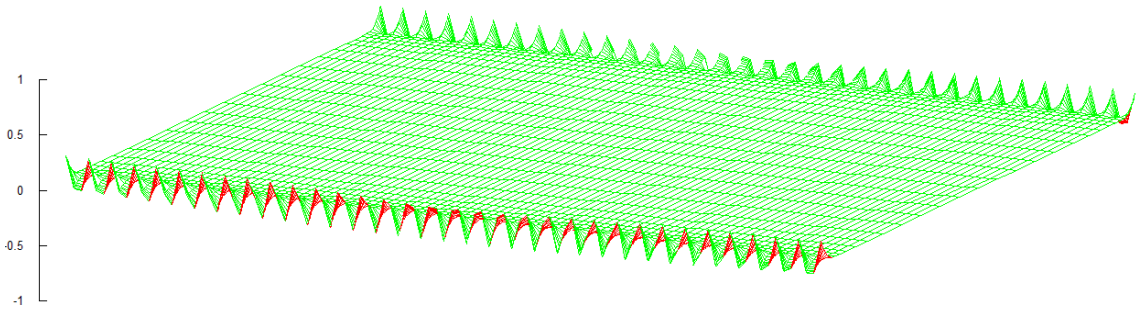

(c): $\mu = 0.025$, WRB= 480 KN, $a = 0.197$ mm, wavelength= 84 mm, 36 waves

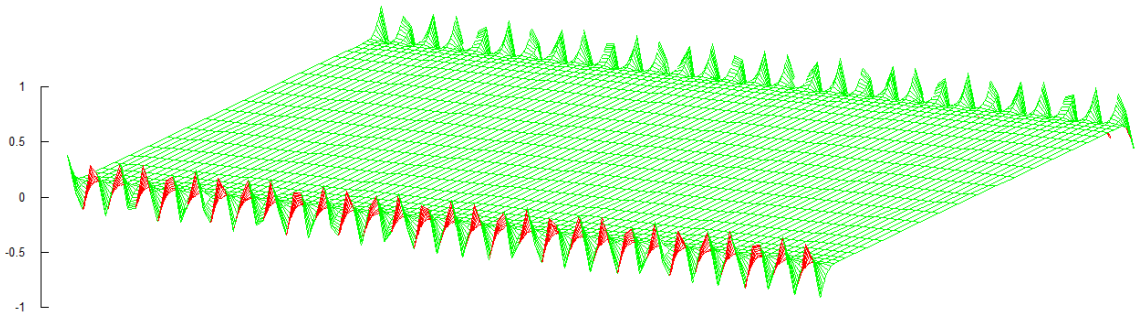

(d): $\mu = 0.03$, WRB= 480 KN, $a = 0.26$ mm, wavelength= 93 mm, 32 waves

Figure 5.7: The defective strip under tension and residual stress for $WRB = 480$ KN and varying friction coefficient μ.

The post-buckling transverse stress profiles computed by **MSBM** are presented in Figure 5.8a) and compared with the profiles computed by Lam3/Tec3-Abdelkhalek (Figure 5.8b)). Both models have qualitatively the same behavior. Though the stresses are relaxed on the edges where the defects were detected, the stress is not fully redistributed as in Lam3/Tec3-Abdelkhalek.
For $\mu = 0.01$, though no defect is detected under strip tension, both models predict center buckles once the tension is canceled.

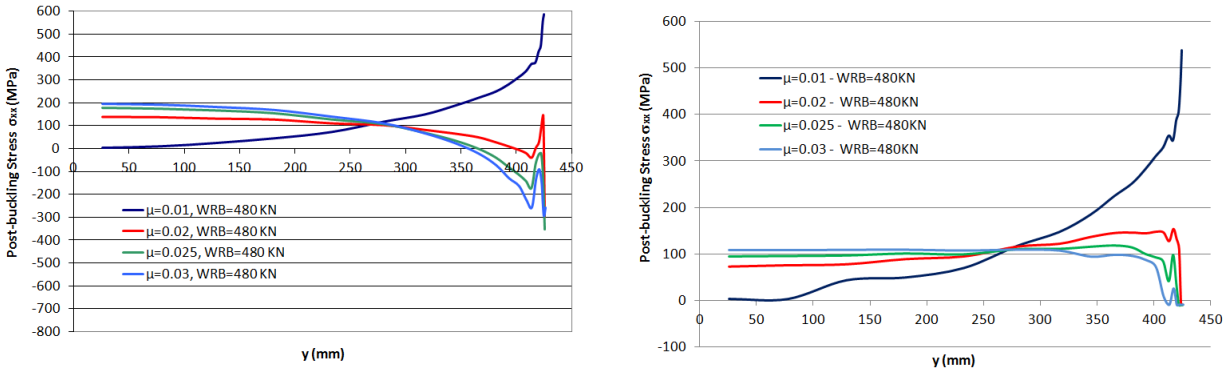

(a): MSBM (b): Lam3/Tec3-Abdelkhalek

Figure 5.8: The post-buckling stress transverse profiles for different friction coefficients.

We suspect that this disagreement between the computed stress profiles, especially their concavity, is due to forbidding in **MSBM** the relaxation of σ_{yy} by the transverse defect appearance (as illustrated in section 2.3.2.3). In other word, it prevents finding the good buckling mode.
This point will be inspected closely in the next chapter, where **MSBM** is coupled with Lam3.

5.3 Flatness and Work Roll Bending

5.3.1 Wavy edges and Work Roll Bending

Conversely in this section, we want to study the effect of work roll bending force on buckling. The rolling operations are modeled with a fixed friction coefficient of $\mu = 0.025$ and using WRB between 350 KN and 900 KN. Once again, the corresponding stress profiles are imported from the rolling software Lam3/Tec3 and used as residual loads for the strip in the **MSBM**. They are illustrated in Figure 5.9. In the **MSBM**, the strip is customized to match the exiting strip dimensions used in Lam3/Tec3 then it is

doubly loaded by the residual stresses and 100 MPa of strip tension. Figure 5.9 shows that increasing the WRB force increases slightly the compressive stress on the edge. In addition, it does not affect the compression zone that much. Thus, it is expected not to change the defective zone as well.

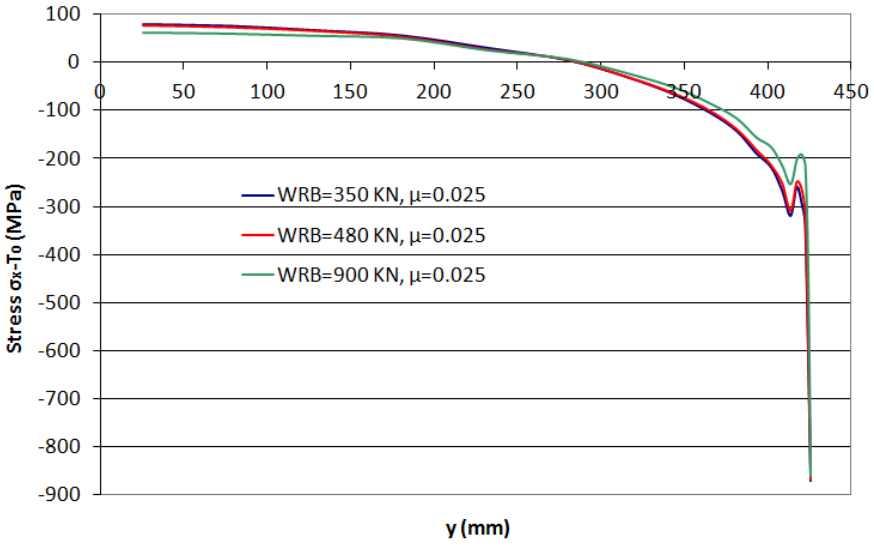

Figure 5.9: The different stress profiles corresponding to the coefficient of friction $\mu = 0.025$ and a varying WRB. Profiles are recovered at 1 m i.e. for downstream bite.

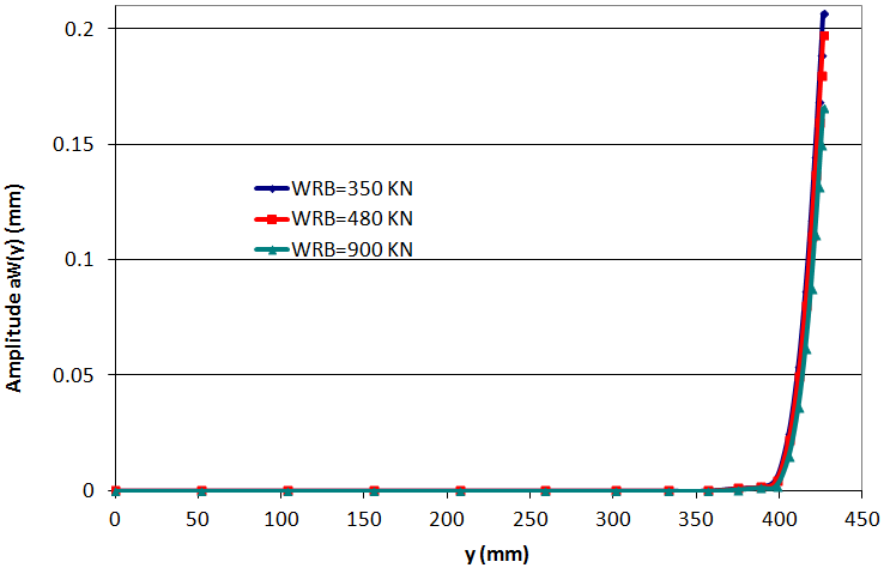

Figure 5.10: Evolution of the defect amplitude transverse profile with varying WRB force.

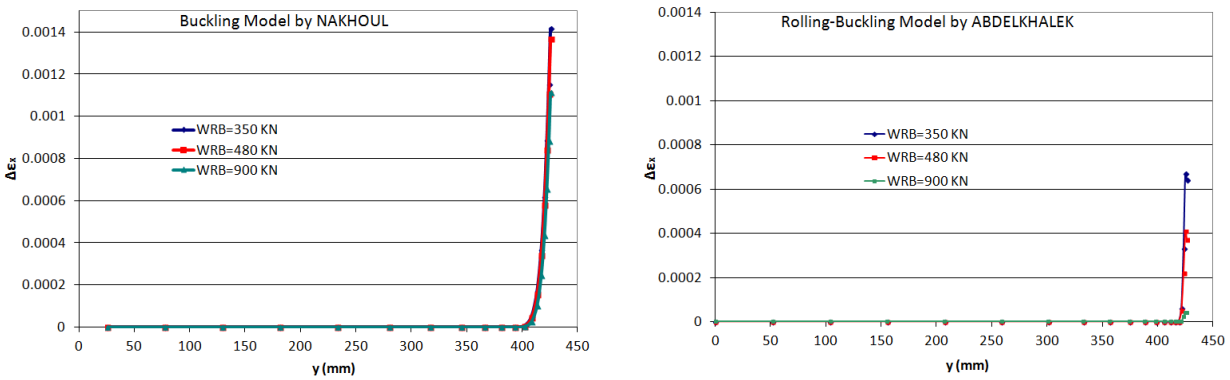

(a): MSBM (b): Lam3/Tec3-Abdelkhalek

Figure 5.11: The additional strain computed due to buckling for different WRB values.

The form of the additional strains for different WRB values presented in Figure 5.11, whether by the decoupled **MSBM** or the rolling-buckling model, concurs with what has been said. Both models detect the defect developing on the edges and the buckling strain curves behave the same way. Though the defective zone is not affected by changing WRB, their magnitude is.

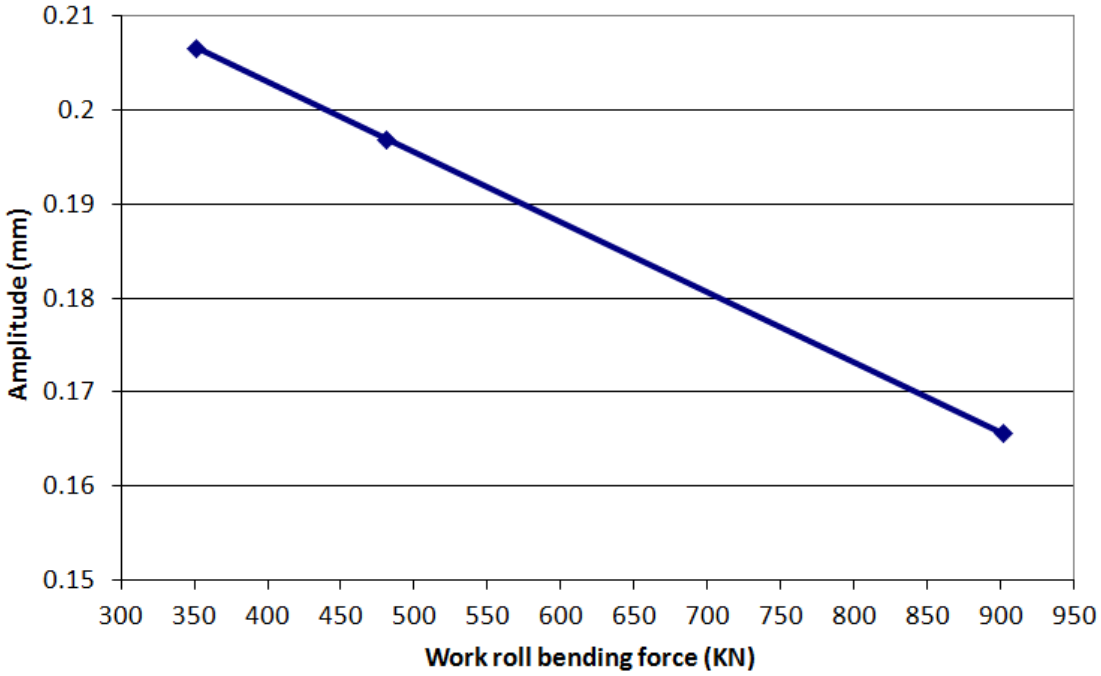

Figure 5.12: Evolution of the defect amplitude with an increasing WRB.

Figures 5.11 and 5.12 show that increasing the WRB force leads to smaller amplitude. That goes side by side with decreasing wavelength, meaning more waves in strip length (Figure 5.13). This response is logical since increasing work roll bending induces smaller rolling force on the edges, thus smaller reduction and more resistance to flatness loss.
We notice that even a high WRB force (900 KN) is unable to correct the edge undulations. This is normal because changing the WRB is not the perfect actuator to correct this type of defect (localized over 15 mm of the edge). The best actuator for localized wavy edge can be a 6-high mill with intermediate shiftable rolls.
Nevertheless adjusting the WRB can be used to correct the appearance of center buckles and this will be explored in the next section.

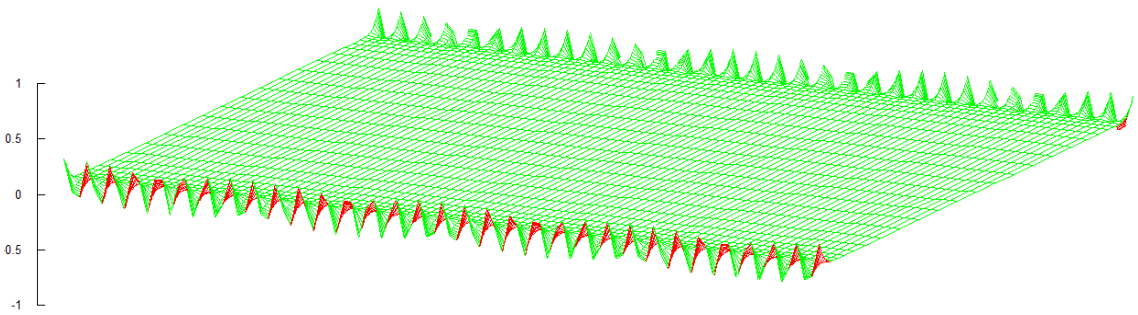

(a): $WRB = 350$ KN, $\mu = 0.025$, $a = 0.21$ mm, wavelength= 91 mm, 33 waves

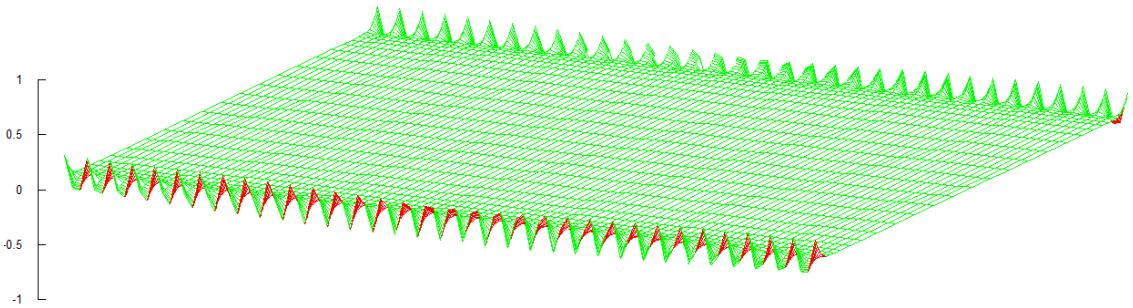

(b): $WRB = 480$ KN, $\mu = 0.025$, $a = 0.197$ mm, wavelength= 84 mm, 36 waves

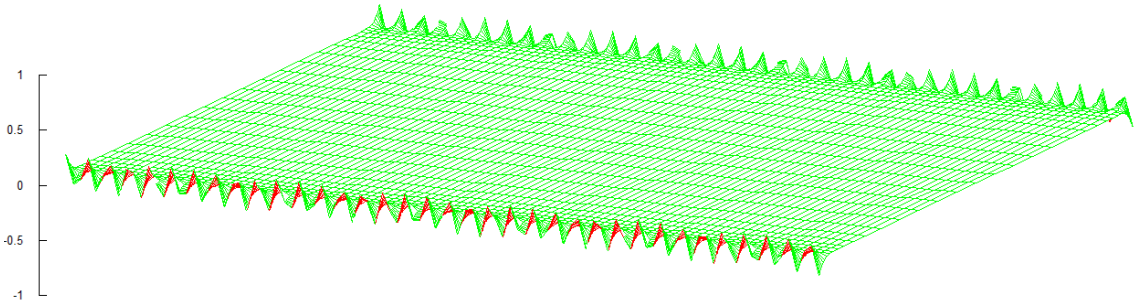

(c): $WRB = 900$ KN, $\mu = 0.025$, $a = 0.166$ mm, wavelength= 77 mm, 39 waves

Figure 5.13: The defective strip under tension and residual stress for $\mu = 0.025$ and varying WRB.

5.3.2 Center buckles and Work Roll Bending

To study the effects of changing the work roll bending force on correcting the center buckles, the rolling operations are modeled with a fixed friction coefficient of $\mu = 0.01$ and using WRB between 480 KN and 900 KN. The corresponding stress profiles are imported from the rolling software Lam3/Tec3 in the stabilized zone after 1 m and used as residual loads for the strip in the **MSBM**. Since in the software Lam3/Tec3 the contribution of the strip tension T_0 is already included in the stress profile, the residual stress profiles are illustrated in Figure 5.9 by subtracting T_0. In the **MSBM**, the strip is customized to match the exiting strip dimensions used in Lam3/Tec3 then it is doubly loaded by the residual stresses and 100 MPa of strip tension. Figure 5.14 shows that the compressive stresses are located in the center; if they are compressive enough, they may induce waviness along the strip center. Increasing the WRB force increases the compressive stress in the center. In addition, it increases slightly the compressive zone and by that affects the width of the defect. Note that, for $WRB = 480$ KN, the stresses do not exceed -100 MPa. Thus, when adding the strip tension 100 MPa, no defect is expected.

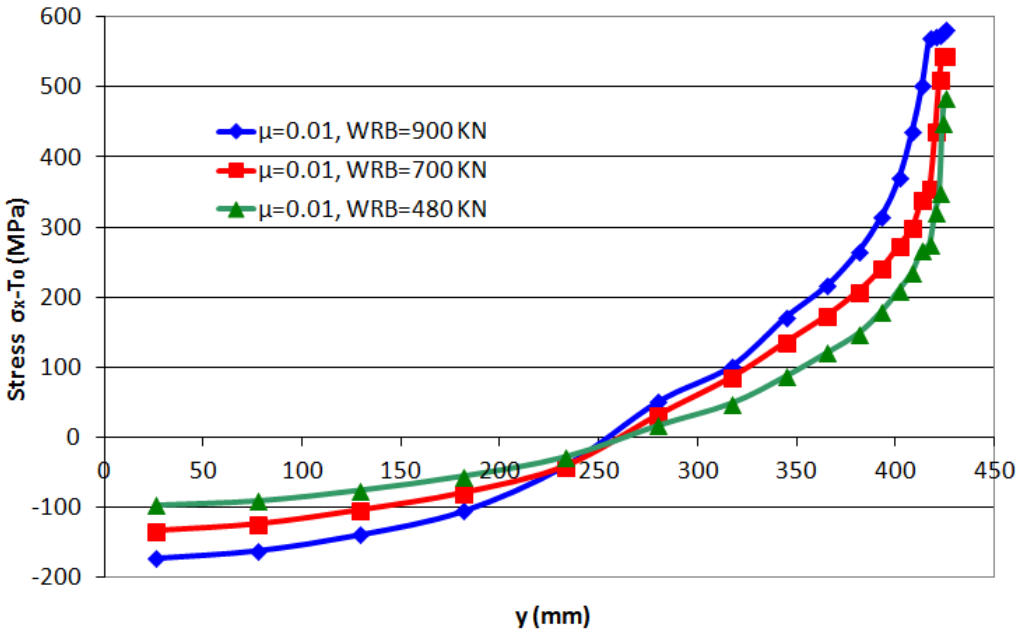

Figure 5.14: The different stress profiles corresponding to the coefficient of friction $\mu = 0.01$ and a varying WRB. Profiles are recovered ~ 1 m downstream of the bite.

Figures 5.15 and 5.16 confirm this discussion. Increasing the WRB means more rolling force especially in the center. This introduces more reduction and therefore more compressive stress in the center. Figures 5.15 and 5.18 show that when increasing the WRB,

the magnitude of the defects and their width get larger. For $\mu = 0.01$ and WRB= 480 KN the strip is perfectly flat, as shown by the amplitude and $\Delta\varepsilon_x$ transverse profiles. Figure 5.16 shows that both models **MSBM** and Lam3/Tec-Abdelkhalek behave in the same way. They both detect the defect in the center and increasing the WRB introduces more defects translated by larger buckling strain in the center. Figure 5.17 shows that the amplitude computed using the **MSBM** increases with the WRB. Though Lam3/Tec3-Abdelkhalek is unable to define the magnitude of the defects, its evolution is approximated using the additional strain ratios. The curves confirms that both models behave qualitatively in the same way. In addition, both models agree that for $\mu = 0.01$ and WRB= 480 KN the strip is flat. This means that the critical bending force giving a flat strip is 480 KN $<$ WRB$_{cr}$ $<$ 700 KN.

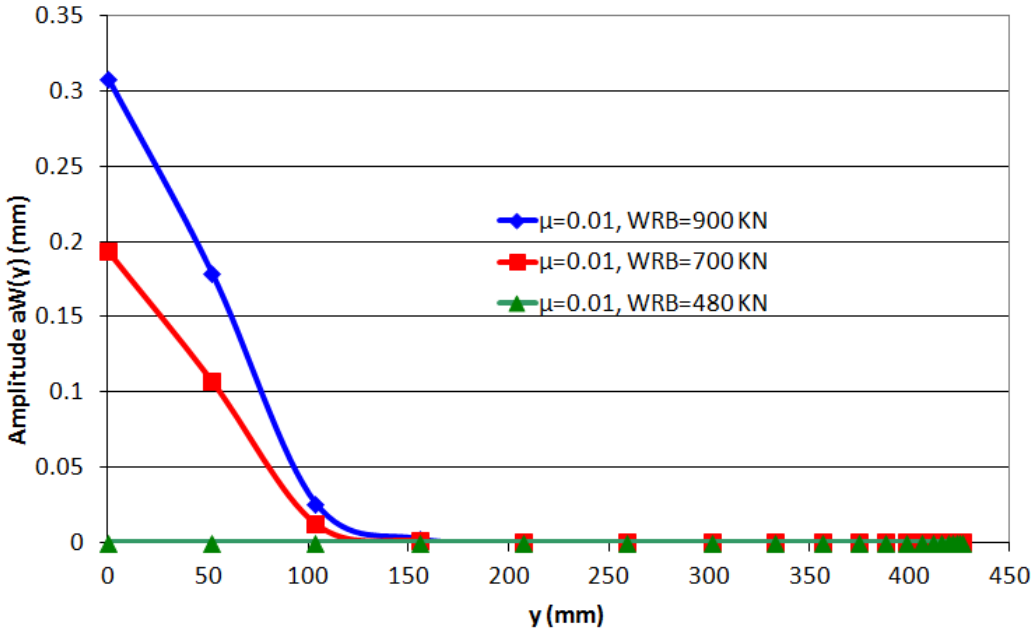

Figure 5.15: Evolution of the defect amplitude transverse profile with and WRB force.

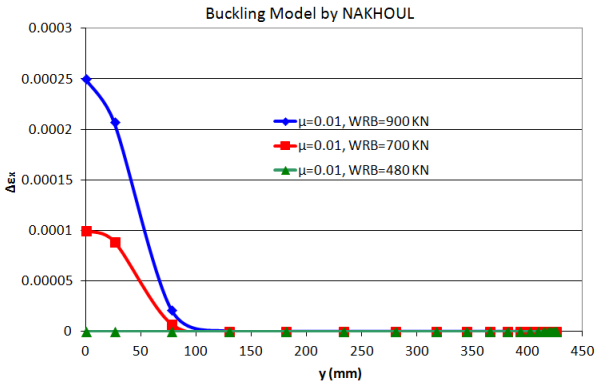

(a): **MSBM**

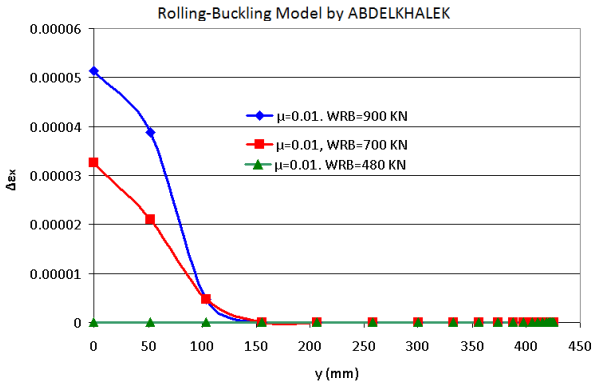

(b): Lam3/Tec3-Abdelkhalek

Figure 5.16: The additional strain computed due to buckling appearance for $\mu = 0.01$ and different WRB values.

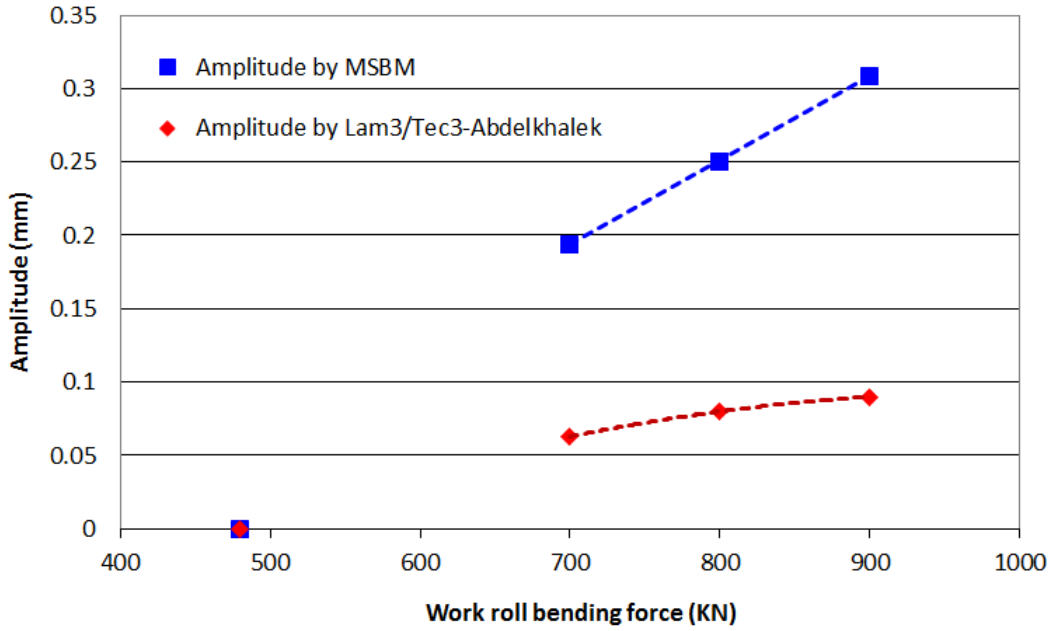

Figure 5.17: Evolution of the defect amplitude with $\mu = 0.01$ and increasing WRB.

Figure 5.18 illustrates the strip shapes under a strip tension of 100 MPa for a fixed friction coefficient $\mu = 0.01$ and changing WRB force. Figure 5.18c) confirms that the strip is perfectly flat for $\mu = 0.01$ and WRB= 480 KN. Decreasing the WRB does not seem to affect significantly the defective zone width or the wavelength, but impacts mainly the magnitude of the defect.

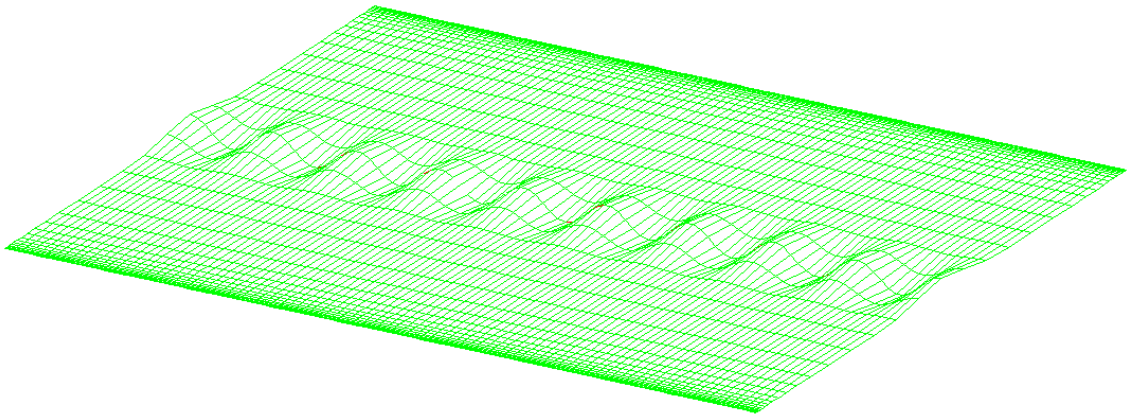

(a): $WRB = 900$ KN, $\mu = 0.01$, $a = 0.308$ mm, wavelength= 333.33 mm, 9 waves

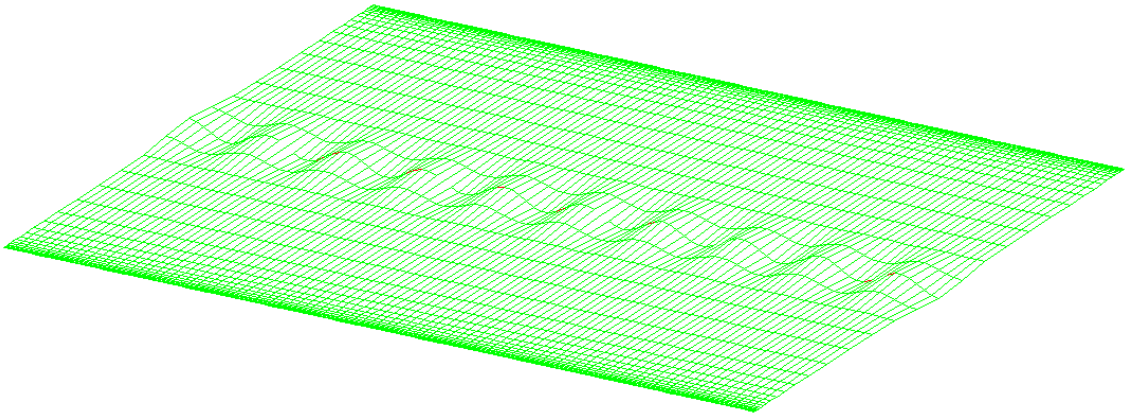

(b): $WRB = 700$ KN, $\mu = 0.01$, $a = 0.194$ mm, wavelength= 315.782 mm, 10 waves

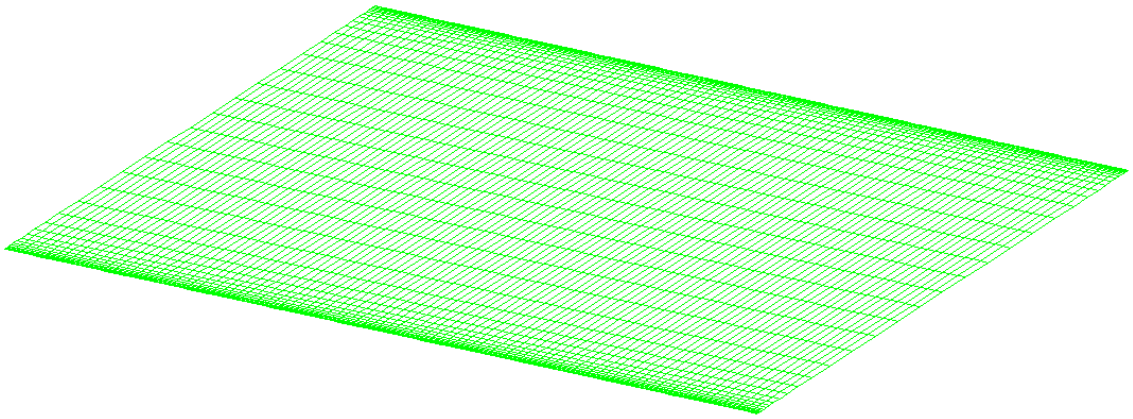

(c): $WRB = 480$ KN, $\mu = 0.01$, $a = 0$ mm

Figure 5.18: The defective strip under tension and residual stress for $\mu = 0.01$ and varying WRB.

5.4 Conclusion

Even decoupled, the **MSBM** seems to have the same response in detecting flatness defects as the coupled Rolling-Buckling software Lam3/Tec3-Abdelkhalek. Qualitatively, they are comparable, whether by detecting the same defective zone or by predicting the same evolution when changing the friction and work roll bending force.
Increasing friction induces more reduction on the edges for this particular operation, which means more compressive residual stresses. Thus, when friction increases the defective zone width increases, the waves and their magnitude are larger.

As for the WRB force, it can neutralize the effects of friction. Though its effects were not obvious for the wavy edges, it was shown that it has significant impact on eliminating center buckles. When the WRB force decreases, the waves amplitude decreases.

These studies establish that the **MSBM** is capable of describing more complex buckling problems and can clarify the strip behavior under different conditions. By itself, it can be considered as an asset to predict flatness defects and which actuators could be adjusted to prevent their appearance. This fact encourages us to push further by coupling the **MSBM** with the rolling model Lam3/Tec3. This will be presented in the following chapter.

5.5 Résumé en Français

Dans le présent chapitre la capacité du modèle de flambage **MSBM** à prédire des défauts de planéité pour de vrais cas de laminage a été explorée. Les profils transversaux de contrainte résiduelle ont été importés d'un logiciel de laminage Lam3/Tec3. Autrement dit, le problème est traité d'une façon découplée dans ce chapitre: la première étape est de simuler un cas de laminage à froid utilisant Lam3/Tec3, fournissant des profils de contraintes résiduelles, et la deuxième est d'utiliser ces profils dans **MSBM** pour étudier le flambage de la tôle sous traction.
Pour étudier son comportement, le modèle de flambage a été utilisé pour prédire l'effet du frottement et de la force d'équilibrage sur l'apparition des défauts de planeité en ligne. Les résultats ont été comparés à ceux obtenus par le modèle Lam3/Tec3-Abdelkhalek (modèle de Laminage-Flambage couplé).
Même découplé, **MSBM** semble avoir la même réponse que le modèle couplé Lam3/Tec3-Abdelkhalek: ils détectent tous les deux la même zone défectueuse et ont qualitativement la même réponse à un changement du frottement et de la force d'équilibrage.

Pour l'opération présentée dans ce chapitre, un frottement croissant induit plus de réduction aux bords ce qui s'y traduit par des contraintes plus compressives. Ainsi, quand le frottement augmente, la largeur des défauts, les ondulations et leur amplitude augmentent aussi.
Quant à la force d'équilibrage, elle est utilisée pour neutraliser les effets d'une variation du frottement. Quoique ses effets ne soient pas évidents pour les bords longs dans les conditions étudiées, il est montré qu' elle a un impact significatif éliminant les centres longs. Une force d'équilibrage décroissante induit une diminution de l'amplitude des ondulations (au centre).

CHAPTER 6

COUPLED ROLLING-BUCKLING MODEL LAM3/TEC3-**MSBM**

Man cannot discover new oceans unless he has the courage to lose sight of the shore.

by André Gide

Contents

The rolling software Lam3/Tec3, in its standard version, shows several limitations:

i) It is not able to describe geometrically thin cold rolled strip when flatness defects occur.

ii) The stress distribution is overestimated and is not in a good agreement with the measurements.

In fact, the latter is the consequence of the former: since the buckling of a strip could not be described, its effects such as the redistribution of the stress is not taken into account. This leads to over/under-estimation of the real stress distribution.
To examine these restraints, a rolling simulation, described in page 79 has been launched using Lam3/Tec3. A thin strip of 855 mm width and 0.355 mm thickness is rolled to an exit thickness of 0.252 mm. The results are represented in Figure 6.1. It is clear that the stress is overestimated (in compression) near the edges. For a thin strip, the tolerated stress is surely not equal to -800 MPa. The critical value σ_{cr} is largely exceeded, thus the strip should buckle. Since Lam3/Tec3 is not engineered to take into account the buckling phenomenon, it fails to represent the strip state post-buckling i.e. relax the stress distribution.

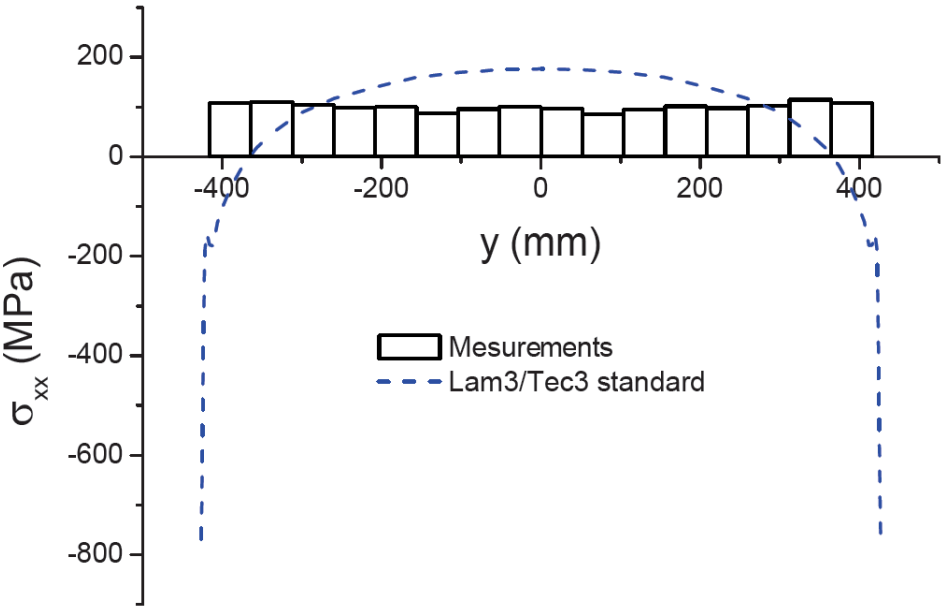

Figure 6.1: Comparison between the stress transverse profile $\sigma_{xx}(y)$ computed by Lam3/Tec3 and the measurements given by the flatness rolls.

The model has therefore been enriched by [Abdelkhalek et al., 2008] where a simple buckling model was implemented completely in Lam3. It allowed Lam3/Tec3 to detect the defective zone, compute the equivalent buckling strain and relax the post-buckling

stress distribution to be in a good agreement with the measurements. With all these improvements, this model -called Lam3/Tec3-Abdelkhalek- remains incapable of describing the type and form of the flatness defects (see section 2.3.2.2 for more details).
A second improvement was developed by [Abdelkhalek et al., 2009] coupling two different models, the rolling model Lam3/Tec3 with the shell buckling model **MAN**. The result is a model called Lam3/Tec3-**MAN** (see section 2.3.2.3 for more details) capable of detecting the defective zones, describing and quantifying the buckling and redistributing the stress post-buckling. This model is difficult to use since:

i) The coupling method is complex and not rigorous (transfer of the boundary conditions).

ii) The necessary steps to use this software are tricky, heavy and consume a lot of time (it is done manually).

In this chapter, a coupled rolling-buckling model -called Lam3/Tec3-**MSBM**- will be presented. The aim is to combine the advantages of both models mentioned above. First, the coupling procedure merging the multi-scale Buckling Model (**MSBM**) (chapter 4) with the rolling model Lam3/Tec3 is presented. Next, the on-line flatness prediction using the resulting model is explored. In addition, comparison with measurements and previous models are examined and analyzed. Finally, a discussion is presented inspecting not only advantages but also difficulties, limitations and what can be done to improve them in future work.

6.1 MSBM implementation in the rolling model Lam3/Tec3

The multi-scale Buckling Model (**MSBM**) has been implemented in Lam3/Tec3 in a manner similar to the simple buckling model introduced by [Abdelkhalek et al., 2011] and summarized in section 2.3.2.2.
Figures 6.2 and 6.3 illustrate respectively the algorithm flow charts of the rolling model Lam3 and the **MSBM**. For each transverse section i- treated independently from the nearby sections- and at every Gauss integration point G of Lam3, the buckling model is activated, the buckling mode (W, q) and amplitude a are computed. Then, the additional deformation $\Delta\varepsilon$ introduced by the buckling phenomenon is estimated in terms of W and a. Next, the buckling deformation is added to the global strain (computed classically by Lam3) on every Newton-Raphson iteration it (illustrated in Figure 6.3(a)). This modifies implicitly the constitutive law and the streamline integration in a way to adjust the post-buckling stress distribution to respect a new equilibrium state.

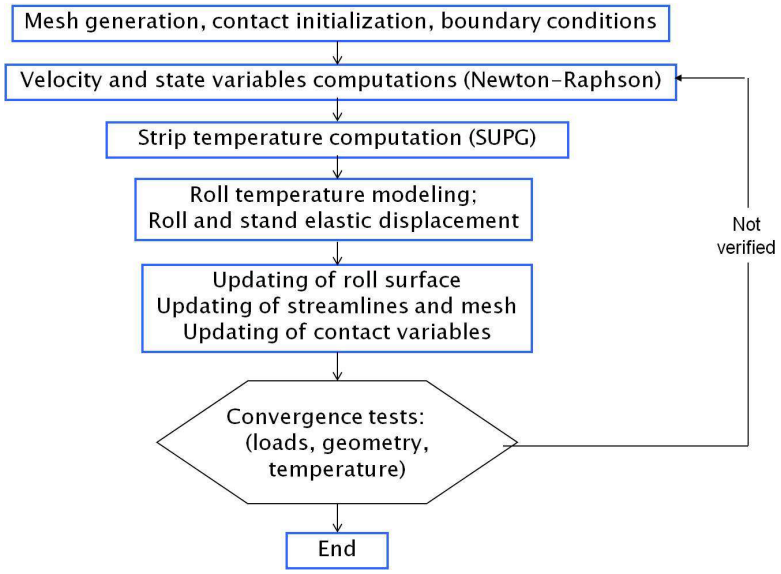

Figure 6.2: General algorithm of the FEM strip rolling model Lam3/Tec3.

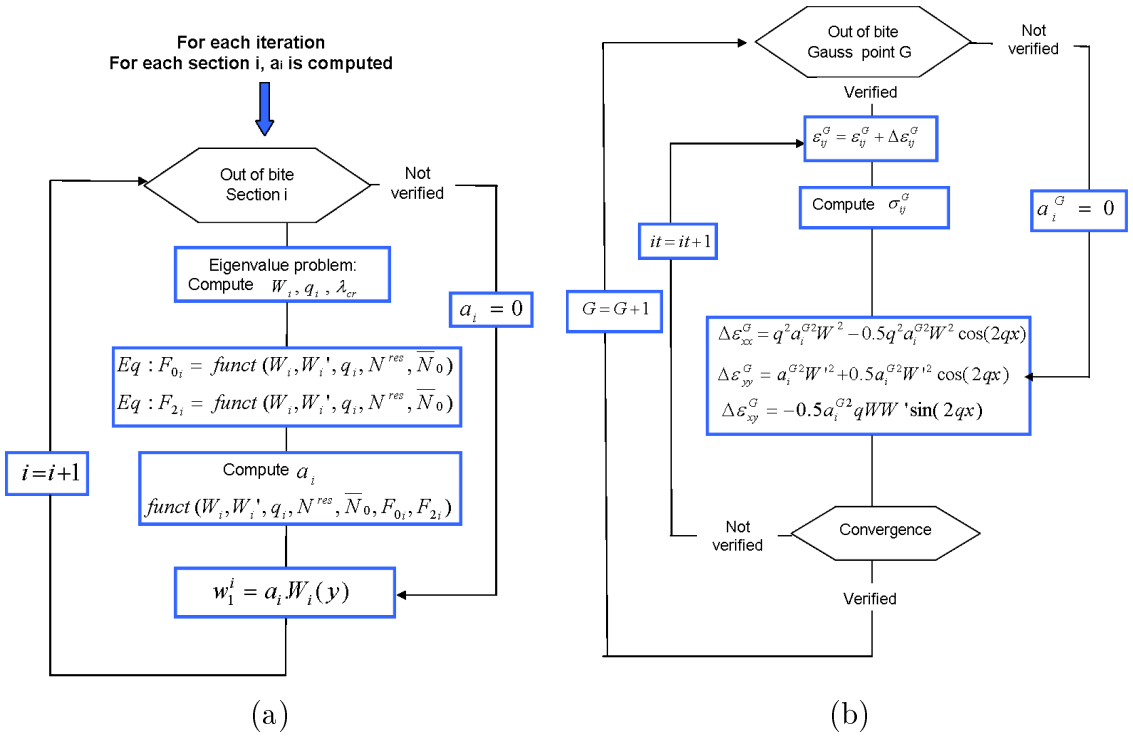

Figure 6.3: General algorithms of the **MSBM** implemented in Lam3: (a) Algorithm of the **MSBM**, (b) Algorithm describing the coupling between Lam3 and the **MSBM**.

Three main objectives are expected from this coupling:

a) The flatness defects are detected, described and quantified;

b) The interaction between the bite deformation and buckling can be analyzed;

c) The out-of-bite stress distribution is relaxed by buckling and is closer to reality than the one computed without buckling.

Before proceeding, several points/difficulties should be clarified:

6.2 Implementation difficulties

Since the following form was chosen,

$$w(x,y) = \sum_m w_m(y) e^{imqx} \tag{6.1}$$

where q is the half-wave number in the $x-$direction, our model is unable to detect and represent the waves developed in the $y-$direction which can happen often during cold rolling -near the bite exit- (see Figure 6.4, "longitudinal folds").

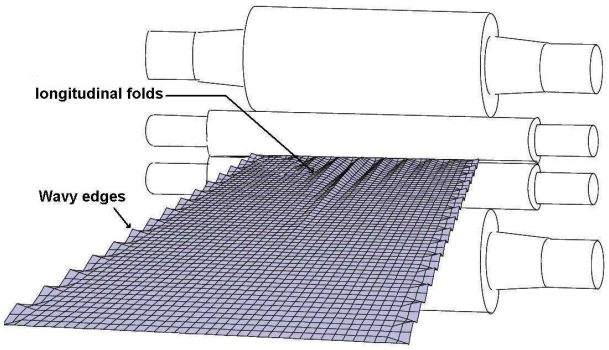

Figure 6.4: Schematic view of flatness defects during strip rolling.

This can have a significant impact on the results:
i) Similar to what happens in the x-direction, if the stress $\sigma_{yy}(y)$ exceeds the critical value σ_{cr}, waves are formed in the $y-$direction i.e. σ_{yy} is relaxed by an additional wrinkling stress $\sigma_{yy}^{wr}(y)$.
ii) The fact that σ_{xx} and σ_{yy} are not relaxed properly in an area presenting longitudinal waves may cause convergence problems : as presented in Figure 6.5 the amplitude map presents unreasonable values causing excessive strain values $\Delta\varepsilon$, inducing convergence

problems in Newton-Raphson algorithm. Moreover in this vicinity, σ_{yy} changes quickly from one section to the next -resulting in disordered amplitude (Figure 6.6); thus, Hypothesis 3 (page 105) is no longer valid (i.e. the envelope does not vary slowly) and the **MSBM** ceases being effective.

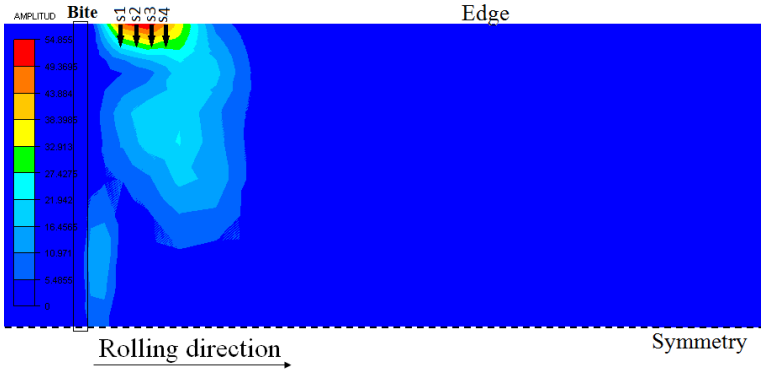

Figure 6.5: Chaotic amplitude mapping due to omitting waves in the $y-$direction - computed as illustrated in Figure 6.3 .

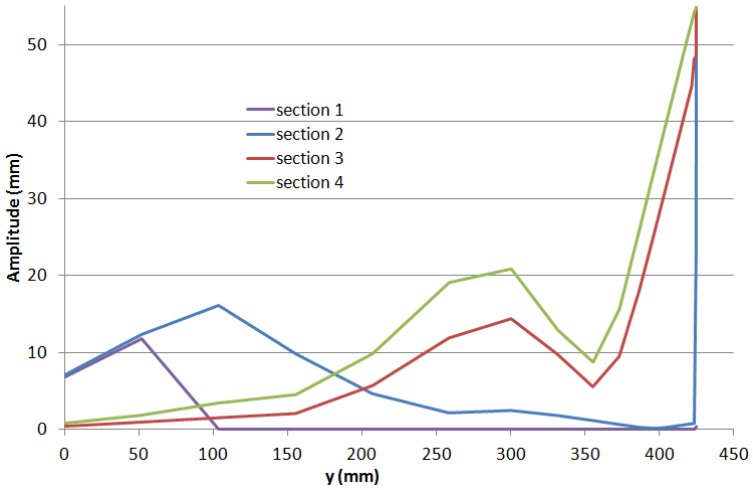

Figure 6.6: Amplitude transverse profiles on four consecutive sections s1, s2, s3 and s4.

When rolling thin strips (section 6.3), this difficulty will most definitely appear and some measures should be taken. Two main options are available:
1) The **MSBM** is activated only a chosen distance after bite-exit where the stress σ_{yy} respects again Hypothesis 3 (page 105).
2) The **MSBM** is activated directly after bite-exit, omitting the transfer of σ_{yy}.

In this chapter, all transverse profiles are plotted only for $y > 0$ by symmetry.

6.3 Results: On-line Flatness prediction using Lam3/Tec3-MSBM

Using the coupled rolling buckling software, Lam3/Tec3-**MSBM**, the rolling operation described on page 79 is simulated to predict on-line flatness defects (i.e. under strip tension) .

In this particular rolling operation, it is noted that σ_{yy} does not verify Hypothesis 3 (page 105) in the bite-exit vicinity. As discussed in the previous comment, we choose to dismiss transferring σ_{yy} in the 100 mm following the bite exit. This insures that no numerical problem will appear during the simulation. This simplification does not go without side effects. They will be discussed in the last section.

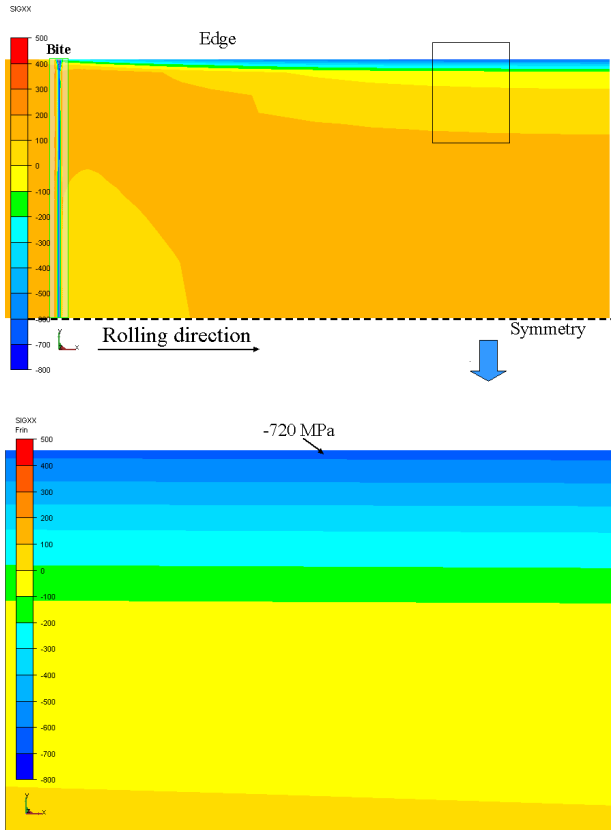

Figure 6.7: (a) The stress σ_{xx} map in the strip without taking into account buckling effects. (b) zoom of the stress σ_{xx} map near the edge.

Examining Figure 6.7, the stress map computed using the standard version of Lam3/Tec3, indicates that the strip is under severe compression on its edges: around -700 MPa. Normally, this compression is enough to induce buckling in the strip. Thus, when taking into account that buckling may happen, the model finds that the strip can tolerate on its edges a critical value of -250 MPa. The gap on the edges between the actual stress value $\sigma_{xx} = -700$ MPa and the critical value $\sigma_{cr} = -250$ MPa under a strip tension of 100 MPa must be translated into waves near the edges.

This is confirmed in Figures 6.8 to 6.10. The software detects a defective zone. It varies from a transverse section to another since our model sweeps one section after another predicting its state. For instance, Figures 6.9c) and 6.9d) -plotted 1500 mm after the bite exit-, give an idea of the defective zone on the edge, around 45 mm deep.
Overall, the strip under tension is presenting wavy edges of height equal to 0.35 mm (Figure 6.10). Note that the undulations are not identical along the strip, neither by it amplitude nor by its shape (Figure 6.8). This is expected since the strip is treated as continuous series of sections; so that the mode and amplitude depend mainly on the residual stresses and strip tension in each section.

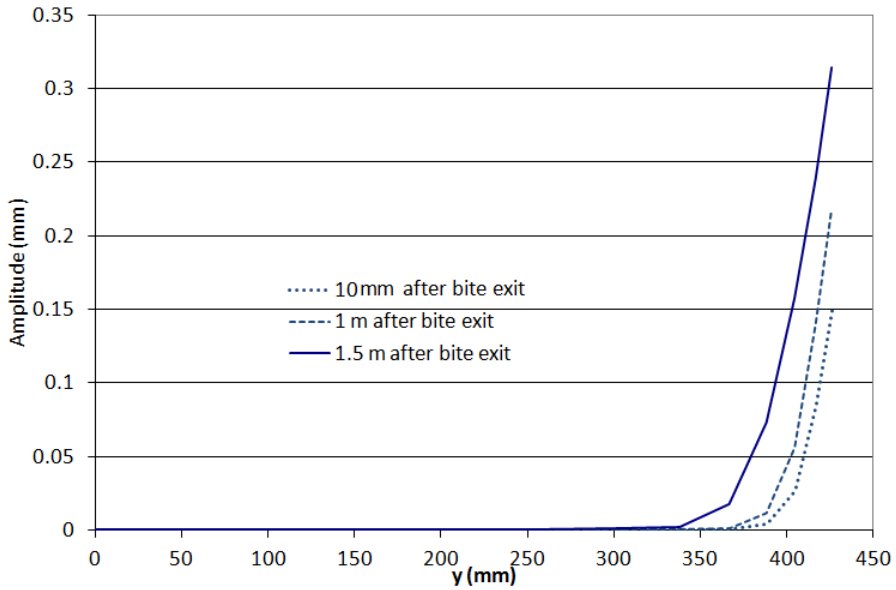

Figure 6.8: The amplitude transverse profile plotted on different sections after bite exit: after 10 mm, 1 m and 1.5 m.

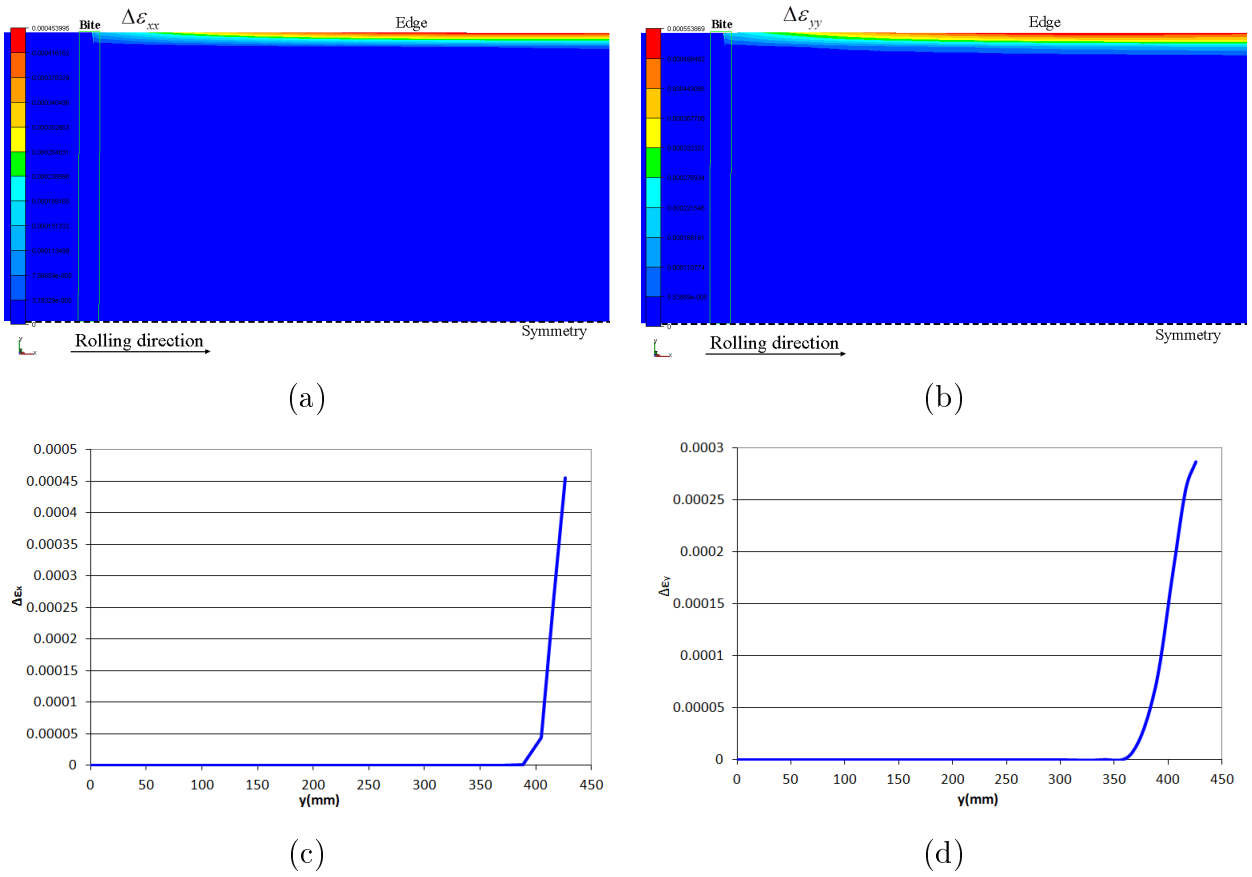

Figure 6.9: The buckling strain or the additional strain introduced due to buckling. The curves are plotted 1 m after bite exit.

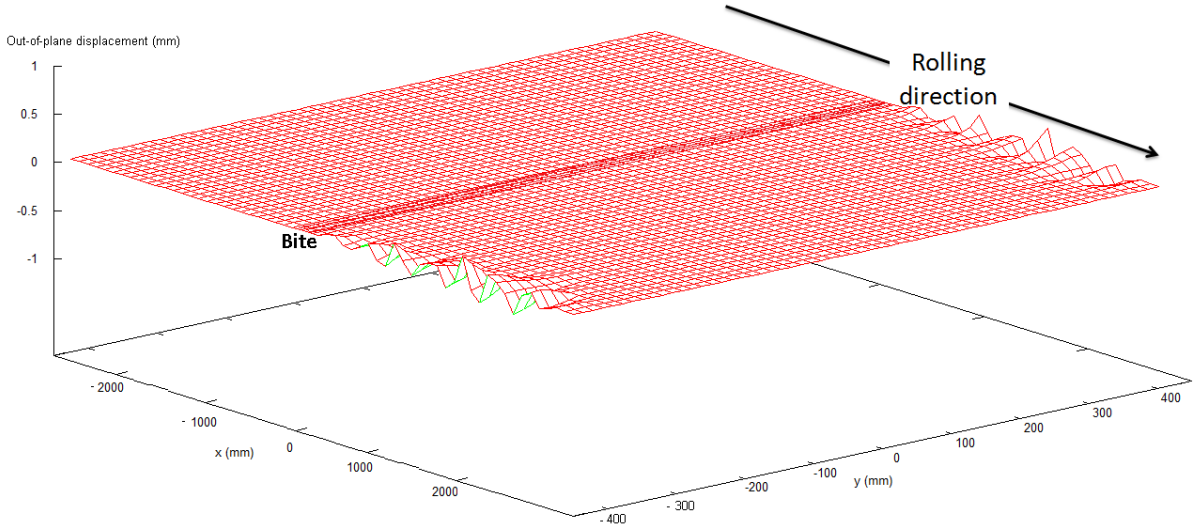

Figure 6.10: The defected plate under strip tension showing wavy edges of approximately 0.35 mm high.

In the defective zone, the additional buckling strain $\Delta\varepsilon_{xx}$ and $\Delta\varepsilon_{yy}$ -eventually transformed into buckling stresses- are computed and their mapping is presented in Figures 6.9a) and 6.9b). Once computed, they are added to the global strain computed by the standard version of Lam3/Tec3 and help relaxing the stresses to respect a new distribution after the strip buckling. $\Delta\varepsilon$ is computed according to the formulas recalled in Figure 6.3b) . The new stresses distributions are presented in Figure 6.11 as well as Figure 6.12. We notice that the stress profile is relaxed to respect the edge critical value but is not what we expected when it is compared with the measurements. The profiles present poor agreement.

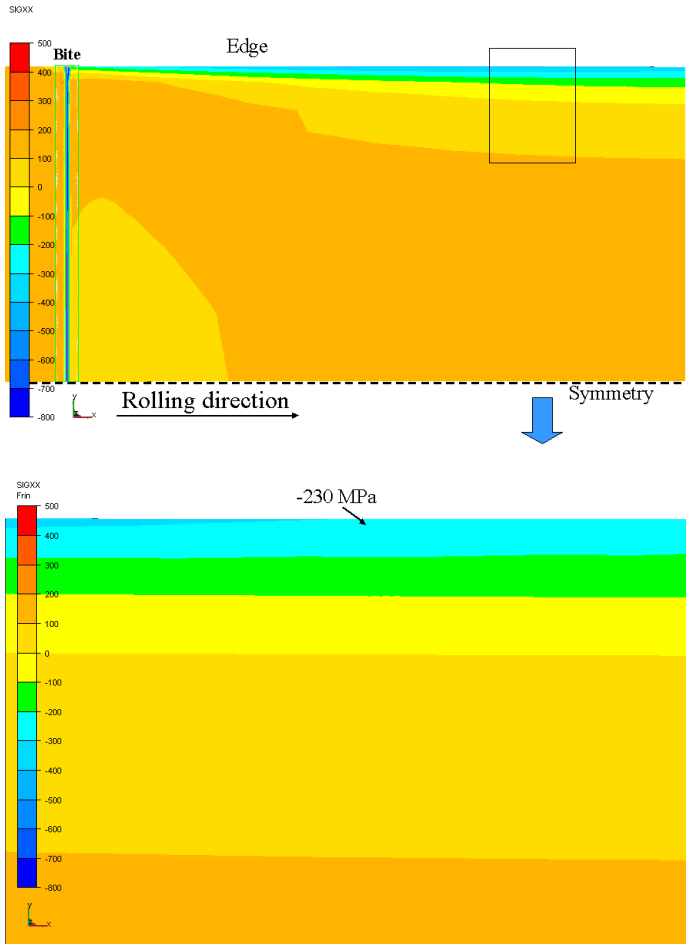

Figure 6.11: (a) The stress σ_{xx} map in the strip taking into account buckling effects. (b) zoom of the stress σ_{xx} map near the edge.

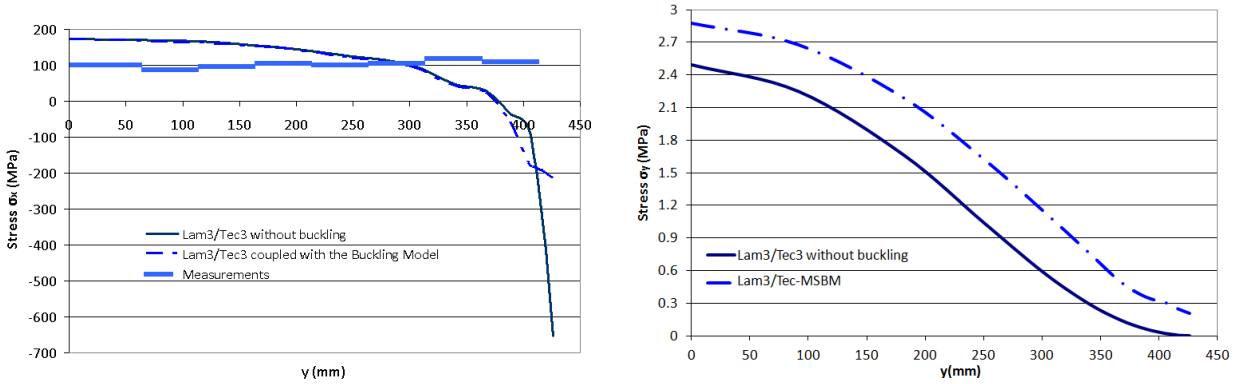

(a) (b)

Figure 6.12: Comparison between the stresses profiles σ_{xx} and σ_{yy} before and after coupling the rolling model Lam3/Tec3 with the **MSBM**. The curves are plotted 1 m after bite exit.

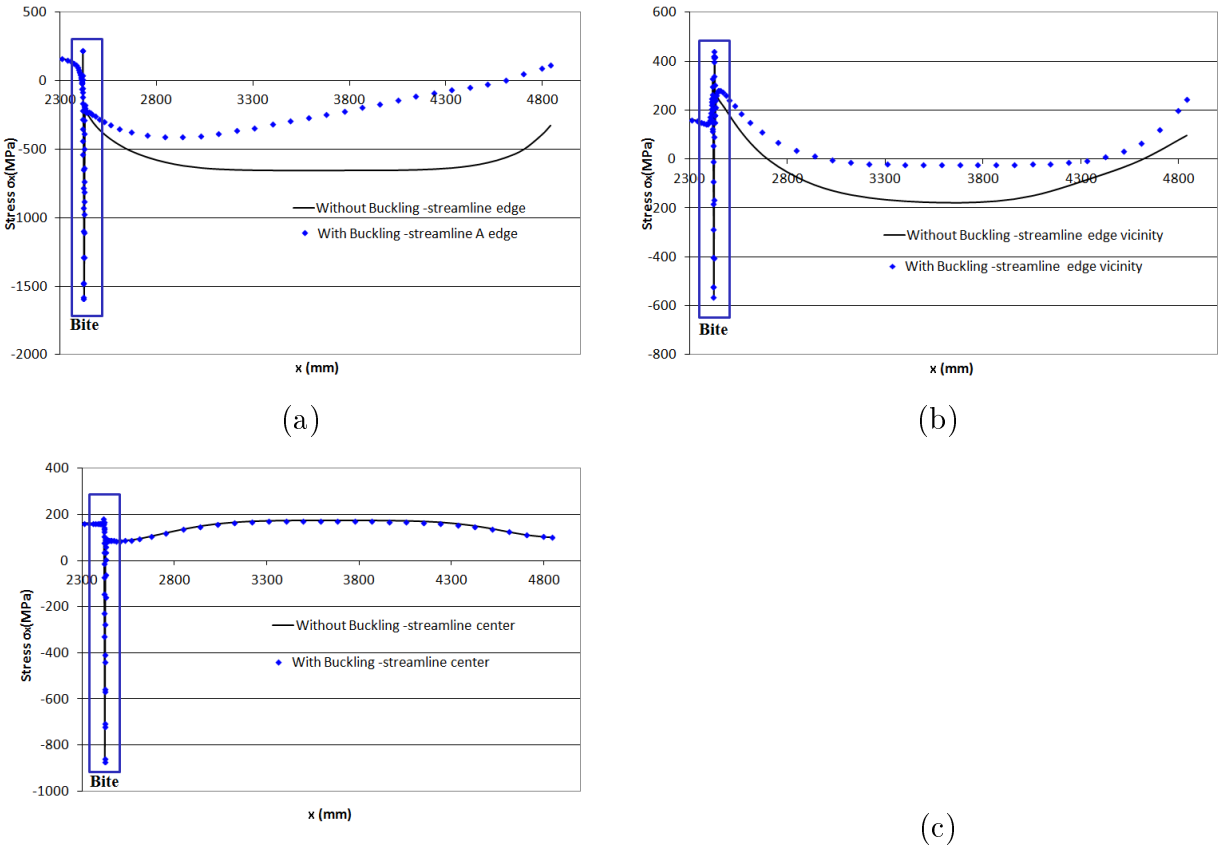

(a) (b) (c)

Figure 6.13: The stress distribution plotted on different streamlines: (a) on the extreme edge (at $y = 427.5$ mm), (b) near the edge (at $y = 423$ mm) and (c) in the strip center (at $y = 0$).

If we examine the stress distribution σ_x along streamlines, mainly where buckling happens i.e. on the edges, we notice that the stresses in compression are relaxed and balanced by buckling (see Figures 6.13a) and 6.13b)). The redistribution is not homogeneous all along the streamlines since this problem is treated on each section separately and the criterion is supposed to be respected locally where buckles appear i.e. the extreme edge. Figure 6.13c) shows that no significant changes were noticed in the center since the **MSBM** did not detect any defect there (strip center).

6.4 Results: Lam3/Tec3-MSBM vs. Lam3/Tec3-Abdelkhalek and Lam3/Tec3-MAN

6.4.1 Lam3/Tec3-MSBM vs. Lam3/Tec3-Abdelkhalek

To recapitulate, the software Lam3/Tec3-Abdelkhalek is capable of detecting the defective zone and relaxing the stresses due to buckling appearance. Note that, the critical value σ_{cr} is not computed by the model itself, but entered as an input datum. In addition, the defect form and height remain undetermined, only the shortening/lengthening of the material line is computed.
Suppose that we adopt the stress tolerated on the edge -250 MPa -computed by **MSBM**- as the critical stress in Lam3/Tec3-Abdelkhalek under a strip tension of 100 MPa.
Both Lam3/Tec3-Abdelkhalek and Lam3/Tec3-**MSBM** detect flatness defects on the edges of the strip (see Figure 6.14). The additional strains are not necessarily of the same order since these models are based on different hypotheses. $\Delta\varepsilon$ is computed by the buckling model of Abdelkhalek according to the formulas recalled in Figure 2.18.

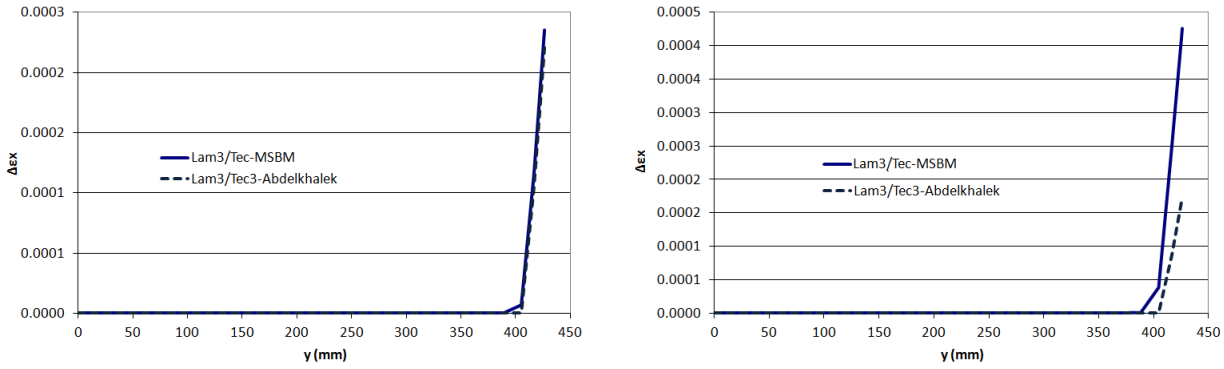

(a) (b)

Figure 6.14: The buckling strain computed by Lam3/Tec3-Abdelkhalek and Lam3/Tec3-MSBM plotted on transverse section. (a): near the bite exit $\simeq$ 10 mm, (b): far from the bite exit $\simeq$ 1 m. In Lam3/Tec3-Abdelkhalek, $\sigma_{cr} = -250$ MPa has been assumed for comparison.

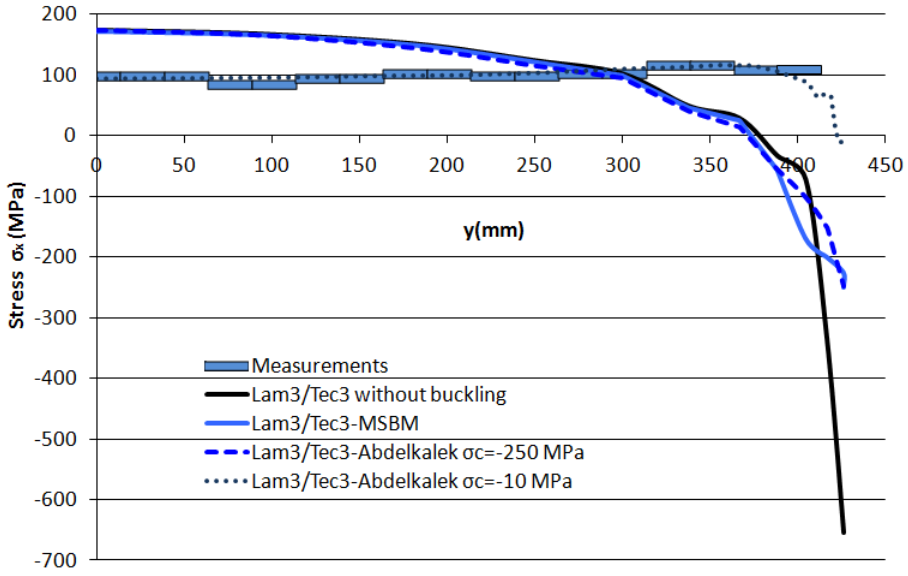

Figure 6.15: Comparison between the stress transverse profile $\sigma_{xx}(y)$ computed by Lam3/Tec3 standard version, by Lam3/Tec3-Abdelkhalek, by Lam3/Tec3-**MSBM** and the measurements provided by the flatness rolls.

As for the post-buckling stresses, Figure 6.15 presents a confrontation between profiles $\sigma_{xx}(y)$ provided by the measurements and the two rolling buckling models Lam3/Tec3-Abdelkhalek and Lam3/Tec3-**MSBM**. Note that both numerical profiles match well and behave alike on the edge. In addition they show, on this particular section (far from the bite exit), that the detected edge defects are able to relax the stresses up to the critical

value −250 MPa. However in the center, neither numerical stress profile matches the experimental curve.

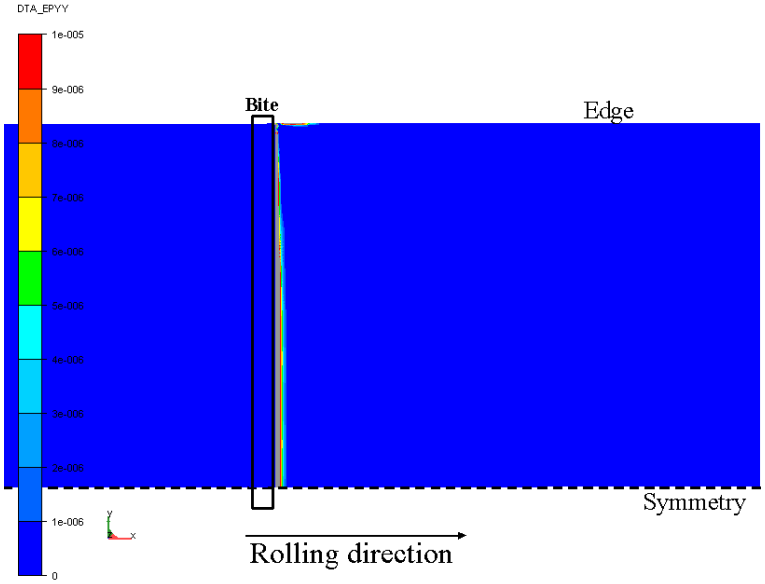

(a): Lam3/Tec3-Abdelkhalek; $\sigma_{cr} = -10$ MPa

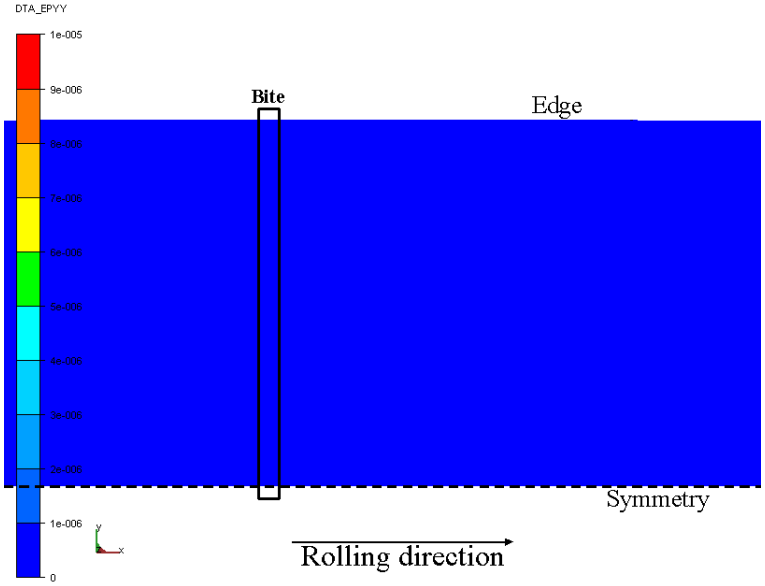

(b): Lam3/Tec3-Abdelkhalek; $\sigma_{cr} = -250$ MPa

Figure 6.16: The additional strain $\Delta\varepsilon_y$ map using Lam3/Tec3-Abdelkhalek for $\sigma_{cr} = -10$ MPa and $\sigma_{cr} = -250$ MPa.

In Lam3/Tec3-**MSBM**, no defects were detected in the strip center near the bite exit since the **MSBM** cannot describe the transverse defects such as folds appearing near the bite exit due to compressive stresses $\sigma_{yy}(y)$. Normally, if transverse waves can be detected in the bite exit, additional strains $\Delta\varepsilon_x$ and $\Delta\varepsilon_y$ are computed and can adjust the stress

profiles in the center to match at least the concavity of the measurements.
To confirm that detecting folds in the strip center after bite exit is one of the main reasons behind this mismatch, we plot the transverse stress profile using Lam3/Tec3-Abdelkhalek with $\sigma_{cr} = -10$ MPa. The new stress profile is in a good agreement with the measurements. A lower critical stress value allows the compressive stress $\sigma_{yy}(y)$ to be treated after bite-exit. Figure 6.16 shows that transverse folds can be detected in the center and lead to additional strains $\Delta\varepsilon$ changing the concavity of the stress profile in the center. For $\sigma_{cr} = -250$ MPa no center defect is detected and the stress profile does not match the measurements. As for $\sigma_{cr} = -10$ MPa defects are detected in the center suggesting the forming of transverse folds after bite-exit and the corresponding post-buckling stress profile match the measurements.
This suggests that the post-buckling stresses computed using Lam3/Tec3-**MSBM** are not properly redistributed due to the incapacity of **MSBM** to detect defect forming in the $y-$direction such as transverse folds.

6.4.2 Lam3/Tec3-MSBM vs. Lam3/Tec3-MAN

The software Lam3/Tec3-**MAN** is not only capable of computing the critical value, detecting the defected zone and relaxing the stresses by buckling, but also determining the defect height and following its evolution on-line and off-line (under and after release of strip tension).
Again using the same rolling operation, the results are confronted and analyzed below:

- The stress value tolerated on the edges -corresponding to $\lambda^{res} \sim 0.24$- computed respectively by Lam3/Tec3-**MSBM** and Lam3/Tec3-**MAN**2013 under a strip tension of 100 MPa are -250 MPa and -252 MPa. This confirms that for the linear problem both models find the same results.

- Figure 6.17 presents the stress profiles supplied by the measurements and the two rolling-buckling softwares Lam3/Tec3-**MAN** and Lam3/Tec3-**MSBM**.

  - For $\lambda^{res} \sim 0.24$ Lam3/Tec3-**MAN**, similar to Lam3/Tec3-**MSBM**, relax the stress on the edges to -250 MPa. The concavity in the center changes as well, yet still far from respecting the experimental curve.

  - For $\lambda^{res} = 1$, it is clear that the concavity of the stress profile provided by Lam3/Tec3-**MAN** is in a good agreement with the experimental curve. The concavity of both curves match and the stress profile is redistributed and is equal to 38 MPa on the edge.

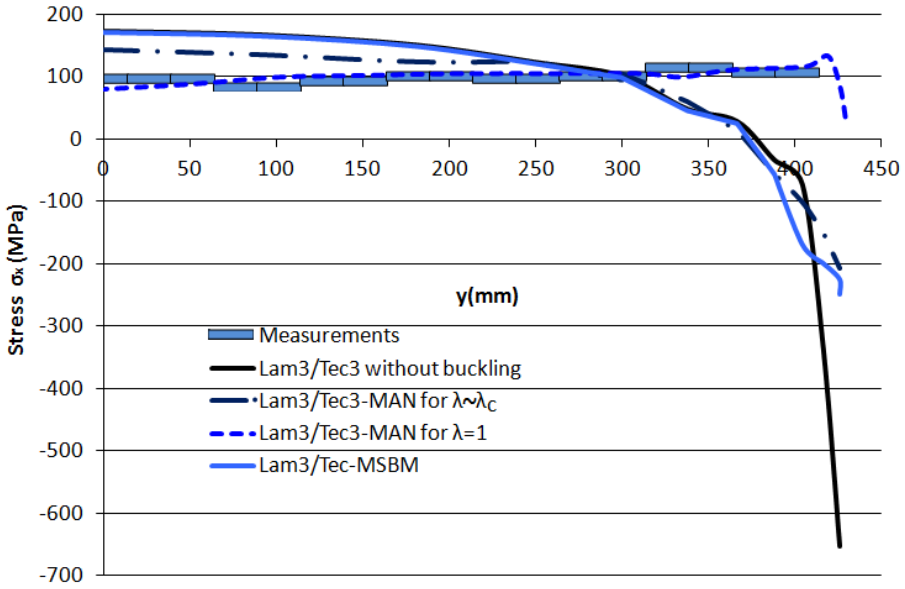

Figure 6.17: Comparison between the stress transverse profile $\sigma_{xx}(y)$ computed by Lam3/Tec3 standard version, by Lam3/Tec3-**MAN**, by Lam3/Tec3-**MSBM** and the measurements provided by the flatness rolls.

◇ The latter points imply that two reasons may be behind the poor agreement of the stress profile computed by Lam3/Tec3-**MSBM** and the experimental results. It is partially caused by

- the incapacity of **MSBM** to describe transverse waves as **MAN** does (see Figure 6.19) and by that cannot change the concavity of the stress profile σ_{xx}.
- fixing the mode W corresponding to λ_{cr} and adopting it for every $\lambda > \lambda_{cr}$. This simplification affects the waves amplitude and by that fails to relax properly the stress profile. It is confirmed in Figures 6.18 and 6.19.

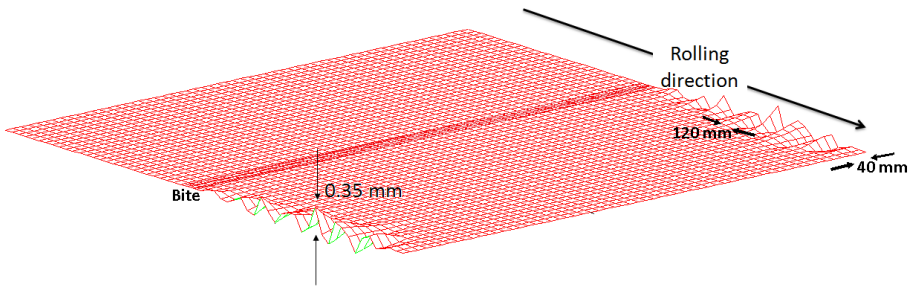

Figure 6.18: The defected plate under strip tension described using Lam3/Tec3-MSBM obtained for $\lambda = 1$.

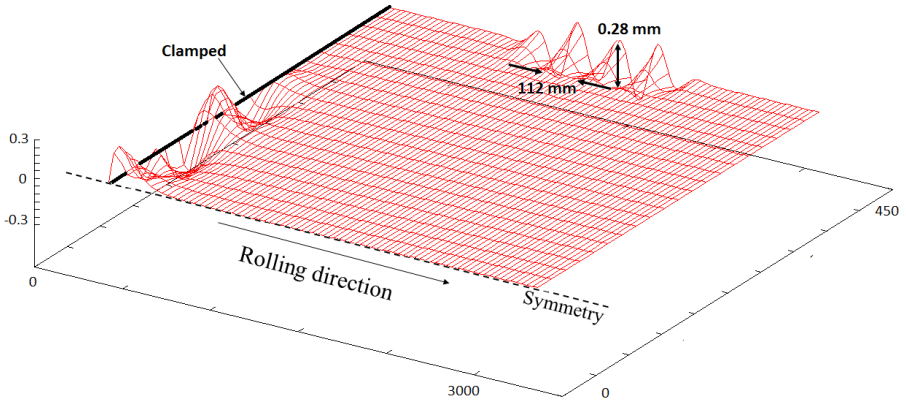

(a): $\lambda^{res} \sim 0.24$, wavelength= 224 mm, amplitude= 0.28 mm

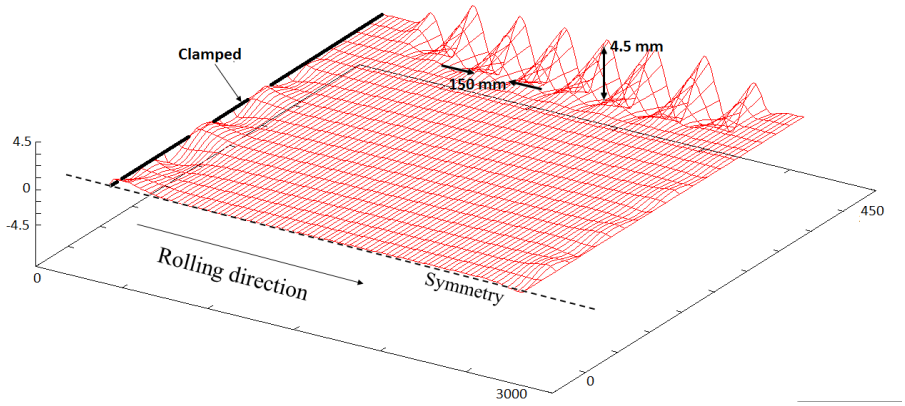

(b): $\lambda^{res} = 1$, wavelength= 300 mm, amplitude= 4.5 mm

Figure 6.19: The defective plate under strip tension illustrated using Lam3/Tec3-**MAN**2013 for $\lambda^{res} \sim 0.24$ and $\lambda^{res} = 1$

When studying the buckling of the strip using Lam3/Tec3-**MAN** (for this particular rolling operation), the longitudinal folds appear first (for $\lambda^{res} = 0.03$). Then, they are followed by the undulation generation along the edges.

Comparing the strip post-buckled state, Figures 6.18 and 6.19 confirms that both models detect defects along the edges. The depth of the waves are more or less comparable, equal to 40 mm approximately. For $\lambda^{res} \sim 0.24$ Lam3/Tec3-**MAN** computes an amplitude of 0.28 mm, as for $\lambda^{res} = 1$ it is equal to 4.5 mm. Lam3/Tec3-**MSBM** detects waviness of 0.35 mm height. It is rather comparable with the results of Lam3/Tec3-**MAN** at $\lambda^{res} \sim 0.24$.
This indicates that blocking the same mode W for the whole post-buckling study affects significantly the wave magnitude and by that induces poor agreement between the numerical stress profile and the experimental one. It is advised to reconsider this point trying to follow the evolution of the buckling mode beyond the bifurcation point (maybe consider

an iterative scheme as the one used in **MAN**), especially if we aim to a more general model -capable of describing the defects before and after cancellation of strip tension -.
For this same rolling operation, Counhaye in his thesis [Counhaye, 2000] measured the wave defect: the wave depth was equal to 10 mm, the wavelength was 70 mm and the amplitude was approximately equal to 1 mm. This certifies that the type of defect predicted by both models is the same as observed by Counhaye.
Note that, even though Lam3/Tec3-**MAN** is yet the most powerful model of all these mentioned above, the magnitude of the defects amplitude is still not validated due to lack of experimental data and literature studies treating exactly the same problem.

6.4.3 Discussions

The same rolling operation is modeled using all the above-mentioned coupled rolling - buckling models. The computational cost is summarized in Table 6.1.

Model	Computing time (CPU)
Lam3/Tec3	$T_{CPU} = 4h$ 22 min
Lam3/Tec3-Abdelkhalek	(1.2 to 1.5) $\times T_{CPU}$
Lam3/Tec3-MAN	(3 to 4) $\times T_{CPU}$
Lam3/Tec3-MSBM	(1.4) $\times T_{CPU}$

Table 6.1: Summary of the cost in terms of computing time (CPU) for : the standard rolling model Lam3/Tec3, The simple rolling-buckling model Lam3/Tec3-Counhaye, Lam3/Tec3-MAN the Finite element rolling model coupled with the shell element buckling model MAN and Lam3/Tec3-**MSBM** the rolling model Lam3/Tec3 coupled with the multi-scale buckling model.

Compared with the non-buckling model (Lam3/Tec3), both Lam3/Tec3-Abdelkhalek and Lam3/Tec3-MSBM mean an extra-cost of 20 to 50%, representing the time needed to process the stress field and the price of more iterations due to the more complex strain decomposition. By contrast, Lam3/Tec3-MAN costs 200 to 300% more, to which the user's manipulation time must be added. One of the reasons for the difference is the full integration of the first two buckling models, which means that the rolling and buckling computations are performed in one shot. On the contrary, the latter requires typically three full Lam3/Tec3 simulations.
This observation must be balanced against the difference in performance. It must be recalled first that in the absence of precise experimental, quantitative assessment of the waves geometry, all that can be done is judge 1) quantitatively by the stress profile -as measured by the flatness roll, 2) qualitatively by the likelihood of the shape of the com-

puted waves compared with the stress profile.

Lam3/Tec3-MAN2013 is clearly the most powerful in this respect. Not only does it compute a stress profile $\sigma_{xx}(y)$ in good agreement with the measurement, but is also detects the two sets of waves, longitudinal in the center at bite exit, and transversal on the edge further down the line. The amplitude of the latter, though apparently larger than measured by [Counhaye, 2000], remains realistic.
Lam3/Tec3-Abdelkhalek also gives a correct $\sigma_{xx}(y)$ profile, and detects the two types of waves. Its drawback is the limited information it gives on the wave amplitude. Not that it is completely absent: the shortening is a function of two variables which are not computed in this model, the wavelength and the amplitude - if one chooses a wavelength, the amplitude comes out. The reason is that the technique of Roddeman - Counhaye - Abdelkhalek never chooses a wave shape or mode, contrary to all other models where a mode is pre-shaped or computed - sinusoidal in one or even two directions. This geometrical choice therefore has to be made afterwards if the ambiguity between wavelength and amplitude is to be eliminated.
The choices made here for the Multi-Scale model, namely a sinusoidal development in the $x-$direction only, allow only an estimate of the edge waves amplitude and wavelength. It is different from those given by Lam3/Tec3-MAN, but compatible with what is known from the experiments. The longitudinal waves cannot be predicted, by construction of the model, and it turns out that this does not allow computing a good stress profile. This by the way shows the strong interaction between the longitudinal waves formed under σ_{yy} and the mechanical process which leads to the σ_{xx} stress relaxation by the transverse waves.

Another important argument in favor of Lam3/Tec3-**MAN** is that it allows determining flatness not only on line, under strip tension, but also after strip tension release. This is of course essential in terms of product quality. With the other two models, the state after tension release can be more or less qualitatively guessed from the residual stress profile relaxed after buckling, by subtracting T_0 and analyzing the resulting profile, but the non-linearity of the relaxation process, with possible mode changes, might well yield questionable results in some cases.

Therefore, if coupled models are preferred, the choice in the present state is clearly between the most powerful Lam3/Tec3-**MAN** and the less costly Lam3/Tec3-Abdelkhalek, under the reservation of the verification by experiments of the conclusions on wave geometry, and also of more tests in different rolling cases. Lam3/Tec3-**MSBM** lies in be-

tween, giving quantitative results on the wave geometry which Lam3/Tec3-Abdelkhalek can hardly suggest, but an erroneous final, residual stress state. Is the latter important in practice? It should condition the wrinkling and twisting of the blanks cut from the strip in the press shop, which is not a small deal.

Now the question is: in scientific terms, calculating altogether elastic-plastic strip deformation, roll stack elastic deformation, buckling of the free strip is a beautiful problem of solid mechanics, accounting for all the possible couplings, feedbacks, interactions, but is it really necessary *in practice?*

Abdelkhalek has not found a significant impact of buckling, although it completely redistributes stress away from the bite, on the strain and stress fields in the bite. The absence of this interaction suggests that a two-step, decoupled model could be sufficient to characterize the behavior even on-line (under tension). Indeed, the two-step computation using MAN (2013 version) gives seemingly good results, in terms of shape and of relaxed stress profile (see Figures 2.23 and 2.24), little different from the coupled version.
Lam3/Tec3-**MSBM** cannot detect longitudinal folds, neither in the coupled nor in the decoupled version. However, these particular defects do not impact product quality. On the contrary, it does detect edge waves, although much smaller (0.2 mm amplitude) than Lam3/Tec3-MAN (3 mm). It can therefore be said that its performance is good in the decoupled strategy, with the advantage over Lam3/Tec3-Abdelkhalek that it attributes an amplitude and a wavelength to the waves. It thus appears, in the decoupled version, as a good compromise between performance and cost.

Finally, the **MSBM** can still be improved for a better performance. Two options are available:

i) Choose a more general form for the solution, taking into account buckling in both directions x and y:

$$w(x,y) = \sum_m w_m(x,y) e^{im[q_1 x + q_2 y]} \tag{6.2}$$

where q_1 and q_2 are respectively the half-wave number in the $x-$direction and $y-$direction.
The Fourier coefficients are no longer dependent of a single variable x and there will be in addition m orders for each direction x and y. The **MSBM** will be transformed into $2D$ Finite Element Model costing more computational time. Some hypotheses similar to the ones proposed previously in chapter 4 could be proposed to reduce the microscopic system: simplification regarding the form of the defects and its

derivatives (if the defect amplitude is changing more slowly in one direction than in the other) etc. Anyway, these equations will be considerably more complex and will consume more computational time than the ones presented for the current **MSBM**. This modification could allow fold detection changing the center concavity and redistributing stresses on the edges to respect hopefully the experimental measurements. Note that these changes could affect the amplitude of the edge waviness as well.

ii) Another alternative is to preserve the same **MSBM** (i.e the same development) but use it two times to detect both defects. In a first stage, the **MSBM** could be used to detect defects in the $y-$direction. It could be studied all over the plate or in a particular zone such as the bite-exit, where σ_y is highly compressive. In a second stage, the **MSBM** could be used to detect waviness in the $x-$direction all over the strip as before. Note that using the same **MSBM** to detect the folds in the $y-$direction can be easily done by switching x by y and σ_x by σ_y in the microscopic system. Of course the transverse sections should be switched as well to longitudinal ones to keep the same foundations.
It is likely that once transverse folds are detected, the stresses in particular σ_y would be relaxed and no longer cause problems as the ones faced before.

These improvements, if successful, could be used in the coupled model to simultaneously detect the longitudinal folds, and find the correct stress profile. In the decoupled version, it could improve the computation of the amplitude of the edge waves by treating the interaction between the two types of waves.

6.5 Conclusion

First, the coupling of the buckling model **MSBM** and the rolling model Lam3/Tec3 has been presented. Then, predicting flatness defects using the resulting model Lam3/Tec3-**MSBM** was explored. To analyze the results and the limitation of this model, several comparisons were examined. With the experimental measurements as well as with other available numerical results (Lam3/Tec3-Abdelkhalek and Lam3/Tec3-**MAN**), it was established that the model Lam3/Tec3-**MSBM** needs to be extended. To simulate accurately industrial applications such as buckling during cold rolling operations, it should be capable of describing defects in both directions x and y as well as following the mode evolution post-buckling. Finally, the possible improvements were explored and discussed in the last section.

6.6 Résumé en Français

Dans ce chapitre le couplage entre le modèle de flambage (basé sur une méthode multi-échelle) **MSBM** et le modèle de laminage Lam3/Tec3 a été présenté.
D'abord, la capacité du modèle résultant, nommé Lam3/Tec3-**MSBM**, à prédire les défauts de planéité sous traction (en ligne) a été explorée. Puis, les résultats et limitations de ce modèle ont été analysés en utilisant des comparaisons avec des mesures expérimentales et d'autres résultats numériques disponibles (Lam3/Tec3-Abdelkhalek et Lam3/Tec3-**MAN**). Ces derniers ont établi que le modéle Lam3/Tec3-**MSBM** doit être enrichi pour simuler précisement des applications industrielles telles que les opérations de laminage à froid. Cela devrait être capable de décrire des défauts dans les deux directions x et y aussi bien que suivre l'évolution du mode de flambage au delà du premier point de bifurcation. Finalement, les améliorations possibles ont été explorées et discutées dans la dernière section.

CONCLUSIONS AND RECOMMENDATIONS

1 Conclusions

This work is a first attempt investigating the feasibility of the implementation of a multi-scale based buckling model in a strip rolling software (Lam3/Tec3), where the resulting model is capable of:

- Detecting and describing on-line defects geometrically i.e. under strip tension
- Taking into account the roll-stack deformation coupling
- Taking into account the bite-buckling interactions

We started from the standard version of the rolling software Lam3/Tec3, where the coupling between the strip and roll stack deformation is already realized. A simulation accomplished using Lam3/Tec3 showed that the stress transverse profiles are unrealistic and in poor agreement with the experimental measures. As proved in previous works [Counhaye, 2000] and [Abdelkhalek, 2010], the strip-roll stack coupling is not enough. Buckling must be taken into account if it occurs on-line under strip tension (manifest defect) as is often the case for very thin strips.

To upgrade the performance of Lam3/Tec3, two improvements were introduced by Abdelkhalek in [Abdelkhalek, 2010]:

- The first is a simple buckling model implemented completely in Lam3/Tec3. The resulting model was called Lam3/Tec3-Abdelkhalek. It is able to detect the defective

zone and redistribute the stress post-buckling. But it is unable to quantify the flatness defects (their magnitude), only the shortening/lengthening of the material lines.

- The second is coupling the $3D$ finite element model Lam3/Tec3 with the shell buckling model **MAN**. The resulting model -called Lam3/Tec3-**MAN**- is able of detecting the defective zone, quantifying the waviness and relaxing the stresses due to buckling. Due to two different formulations ($3D$ vs. shell FE) the coupling was done manually. As a result, the use of this model is tricky and costly.

In the present Ph.D. work, the aim was to find a buckling model simple enough to be implemented completely in Lam3/Tec3 yet rich enough to be able to describe and quantify also the strip buckled shape.
After an overview of the origin of flatness defects in cold rolling (Chapter 1), the literature was scanned to find a potential model corresponding to our needs (Chapter 2). The multi-scale approach proposed in [Damil & Potier-Ferry, 2006] was considered a good candidate. Combined with von Kármán's equations, the multi-scale approach applied on predicting on-line flatness defects during rolling processes was presented in Chapter 4. Several simplifications were imposed such as supposing that the waves will only appear in the $x-$direction (rolling direction). This allows transforming the problem into a $1D$ problem browsing the strip transverse section by transverse section.
In the same chapter, the capacity of the multi-scale buckling model called **MSBM** was tested using academic examples (parabolic stress profiles) then confronted to other available buckling studies such as **MAN**, Abaqus and the analytic study presented by [Fisher et al., 2001]. The results were found satisfactory.
Chapter 5, explored the capacity of the decoupled **MSBM** applied on real rolling operations i.e. with complex stress profiles imported from the rolling software Lam3/Tec3. Different studies tested the behavior of the **MSBM** with changing parameters such as friction and work roll bending. The decoupled model gave good results -describing the flatness defects- with very reasonable tendencies -evolution of the defect with friction and the WRB force.
The coupling of the **MSBM** with Lam/Tec3 (Chapter 6) has met several difficulties due to the rapidly varying stress σ_y just after bite exit. Since it is supposed that waves will only develop in the rolling direction, the **MSBM** is unable to detect defects in the transverse direction. Not redistributing the stresses σ_y has caused numerical instabilities after bite exit.

2 Recommendations

In summary, the future work should be directed to:

- ◇ Enriching the current **MSBM** to be capable of :
  - describing waviness in all directions,
  - following the evolution of the buckling mode beyond the first bifurcation point λ_{cr} i.e. similar to the shell model **MAN**.
- ◇ Coupling the enriched buckling model in Lam3/Tec3 and validate the results by confrontation with the experimental measurements:
  - the Meplaca device and/or the laser measurement instruments for manifest defects,
  - the flatness roll for latent defects.
- ◇ Revisit the bite-buckling interaction study using the upgraded multi-scale buckling model.
- ◇ Repeat the same studies, presented for the decoupled approach in chapter 5, using instead the coupled approach Lam3/Tec3-**MSBM**. The effects of friction and the work roll bending force on the strip flatness established for both approaches should be confronted.
- ◇ Take into account the thermal effects in Lam3/Tec3-**MSBM** and confirm if they are insignificant as supposed in this study.

Another important point, that remains an open debate, is whether the rolling-buckling problem should be treated in the context of a coupled approach or not.
The results presented by Abdelkhalek in [Abdelkhalek, 2010], for the treated rolling operations, suggest that the bite and post-bite states are nearly decoupled. Thus, it favors the use of decoupled approaches that are widely spread in the literature.
Future works should investigate, via numerical and experimental means, the truth behind this suggestion. If it is the case, one must consider seriously treating the problem in a decoupled manner. It simplifies considerably the problem and allows the use of all the available techniques from the simplest to the most complicated ones, avoiding all sorts of compatibility restrictions with the software to be coupled with.

APPENDIX A

A.I Roll crown

The crown of the roll C_r is defined as the difference between its center diameter D_c and its edge diameter D_e:

$$C_r = D_c - D_e \tag{A.1}$$

The curvature of the roll affects the way the roll interacts with the strip. For the ideal flat strip, both the shape of the strip and the roll should match perfectly. Figure A.1 illustrates rolls presenting negative, positive and neutral crown.

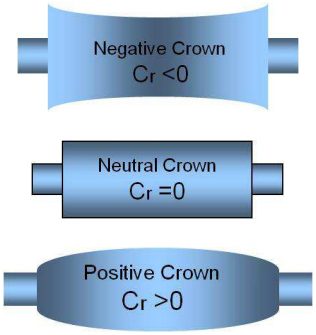

Figure A.1: The different types of roll crown

A.II Strip crown

At the exit of a hot roll mill, a strip can present a non-uniform thickness along its width. H_c denotes the thickness of the strip along its vertical centerline and H_e its thickness along the edges. A choice has been made to define a third value called feather thickness H_f

measured on a feather slightly distant from the edge where the measurement are judged reliable. Similar to the rolls, the strip profile is also measured by crown. Equation 1.4 defines the strip crown C_s:

$$C_s = H_c - H_f \tag{A.2}$$

as the difference in thickness between the center of the strip H_c and the feather H_f . Figure A.2 shows the different strip crown types.

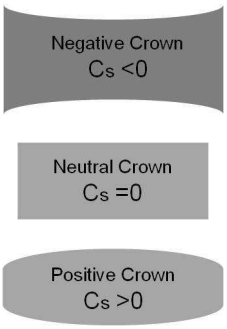

Figure A.2: The different types of strip crown.

APPENDIX B

B.I Lam3

Lam3, the rolling model devoted to rolling thin strips uses a quasi-Eulerian formulation. The equilibrium equation and the Elastic-visco-plastic behavior law are presented respectively in equations ((B.1)), ((B.2)) and ((B.3)).

$$\text{For every } V^*, \int_\Omega \sigma(V) : D^* d\Omega - \int_{\partial\Omega_c} \tau_t V^* dS - \int_{\partial\Omega_c} \sigma_n . n V^* dS - \int_{\partial\Omega_f} T^{imp} V^* dS = 0 \quad \text{(B.1)}$$

$$\text{Plastic formulation : } \begin{cases} \dot{p} = -\chi tr(D) \\ d = \dfrac{\dot{s}^J}{2\mu} + \dfrac{3}{2}\dfrac{\dot{\bar{\varepsilon}}}{\sigma_0(\bar{\varepsilon}, \dot{\bar{\varepsilon}})} s \text{ if } \dot{\bar{\varepsilon}} \in \mathbb{R}^+ \quad \text{or,} \\ \sqrt{\dfrac{3}{2} s : s} = \sigma_0(\bar{\varepsilon}, \dot{\bar{\varepsilon}}) \end{cases} \quad \text{(B.2)}$$

$$\text{Elastic formulation : } \begin{cases} \dot{p} = -\chi tr(D) \\ d = \dfrac{\dot{s}^J}{2\mu} \text{ if } \dot{\bar{\varepsilon}} \in \mathbb{R}^{-*} \end{cases} \quad \text{(B.3)}$$

We recall that Lam3/Tec3 uses a structured meshing formed by hexahedric elements. The mesh nodes form streamlines and are updated to conserve the streamlines properties. Thus the nodes position $x = (x, y, z)$ respect always equations (B.4), where V is the speed

field, solution of equation ((B.1)):

$$\begin{aligned} y_{k+1} &= y_k + \int_{x_k}^{x_{k+1}} \frac{V_y(x)}{V_x(x)} dx \\ z_{k+1} &= z_k + \int_{x_k}^{x_{k+1}} \frac{V_z(x)}{V_x(x)} dx \end{aligned} \tag{B.4}$$

where k and $k+1$ are the indices of two consecutive nodes belonging to the same streamline.
This equation ((B.4)) is iteratively solved with the system ((B.1))-((B.3)) to improve the computing domain shape approximation. Between two iterations are also computed the elastic roll stack deformation (if activated - see section B.II) and the rolls/strip temperatures (if the thermal coupling is activated).

Since the used formulation is stationary, the time step integration is replaced by a space step (where the speed/space ratio replace the time step). To solve the elasto-plastic and differential equations, the time step represents the time needed to pass from a Gauss integration point to the next one (on the same streamline). This fictive time step depends from the Gauss point positions and this scheme is called GLHTS (Generalized Large Heterogeneous Time-Step).

B.II Tec3

Tec3 is a stand-alone model containing several features:

- ◇ A steady/unsteady thermal model
- ◇ A work roll thermal crown estimation model
- ◇ A work roll and strip meshing model
- ◇ A roll stack deformation model with a coupling option with Lam3

Tec3 uses the strip stress distribution computed by Lam3 to determine the strip-WR contact pressure as:

$$\sigma_n = \sigma.n_c \tag{B.5}$$

where n_c is the orthonormal vector on the strip-WR contact surface.
The stress σ_n is used for the $3D$ elastic stack deformation modules where the roll bending/flattening are described using Timoshenko beam theory and Boussinesq model. The

contact between the rolls (work and backup rolls) including the 'Roll Kiss' phenomenon is taken into account using the $3D$ Hertzian contact model.

B.III Shell element description used by MAN

The basis used within the **MAN** formulation is simple; it rests on the classic theories of plates and shells.
The position of any point of the deformed geometry -described in Figure B.1- is located on the initial configuration by a vector x expressed as follows:

$$x(\theta_1, \theta_2, \theta_3) = r(\theta_1, \theta_2) + \theta_3 a_3(\theta_1, \theta_2) \tag{B.6}$$

where r is a vector defining the position of the mid-surface, $(\theta_1, \theta_2, \theta_3)$ indicate the convective curvilinear coordinates and a_3 is the normal vector defined on this point.
Supposing that the displacement in the thickness direction is linear, it can be defined as:

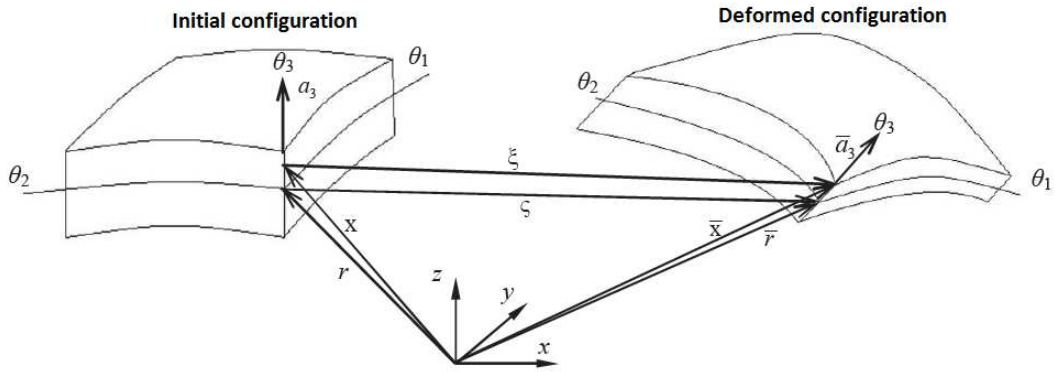

Figure B.1: Geometric and kinematic description of the shell element used by **MAN**.

$$\xi(\theta_1, \theta_2, \theta_3) = \xi(\theta_1, \theta_2) + \theta_3 \omega(\theta_1, \theta_2) \tag{B.7}$$

where ξ and ω are respectively the displacement defined on a mid-surface point and the variation between the initial normal vector and the deformed normal vector. Now, the vector $\bar{x}$ describing the deformed configuration can be defined as:

$$\bar{x} = (r + \xi) + \theta_3(a_3 + \omega) = \bar{r} + \theta_3 \bar{a}_3 \tag{B.8}$$

From equations ((B.7)) and ((B.8)), the components of the contravariant Green-Lagrange strain tensor γ^c can be deduced as follows:

$$\gamma^c_{ij} = \alpha_{ij} + \theta_3\beta_{ij} + (\theta_3)^2 Q_{ij} \tag{B.9}$$

$$a_3 = \frac{\partial x}{\partial \theta_3};\ \bar{a}_3 = \frac{\partial \bar{x}}{\partial \theta_3}$$

$$a_i = r_i;\ \bar{a}_i = \bar{r}_i$$

$$\alpha_{ij} = \frac{1}{2}(\bar{a}_i\bar{a}_j - a_i a_j)$$

$$\beta_{ij} = \frac{1}{2}(\bar{a}_{3,i}\bar{a}_j + \bar{a}_{3,j}\bar{a}_i + a_{3,i}a_j + a_{3,j}a_i)$$

where $\beta_{i,3} = \frac{1}{2}(\bar{a}_{3,i}\bar{a}_3 + a_{3,i}a_3)$

$$\beta_{33} = 0$$

$$Q_{ij} = \frac{1}{2}(\bar{a}_{3,i}\bar{a}_{3,j} - a_{3,i}a_{3,j})$$

$$Q_{i3} = 0$$

$$Q_{33} = 0$$

The term β_{33} is equal to zero due to the the linearity hypothesis of the displacement vector in the thickness direction. This can generate locking problems in some cases. To avoid this kind of problem, Buchter et al. [Buchter et al., 1994] demonstrate that γ^c_{33} must be at least linear in the thickness; meaning that β_{33} has to be at least a non-zero constant in the thickness direction. Therefore, an additional strain called the non-compatible or enhanced strain $\tilde{\gamma}$ is introduce into the formulation. By means of the concept Enhanced Assumed Strain (EAS) proposed in [Simo & Rifai, 1990]; this additional strain must be orthogonal to the stress field and independent of the displacement vector.
This deformation represents the linear variation of γ^c_{33} in the thickness and hence should verify:

$$\begin{aligned} &\tilde{\gamma} = \gamma - \gamma^c \\ &\int_\Omega (S^t : \tilde{\gamma}) d\Omega = 0 \end{aligned} \tag{B.10}$$

BIBLIOGRAPHY

[IHI website] www.ihi.co.jp

[ARKU website] www.arku.com

[Arcelormittal website] www.arcelormittal.com

[Indwitech website] www.indwitech.com

[ltvsteel website] www.ltvsteel.com

[Steel website] www.steel.org

[Abaqus, 2008] Abaqus Inc. *ABAQUS documentation* version 6.8, Dassault Systems, 2008.

[Abdelkhalek et al., 2008] S. Abdelkhalek, P. Montmitonnet, N. Legrand, P. Buessler. *Manifested flatness predictions in thin strip cold rolling.* Int. J. Mater. Form., 2008, Vol.1, pp. 339-342.

[Abdelkhalek et al., 2009] S. Abdelkhalek, H. Zahrouni, M. Potier-Ferry, N. Legrand, P. Montmitonnet, P. Buessler. *Coupled and uncoupled approaches for thin cold rolled strip buckling prediction.* Int. J. Mater. Form., 2009, Vol.2, pp. 833-836.

[Abdelkhalek, 2010] S. Abdelkhalek. *Un exemple de flambage sous contraintes internes: Étude des défauts de planéité en laminage à froid des tôles minces.* PhD Thesis, MINES ParisTech, 2010 (in French).

[Abdelkhalek et al., 2011] S. Abdelkhalek, P. Montmitonnet, N. Legrand, P. Buessler. *Coupled approach for flatness predictions in thin strip cold rolling.* Int. J. Mech. Sci. 2011, Vol. 53, pp. 651-675.

[Ben Dhia, 1998] H. Ben Dhia. *Problèmes mécaniques multi-échelles : la méthode Arlequin.* CRAS - IIB - Mechanics- Physics-Astronomy, 1998, Vol. 326, pp. 899-904. (in French)

[Ben Dhia & Rateau, 2001] H. Ben Dhia, G. Rateau. *Analyse mathématique de la méthode Arlequin mixte.* CRAS - I - Mathematics, 2001, Vol. 332, pp. 649-654. (in French)

[Ben Dhia & Jamond, 2010] H. Ben Dhia, O. Jamond. *On the use of XFEM within the Arlequin framework for the simulation of crack propagation.* Comput. Meth. Appl. Mech. Engg, 2010, Vol. 199, pp. 1403-1414.

[Berger & Fife, 1996] M. S. Berger, P. C. Fife. *On von Kármán's equations and the buckling of a thin elastic plate*, Bull. Am. Math. Soc., 1966, Vol. 72, pp. 1006-1011 .

[Berger, 1967] M. S. Berger. *von Kármán's equations and the buckling of a thin elastic plate. I, The clamped plate*, Commun. Pure Appl. Math., 1967, Vol. 20, pp. 687-719.

[Berger et al., 1976] B. Berger, O. Pawelski, P. Funke. *Die elastische Verformung der Walzen von Vierwalzengerüsten.* Arch. Eisenhüttenwes. 1976, Vol. 47, 6, pp. 351-356 (in German).

[Bland & Ford, 1952] D.R. Bland, H. Ford. *An approximate treatment of the elastic compression of the strip in cold rolling.* J. Iron Steel Inst.,1952 Vol. 171, p.245.

[Boutyour et al., 2004] E.H. Boutyour, H. Zahrouni, M. Potier-Ferry, M. Boudi. *Bifurcation Points and Bifurcated Branches by an Asymptotic Numerical Method and Padé Approximants.* Int. J. Num. Meth. Engrg, 2004, Vol. 60, pp. 1987-2012.

[Buchter et al., 1994] N. Buchter, E. Ramm, D. Roehl. *Three dimensional extension of non-linear shell formulation based on the Enhanced Assumed Strain Concept.* Int. J. Numer. Meth. Engg, Vol. 37, No. 22, 1994, p. 2551-2568.

[Budiansky, 1974] B. Budiansky. *Theory of Buckling and Post-Buckling Behavior of Elastic Structures*, Adv. Appl. Mech., Academic Press, N.Y., 1974, Vol. 14, pp. 1-65.

[Bush et al., 2001] A. Bush, R. Nicholls, J. Tunstall. *Stress levels for elastic buckling of rolled strip and plate.* Ironmaking and steelmaking, 2001, Vol. 28, pp. 481-484.

[Cochelin, 1994] B. Cochelin. *Méthode asymptotique-numérique pour le calcul non-linéaire géométrique des structures élastiques, Habilitation à diriger des recherches*, Université de Metz, 1994 (in French).

[Cochelin et al., 1994] B. Cochelin, N. Damil, M. Potier-Ferry. *The asymptotic-numerical method: an efficient perturbation technique for non-linear structural mechanics*, Revue Européenne des Éléments Finis, 1994, Vol.3, pp. 281-297.

[Counhaye, 2000] C. Counhaye. *Modélisation et contrôle industriel de la géométrie des aciers laminés à froid.* PhD Thesis, Liège University, 2000 (in French).

[Damil & Potier-Ferry, 1986] N. Damil, M. Potier-Ferry. *Wavelength selection in the post-buckling of a long rectangular plate.* Int. J. Solids and Structures, 1986, Vol. 22, pp. 511-526.

[Damil & Potier-Ferry, 1990] N. Damil, M. Potier-Ferry. *A new method to compute perturbed bifurcation. Application to the buckling of imperfect elastic structures*, Int. J. Engrg. Sci. , 1990, Vol. 26, pp. 943-957.

[Damil & Potier-Ferry, 2006] N. Damil, M. Potier-Ferry. *A generalized continuum approach to describe instability pattern formation by a multiple scale analysis.* Comptes Rendus Mécanique, 2006, Vol. 334, pp. 674-678.

[Damil et al., 2013] N. Damil, M. Potier-Ferry, H. Hu. *New nonlinear multi-scale models for wrinkled membranes.* Comptes Rendus Mécanique, 2013, Vol. 331, pp. 616-624.

[Euler, 1744] L. Euler. *Additamentum I de curvis elasticis, methodus inveniendi lineas curvas maximi minimive proprietate gaudentes*, Bousquent, Lausanne, in Opera Omnia I, 1744, Vol. 24, pp. 231-297. (English translation by W. A. Oldfather, C. A. Ellis and D. M. Brown, 1933)

[Fisher et al., 2001] F.D. Fischer, F.G. Rammerstorfer, N. Friedl. *Buckling of free infinite strips under residual stress and global tension.* ASME, J. App. Mech., 2001, Vol 68, pages 339-404.

[Fisher et al., 2003] F.D. Fischer, F.G. Rammerstorfer, N. Friedl. *Residual Stress-Induced Center Wave buckling of rolled strip metal.* ASME, J. App. Mech., 2003, Vol 70, pages 84-90.

[Gere & Goodno, 2012] J. M. Gere, B. J. Goodno. *Mechanics of Materials*, Course Technology, 8th edition. 2012.

[Ginzburg, 2009] V. B. Ginzburg. *Flat-Rolled Steel Processes: Advanced Technologies*, CRC Press, Taylor and Francis Group, 2009.

[Gratacos et al., 1992.a)] P. Gratacos, P. Montmitonnet, J.L. Chenot. *An integration scheme for Prandtl-Reuss elastoplastic constitutive equations.* Int. J. Num. Meth. Eng.1992, Vol. 33, pp. 943-961.

[Gratacos et al., 1992.b)] P. Gratacos, P. Montmitonnet, C. Fromholz , J.L. Chenot. *A Plane Strain Elastoplastic Finite Element Model for Cold Rolling of Thin Strip.* Int. J. Mech. Sci. 1992, Vol. 34, 3, pp. 195-210.

[Hacquin, 1996] A. Hacquin. *Modélisation thermomécanique tridimensionnelle du laminage.* PhD Thesis, MINES ParisTech, 1996 (in French).

[Hacquin et al., 1998.a)] A. Hacquin, P. Montmitonnet, J.P. Guilleraut. *A steady state thermo-elastoviscoplastic finite element model of rolling with coupled thermo-elastic roll deformation.* J. Mat. Proc. Tech. 1998, Vol. 60, pp. 109-116.

[Hacquin et al., 1998.b)] A. Hacquin, P. Montmitonnet, J.P. Guillerault. *A 3D semi-analytical model of rolling stand deformation with finite element validation.* Eur. J. Mech. A (Solids), 1998, Vol. 17, 1, pp. 79-106.

[Hitchcock, 1935] J.H. Hitchcock. *Roll neck bearings.* Report ASME Research Committee, 1935.

[Hosfor & Caddell, 1993] W. F. Hosfor, R. M. Caddell. *Metal Forming: Mechanics and Metallurgy*, Prentice Hall, 1993, 2nd edition.

[Howison, 2005] S. Howison. *Practical Applied Mathematics*, Cambridge University Press, Cambridge, 2005.

[Jiang et al., 2003] Z.Y. Jiang, A.K. Tieu, X.M. Zhang, C. Lu, W.H. Sun. *Finite element simulation of cold rolling of thin strip*, 2003 . J. Mat. Proc. Tech. Vol. 140, pp. 542-547

[Jiang et al., 2007] Z.Y. Jiang, H.T. Zhu, D.B. Wei, A.K.Tieu. *Asymmetric Cold Rolling of thin Strip with Roll Edge Kiss*, 2007. Proc. ICIEA 2007 (Harbin, PR China, May 23-25, 2007), pp. 2781-2786, published by IEEE

[Jiang et al., 2008] Z.Y. Jiang, S.W. Xiong, A.K. Tieu, Q.J. Wang. *Modelling of the effect of friction on cold strip rolling*, 2008. J. Mat. Proc. Tech. Vol. 201, pp. 85-90.

[Kalpakian & Schmid, 2003] S. Kalpakian, S.R. Schmid. *Manufacturing Processes for Engineering Materials*, Prentice Hall, 2003, 4th edition.

[Kantola et al., 1996] P. Kantola, T. Pironen, J. Kinnula, J. Pakkari. *An automated flatness monitoring system for steel plate inspection.* Proc. Conference "The control of Profile and Flatness", The Institute of Materials, International Convention Centre, Birmingham, UK, 1996, pp. 34-46

[Knightly, 1967] G. H. Knightly. *An existence theorem for the von Kármán equations.* Arch. Rat. Mech. Anal., 1967, Vol. 27, pp. 233-242.

[Knightly & Sather, 1970] G. H. Knightly, D. Sather. *On nonuniqueness of solutions of the Von Kármán equations* . Arch. Rat. Mech. Anal., 1970, Vol. 36, pp. 65-78.

[Koiter, 1970] W.T. Koiter. *Over de Stabiliteit van het Elastisch Evenwicht*, Thesis, Delft: H.J. Paris, Amsterdam, 1945. English translation issued as Technical Report AFFDL-TR- 70-25, Air Force Flight Dynamics Lab, Wright-Patterson Air Force Base, Ohio, 1970.

[Kpogan, 2011] K. Kpogan. *Flambage sous contraintes résiduelles et application au laminage*, MSc Memoir, Metz, LEM3 - Université de Lorraine, Juin 2011. (in French).

[Krimpelstätter, 2005] K. Krimpelstätter. *Non circular arc temper rolling model considering radial and circumferential displacements*, PhD thesis, Linz University, Austria, 2005.

[Lewicka et al. , 2011] M. Lewicka , L. Mahadevan , R. Pakzad. *The Von Kármán equations for plates with residual strain.* Proc. R. Soc. London, 2011, A. 467, pp. 402-426.

[Marchand, 2000] H. Marchand. *Modélisation de la planéité en sortie de laminage des produits plats.* PhD Thesis, MINES ParisTech, 2000 (in French)

[Meadows et al. , 1970] D. M. Meadows, W.O. Johnson, J.B. Allen. *Generation of surface contours by Moiré patterns.* App. Opt. 1970; Vol. 9, No.4, pp. 942-947.

[Naumann, 1974] J. Naumann. *An existence theorem for the V. Kármán equations under the condition of free boundary.* Aplikace matematiky, 1974, Vol. 19 , No. 1, pp.17-27.

[Newmark, 1943] N.M. Newmark. *Numerical Procedures for Computing Deflections, Moments and Buckling Loads*, Transactions ASCE, Vol. 108, 1943.

[Note MAN v2.0, 2013] S. Abdelkhalek. *Note interne ArcelorMittal Maizières sur les développements de MAN : MAN V2.0, principe physique et mode d'emploi*, 15 Janvier 2013 (in French), Ref 2013-18242.

[Paakkari, 1998] J. Paakkari. *On-line flatness measurement of large steel plates using moiré topography*, Technical Research Centre of Finland (VTT), 1998

[Pardo & Weckman, 1990] E. Pardo, D.C. Weckman. *A fixed grid FE technique for modelling phase change in steady state conduction-advection problems.* Int. J. Num. Meth. Engg 1990, Vol. 29, pp. 969-984.

[Person, 1964] W. J. K. Person. *Shape measurement and control.* J. Inst. Metals, Vol. 93, 1964, pp. 169-178.

[Montmitonnet, 2003] P. Montmitonnet. *Analyses thermomécaniques et applications.* Les Techniques de l'Ingénieur, 2003 (in French).

[Pittner & Simaan, 2011] J. Pittner, M. Simaan. *Tandem Metal Rolling Mill Control*, Springer-Verlag London, limited edition 2011.

[Poincare, 1885] H. Poincaré. *Sur l'équilibre d'une masse fluide animée d'un mouvement de rotation*, Acta Math, 1885, Vol. 7, pp. 259-380.

[Potier-Ferry, 1987] M. Potier-Ferry. *Foundations of Elastic Postbuckling Theory*, of Lecture Notes in Physics, Springer-Verlag, N.Y. 1987, Vol. 288, pp. 1-82.

[Potier-Ferry & Damil, 2010] M. Potier-Ferry, N. Damil. *Influence of local wrinkling on membrane behaviour: A new approach by the technique of slowly variable Fourier coefficients*, J. Mech. Phys. Solids, 2010, Vol. 58, pp. 1139-1153.

[Roberts, 1983] W. Roberts. *Hot Rolling of Steel*, Marcel Dekker, New York, 1983

[Roberts, 1978] W. Roberts. *Cold Rolling of Steel*, Marcel Dekker, New York, 1978

[Roberts, 1988] W. Roberts. *Flat Processing of Steel*, Marcel Dekker, New York, 1988

[Roddeman et al. , 1987.a)] D.G. Roddeman, J. Drukker, C.W.J. Oomens, J.D. Janssen. *The Wrinkling of Thin Membranes: Part I Theory.* ASME Trans., J. Appl. Mech. 1987, Vol. 54, 884-887.

[Roddeman et al. , 1987.b)] D.G. Roddeman, J. Drukker, C.W.J. Oomens, J.D. Janssen. *The Wrinkling of Thin Membranes: Part II Numerical Analysis.* ASME Trans., J. Appl. Mech. 1987, Vol. 54, pp. 888-892.

[Roddeman, 1991] D.G. Roddeman. *Finite Element Analysis of Wrinkling Membranes.* Comm. Appl. Numer. Meth. 1991, Vol. 7, pp. 299-307.

[Schmidt, 1908] E. Schmidt. *Zur Theorie der Linearen und nichtlinearen Integralgleichungen*, Math. Ann., 1908, Vol. 65, pp. 370-379 (in German).

[Shohet & Townsend, 1968] K. N. Shohet, N.A. Townsend. *Roll bending methods of crown control in four-high plate mills.* J. Iron Steel Inst., 1968, pp. 1088-1098.

[Simo & Rifai, 1990] J.C. Simo, M.S. Rifai. *A class of mixed assumed strain methods and method of incompatible modes*, Int. J. Numer. Methods Engrg. Vol. 37, 1990, pp.1595-1636.

[Takasaki, 1970] H. Takasaki. *Moiré topography.* Applied Optics, 1970, Vol. 9, No. 6, pp. 1467-1472.

[Timoshenko & Gere, 1961] S. Timoshenko, J.M. Gere. *Theory of Elastic Stability*, McGraw-Hill, N.Y., 1961, 2nd edition.

[Timoshenko & Krieger, 1959] S. Timoshenko, S. Woinowsky-Krieger. *Theory of Plates and Shells*, McGraw-Hill, N.Y., 1959.

[Ventsel & Krauthammer, 2001] E. Ventsel, T. Krauthammer. *Thin Plates and Shells: Theory: Analysis, and Applications.* CRC Press, 2001.

[von Kármán, 1910] T. von Kármán. *Festigkeitsprobleme im Maschinenbau*, in Encylopädie der Mathematischen Wissenschaften IV/4C, 1910, pp. 311-385.

[Wang et al., 2007] X.C. Wang, Q. Yang, X.Z. Du, Z.Y. Jiang. *Allowable variation of cold-rolled strip transverse profiles in high tension*, 2007, Int. J. Minerals, Metallurgy and Materials, Vol. 17, 5, pp. 608-616.

[Wesfreid & Zaleski, 1984] J.E. Wesfreid, S. Zaleski. *Cellular Structures in Instabilities: Proceedings of the Meeting "Structures cellulaires dans les instabilités - périodicité, défauts, turbulence de phase"*, Lecture Notes in Physics, Springer-Verlag, Heidelberg, 1984, Vol. 210, pp.1-32.

[Wistreich, 1968] J. Wistreich. *Control of strip shape during cold rolling.* Journal of Iron and Steel Institute 1968, pp. 1203-1206.

[Yamada et al., 1992] K. Yamada, S. Ogawa, M. Ataka. *3D analysis of flat rolling using rigid-plastic FEM coupled with roll deformation analysis.* Proc. Numiform 92, Chenot JL, Wood RD & Zienkiewicz OC, eds, Balkema, Rotterdam, 1992.

[Yuen et al., 2003] W. Y. D. Yuen, Z. H. J. Gu, B. Shumack, Y. Popelianski. *Eliminating tight edge waves in the cold rolling of thin-gauge strip.* SEAISI quarterly 2003 Vol. 32, pp. 29-37.

[Yukawa, 1986] N. Yukawa, T. Ishikawa, Y. Tozawa. *Numerical analysis of the shape of rolled strip.* In Proc. NUMIFORM Conference, Gothenburg, Sweden, 1986, pp. 249-254.

[Zahrouni, 1998] H. Zahrouni. *Méthode Asymptotique Numérique pour les coques en grandes rotations.* Thèse, LPMM - Université de Metz, 1998 (in French).

[Zahrouni et al., 1999] H. Zahrouni, B. Cochelin, M. Potier-Ferry. *Computing finite rotations of shells by an asymptotic numerical method.* Comput. Meth. Appl. Mech. Engg, 1999, Vol. 175, pp. 71-85.

Méthode multi-échelle pour la modélisation du flambage des tôles minces sous contraintes résiduelles – Application au laminage à froid

RESUME La modélisation des défauts de planéité apparaissant en ligne en laminage à froid des tôles minces est abordée comme un problème de flambage de tôles minces sous contraintes résiduelles. Celles-ci sont les contraintes engendrées au-delà de l'emprise par le laminage lui-même. Pour cela, un modèle de flambage et post-flambage de tôle (forme, amplitude, contraintes) fondé sur la méthode multi-échelle de Damil et Potier-Ferry, et nommé **MSBM** pour Multi-Scale Based Method**,** a été développé. En entrée, on y introduit une carte de contraintes post-emprise venant d'un calcul de laminage. Les hypothèses simplificatrices du modèle de flambement permettent de ramener sa résolution à un ensemble de problèmes éléments finis 1D, mais de ce fait restreignent l'analyse aux défauts de type bord long ou centre long. Dans sa version découplée, ce modèle a été comparé avec succès à des résultats de la littérature. Il permet d'effectuer des études paramétriques d'intérêt pratique, comme l'influence du frottement ou de la force de contre-flexion des cylindres sur l'état de contrainte et la géométrie de la tôle.
Dans un second temps, ce modèle est introduit comme modèle de flambage intégré dans le logiciel éléments finis de laminage Lam3/Tec3. Comme dans le modèle précédent implémenté par Abdelkhalek en 2010, **MSBM** calcule un champ de déformation lié spécifiquement aux déplacements hors-plan caractérisant le flambage, champ de déformation qui est ajouté à la décomposition élastique – plastique et réactualisé à chaque itération du calcul éléments finis. Des comparaisons ont été effectuées avec les deux modèles couplés précédemment implantés par Abdelkhalek. Elles montrent les insuffisances du présent modèle de flambage, unidirectionnel, qui ne permet pas de traiter toutes ensemble les diverses instabilités, d'orientations différentes, qui ont lieu après la sortie d'emprise et se révèlent fortement couplées entre elles. Des pistes d'amélioration sont proposées en conséquence.

Mots clés : Laminage à froid, Tôle mince, Flambage, Post-flambage, Contraintes résiduelles, Méthode éléments finis, Méthode multi-échelle

Multi-scale method for modelling thin sheet buckling under residual stress in the context of cold strip rolling

ABSTRACT : Modelling of on line manifest flatness defects in thin strip cold rolling is addressed as a problem of buckling under residual stresses. The latter are stresses built beyond the roll bite by the rolling process itself. To this aim, a buckling / post buckling model has been developed, giving strip shape, amplitude and stresses, based on Damil and Potier-Ferry's method and hereafter named MSBM like Multi-Scale Based Method. Its input is a post-bite stress map computed by a rolling model. Simplifications of the buckling model make it amenable to a series of 1D FEM solutions, but restrict its application to simple flatness defects such as wavy edges or wavy centre. In a decoupled version, it has been successfully compared with literature results. It allows parametric studies of practical interest, such as the influence of friction or work roll bending force on post-buckled strip shape and stress.
In a second stage, this model is implemented as the internal buckling model in the FEM software Lam3/Tec3. As the previous one, implemented by Abdelkhalek in 2010, MSBM computes a strain field strictly due to the out-of-plane displacement which characterizes buckling. This strain field is introduced into the elastic – plastic decomposition and updated at each iteration of the finite element computation. Comparisons have been performed with the two models previously coupled to Lam3/Tec3 by Abdelkhalek. They show the limits of the present unidirectional buckling model, which cannot deal with all instabilities together, which have different orientations and take place after roll bite exit, which furthermore prove to be strongly interacting. Ideas for future generalization of the coupled model are proposed accordingly.

Keywords : Cold rolling, Thin strip, Buckling, Post-buckling, Residual stress, Finite element method, Multi-scale method

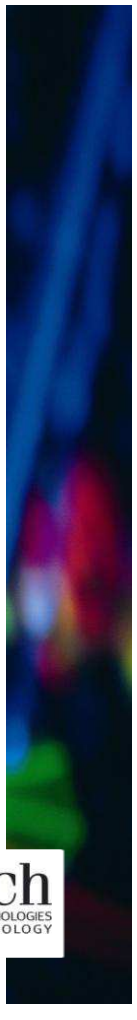

MINES ParisTech

ParisTech
INSTITUT DES SCIENCES ET TECHNOLOGIES
PARIS INSTITUTE OF TECHNOLOGY